

Quantum Information Processing with Two Trapped Cadmium Ions

by

Patricia J. Lee

A dissertation submitted in partial fulfillment

of the requirements for the degree of

Doctor of Philosophy

(Physics)

in The University of Michigan

2006

(reprinted in 2016, text searchable)

Doctoral Committee:

Professor Christopher R. Monroe, Chair

Professor Philip H. Bucksbaum

Associate Professor Cagliyan Kurdak

Assisitant Professor Luming Duan

Assistant Professor Yaoyun Shi

To Mom and Dad

Acknowledgements

First, I would like to thank my advisor Chris Monroe for the opportunity to work on this exciting research and for the experience of building a new lab. The past five years have been a lot of fun, and I really appreciate the guidance and support he has given me.

I would also like to thank the other members of the group for the work their contribution to the experiments in this thesis and for their camaraderie in the lab. I thank Louis Deslauriers for offering me way too many hours of enjoyable conversation both physics and non-physics related; Paul Haljan for showing me how to be a better experimental physicist; Winfried Hensinger for the discussion sessions that made me learn, teach, and argue about physics more than I would ever do otherwise; Kathy-Anne Brickman for working on the L-table together; Boris Blinov for those early years when I had no clue how a lab works let alone how to set one up; Mark Acton for working on the experiments together and providing hardware and software support; Martin Madsen for the design of the three layer linear trap and the LabView programs; also Russ Miller, David Moehring, Dan Stick, Peter Maunz, David Hucul, Rudy Kohn, and Mark Yeo for all their assistance in lab. And for Steve Olmschenk, Jon Sterk, Kelly Younge and Elizabeth Otto who have joined the group more recently, I hope they will have a wonderful experience working in lab as I had.

Special thanks to the members of my committee, Phil Bucksbaum, Cagliyan Kurdak, Luming Duan, and Yaoyun Shi, for their helpful feedback on my dissertation. Thanks also to Jens Zorn, Jim Rabchuck, Chitra Rangan, and Ralph Conti for their involvement in our lab. I would also like to thank Paul Berman, Ted Norris, Roberto Merlin, Tim Chupp, Herb Winful, and the rest of the faculty in the physics department and the EECS department at University of Michigan who have taught me so much. Thanks too to Dave Wineland, Wayne Itano, John Bollinger, Jim Berquist and others in the Ion Trapping and Storage Group at NIST and in other ion trap research groups around the world, for sharing their knowledge and expertise. I am also grateful to my alma mater Caltech for introducing me to a whole new world that I couldn't even imagine before.

I would also like to say thanks to the physics department staff for their diligent work in maintaining smooth operation in the department. Special thanks to Kimberly

Smith in the Graduate Student Affairs Office, Katherine Richards and Michelle Young in the AMO/FOCUS Business Office, Julian Broad and Ted Webster at the Student Machine Shop. Thanks also to the staff at the Office of Computing Services, Technical Services, Business office, and Gordon Cooper and the custodial staff.

I am very fortunate to have good friends along my journey through graduate school. Thanks to Yanwen Wu for tackling physics together, whether it's in the classroom or in the pool room; to Erica Newman for giving me the best advice ever; also to Joel Murray, Tara Cubel, Jimin Zhao, Elaine Li and Jie Li. Thanks to Walter Collins for the years at Willowtree, and to the Avery Upper Guard Tower gang for technical advice and etc. And a very loud meep to Vidya Bhalodia for the ytalk therapy.

Finally, I want to thank my parents for all the sacrifices they have made for me to be where I am today. Their courage is an inspiration to me, and their encouragement for me to pursue my dreams means a lot to me. I also want to thank my brother Steven and my sister Amy for always being there for me and always challenging me to do better. I would also like to thank my grandparents, who understood the importance of education even when they had none, and had the wisdom to instilled those values in their children and grandchildren. I am very fortunate to have another set of wonderful parents, Judy and Stephen Lucchetti, who have done so much for me while I am in graduate school and are always interested in my research. And to my husband Dominic, who started me down this path many years ago by making me believe I can do it, my love and gratitude.

Contents

Dedication	ii
Acknowledgements	iii
List of Figures	vii
Abstract	x
Chapter 1. Introduction	1
1.1. Quantum Information	1
1.2. Ion Trap	2
1.3. Requirements of a Quantum Computer	3
Chapter 2. Ion Trapping	4
2.1. Trapping Ions	4
2.2. Cadmium 111 as a Qubit	17
2.3. Lasers and Imaging System	19
2.4. Experiment Setup	27
Chapter 3. Single Ion Coherent Operations	34
3.1. Notation	34
3.2. Single Qubit Rotation	35
3.3. Coupling Spin to Motion	37
3.4. Microwave Transitions	40
3.5. Stimulated Raman Transitions	41
3.6. Generating Coherent Optical Fields with a Microwave Frequency Splitting	49
3.7. Experiment Details	51
3.8. Experiment Data	54
3.9. Cooling to the Ground state of motion	58
Chapter 4. Spin-Dependent Forces	65
4.1. Spin-Dependent Forces	65
4.2. The $\hat{\sigma}_\phi$ -force	68
4.3. The $\hat{\sigma}_z$ -force	84

Chapter 5. Two-Ion Entangling Gates	88
5.1. Entanglement through geometric phases	89
5.2. σ_ϕ force gate	91
Chapter 6. Quantum State Tomography	103
6.1. Tracking the phase	104
6.2. Individual qubit rotation	106
6.3. Tomography	109
Chapter 7. Conclusion	116
Appendices	118
Appendix A. Interaction Picture	118
Appendix B. Cavity Modifications	121
Appendix C. Mixing of EOM Frequency Sidebands	125
Appendix D. Forced Harmonic Oscillators	127
Appendix E. Quantum Interference between Coherent States	129
Appendix F. Differential Stark Shift on Magnetic Field Insensitive States	133
Appendix G. Two-ion Interactions	135
G.1. carrier transition	135
G.2. First sideband transitions	136
Bibliography	138
Index	142

List of Figures

2.1.1	Schematic diagrams of the ion trap electrodes	6
2.1.2	Vacuum apparatus enclosing the three-layer linear trap	7
2.1.3	Helical resonator for transforming rf	9
2.1.4	Energy levels of neutral cadmium ions	11
2.1.5	CCD image of 6 ions in the three-layer linear trap	14
2.1.6	Cadmium isotope abundances and energy shifts	14
2.1.7	Effect of micromotion on the Doppler lineshape	15
2.2.1	Internal energy levels of a $^{111}\text{Cd}^+$ ion	17
2.3.1	Schematic of the laser system for detecting Cd^+ ions	20
2.3.2	Schematic diagram of the MBR-110 Ti:Sapphire laser	21
2.3.3	Setup for saturated absorption spectroscopy of tellurium	22
2.3.4	Circuit diagram for the servo lock in the tellurium setup	23
2.3.5	Circuit diagram for laser frequency sweep and offset	23
2.3.6	Tellurium absorption lock-in error signal	25
2.3.7	Relative frequencies for detection, initialization, and Doppler cooling	26
2.4.1	General experiment pulse sequence	28
2.4.2	Histogram of photon counts from a single ion	30
2.4.3	Poisson distribution of photon numbers for two ions	31
2.4.4	Histogram of photon counts from two ions	31
2.4.5	Detection error for two ions	32
2.4.6	Detecting the state of two qubits with an intensified CCD camera	32
3.4.1	Orientation of the microwave horn	39
3.4.2	Rabi oscillations driven by microwaves	40
3.5.1	Stimulated Raman transition via an excited state	42
3.5.2	Stimulated Raman transition between vibrational levels	44
3.5.3	Diagram of non-copropagating Raman beam setup	45

3.5.4	Branching ratios of the $S_{1/2} \leftrightarrow P_{1/2}$ transitions	46
3.5.5	Branching ratios of the $S_{1/2} \leftrightarrow P_{3/2}$ transitions	47
3.7.1	Synthesizers with phase lock capability for generating coherent Raman beams	53
3.8.1	Single ion Raman spectrum from scanning the EOM frequency	55
3.8.2	Single ion Raman spectrum from scanning the AOM frequency	57
3.8.3	Rabi flopping on a single ion using stimulated Raman transition	58
3.8.4	Rabi frequency vs. Mach-Zehnder path length difference	58
3.8.5	Rabi flopping on a single ion driven by copropagating Raman beams	58
3.8.6	Rabi frequency vs EOM modulation index at different cavity detuning δ	59
3.9.1	Rabi flopping at high temperature vs low temperature	59
3.9.2	Raman sideband cooling process	60
3.9.3	Raman spectra for Doppler cooling and sideband cooling	63
3.9.4	An example of heating data taken in the quadrupole trap	64
4.1.1	A spin-dependent force applied to the eigenstates of $\hat{\sigma} \cdot \mathbf{n}$	67
4.2.1	Optical fields generating a $\hat{\sigma}_\phi$ -dependent force	69
4.2.2	Fluorescence signal vs detuning of the $\hat{\sigma}_\phi$ force	70
4.2.3	Fluorescence signal vs duration of the $\hat{\sigma}_\phi$ force	71
4.2.4	Fluorescence signal from a thermal ion vs detuning of the $\hat{\sigma}_\phi$ force	72
4.2.5	Fluorescence signal from a thermal ion vs detuning of the $\hat{\sigma}_\phi$ force	72
4.2.6	Vector and frequency configurations for applying the $\hat{\sigma}_\phi$ force	74
4.2.7	Calibration of sideband detunings δ_r and δ_b	75
4.2.8	Probability $P(\downarrow)$ plotted vs. detuning δ of the $\hat{\sigma}_\phi$ force	76
4.2.9	Single ion evolution due to a spin-dependent bichromatic force	77
4.2.10	Possible beam configurations for the σ_ϕ gate	79
4.2.11	Phase sensitivity of the σ_ϕ force for different beam configurations	81
4.3.1	Optical fields generating a $\hat{\sigma}_z$ -dependent force	83
4.3.2	Probability $P(\downarrow)$ vs. detuning of the $\hat{\sigma}_z$ -force	86
4.3.3	Ramsey experiment to test the coherence of qubits	87
5.2.1	Two views of the Mølmer-Sørensen $\hat{\sigma}_\phi \otimes \hat{\sigma}_\phi$ entangling gate	91
5.2.2	Schematic of the noise eater feedback loop	94

5.2.3	Circuit diagram for the noise eater	95
5.2.4	Noise spectrum comparison with and without the noise eater	96
5.2.5	Measurement of differential AC Stark shifts on two ions	98
5.2.6	Raman spectrum of two ions in the trap	99
5.2.7	Average brightness S versus σ_ϕ force gate detuning δ	99
5.2.8	Time scan of σ_ϕ force gate showing	101
5.2.9	Histogram of photon counts collected from the entangled state	101
5.2.10	Parity vs phase of analysis $\pi/2$ pulse applied to the Bell state Ψ_1	102
6.2.1	Composite pulse sequence for individual qubit rotations	107
6.2.2	Measurement of the differential AC Stark shift between two ions	108
6.3.1	Projective measurements for tomography	110
6.3.2	Tomography of $ \uparrow\uparrow\rangle$ state	111
6.3.3	Tomography of $ \downarrow\uparrow\rangle$ state	112
6.3.4	Tomographically reconstructed density matrices for the four Bell-like entangled states	113
B.0.1	Schematic of the WaveTrain BBO cavity	123
B.0.2	Cavity parameters for the WaveTrain frequency doubler	123
B.0.3	Optical power of the BBO output vs modulation frequency of the EOM	124
G.2.1	Vibrational sideband transition with two ions	136

Abstract

Quantum information processing combines information theory with laws of quantum mechanics to provide an interesting new study that promises significant technological advances in the field of computation. The quest for a physical quantum information processor not only tests the limits of quantum mechanics but also motivates the development of new control techniques for quantum systems.

This thesis documents the implementation of the necessary components of a quantum computer in a new atomic ion species, while demonstrating an entangling procedure that is uniquely insensitive to certain types of phase noise. Quantum bits are stored in the ground state hyperfine levels of individual trapped cadmium ions, and the collective vibration of the ions in the trap potential form a quantum databus through which information can be transferred. Quantum state measurements and initialization processes are accomplished through optical pumping, and quantum logic operations are performed through interactions with applied electromagnetic fields. The spin-dependent force, which is the underlying principle of many entanglement schemes for trapped ions, is investigated in detail in a series of "Schrödinger cat" experiments that generates entangled wavepackets well separated in the momentum-position phase space ($\alpha = 6$). Phase control of the interaction in the gate scheme proposed by Mølmer and Sørensen results in phase coherence between single-qubit rotations and a robust two-qubit entangling logic gate that can operate on magnetic-field insensitive "clock" qubits at finite temperature. The coherence time of the clock qubit (~ 1 s) is long compared to the gate time ($\sim 100\mu\text{s}$). Finally, quantum state tomography is performed on two ions, featuring a set of universal quantum logic gates that is sufficient for any quantum computation, with an entangling gate fidelity of 0.83.

The combination of the tools developed here is sufficient to perform universal quantum computation. With the advent of scalable, multi-zone ion trap structures, the concept of a quantum computation device may become reality in the not so distant future.

CHAPTER 1

Introduction

1.1. Quantum Information

In recent years there has been exciting and active research in the field of quantum information. This strong interest is based on the idea of exploiting the properties of quantum mechanics to perform computations, which in certain cases can vastly exceed the capabilities of classical computers. While this concept was conceived by Richard Feynman [1] more than twenty years ago, the field of quantum information has only begun to change from science fiction to reality in the past decade.

Quantum information gained much attention in 1994 when Peter Shor presented an explicit quantum factoring algorithm that was exponentially more efficient than any known classical algorithm [2]. The realization of Shor's algorithm would make many current encryption schemes obsolete, since they can be neutralized if large numbers can be factorized easily. Using classical computers, the resources required to factor a large number grow exponentially with each additional digit, and currently there exist insufficient computing resources to factor the large numbers used in encryption by our government and financial institutions. The creation of a quantum computing device could alter this fact. Ironically, quantum mechanics also provides an alternative method for secure information transfer by sending correlated quantum bits for encoding and decoding a message using Quantum Key Distribution schemes [3, 4], which have been proven to be unconditional secure, in contrast with the fact that most parts of classical cryptography are based on unproven assumptions. Thus, the development of quantum information processing devices became a serious pursuit in the research community.

From a scientific standpoint, quantum information processing has the potential to remove certain limitations of classical computer. For example, Grover's algorithm, which performs exhaustive searches over the set of possible solutions for ones that satisfy certain requirements, can achieve quadratic speed up for solving non-determinant polynomial (NP) complete problems [5]. Another application is modeling quantum systems using a "quantum simulator", providing access to degrees of freedom unavailable in physical systems for testing theories in condensed matter and other fields,

which can lead to better understanding of the world on a quantum level. Constructing a physical quantum computer is also a fantastic testbed for quantum mechanics at a macroscopic scale. However, the implementation of quantum computation devices is still in its infant stage, and may take many more decades of research to achieve the predicted results. This thesis is part of a long term effort toward these foreseeable advances using quantum computation, with the goal of eventually developing a quantum mechanical version of the universal Turing machine.

The rate of advancement of computers has been guided by Moore's Law, which claims that the number of transistors in the most advanced computer will double every eighteen months. At the current rate, the size of the transistors in classical computers will reach a scale where quantum effects become significant. Therefore it is inevitable that quantum mechanics will play an important role in computer technology.

1.2. Ion Trap

Since Hans Dehmelt and Wolfgang Paul developed the first ion traps [6, 7], for which they received the Nobel prize in 1989, the ability to trap ions has contributed to many advances in atomic physics, including laser cooling [8] and atomic clocks [9], as well as applications such as mass spectrometers. Quantum information was first introduced to the ion trap system in 1995 when Cirac and Zoller proposed a scheme for implementing a quantum controlled-NOT gate in trapped ions by coupling the internal state of two ions with their external vibration [10]. Since then a host of theoretical and experimental work has pushed the trapped ion system to become one of the most promising architectures for quantum computing. The key step in the Cirac and Zoller scheme was demonstrated experimentally by Monroe *et al* in the same year [11], though the complete gate operation was realized more recently by Schmidt-Kaler *et al* in 2003 [12]. However, other quantum gate schemes equivalent to the controlled-NOT gate have been proposed and implemented in trapped ion systems in the meantime [13–17]. These gates rely on the concept of a spin-dependent force and have many improved characteristics compared to the original Cirac and Zoller proposal. In addition, the idea of a quantum charge-coupled device has also been proposed as a scalable architecture for trapped ion quantum computing, using an array of trap zones where ions can be stored and transported to specific locations for computation when required [18]. These theoretical and experimental work provide a foundation for trapped ion quantum computing and a complete framework for a scalable universal quantum processor.

1.3. Requirements of a Quantum Computer

The criteria for the physical realization of quantum computation are [19]: 1) a scalable physical system with well characterized qubits; 2) the ability to initialize the state of the qubits to a simple fiducial state; 3) long relevant decoherence times, much longer than the gate operation time; 4) a “universal” set of quantum gates; and 5) a qubit-specific measurement capability. This thesis presents the complete development of a two qubit quantum computer in a new trapped ion species. While all of the criteria listed above have also been demonstrated in other trapped ion systems, many of which are concurrent with this thesis work, the experiments here are performed using cadmium ions, which have atomic properties that are favorable for long coherence in terms of qubit memory as well as gate operations. A careful analysis of the spin-dependent force reveals that the two-qubit entangling gate scheme proposed by Mølmer and Sørensen [13, 20] can be phase stabilized, and its insensitivity towards fluctuating background electric and magnetic fields makes it a robust gate scheme. Finally, the components are combined to perform more complicated operations involving multiple gate operations. These demonstrations show that the system has the capability of performing sequences of quantum logic operations. Although the experiments here are limited by two qubits of quantum memory, the techniques developed here are applicable to a large number of qubits in scalable, multi-zone trap structures.

CHAPTER 2

Ion Trapping

This chapter outlines the physical apparatus and the basic functions of ion trapping, including the ion traps and its loading mechanisms, and the laser system for probing the ions. The details are provided here without the more complicated quantum logic operations, which are discussed in the following chapters. Although ion trapping has been available for several decades, the specific parameters for the experiments are carefully chosen and tested in the laboratory for quantum computation with trapping cadmium ions. The physical system contains quantum mechanical degrees of freedom which are employed for computing purposes, such as the qubit stored in the internal electronic structure of the ion and the external quantum mechanical motion of the ions in the trap available for quantum information transfer. Basic operations such as initialization and detection of the qubits can be performed with a specialized laser and imaging system. This chapter sets up the complete framework within which quantum information processing can be implemented.

2.1. Trapping Ions

2.1.1. Ion Trap Basics. The ion traps used in this thesis operate based on the design invented by Wolfgang Paul [21] that confine charged particles with an electric quadrupole field oscillating at radio frequency (rf), also called “Paul” or “rf” traps. Two types of traps are used in the experiments in this thesis: a “ring-and-fork” asymmetric quadrupole trap and a three-layer linear trap (see figure 2.1.1). In the ring-and-fork trap, the potential near the center of the trap can be modeled as an asymmetric quadrupole potential when a rf potential $V_0 \cos(\Omega_T t)$ is applied to the ring electrode and a static potential U_0 is applied to the end-caps. The potential at coordinate (x, y, z) is given by

$$(2.1.1) \quad V(x, y, z) = \kappa (U_0 + V_0 \cos(\Omega_T t)) \left(\frac{\alpha x^2 + (2 - \alpha)y^2 - 2z^2}{d_0^2} \right),$$

where $\alpha \sim 0.8$ and $\kappa \sim 0.8$ are parameters determined by the geometry of the electrodes, $d_0 = \sqrt{r_0^2 + 2z_0^2}$ is the characteristic internal dimension of the trap, with r_0 being the radius of the ring electrode and $2z_0$ being the separation between the two end-caps (see figure 2.1.1a). For ideal hyperbolic electrodes, $\alpha = \kappa = 1$. The

equations of motion are

$$\begin{aligned}
& \ddot{x} + \frac{2e\alpha\kappa}{md_0^2}(U_0 - V_0\cos(\Omega_T t))x = 0 \\
& \ddot{y} + \frac{2e(2-\alpha)\kappa}{md_0^2}(U_0 - V_0\cos(\Omega_T t))y = 0, \\
(2.1.2) \quad & \ddot{z} - \frac{4e\kappa}{md_0^2}(U_0 - V_0\cos(\Omega_T t))z = 0.
\end{aligned}$$

where m is the mass of the ion and e is the electric charge. For now let's consider the motion along one dimension, say the x axis. The equation of motion can be transformed into the standard Mathieu equation [22] with dimensionless parameters

$$(2.1.3) \quad \frac{d^2x}{d\tau^2} + (a + 2q\cos 2\tau)z = 0,$$

where

$$\begin{aligned}
(2.1.4) \quad & a = \frac{8eU_0\alpha\kappa}{md_0^2\Omega_T^2} \\
& q = \frac{4eV_0\alpha\kappa}{md_0^2\Omega_T^2} \\
& \tau = \frac{\Omega_T t}{2}.
\end{aligned}$$

The lowest-order approximation yields a solution

$$(2.1.5) \quad x(t) = x_0 \cos\left(\beta \frac{\Omega_T}{2} t\right) \left[1 - \frac{q}{2} \cos(\Omega_T t)\right],$$

where $\beta = \sqrt{a + q^2/2}$, and x_0 depends on the initial conditions. The slower oscillation at frequency $\omega_x = \beta\Omega_T/2$ is called the “secular motion”. When $a \ll q^2 \ll 1$ and $U_0 \simeq 0$, then the ion acts as though it is confined in a harmonic pseudo-potential where

$$(2.1.6) \quad V = \frac{1}{2}m\omega_x^2 x^2,$$

with $\omega_x = \sqrt{2}eV_0\alpha\kappa/(md_0^2\Omega_T)$ being the secular frequency. The secular motion is used as a quantum databus where information can be transferred from one ion to another. The oscillation at the faster rf frequency $\cos(\Omega_T t)$ is called the “micromotion” because the amplitude is suppressed by $q/2 = 2\sqrt{2}\omega/\Omega_T$.

The secular frequencies of the asymmetric quadrupole trap are non-degenerate in all three dimensions, with ratios of $\omega_x : \omega_y : \omega_z$ being approximately 2 : 3 : 5. These ratios can be changed by biasing the static potential U_0 . In general, the trap

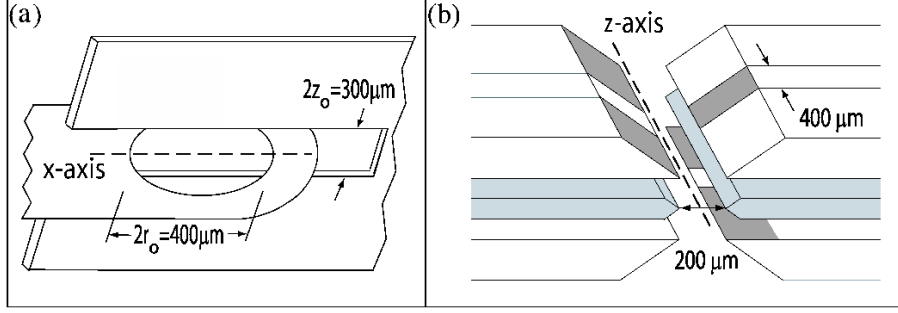


FIGURE 2.1.1. Schematic diagrams of the ion trap electrodes. (a) Asymmetric quadrupole trap with a $400\mu\text{m}$ diameter ring electrode and a $300\mu\text{m}$ gap between the fork electrodes. The rf is applied to one electrode while the other electrode is held at rf ground with a possible dc offset. (b) Three-layer linear trap made of gold-coated electrodes on alumina substrates. The rf is connected to the middle layer which is $125\mu\text{m}$ thick, while static voltages are connected to the electrodes on the segmented outer layers that are $250\mu\text{m}$ thick (the grounded electrodes are shaded in dark gray while bias potentials are applied to the others). The layers are separated by alumina spacers (not shown) with a thickness of approximately $0.3\mu\text{m}$. In the experiments, the ions are coupled to motion in the direction z_T defined to be the x-axis in the asymmetric quadrupole trap shown in (a) and the z-axis in the linear trap shown in (b).

frequencies in the three principal axes is best kept non-degenerate to simplify the normal oscillation modes of the ions and for Doppler cooling to be effective.

The idealized linear trap consists of four rods running parallel along the z axis. Rf is applied to a pair of diagonal electrodes while static potential is applied to the other two, which are segmented. The outer segments are held at U_0 while the middle segments are held at ground. In this case, the potential becomes

$$V = V_0 \cos \Omega_T t \left(\frac{x^2 - y^2}{r_0^2} \right) + \kappa U_0 \left(\frac{2z^2 - x^2 - y^2}{2} \right),$$

where κ is a geometric factor. The trap provides a static harmonic potential in the z direction, with oscillation frequency $\omega_z = \sqrt{2\kappa U_0 q/m}$. Along the axis of the trap where $x = y = 0$, there is no micromotion. Compared to the ring-and-fork trap, where the rf node is a single point at the center of the trap, the linear trap can support many ions at its rf nodal line simultaneously and avoid unwanted micromotion.

The actual linear trap used in the experiments consist of gold electrodes plated on three layers of alumina substrates. Rf is applied to the center layer, while the outer layers are segmented in the axial direction and held at DC voltages. Positive voltages are applied to the end segments and negative voltages to the middle segments to

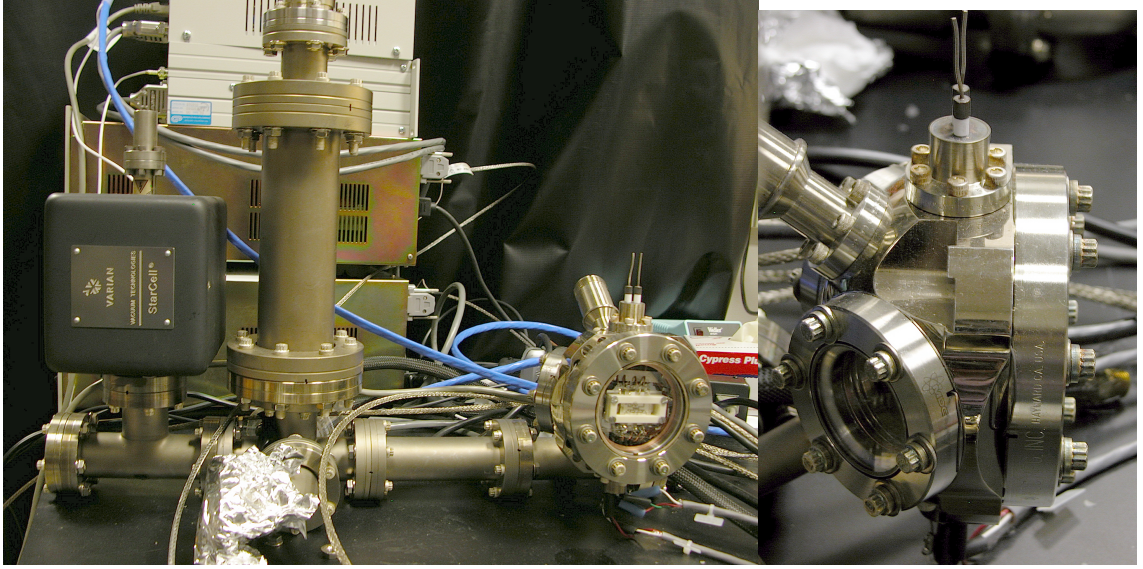


FIGURE 2.1.2. (Left) Vacuum apparatus enclosing the three-layer linear trap. Located inside the 4 inch diameter hemispheric chamber in the lower right corner, the trap is visible from the large quartz window. The rf resonator is connected to the trap electrodes by the feedthroughs on top of the chamber. The vertical structure in the middle is the titanium sublimation pump, with the ion pump to its left. The feedthroughs for the ion gauge is not visible from this angle. (Right) Side view of the vacuum chamber. Two windows at 45° allow laser access to the ions inside the trap.

provide axial confinement. Voltage differentials are applied to the electrodes in the front and the back layer to tilt the transverse principle axes defining the independent modes of oscillation. This is important for effective Doppler cooling in all dimensions in a later discussion. The flexibility of biasing the static potential at each electrode independently also allows us to cancel excess micromotion due to background static electric fields (see section 2.1.6 for further discussion).

2.1.2. The vacuum system. Each ion trap is positioned under ultra high vacuum ($< 10^{-11}$ Torr) inside a 4 inch diameter hemispheric chamber (see fig 2.1.2). The chamber has optical access from the cross section of the hemisphere and two smaller windows at 45° around the equator and forming a right angle with each other. Each trap is placed so the weakest axis is horizontal and parallel to the large vacuum window and the geometry allows optical access to the trap region from every window. The chamber is attached to a continuously running Varian ion pump with nominal pumping speed of 20 liter/second, and also outfitted with a titanium sublimation pump. The system also contains an ion gauge capable of detecting pressures down

to 10^{-11} Torr, and sometimes a mass spectrometer/residual gas analyzer (RGA) to monitor the concentrations of cadmium vapor or detect leaks.

To achieve ultra-high vacuum (UHV) pressures, the stainless steel vacuum parts are first baked at 400°C for a day or two before assembly. This forms an oxide layer on the surfaces which reduces the outgassing of stainless steel. Surfaces to be exposed to a vacuum are cleaned with an ultrasonic hot acetone bath for at least half an hour. The vacuum system is then assembled with the trap, electron guns, cadmium ovens, and electrode connections installed. A mechanical pump (model TSU 071 from Pfeiffer Vacuum) is used to attain pressures down to 10^{-6} Torr before the final bake. The temperature is raised slowly in 20°C increments about every hour, in order to prevent differential expansion between vacuum parts that may cause a leak. Baking removes water and hydrocarbons from vacuum system walls [23], and the final temperature at 200°C for our system is restricted by the temperature tolerance of the seal for the quartz windows, which allow UV optical access to the trap. Current is passed through the electron guns and the cadmium ovens to remove dirt that may outgas later when these equipment are in use. At 200°C and 10^{-6} Torr, the valve connecting the vacuum system to the mechanical pump is closed and a 500 liter/second ion pump (model P-E 500 STD by Perkin Elmer) is connected to the vacuum system and turned on. The bake continues for more than a week and is closely monitored as the ion pump reduces the pressure to 10^{-7} or 10^{-8} Torr. Finally, the valve to the large 500 liter/second ion pump is closed, and the system is returned to room temperature slowly, again at the rate of about $20^{\circ}\text{C}/\text{hour}$. The vacuum system is rested for a few days until the pressure level reaches steady state, and the small 20 liter/second ion pump can be turned on in the mean time. The titanium sublimation pump, which operates by heating a filament containing titanium to a temperature where the metal sublimates from the filament to the nearby walls of the vacuum system, is turned on for 2 minutes with 40 Amps of current once each hour for 5 to 10 times. The titanium film on the vacuum system walls combines with the active gases as the gas molecules strike the wall and removes them from the vacuum system. The final pressure should reach below 10^{-10} Torr. The small ion pump runs continuously as long as the system is under vacuum.

Trap voltages are controlled from the outside and connected to the electrodes via feedthroughs. An rf resonator consisting of a helical coil inside an enclosed cylinder made of copper [24] transforms a 2W rf signal from an amplified source to high voltage and is attached to the trap electrodes via vacuum feedthroughs (see figure). The input rf is coupled capacitively to the resonator via a wire loop inside the cylinder,



FIGURE 2.1.3. Helical resonator for transforming rf. The helical coil design reduces the length of the resonator (compared to $\lambda/4$ for a linear coil design). The rf load is connected to the outer conductor (ground) and the inner coil. The rf input (typically 2W at 50MHz) is connected to the capacitively-coupled wire loop on one end of the resonator, and the transformed rf has amplitude $V_0 \approx 200\text{V}$, with a loaded Q of ~ 300 .

and has a typical resonant frequency at around 50MHz. Typical loaded Q factor is >300 , translating to approximately $V_0 = 200\text{V}$ at the trap electrodes.

2.1.3. Loading Ions. The original design for loading ions is as follows: cadmium or cadmium oxide metal inside an alumina tube is heated by passing current through a tungsten coil to produce a beam of atomic vapor aimed in the vicinity of the trap; an electron gun consisting of a charged plate with an aperture in front of a heated tungsten coil generates a beam of electrons also aimed at the trap region. The high velocity electrons ($\sim 100\text{eV}$) collide with the neutral cadmium atoms and ionize them, leaving the positively charged cadmium ions inside the trap. If the atoms are ionized outside the trap region, conservation of energy dictates that the ion entering the trap region has higher energy than the trap barrier, therefore these ions will not stay trapped. On the other hand, if the atoms are ionized inside the trapping region, then the ions can not escape as long as the depth of the trap is larger than the initial kinetic energy of the ion. With careful alignment of the cadmium oven and the electron gun with respect to the trap electrodes, this method is very effective at loading ions into the trap.

The difference between cadmium and cadmium oxide ovens is the melting temperature: 765°C for cadmium and 1559°C for cadmium oxide. Since the vacuum chamber needs to be baked at 200°C for about a week in order to reach ultra high vacuum (maximum temperature limited by the vacuum window seal), the result is an

observable layer of cadmium coating on the trap electrodes if cadmium metal is used. This atomic deposition can be avoided by using cadmium oxide metal, at the cost of heating the alumina tube casing to a much higher temperature to produce cadmium atomic vapor for loading ions. The cadmium oxide ovens often require several minutes of continuous heating to reach melting temperature where a pressure increase can be observed, while cadmium ovens reach melting point on the order of seconds. For the electron gun, the tungsten coil is usually heated until the black body radiation is visible, but the electron emission is not noticeable unless the aperture plate is biased to 100V. Normally, the electron gun is turned on for no more than the time it takes to collect $100\mu\text{A}$ of total emission current.

However, there are several drawbacks to ionizing cadmium atoms with high velocity electrons. The cadmium oven and especially the electron gun create a significant increase in pressure (from $< 10^{-11}$ to 10^{-8}) inside the vacuum chamber, which remains relatively high even after they are turned off for half an hour or more (pressure typically drops to 10^{-10} a few minutes after the electron gun is turned off). This increase in the background gas and ion collision rate reduces the ion lifetime in the trap from several hours to several minutes, leaving insufficient time to perform experiments. The ionization rate can also be too high that a cloud of ions always result from loading, making it nearly impossible to isolate exactly one or two ions of the desired isotope in the trap.

While experimenting with the ion traps, new techniques were discovered that conveniently avoids the problem with pressure built up. When a couple milliwatt of the 214.5nm laser used to Doppler cool the ion is directed on the electrode, ions appear in the trap. Although the exact mechanism is not understood, the hypothesis is that the laser excites the electrons in the metal to overcome the work function at the metal/vacuum interface or to allow electrons to tunnel through that potential barrier during certain phases of the rf. The electrons are then accelerated through the trap region within less than a cycle of the rf and ionizes neutral atoms in their path. This effectively creates a localized electron beam at the trap, resulting in a barely detectable increase in pressure. This method still requires the oven to be on during loading to maximize the electron-cadmium collision rate, and the ionization rate is very low compared to the large electron gun such that individual ions can be loaded into the trap. However, this slow rate could take several minutes and sometimes up to hours to trap an ion, which is less than ideal. The continual production of cadmium vapor also results in coating the trap electrodes with cadmium, and while no direct evidence has been obtained, the atomic deposition layer has long been suspected to be the origin of patch potentials on the electrodes that may be responsible for the

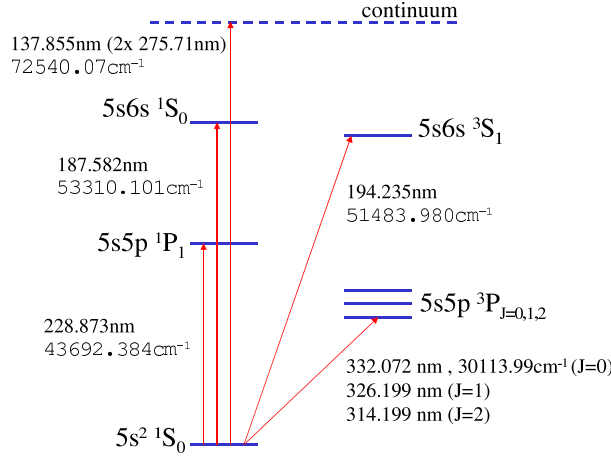


FIGURE 2.1.4. Energy levels of neutral cadmium atoms. A 915.4nm pulsed laser is frequency quadrupled to drive the 5s to 5p transition in neutral cadmium at 228.87nm. Two photons at this wavelength (equivalent to 5.41eV each) have sufficient energy to overcome the ionization threshold (8.99eV) and produce Cd^+ ions. [25]

anomalous vibrational heating observed in these traps as well as traps of other atomic species.

Neutral cadmium can also be photoionization in the trap region using a pulsed laser tuned to the 229nm S to P transition of neutral cadmium. The ionization energy of neutral cadmium is 8.99eV, which can be overcome with a two photon process (each photon carries 5.41eV of energy) [25]. The high peak intensity of the pulsed laser results in a very reasonable ionization rate. In the laboratory, we have tested two different pulsed lasers for photoionization of cadmium atoms: both are mode-locked Ti:Sapphire lasers, one operating in the picosecond regime and the other operating on the femtosecond regime. They operate at four times the desired wavelength at 915.40nm, and the high peak intensity during the short pulses allows efficient frequency doubling with a lithium borate (LBO) crystal and a second stage frequency doubling with a thin alpha barium borate (BBO) crystal. Both the 2 picosecond and the 150 femtosecond pulse lasers require an average optical power between 0.3 to 3 mW to produce cadmium ions in the trap at the rate of ~ 1 ion per second. The background cadmium gas has sufficient ionization cross section that in general no additional atomic vapor from the oven is required. This method creates no detectable increase in pressure, and the lifetime of the ion in the trap remains on

the order of several hours, making this by far the most preferred method of loading ions into the trap.

Residual background gas collisions can be important to the ion lifetime in the trap [26]. Inelastic collisions can alter the internal state of the trapped ion or even change the species of the ion, while elastic collisions only add kinetic energy to the ion. The most troublesome inelastic processes are chemical reactions and charge exchange, which can occur only if the interparticle spacing of the two colliding particles approaches atomic dimensions. An upper limit is given by the Langevin rate, where background neutrals penetrate the angular momentum barrier and spirals into a collision with the ion. In these collisions, the electric field from the trapped ion polarizes the background neutral, creating an attractive potential

$$(2.1.7) \quad U(r) = -\frac{\alpha q^2}{8\pi\epsilon_0 r^4},$$

where α is the electric polarizability of the neutral atom and q is the electric charge. Solving the Lagrangian for a two-body system:

$$L = \frac{1}{2}\mu (\dot{r}^2 + r^2\dot{\theta}^2) - U(r),$$

where $\mu = m_1 m_2 / (m_1 + m_2)$ is the reduced mass, impact parameters less a critical value

$$b_{critical} = \left(\frac{\alpha q^2}{\pi \epsilon \mu v^2} \right)^{1/4}$$

will result in spiraling collisions for an particle approaching at velocity v toward the mainly stationary ion. The Langevin rate

$$k_{Langevin} \equiv \sigma v = \pi b_{critical}^2 v,$$

where σ is the collision cross section, leads to an overall reaction rate

$$\gamma_{Langevin} = n k_{Langevin} = n q \sqrt{\frac{\pi \alpha}{\epsilon v}},$$

where $n = P/k_B T$ is the density of the background gas, dependent on the pressure P and temperature T . For collisions with the dominant background gas H_2 at a pressure of $P = 10^{-11}$ Torr = 1.33×10^{-9} Pa and room temperature $T = 300$, with $\mu \approx 3.32 \times 10^{-27}$ kg and $\alpha_{H_2} \sim 8 \times 10^{-31}$ m³, the collision rate is $\gamma_{Langevin} \approx 4.6 \times 10^{-4}$ s⁻¹, or once every 36 minutes. Our observation of the ion lifetime in the trap is on the order of an hour, which is consistent with these calculations since not every collision results in ion loss.

2.1.4. Doppler Cooling. The $S_{1/2}$ to $P_{3/2}$ transition in Cd^+ ion can be resonantly coupled with an electromagnetic field at 214.5nm. Dipole interaction results

in an absorption/spontaneous emission rate of

$$(2.1.8) \quad \gamma_s = \frac{s_0 \gamma / 2}{1 + s_0 + (2\Delta/\gamma)^2},$$

where Δ is the detuning from resonance, $\gamma = 2\pi \times 60\text{MHz}$ is the natural linewidth, and $s_0 = I/I_{sat}$ is the saturation parameter with $I_{sat} = \pi\gamma\hbar c/(3\lambda^3) = 7.9\mu\text{W}/\text{mm}^2$ being the saturation intensity. A particle in motion observes the Doppler effect and the field appears to have a different detuning $\Delta' = \Delta - \mathbf{k} \cdot \mathbf{v}$ when the particle has a velocity \mathbf{v} . If the field is red detuned, then the particle will scatter more frequently when $\mathbf{k} \cdot \mathbf{v} < 0$ and less frequently when $\mathbf{k} \cdot \mathbf{v} > 0$, assuming the Doppler shift is less than the detuning ($\mathbf{k} \cdot \mathbf{v} < \Delta$). This imbalance in scatter rate results in more recoil energy being transferred to the particle when it is traveling towards the beam source, and when two counter-propagating beams are both red detuned, the particle becomes trapped in the middle. This process is called Doppler cooling.

In the case of ions in a Paul trap, only one Doppler beam is necessary since the restoration force of the trap guarantees that any excess kinetic energy from the ion can be removed on an approach where $\mathbf{k} \cdot \mathbf{v} < 0$. The wave vector must couple to all three principal axes of the trap to ensure Doppler cooling in all dimensions. In general, the Doppler cooling limit is $\langle E \rangle = \hbar\gamma/2 = \hbar\omega\bar{n}$, where \bar{n} is the average number of phonons in the vibrational mode. However, because the Doppler beam is at a 45° angle with respect to the dimension that is used for quantum information transfer, the cooling limit includes a factor that is dependent on the polarization of the field and integrated over the radiation pattern of the emitted field. The calculated Doppler limit is $\langle E \rangle = 0.425\hbar\gamma$, which is approximately the same as the general case where $\langle E \rangle = \hbar\gamma/2$. For a trap frequency of $\omega \sim 2\text{MHz}$, the Doppler limit is $\bar{n}_D = 13$.

The spontaneous emitted photons from the Doppler cooling beam are collected by an objective lens, and individual ions can be distinguished on the camera when they are localized at their equilibrium positions in the trap (see section 2.3 for details on the optics setup). As the laser approaches resonance from a lower frequency, the fluorescent rate increases and the ions become visibly brighter on the camera. When the laser frequency is tuned to just above resonance, the ions become non-localized due to Doppler heating (or lack of cooling) and disappears from the camera image. However, a single ion usually remains trapped if the Doppler heating is kept to less than a few seconds and Doppler cooling is immediately turned on afterwards.

2.1.5. Isotope Selectivity. The isotope shifts in cadmium ions allow us to distinguish the isotopes from one another. This is important since the even isotopes of cadmium have no nuclear spin and therefore have no hyperfine splitting, and only odd isotopes (111 and 113) have hyperfine levels which can be used as qubits (see section

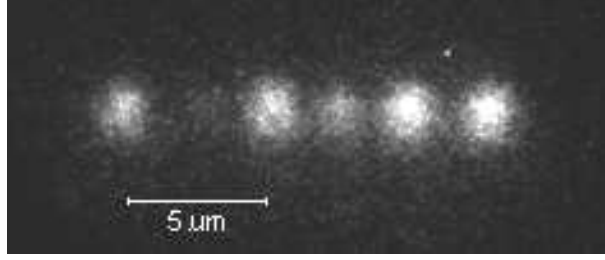


FIGURE 2.1.5. CCD image of 6 ions in the three-layer linear trap. The different brightness of the ions indicate different isotopes.

FIGURE 2.1.6. Cadmium isotope abundances and the isotope shifts in the resonant frequency of the $S_{1/2}$ to $P_{3/2}$ transition in cadmium ions. The vertical height indicates the relative abundance of each isotope of cadmium, and the relative frequency of each isotope is shown on the horizontal axis, in both GHz in the UV and also in terms of the wavelength of the Ti:Sapphire laser before the field is frequency quadrupled.

2.2 on qubits). In the experiments, only isotope 111 ions are used, since isotope 111 and 113 have different ground state hyperfine splitting (14.5GHz for 111 and 15.3GHz for 113) and their mass difference results in different secular frequencies, creating an unnecessarily complicated scenario when multiple isotopes are present in the trap. However, other isotopes can still be potential candidates for sympathetic cooling, as experiments have shown [27]. Each time the trap is loaded with ion(s), the laser is tuned to the resonance peak of the ion(s) and the wavelength of the laser in the infrared (IR) is read by a wavemeter (Burleigh WA-1500) to determine the isotope number. The undesired isotopes are released from the trap and new ions are loaded into the trap until the desired isotope is captured. The probability of capturing the desired isotope increases if the laser is slightly red detuned from the resonance of the desired isotope to where Doppler cooling is efficient. In the case of isotope 111, the other isotopes can be Doppler heated while isotope 111 is Doppler cooled, ensuring only isotope 111 will remain in the trap. The probability of loading isotope 111 is also increased with an isotope-enriched cadmium or cadmium oxide source.

2.1.6. Micromotion due to background electric field. In the presence of a background electric field E_0 , the equation of motion (from eq 2.1.2) becomes

$$(2.1.9) \quad \ddot{x} + \frac{2e}{md_0^2}(U_0 - V_0 \cos(\Omega_T t))x = \frac{eE_0}{m}.$$

FIGURE 2.1.7. Effect of micromotion on the Doppler lineshape. Frequency is scanned by changing the offset between the tellurium reference and the laser in the feedback loop. The laser is on resonance at 992MHz on the axis, and the actual frequency shift in the UV is 4 times the scale shown on the axis. The square boxes show the minimized micromotion with a HWHM of 9MHz, translating to a linewidth of 72MHz (compared to the natural linewidth of 60MHz). The triangles and the circles show different sets of data with much wider Doppler lineshapes, indicating a large micromotion amplitude. The sharp drop at 955MHz for the circle and 979MHz for the triangle are suspected to be caused by Doppler heating from the third and the first micromotion sideband respectively (rf frequency 50MHz). The resonant scatter rate is increased by a factor of 2.5 when micromotion is minimized, which increases the detection efficiency. The actual voltage settings used for each data set are shown in the legend (data was taken in the asymmetric quadrupole trap). For example, 30VDC -2.6kV v -2.0kV h indicates a 30V bias applied to the endcap electrodes, a -2.6kV bias applied to the vertical compensation electrode, and a -2.0kV bias applied to the horizontal compensation electrode.

Then the solution is

$$(2.1.10) \quad x(t) = x_0 \left[1 + \sqrt{2} \frac{\omega_x}{\Omega_T} \cos(\Omega_T t) \right] \cos(\omega_x t) + \frac{\sqrt{2} e E_0}{m \omega_x \Omega} \cos(\Omega_T t) + \frac{e E_0}{m \omega_x^2}.$$

The first term is the usual solution using the pseudopotential approximation for $\omega_x \ll \Omega_T$. The second term contributes extra micromotion with an amplitude proportional to the background electric field E_0 , and the third term produces a constant offset in the position of the ion. The problem with the extra micromotion from the second term in eq 2.1.9 is that the amplitude could be significantly larger than the actual secular motion, which could result in excess Doppler shifts and ultimately interferes with laser cooling. The experiments have shown that without canceling micromotion due to background electric field, Doppler cooling is ineffective and efforts to laser cool to sub-Doppler limits results in complete failure.

There are several ways to cancel the background electric field and remove the extra micromotion. First, the vacuum chambers are equipped with compensation electrodes positioned near the trap in three orthogonal directions, and high voltage can be applied to these electrodes to offset the background electric field. For the three-layer linear trap, the segmented electrodes allow multiple degrees of freedom to cancel any background electric field. The static potential U_0 on the electrode in the ring-and-fork trap also has an effect on the micromotion.

To assess the magnitude of micromotion, one method is to observe the Doppler lineshape, as in the example shown in fig 2.1.7. Normally, the photon scatter rate is a function of frequency following eq 2.1.8, with a FWHM of approximately 60MHz when the ion is undersaturated ($I < I_{sat}$). When the micromotion amplitude is large, the linewidth broadens due to Doppler shift from the ion's micromotion. Alternatively, the process can be viewed as a phase modulation of the field at the rf frequency as observed by the ion, which produces sidebands at intervals matching the rf frequency. The sideband strengths are proportional to the Bessel functions $J_n(\phi)$ with modulation index ϕ proportional to the amplitude of micromotion. In fig 2.1.7, the resonant scatter rate in the absence of micromotion is much higher than when micromotion is present, due to the fact that optical power is not diverted to sidebands and there is no Doppler heating from the sidebands. The field compensation parameters can be changed with real time feedback from the linewidth measurement and the increased resonant scatter rate.

Another method to measure micromotion is by comparing the arrival time of the photons with the rf signal. When the laser is red detuned from resonance, the scatter rate is correlated with the rf due to the Doppler effect when micromotion becomes significant. A time-to-digital (TDC) converter digitizes the time interval between photon arrival and the start of the next rf cycle, and the collected histogram shows a sinusoid variation in the probability of arrival with respect to the rf phase when there is a significant micromotion amplitude. Micromotion can be nullified by suppressing the correlation with the rf phase.

The two methods described previously can only detect micromotion along the direction of the laser. For micromotion in the other dimensions, the information can be extracted from the position of a single ion in the trap. Eq 2.1.10 shows that there is a constant offset $eE_0/m\omega_x^2$ in the position of the ion. The position of the ion is measured at two different secular frequencies ω_1 and ω_2 , which can be controlled by changing the amplitude of the rf. The difference in position is

$$(2.1.11) \quad \Delta x = \frac{eE_0}{m} \left(\frac{1}{\omega_1} - \frac{1}{\omega_2} \right).$$

The strength of the electric field can be determined by rearranging the equation:

$$(2.1.12) \quad E_0 = \frac{m\Delta x}{e} \left(\frac{1}{\omega_1^2} - \frac{1}{\omega_2^2} \right)^{-1}.$$

Micromotion amplitude in the plane of the camera view can be minimized by eliminating the position shift corresponding to the change in rf amplitude.

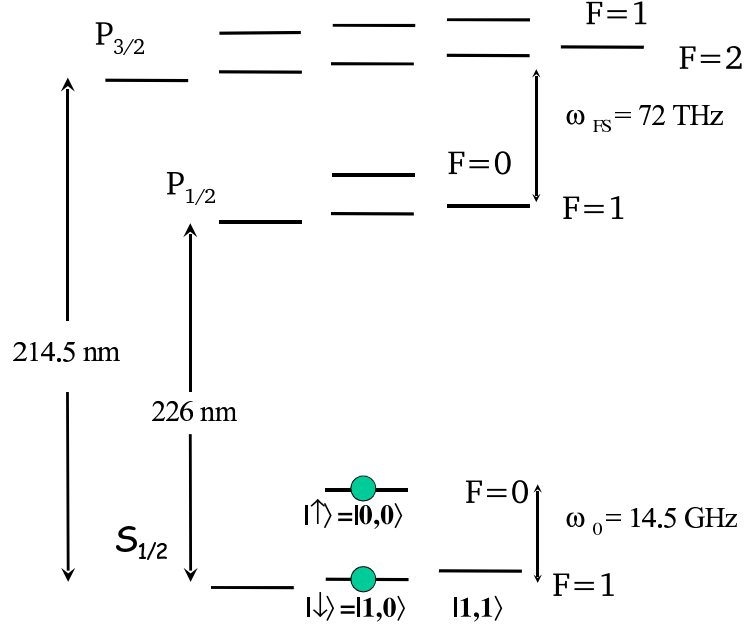


FIGURE 2.2.1. Internal energy levels of a $^{111}\text{Cd}^+$ ion. Ground state hyperfine levels (nuclear spin $I = 1/2$) serve as a qubit, with a frequency splitting of 14.5GHz. The excited states $P_{1/2}$ and $P_{3/2}$ are separated by a fine structure splitting of 72 THz, and the transition from $S_{1/2}$ ground state is resonant with a 214.5nm and a 226nm ultraviolet radiation respectively. The qubit levels $|F = 0, m_F = 0\rangle$ and $|F = 1, m_F = 0\rangle$ states are magnetic field insensitive to first order, resulting in a coherence time on the order of a few seconds.

2.2. Cadmium 111 as a Qubit

The choice of ion was selected with careful consideration for the technology available and for properties favorable towards quantum computation. Typical atomic ion species for quantum information applications are hydrogen-like, with a single valence electron with a $^2S_{1/2}$ ground state. The ions' internal electronic states serve as quantum memory, and two states are designated as the qubit levels $|0\rangle$ and $|1\rangle$, where information can be stored in the amplitude and phase of these states. A “hyperfine qubit” uses two ground state hyperfine levels, while a “optical qubit” uses a ground state and an excited D state with energy lower than the P state. A hyperfine qubit has the advantage of extremely long life time on the order of thousands to millions of years, compared to the life time on the order of seconds for the excited D state. In addition, hyperfine qubits can be manipulated using stimulated Raman transition via coupling to excited states, thus having a less stringent requirement on the frequency

stability of the laser than optical qubits, which are coupled using electric quadrupole transitions with linewidths on the order of less than 1 kHz.

The experiments in this thesis uses ground state hyperfine levels of $^{111}\text{Cd}^+$ ions as qubits. Hyperfine interaction exists only in isotopes with a non-zero nuclear spin ($I = 1/2$ for $^{111}\text{Cd}^+$). The qubit states are defined as $|0\rangle = |F = 0, m_F = 0\rangle$ state and $|1\rangle = |F = 1, m_F = 0\rangle$ state, where F denotes the total angular momentum of the electron and nucleus and m_F denotes the z component of the total angular momentum. These levels are specially chosen for their insensitivity to magnetic field (to first order), with the coherence time of the qubit memory on the order of a few seconds according to our measurements. The frequency splitting is $\omega_0 = 2\pi \times 14.53\text{GHz}$ [28].

2.2.1. Initializing the Qubits. A quantum register needs to be initialized to a definite state before operations can be performed. For trapped $^{111}\text{Cd}^+$ ions, the qubits are prepared in the $S_{1/2}(F = 0, m_F = 0)$ state at the onset of computation by optical pumping with radiation near-resonant to the $S_{1/2}(F = 1) \rightarrow P_{3/2}(F' = 1)$ transition. For this transition, there is always a dark state composed of a superposition of the $S_{1/2}(F = 1)$ manifold for any polarization of the light. Therefore, the optical pumping field is tuned to be in between the $S_{1/2}(F = 1) \rightarrow P_{3/2}(F' = 1)$ and the $S_{1/2}(F = 1) \rightarrow P_{3/2}(F' = 2)$ transitions in order to remove any remaining population in the dark state. The exact polarization of the laser is not critical as long as it is not purely σ^+ (or σ^-) polarized. Preparing the ions in the $S_{1/2}(F = 0, m_F = 0)$ state with a $60\mu\text{W}$ beam focused to a $20\mu\text{m}$ waist typically takes about $1\mu\text{s}$ (see section 2.3 for the laser setup).

Assuming sufficient time is always given to the optical pumping process, the initialized state $S_{1/2}(F = 0, m_F = 0)$ still maintain a small probability of coupling off-resonantly to the $P_{3/2}(F = 1)$ states and decaying to a $S_{1/2}(F = 1)$ state through spontaneous emission. In the time for one scatter from the $S_{1/2}(F = 1)$ to the $P_{3/2}(F' = 2)$ state, the probability of the $S_{1/2}(F = 0, m_F = 0)$ state leaking to the $S_{1/2}(F = 1)$ state from undesired scattering is approximately the square of the detuning ratio $(400\text{MHz}/14.1\text{GHz})^2 = 8 \times 10^{-4}$. This error is sufficiently small as to not be a significant contributor to the fidelity of qubit measurements or operations.

2.2.2. Detecting the Qubit State. In quantum computation, a qubit can be in a superposition of both $|0\rangle$ and $|1\rangle$ states and/or be entangled with the state of other qubits while quantum operations are performed. However, the results of the computation can be obtained by the user only through measurements, which collapse the qubit into a $|0\rangle$ or $|1\rangle$ state and potentially alter the state of the entangled system.

In the Cd 111 system, the state of an ion can be detected by applying a σ_- -polarized radiation resonant with the cycling transition $S_{1/2}(F = 1) \rightarrow P_{3/2}(F = 2)$

and collecting the fluorescence. The $|1\rangle$ state is optically pumped to the $S_{1/2}(F = 1, m_F = -1)$ state and continuously cycled and scattered from the $P_{3/2}(F = 2, m_F = 2)$ state. Since the other qubit state is far detuned from the only available scattering channel $S_{1/2}(F = 0) \rightarrow P_{3/2}(F = 1)$ (by $13.7\text{GHz}/60\text{MHz}=228$ linewidths), the ions in this state remain dark. A photomultiplier tube (PMT) or a camera collects the emitted photons for a certain amount of time. If the photon count exceeds a certain threshold, the ion is determined to be in one state. Otherwise the ion is determined to be in the other state.

The collection rate is countered by several error mechanisms. First, the dark state can scatter off-resonantly via the $P_{3/2}(F = 1, m_F = -1)$ state, resulting in large number of scatters after the ion decays into the cycling transition. Second, the bright state can also scatter off-resonantly via the $P_{3/2}(F = 1, m_F = -1)$ state and decay into the dark state. The probability of these errors occurring increases with intensity, as the off-resonant scatter rate increases disproportionately with intensity (a direct result of eq 2.1.8, a phenomenon known as power broadening). Hence the intensity is kept at below saturation intensity, where power broadening is less pronounced. These errors are also more likely to occur as the duration of illumination increases. Therefore, the photon collection time is a balance between the errors due to photon statistics (the longer the better) and the errors induced by off-resonant scattering (the shorter the better). The actual light level and photon collection time is determined experimentally (see section 2.4.2).

2.3. Lasers and Imaging System

So far the discussion has involved a different laser frequency near 214.5nm for each individual task such as Doppler cooling, qubit initialization, and qubit detection. In this section, we will discuss in detail the laser system that generates a tunable 214.5nm ultraviolet (UV) radiation, methods to generate different frequencies required, and locking the laser to a known molecular transition.

2.3.1. Ti:Sapphire Laser. The source of the excitation laser is a Coherent MBR-110 continuous wave (cw) Ti:Sapphire laser pumped by a 10.5W frequency doubled Nd:YAG laser at 532nm (either a Spectra-Physics Millennia Pro or a Coherent Verdi-V10). Figure 2.3.2 shows the schematic of the bow-tie cavity of the MBR-110. The frequency of the laser can be tuned using a birefringent filter and an etalon inside the cavity. An external reference cavity stabilizes the laser and allows smooth tuning of the frequency. The reference cavity also accepts an external voltage control for further stabilization of the laser. The Ti:Sapphire laser typically generates 1.5W at 858.0265nm.

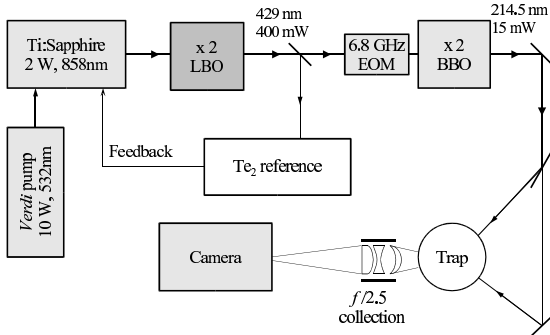


FIGURE 2.3.1. Schematic of the laser system for detecting Cd^+ ions. A Ti:Sapphire laser pumped by a 10W Nd:YAG laser produces 1.5W of infrared radiation at 858nm. The field is frequency doubled by an LBO crystal inside a cavity and subsequently frequency doubled again by a BBO crystal inside another cavity. The resulting 15mW of 214.5nm radiation excites the $S_{1/2}$ to $P_{3/2}$ transition in the cadmium ions in the trap, and the fluorescence is collected by imaging optics and captured by the camera or PMT. A feedback signal locks the laser to a known tellurium atomic resonance to within a 1MHz bandwidth.

2.3.2. Frequency Doublers. The output of the Ti:Sapphire laser is converted to 214.5nm UV light through two stages of frequency doubling. A WaveTrain cw frequency doubler from Spectra-Physics converts the infrared (IR) to a 429nm blue light using a LBO crystal inside a build-up cavity. An optical isolator (IO-3G-852-HP by Optics for Research) sits between the Ti:Sapphire laser and the LBO cavity to prevent feedback from the cavity reflection. The LBO cavity outputs 300mW from a 1.4W input, with conversion efficiency of 20%, and the output is frequency doubled again by another WaveTrain frequency doubler containing a BBO crystal in a build-up cavity to produce the 214.5nm radiation. The BBO can output 10mW of UV from a 250mW input, with conversion efficiency of 4%. However, the BBO crystal is hydrophilic and can easily be damaged by the blue and UV light. Dry oxygen is constantly flowing through the cavity to preserve the quality of the surface and lengthen the lifetime of the BBO crystal, and adjustment of the crystal and cavity is required on a daily to weekly basis as the crystal acquires defects.

2.3.3. frequency lock with a Te_2 vapor cell. Standard molecular references for calibrating tunable lasers are $^{127}\text{I}_2$ (resonances in the 500-675nm range) [29] and $^{130}\text{Te}_2$ (resonances in the 420nm-540nm range) [30]. In this case $^{130}\text{Te}_2$ is more appropriate since an absorption line can be found near 429nm, or twice the $^{111}\text{Cd}^+$ resonance for the $S_{1/2}$ to $P_{3/2}$ transition. Doppler-free saturated-absorption spectroscopy

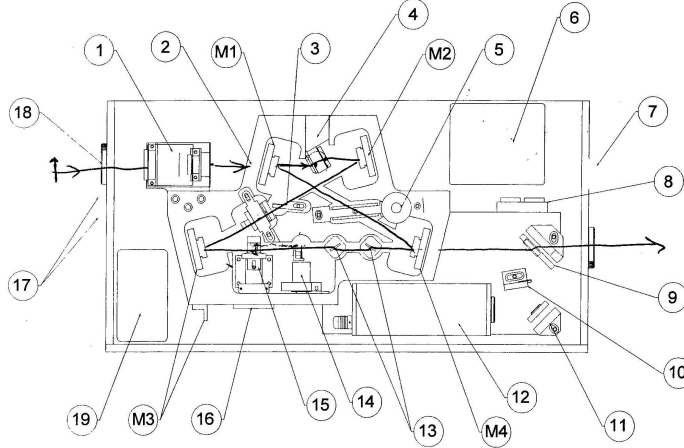


FIGURE 2.3.2. Schematic diagram of the MBR-110 Ti:Sapphire laser (from Coherent Inc). The bowtie cavity consists of 4 mirrors M1-M4, and resonance is tuned using the birefringent filter (5) and the etalon mounted on a galvanometer (14). The output of the laser is partially deflected to the temperature controlled Fabry-Perot reference cavity (12), and the reflected signal detected by the photodiodes (8) is used to lock the laser (a piezo behind mirror M3 allow the electronics to control the cavity). The reference cavity can be tuned from the front panel or controlled by an external scan signal. Additional Doppler-free saturated absorption spectroscopy on tellurium provides feedback for the reference cavity and locks the MBR-110 to within 1MHz bandwidth for the detection beam (see section 2.3.3).

is used to observe the reference line and the reference cavity of the MBR-110 is locked to this reference line to prevent long term drifts due to temperature or mechanical vibrations.

The $^{130}\text{Te}_2$ vapor cell obtained from Ophos Instruments Inc is placed inside an enclosed 2-1/2" vacuum nipple with optical access on both ends and heated by a tape heater to near 500°C to obtain proper vapor pressure of Te. The quartz cylindrical cell is 25mm in diameter and 10cm in length, and is wrapped in a layer of ceramic fiber insulation to avoid large temperature gradients from direct contact with the heating tape. The temperature is controlled by a temperature servo with feedback from a thermal couple attached to the insulation near the cell. The bundle is then further insulated with heavy ceramic fiber layers both inside and outside the stainless holder to maintain consistent temperature around the cell.

At 500°C , the absorption line is Doppler broadened to several GHz, which allows too large of a frequency drift for the Ti:Sapphire laser. Therefore a pump-probe experiment is setup to remove the Doppler effect and lock the laser to within the much narrower natural molecular linewidth. The experiment apparatus is shown

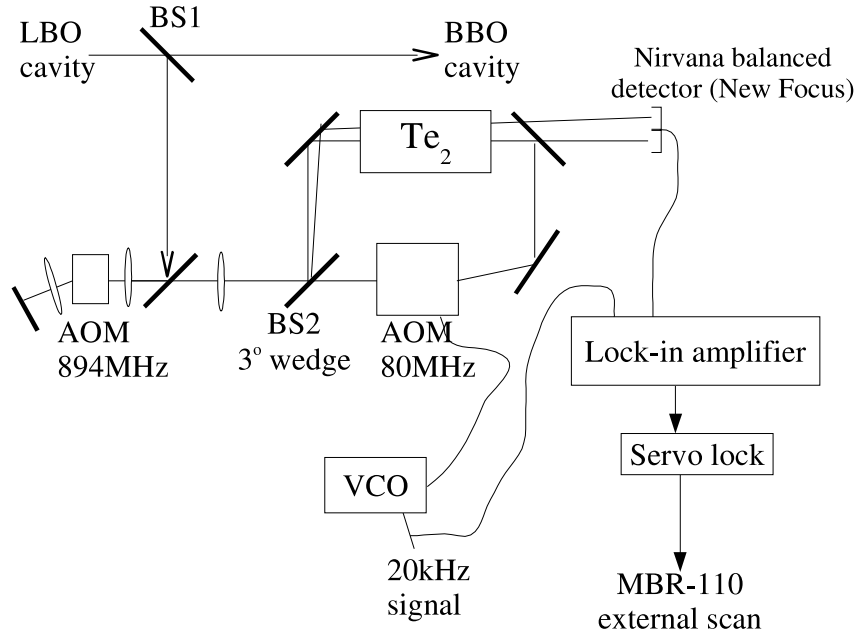


FIGURE 2.3.3. Setup for saturated absorption spectroscopy of tellurium. A $\sim 1\text{mW}$ pump beam and a weaker, counter-propagating $50\mu\text{W}$ probe beam overlaps inside a tellurium vapor cell. As the frequency of the laser is scanned, each beam excites a different velocity group whose Doppler-shifted frequency is resonant with the excitation frequency of the ions. At a certain laser frequency where both beams are resonant with the same velocity group, the pump beam saturates the transition, resulting in a decrease in the absorption of the probe beam. The transmission of the probe beam is monitored by a photodetector (New Focus model 2007) as the probe beam is being frequency modulated. A lock-in amplifier (model SR510 by Stanford Research Systems) mixes the detected signal with the frequency modulation signal (with a low-pass filter typically set to a 3ms time constant), and an integrator circuit locks the Ti:Sapphire laser source to the resulting error signal. A double pass AOM frequency shifts the laser by 1.8GHz before entering the tellurium setup to bridge the frequency difference between the desired transition and the nearest tellurium transition.

schematically in Fig 2.3.3. Approximately 10 mW of optical power is diverted from the 429nm beam and passes through a 894MHz AOM (model TEF-1000-300-.429 from Brimrose Corp) twice to provide the appropriate frequency offset (1.8GHz) between the $S_{1/2}$ to $P_{3/2}$ transition in $^{111}\text{Cd}^+$ and the tellurium absorption line. The beam is then split into a pump ($\sim 2\text{mW}$), a probe ($\sim 300\mu\text{W}$), and a reference beam ($\sim 300\mu\text{W}$). The probe and the reference beams enter the vapor cell from the same direction, while the pump beam travels in the opposite direction while overlapping the probe beam. When the field is off-resonant, the pump and probe fields are absorbed

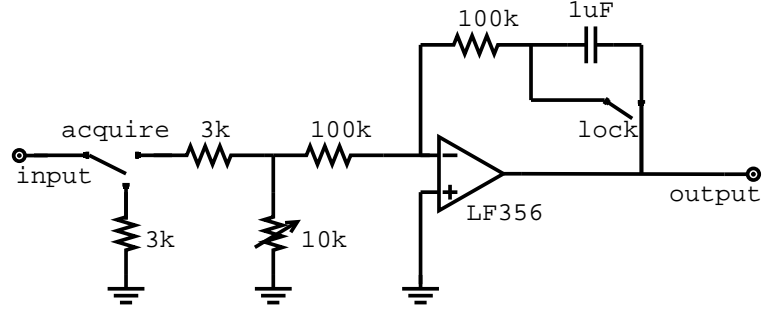


FIGURE 2.3.4. Circuit diagram for the servo lock in the tellurium setup. The input of the circuit is the error signal from the lock-in amplifier, and the acquire switch closes the circuit for an inverting amplifier. The lock switch converts the circuit to an integrator, with the gain controlled by a $10\text{k}\Omega$ potentiometer. The output is sent to the external lock on the MBR-110. The bandwidth of the feedback system is limited by the bandwidth of the lock-in amplifier, typically between 10-100Hz.

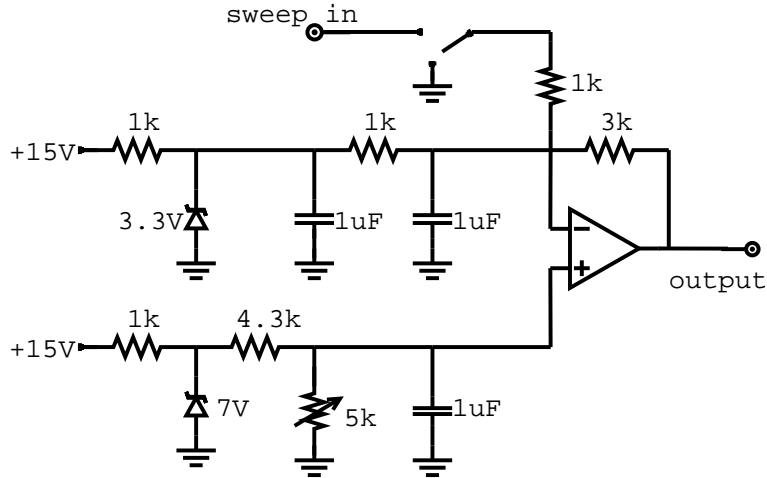


FIGURE 2.3.5. Circuit diagram for laser frequency sweep and offset. To scan the MBR-110 for the tellurium absorption line, a 20kHz sweep signal is sent to the external scan input on the laser control box. The output of the lock-in amplifier shows a dispersion shape as the frequency of the laser is ramped, pinpointing the tellurium absorption line, as shown in figure 2.3.6. If the frequency of the laser is too far from the tellurium absorption resonance, an offset knob (5k potentiometer) in the circuit is used to bring the laser closer to resonance. The laser must be on the tellurium absorption resonance (within the peak and valley of the dispersion shape signal) when the lock is acquired.

by different velocity groups, resulting in the probe and the reference beams having the same optical attenuation across the length of the vapor cell. When the field is resonant with the tellurium absorption line, then the pump beam saturates the zero

velocity group of molecules, allowing the probe beam to pass through the vapor cell with very low attenuation, while the reference beam continues to be absorbed by the molecules in its path. The optical power of the probe and the reference beams are measured upon exiting the vapor cell, and the difference between the two signals clearly presents the Doppler-free profile of the absorption lineshape.

To use this resonance signal in a feedback system involving the source laser, the pump beam is frequency modulated to provide a lock-in signal. An acousto-optic modulator is driven by a 80MHz signal from a voltage-controlled oscillator (VCO). The voltage control is modulated at 20kHz with amplitude that varies the output frequency by 2MHz. When the frequency of the field is on the slope of resonance, the reference-subtracted probe signal oscillates with the frequency modulation, and the output can be mixed with the source to generate an error signal. As the laser frequency is scanned, the error signal shows a dispersion-like shape as shown in Fig 2.3.6. This signal can be used in a feedback loop that restores the error signal to the zero-crossing point, corresponding to the resonant frequency of the tellurium absorption feature. The feedback loop uses the external scan input on the MBR-110. The external scan input accepts a signal between 0 to 10V, which scans the reference cavity within a range corresponding to a scan bandwidth (typically set to 10GHz) in the Ti:Sapphire laser.

2.3.4. generating multiple frequencies. Starting with the 214.5nm laser locked to the tellurium reference, the different frequency fields required can be generated using various types of modulators. As shown in fig 2.3.7, the resonant frequency of the $S_{1/2}(F = 1) \rightarrow P_{3/2}(F' = 2)$ transition is reached by up-shifting the frequency of the laser by 215MHz with an acousto-optic modulator (AOM). This also determines the frequency shift for the beam directed towards the tellurium lock, which must be 1.748GHz (or double-pass through a 894MHz AOM plus a -40MHz shift due to the pump beam AOM shift) below the laser's frequency. For Doppler cooling, a 185MHz modulation frequency is sent to the same AOM used for the resonant detection beam, which red-detunes the frequency by half a linewidth. The optical pumping beam used for initializing the qubit needs to be between the $S_{1/2}(F = 1) \rightarrow P_{3/2}(F = 1)$ and $S_{1/2}(F = 1) \rightarrow P_{3/2}(F = 2)$ resonances, so the zero-th order unshifted beam from the detection AOM is double-passed through a 450MHz AOM, resulting in a frequency 685MHz above the $S_{1/2}(F = 1) \rightarrow P_{3/2}(F = 2)$ resonance.

Since the 14.5GHz ground state hyperfine splitting is much larger than the ~ 800 MHz $P_{3/2}$ excited state hyperfine splitting, the ion can be trapped in the $S_{1/2}(F = 0)$ hyperfine state that is not resonantly coupled to the excited state by the laser

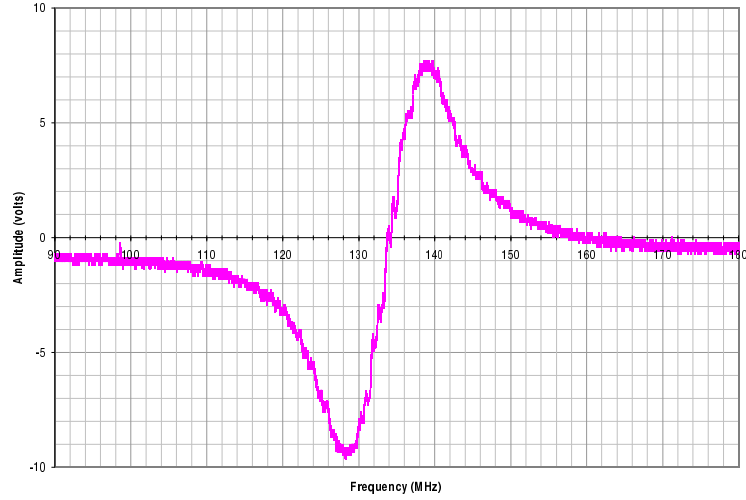


FIGURE 2.3.6. Tellurium absorption lock-in error signal. The laser frequency is swept using a 2V peak to peak modulation at 2Hz applied to the external scan input of the MBR-110, scanning a range of 20% (2V out of 10V) of the 5GHz total bandwidth. The oscilloscope trace of the error signal is plotted, with the x-axis calibrated to the frequency sweep. The data show a linewidth of 13MHz. To lock the laser to the tellurium resonance, the laser is tuned to within the maximum and the minimum of the loop and a servo loop is activated to keep the error signal at zero-crossing. The noise on the error signal when the servo is active is less than 10% of the peak to peak amplitude difference, from which an upper limit on the bandwidth of the laser can be inferred to be $<1\text{MHz}$ at 429nm.

during Doppler cooling. To avoid this population trapping, a frequency 13.7GHz detuned from the laser is added to the field using an electro-optic modulator (EOM).

2.3.5. Acousto-optic modulators (AOM). In addition to shifting the frequency of the incident field, acousto-optic modulators also act as switches for the optical beams. They operate by launching a standing wave with frequency ω_{rf} inside the crystal, causing a periodic change in the index of refraction. An incident field at frequency ω_L passing through this periodic medium Bragg diffracts with the n -th order diffraction carrying a frequency $\omega_L + n\omega_{rf}$. Usually, the \pm first order is used, and the incident angle is tuned to maximize the optical power in the desired order. When the modulating rf signal is disconnected from the AOM, the Bragg diffraction disappears and the n -th order beams are switched off for $n \neq 0$. These AOMs (model QZF-210-40-214) are specially made by Brimrose Corp with anti-reflection(AR) coating specifically for the 214nm wavelength on a fused silica substrate. The AOMs have

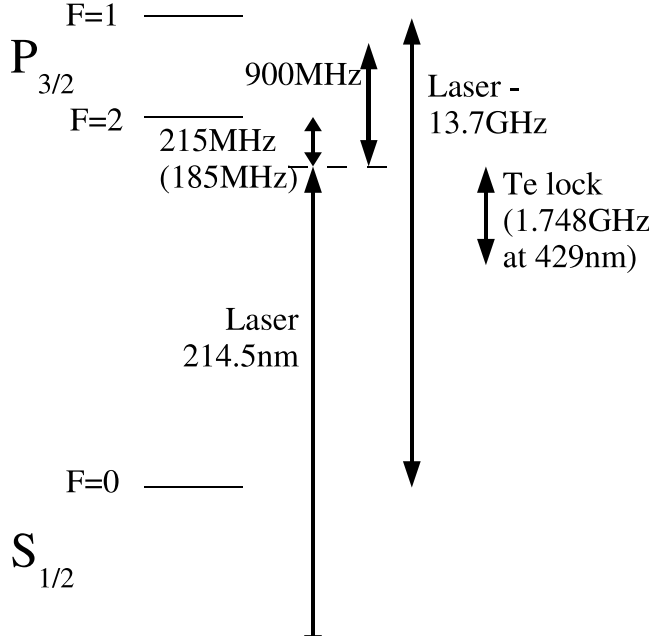


FIGURE 2.3.7. Relative frequencies for detection, initialization, and Doppler cooling. The laser is locked to the tellurium reference at 215MHz below the $S_{1/2}(F = 1) \leftrightarrow P_{3/2}(F = 2)$ resonance, as indicated by the dashed line. An AOM operating at 215MHz serves as a beam switch and bridges the frequency gap to resonance. The same AOM modulating at 185MHz generates a red detuned field that Doppler cools the ions. And an EOM phase modulating at 6.8GHz can prevent population trapping in the $S_{1/2}(F = 0)$ state with the second modulation sideband of the resulting field. For initialization, a separate double pass AOM operating at 450MHz can couple to the $S_{1/2}(F = 1) \leftrightarrow P_{3/2}(F = 1)$ transition and optically pump the ions into the $S_{1/2}(F = 0)$ state.

a bandwidth of 40MHz centered around 210MHz, with greater than 50% diffraction efficiency. However, the beam focusing to $\sim 50\mu m$ is required for high diffraction efficiency, and we have observed that the optical transmission degrades over time (on the order of a year), probably due to damage to the AR coating from the focused UV laser. More recently acquired AOMs made by IntraAction (model ASM-2102LA61) are designed for a collimated beam which should prevent similar problems, though there has been insufficient time to observe long term trends on these models.

2.3.6. electro-optic modulators (EOM). Since no high frequency EOM for 214.5nm light is available, a New Focus EOM (model 4851) designed for 429nm light modulating at 6.8GHz is placed in between the LBO cavity and BBO cavity. The BBO cavity is tuned to match its free spectral range to one quarter of the 6.8GHz so all

sidebands from the EOM can resonate in the cavity. The frequency doubled/summed field produced by the BBO then contains a frequency component 13.6GHz detuned from the carrier, and can effectively depopulate the $S_{1/2}(F = 0)$ state. (For cavity modification, see appendix B.)

2.3.7. Imaging System. Fluorescence from the ions is collected by a 1 inch objective lens outside the vacuum chamber, and a second set of lenses images the ions onto a camera, with a total magnification of approximately 200. The cameras are UV sensitive, and two different models have been used in the experiments. The first is a Quantar Technology single-photon imaging detector system (model 2601B). The detector has capability of single-photon counting like a photomultiplier but also is sensitive to the xy position. Its 23mm circular active area is sensitive from below 180nm to beyond 900nm. The other camera is a Princeton Instrument PI-MAX intensified CCD camera. The 512x512 pixel array has its drawbacks: slow image download time on the order of 100ms and large read noise, although the quantum efficiency ($\sim 2\%$) is slightly better than the Quantar detector ($< 1\%$). A third option is a Hamamatsu H6240-01 photomultiplier tube. While it is not position sensitive, the PMT has the highest quantum efficiency ($\sim 20\%$) and conveniently outputs a TTL pulse with a 35ns resolution, which, as explained in later sections, is perfect for detecting the state of a single ion. For an over-saturated ion fluorescing at $\gamma/2 = 2\pi \times 30\text{MHz}$, the photon count rate on the PMT shows 650kHz, giving a collection efficiency of 2% for the entire imaging setup using the PMT.

2.4. Experiment Setup

2.4.1. Generating control pulse sequences. The main control of the experiment is a computer running LabView software. A National Instrument 6534 PCI card outputs a 32-bit TTL signal, with each bit controlling an rf switch. Each rf switch connects a frequency generator/synthesizer to an actual optical modulator in the experiment. Some rf switches also functions as multiplexers, where the TTL signal determines which one of the two input signals is sent to a particular modulator. An example is the two frequencies that are multiplexed to the same AOM that switches the beam between resonant detection and Doppler cooling. A manual override is also built into the rf switches for diagnostic purposes.

Typical pulse sequences have the following format: 1) a Doppler cooling pulse is first turned on for 1 to 2 milliseconds, 2) an optical pumping pulse is turned on to initialize the ion in the $S_{1/2}(F = 0, m_F = 0)$ state, 3) some pulse sequence tailored specifically for the particular experiment, and 4) a pulse of detection laser and collect spontaneous emitted photons. Data in the form of photon counts from the PMT

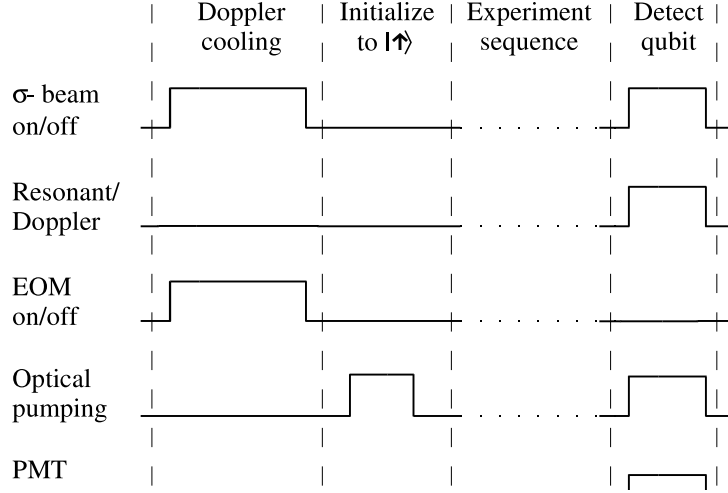


FIGURE 2.4.1. General experiment pulse sequence. The ions are Doppler-cooled for ~ 1 ms and then initialized to the \uparrow state before each experiment. Then a sequence of pulses are applied depending on the specific experiment that is being performed, and the state of the qubits are measured at the end. Each line shows the TTL signal controlling the corresponding rf switch.

during the detection cycle of the experiment is received by a National Instrument 6602 PCI counter card. One of the 32 digital channels from the output of the 6534 pulser card provides the appropriate gate for counting the photons from the qubit detection cycle at the end of the experiment, and photons scattered during the cooling cycle or during the experiment are ignored by the counter. The photon count from each gate pulse is stored in a buffer on the counter card, and the software waits until the user-specified number of experiments have been performed before downloading the buffer. This improves the duty cycle of the experiment since downloading information from hardware is time consuming, possibly taking up to milliseconds per download. The counter card is also used to trigger the 6534 pulser card at the beginning of each experiment to ensure the counter is armed before each experiment starts.

The downloaded data are first converted into a histogram indicating how many trials resulted in a given number of photons collected. The average number of photons can be extracted from the histogram and plotted on a graph. Alternatively, the histogram can be separated into two distributions, one for the state with many photon counts and one for the state with zero photon counts. A discriminator threshold can be set from the dark/bright state photon statistics, and the probability of the ion being in the bright state during the detection phase is plotted in place of the average number of photons. This probability is insensitive to the photon number fluctuations

that appear when the average number of photons is nonzero, but the probability is still sensitive to the quantum statistical fluctuations that may be associated with the state of the ion. For example, an ion in the state $|1\rangle$ fluorescing with an average photon count of X averaging over N trials will have photon number fluctuations $\sqrt{X/N}$ and no quantum fluctuation, and the discriminator can remove this photon number fluctuation. An ion in the state $|0\rangle + |1\rangle$ is collapsed into a bright state or a dark state in the measurement with equal probability and therefore has a quantum fluctuation $1/\sqrt{N}$ in N trials in addition to the photon number fluctuation, which can not be removed by the discriminating between the dark and bright photon counts.

2.4.2. Qubit detection fidelity. The qubit detection setup can be calibrated using a very simple experiment. First we run the pulse sequence shown in fig 2.4.1 without any additional experiment pulses. The ion is prepared in the $|0\rangle$ state and immediately measured. The result is shown in the top graph in fig 2.4.2. Then we run the pulse sequence again but this time without the initialization step. The Doppler cooling pulse should pump the ion to the $|F = 1, m_F = -1\rangle$ state due to its σ^- polarization (in fact, the polarization is set by tuning the quarter-wave plate while using the photon number distribution here as a real-time feedback). Therefore the ion should fluoresce during detection, and the photon number distribution is plotted in the bottom graph in fig 2.4.2. The distributions are clearly distinct, with the dark state having average photon number of almost 0, and the bright state having an average photon number of 12. The dark state has occasionally one or two counts due to background light or PMT dark counts (not temperature cooled) and higher number counts due to off-resonant pumping or imperfect preparation. The bright state has occasionally a zero count due to the tail end of the poisson distribution, imperfect polarization, or error in the preparation of the state. The errors for each discriminator threshold setting are determined by calculating the percentage in the dark state distribution that are above the threshold, and the percentage in the bright state distribution that are at or below the threshold. The optimal value for the threshold (minimum detection error) is where the error from the dark state distribution and the error from the bright state distribution are optimally matched. A systematic study of the detection fidelity at various intensities and gate pulse lengths showed that the highest detection fidelity of 99.7% occurs when the bright state produces an average photon count of 12 over a 200 microsecond detection window (at intensity $I = 0.10I_{sat}$).

Ideally, a fully functional quantum computer for trapped ions should contain multiple trapping zones where qubits in the internal states of the ions can be stored or processed. When a measurement needs to be performed on one ion, it is transported

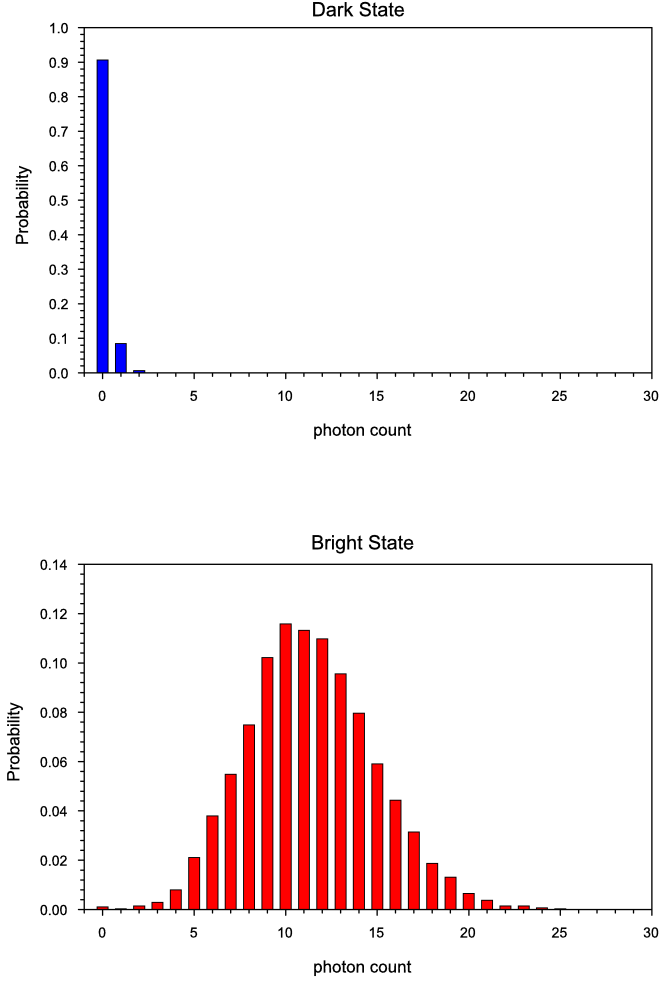


FIGURE 2.4.2. Histogram of photon counts from a single ion. Photons are collected by the PMT from a single ion in the $|\uparrow\rangle$ dark state (top) and the $|\downarrow\rangle$ bright state. The ion in the dark state emits no photons except for the 0.1% chance of off-resonant pumping into the bright state, and the statistics with one or two collected photons shown in the graph are likely due to background or dark counts on the PMT. The average number of collected photons from an ion in the bright state is 12, and the photon number distribution corresponds to a poisson distribution. From this data, a discriminator threshold is set at 2, below which the ion is considered to be collapsed into the dark state and otherwise considered to be collapsed into the bright state. The plots here show a 0.3% error in determining the state of the ion accurately using the discriminator.

to the “measurement zone” and its internal state can be measured using the procedure described above. However, one can imagine scenarios where it would be efficient to

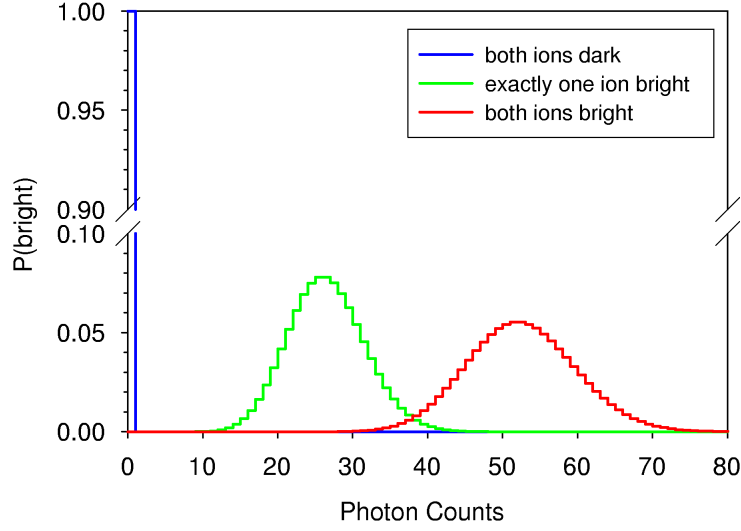


FIGURE 2.4.3. Poisson distribution of photon numbers for two ions (calculated). The distributions are for a mean of 0, 26, and 52, corresponding to two dark ions, exactly one bright ion and one dark ion, and two bright ions in the trap respectively. The distribution for two dark ions has no overlap with the other distributions, but the distributions for a single bright ion and two bright ions overlap, resulting in errors in determining the state of the ions.

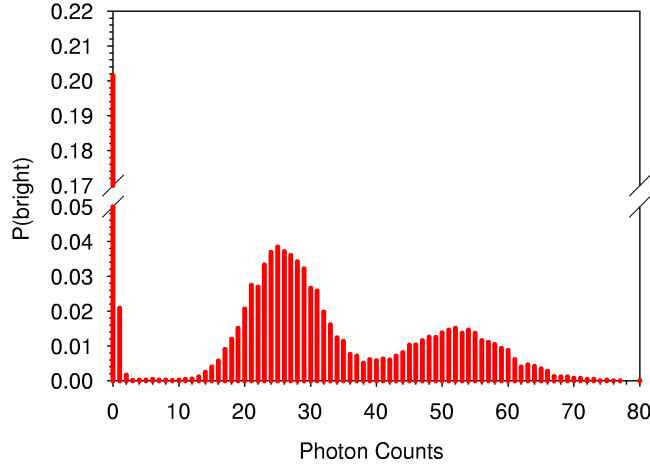


FIGURE 2.4.4. Histogram of photon counts from two ions. The ions are prepared in an equal superposition of $|\uparrow\rangle$ dark state and $|\downarrow\rangle$ bright state before detection. The distributions for zero, one, and two bright ions are distinct, with average photon numbers of 0, 26, and 52 respectively. The single bright ion distribution accounts for half of the probability distribution, and the distributions for two dark ions and two bright ions each account for 25% of the total probability (normalized to 1).

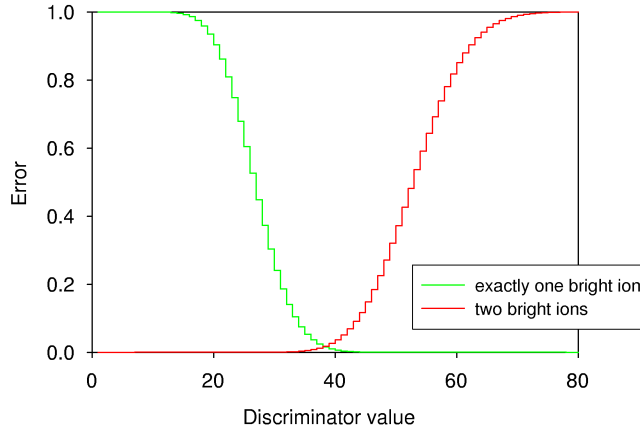


FIGURE 2.4.5. Detection error for two ions (calculated from theory). The corresponding overlapping poisson distributions are centered around a mean of 26 and 52 photon counts, corresponding to exactly one ion in the bright state and both ions in the bright state. The errors for each case is plotted against the discriminator threshold value. The intersect of the two plots at threshold value 38 corresponds to an overall detection error of 1.8%. This statistical error is approximately equal to the contribution due to off-resonant pumping an ion from the dark state to the bright state.

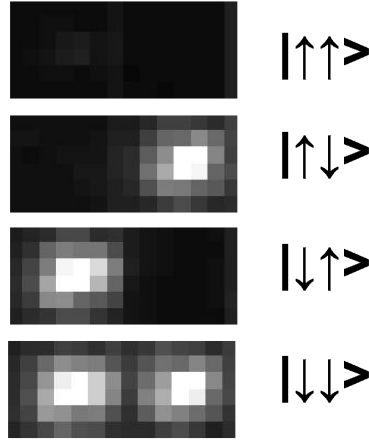


FIGURE 2.4.6. Detecting the state of two qubits with an intensified CCD camera. The images correspond to the states $|\uparrow\uparrow\rangle$, $|\uparrow\downarrow\rangle$, $|\downarrow\uparrow\rangle$, and $|\downarrow\downarrow\rangle$. Using the CCD camera, the states can be differentiated, which can not be done using the PMT. The quantum efficiency of the CCD is less than that of the PMT, but still provides a detection fidelity of $\sim 97\%$.

measure more than one ion at a time. Here, the motivation originates out of experimental necessity since the traps in the two-ion experiments in this thesis can only sustain a single trapping zone.

While a PMT is the most effective photon collecting device (highest quantum efficiency) compared to the other cameras, the photons emitted from one ion is indistinguishable from the photons emitted from the other ion using a PMT. This is problematic for some experiments, but certain measurements such as parity do not require the ions to be distinguishable. For two ions, the histogram of the photons counts shows three distributions: both ions in the dark state, both ions in the bright state, and exactly one ion in the bright state. While the single bright and the double bright distributions are distinct from the double dark distribution, the two poissonian distributions overlap since their widths are \sqrt{X} and $\sqrt{2X}$ respectively for an average photon count of X per bright ion. Typical detection condition has an average photon count of 26 for the single bright ion and an average photon count of 52 for two bright ions. The poisson distributions of the two ion fluorescence are plotted in figure 2.4.3, and the actual photon distribution of two ions in equal superposition of bright and dark states shown in figure 2.4.4. The error of determining the number of bright ions using a discriminator is theoretically 1.8%, as shown in figure 2.4.5.

Figure 2.4.6 shows the fluorescence detected by the CCD camera that allows us to differentiate the two ions during detection. One drawback of the CCD camera is the data download time can be on the order of $15ms$, which can significantly slow the experiment repetition rate. The imager also has a lower quantum efficiency than the PMT and therefore requires higher field intensity to distinguish the bright state from the background pedestal. For two ions, the detection fidelity is about 97%.

CHAPTER 3

Single Ion Coherent Operations

3.1. Notation

Implementing a quantum computer in a physical system requires the melding of different fields, each having its own language and notations. From the computer science perspective, the qubit is a system that can be in an arbitrary superposition of $|0\rangle$ and $|1\rangle$. However, the qubit can also be (and often is) described in terms of a spin-1/2 system, where a rich knowledge base already exists and the interactions are well known in atomic physics. In reality, any two-level quantum system can serve as a qubit, with a pseudo-spin label assigned to each one of the levels. In $^{111}\text{Cd}^+$ ion, the ground state hyperfine levels $|S_{1/2}, F = 0, m_F = 0\rangle$ and $|S_{1/2}, F = 1, m_F = 0\rangle$ are selected as the qubit levels. In this thesis, the following definition is used to translate between the different sets of notation:

$$\begin{aligned} |0\rangle &= |\uparrow\rangle = |S_{1/2}, F = 0, m_F = 0\rangle \\ |1\rangle &= |\downarrow\rangle = |S_{1/2}, F = 1, m_F = 0\rangle. \end{aligned}$$

In the field of quantum information, schemes for logic gates in one system often has direct analogies in other systems, though different physical interactions may be required to generate the desired Hamiltonian. For this thesis, the mathematical descriptions are presented in terms of a spin-1/2 system that physicists are familiar with, and can be applied to many other physical systems for quantum computation. In the experiments, the theories are transcribed into physical interactions with the ions, with results that are actual observables, or more specifically, the probability of measuring a qubit in a certain state.

In a system of trapped ions, the steady-state Hamiltonian consists of the internal energy of the qubits and the collective motion of the ions in the trapping potential. Each qubit is treated as a fictitious spin-1/2 particle in an effective constant magnetic field along a quantization axis (\mathbf{z}). The effective magnetic field accounts for the natural energy splitting $\hbar\omega_0$ between the spin levels $|\uparrow\rangle$ and $|\downarrow\rangle$, though the actual cause of the energy splitting in a real system may be due to some other mechanism (for example, hyperfine interaction in cadmium ion qubits). For simplicity, we restrict the ion's motion along one dimension (call it \mathbf{z}_T), though in special cases it may be

desirable to include motion along other dimensions. For N ions in the trap, there are N collective vibrational modes, and the complete steady-state Hamiltonian can be written as

$$(3.1.1) \quad \hat{H}_0 = \sum_{i=1}^N \frac{\hbar\omega_0}{2} \hat{\sigma}_z^{(i)} + \sum_{\nu=1}^N \hbar\omega_\nu \hat{a}_\nu^\dagger \hat{a}_\nu,$$

where i is the index for the N ions available in the trap and the Pauli spin matrix $\sigma_z^{(i)}$ evaluates the energy of the i -th qubit, ω_ν is the frequency of collective vibration for the normal mode indexed by ν , and \hat{a}_ν^\dagger and \hat{a}_ν are the creation and annihilation operators respectively for the mode ν . This assumes the displacement of each ion from its equilibrium position is small compared to ion spacing so that the Coulomb interaction can be approximated by its lowest order (quadratic) term [31]. Typically, the ions are strongly bound in the transverse \mathbf{x}_T and \mathbf{y}_T directions but weakly bound in the \mathbf{z}_T direction (note that trap axes \mathbf{x}_T , \mathbf{y}_T , and \mathbf{z}_T of the harmonic oscillator potential need not be the same as the quantization axes \mathbf{x} , \mathbf{y} , and \mathbf{z}). Further, logic gates involving one or two qubits are sufficient for universal quantum computing, therefore we will only consider interactions with $N \leq 2$ ions.

As mentioned previously, the harmonic oscillator potential is used as a quantum databus for transferring and processing information between ions. Although many entangling schemes, including the original Cirac and Zoller proposal, are designed specifically for ion trap systems using this feature, the Hamiltonian in eq 3.1.1 appears naturally (or could be engineered) in many other physical systems as well. For example, the Hamiltonian is identical in cavity QED experiments [32], where the internal state of atoms interacts with the photons in the quantized cavity modes described by a harmonic oscillator. This is similarly true for superconducting qubits coupled by the quantized microwave cavity mode of a transmission line [33]. Some of these systems such as cavity QED have been well studied and provide great insights for understanding other analogous systems.

The rest of this chapter explores ways to maneuver this pseudo-spin-1/2 system to perform arbitrary single qubit rotations, and also to couple the spin to the harmonic oscillator databus. In later chapters, the same principles are used to produce more complicated interactions with the harmonic oscillator to perform logic operations on more than one qubit.

3.2. Single Qubit Rotation

This section lays out the most general form for the type of interactions that can lead to coupling between two spin states. Here the system is simplified to only one ion in the trap with one mode of vibration determined by the trap parameters. The

Hamiltonian contains two terms

$$(3.2.1) \quad H_0 = \frac{\hbar\omega_0}{2}\hat{\sigma}_z + \hbar\omega_1\hat{a}^\dagger\hat{a}.$$

The state of the system is represented by

$$(3.2.2) \quad |\Psi(t)\rangle = \sum_{n=1}^{\infty} (a_{\uparrow,n}(t) |\uparrow\rangle + a_{\downarrow,n}(t) |\downarrow\rangle) |n\rangle$$

where $|n\rangle$ denotes the eigenstates of the harmonic oscillator with eigenvalue $n\hbar\omega_1$.

In the spin-1/2 analogy, the two spin levels can be coupled using a magnetic dipole coupling

$$(3.2.3) \quad \hat{H}_1 = -\boldsymbol{\mu} \cdot \mathbf{B}$$

with magnetic field $\mathbf{B}(\mathbf{r}, t) = B_x \cos(\mathbf{k}\mathbf{r} - \omega t + \phi)\mathbf{x}$. In an actual system, the coupling mechanism need not be a magnetic dipole interaction, as long as the interaction yields a Hamiltonian of the form

$$(3.2.4) \quad H_1 = \frac{\hbar\Omega}{2} (\sigma_+ e^{i(\mathbf{k}\mathbf{r} - \omega t + \phi)} + \sigma_- e^{-i(\mathbf{k}\mathbf{r} - \omega t + \phi)}) .$$

Here $\Omega = -\mu_B B_x / (2\hbar)$ is call the Rabi frequency. The other terms in eq 3.2.3 will be removed in the Rotating Wave Approximation (RWA) and are therefore unnecessary.

To understand the evolution of the system under this interaction, first consider a special case where the magnetic field propagates perpendicular to the direction of the harmonic potential, i.e. $\mathbf{k} \cdot \mathbf{z}_T = 0$. Since the photons have no momentum in the \mathbf{z}_T direction, the ion can not couple to the harmonic oscillator via this interaction (see Appendix A for details). Therefore the factor $e^{i\mathbf{k}\cdot\mathbf{r}}$ contributes at most a phase factor e^{ikr_0} , which is assumed to be included phase ϕ . The interaction Hamiltonian $H_I = e^{iH_0 t/\hbar} H_1 e^{-iH_0 t/\hbar}$ in the rotating frame of the qubit is (applying the RWA)

$$(3.2.5) \quad H_I = \frac{\hbar\Omega}{2} (\sigma_+ e^{-i(\delta\omega t + \phi)} + \sigma_- e^{i(\delta\omega t + \phi)}) ,$$

where $\delta\omega = \omega - \omega_0$ is the field detuning from spin resonance. The solution to this Rabi two-level problem can be found in many textbooks [34] :

$$(3.2.6) \quad \begin{aligned} \dot{c}_{\uparrow,n} &= -\frac{i\Omega}{2} e^{-i((\delta\omega)t + \phi)} c_{\downarrow,n} \\ \dot{c}_{\downarrow,n} &= -\frac{\Omega}{2} e^{i((\delta\omega)t + \phi)} c_{\uparrow,n} \end{aligned}$$

where $c_{m,n}(t)$ are the amplitudes of the corresponding levels $|m\rangle |n\rangle$ for the qubit state in the rotating frame

$$(3.2.7) \quad |\psi\rangle = \sum_{n=1}^{\infty} (c_{\uparrow,n}(t)e^{-i\omega_0 t/2} |\uparrow\rangle + c_{\downarrow,n}(t)e^{i\omega_0 t/2} |\downarrow\rangle) e^{in\omega_1 t} |n\rangle.$$

When the field is on resonance, the time-evolution operator $U(t)$ which transforms the initial state to the final state by $|\psi(t)\rangle = \hat{U}(t) |\psi(0)\rangle$ can be written in the $\{c_{\uparrow,n}, c_{\downarrow,n}\}$ basis as

$$(3.2.8) \quad \hat{U}(t) = \begin{pmatrix} \cos\left(\frac{\Omega t}{2}\right) & -ie^{-i\phi}\sin\left(\frac{\Omega t}{2}\right) \\ -ie^{i\phi}\sin\left(\frac{\Omega t}{2}\right) & \cos\left(\frac{\Omega t}{2}\right) \end{pmatrix} = R(\Omega t, \phi).$$

The matrix $R(\Omega t, \phi)$ represents a rotation on the Bloch sphere by angle $\theta = \Omega t$ around a torque vector pointing in the direction $\cos(\phi)\mathbf{x} + \sin(\phi)\mathbf{y}$ on the equatorial plane.

A universal quantum computer must be able to rotate a single qubit by any given angle on the Bloch sphere around any axis. Here we just demonstrated rotation around any vector on the xy-plane. But what about rotation around an axis not in the xy-plane? From Euler's rotation theorem we know that an arbitrary rotation in three-dimensions can be parameterized by three independent variables called the Euler angles, each rotating around an orthogonal axis. The time evolution operator already accounts for rotation around two of the three axis: $R_x(\theta) = R(\theta, 0)$ for rotation around the x-axis, and $R_y(\theta) = R(\theta, \phi)$ for rotation around the y-axis. Rotations around the z-axis can be performed using a composite sequence of rotation along the x-axis and the y-axis: $R_z(\theta) = R_x(\pi/2) R_y(\theta) R_x(-\pi/2)$. The rotation around the z-axis is equivalent to applying a phase shift θ to the qubit. Therefore, the Hamiltonian in eq 3.2.5 is sufficient for arbitrary single qubit rotation given that the user has control of the phase and the duration of interaction.

3.3. Coupling Spin to Motion

However, a mechanism to connect the internal state to the quantum databus for entangling operations is still needed. Now consider the more general case where the field couples to the harmonic oscillator. When the wave vector of the field has a component in the harmonic oscillator potential, then the $\mathbf{k} \cdot \mathbf{z}_T$ does not equal zero. The position operator $\hat{\mathbf{z}}_T = z_0 (\hat{a} + \hat{a}^\dagger) \vec{\mathbf{z}}_T$ (where $\vec{\mathbf{z}}_T$ is the unit vector in the z_T direction) couples to the harmonic oscillator, and the interaction Hamiltonian now becomes

$$(3.3.1) \quad H_I = \frac{\hbar\Omega}{2} (\sigma_+ \exp\{i[\eta(\hat{a}e^{-i\omega_1 t} + \hat{a}^\dagger e^{i\omega_1 t}) - (\delta\omega)t - \phi]\} + h.c.).$$

where $\eta = k_z z_0$ is the Lamb-Dicke parameter, with $k_z = \mathbf{k} \cdot \vec{z}_T$ being the component of the wave vector in the z_T direction and $z_0 = \sqrt{\hbar/(2M\omega_1)}$ being the position spread of the ion in the ground state. In the resolved-sideband limit, where $\Omega \ll \omega_1$, specific vibrational levels $|\uparrow\rangle |n'\rangle \leftrightarrow |\downarrow\rangle |n\rangle$ can be coupled by tuning the frequency $\delta\omega = (n - n')\omega_1 + \delta$ to account for the energy difference between the vibrational levels n and n' (and keeping the detuning $\delta \ll \omega_1$ small). The other levels can then be eliminated, and the coefficients of the two coupled levels evolve as

$$(3.3.2) \quad \begin{aligned} \dot{c}_{\uparrow,n'} &= -D_{n',n} \frac{\Omega}{2} e^{-i(\delta t + \phi)} c_{\downarrow,n} \\ \dot{c}_{\downarrow,n} &= -D_{n',n} \frac{\Omega}{2} e^{i(\delta t + \phi)} c_{\uparrow,n'} \end{aligned}$$

where $D_{n',n}$ is the Debye-Waller factor defined by

$$(3.3.3) \quad \begin{aligned} D_{n',n} &= \left| \langle n | e^{i\eta(a + a^\dagger)} | n' \rangle \right| \\ &= e^{-\eta^2/2} \left(\frac{n_{<}}{n_{>}} \right)^{1/2} \eta^{|n' - n|} L_{n_{<}}^{|n' - n|}(\eta^2), \end{aligned}$$

where $n_{<}(n_{>})$ is the lesser (greater) of n' and n , and L_n^α is the generalized Laguerre polynomial (see Appendix A).

Eq 3.3.2 is analogous to eq 3.2.6 for the two-level Rabi flopping, and the solution is the same, except replacing the two levels with $|\uparrow\rangle |n'\rangle$ and $|\downarrow\rangle |n\rangle$. Note that the same field can also couple $|\uparrow\rangle |n' + 1\rangle$ and $|\downarrow\rangle |n + 1\rangle$. In fact, a field tuned to $\delta\omega = (\Delta n)\omega_1$ will simultaneously couple any two levels $|\uparrow\rangle |n\rangle$ and $|\downarrow\rangle |n + \Delta n\rangle$. However, the Debye-Waller factor $D_{n+\Delta n,n}$ is different for each one of these transitions, and the population of each pair of coupled levels oscillates at Rabi frequency

$$(3.3.4) \quad \Omega_{n,n+\Delta n} = D_{n,n+\Delta n} \Omega_0.$$

If the initial state is not in a single vibrational level, this could result in dephasing as each vibrational level Rabi oscillates at a different frequency. Sometimes a revival of spin oscillation can be observed after the dephasing as the different Rabi oscillations become in phase again. This effect is noticeable when considering the effects of temperature, which will be discussed in section 3.9.

3.3.1. Lamb-Dicke Limit. One of the interesting regimes to consider is when the ion's position spread is small compared to the wavelength, i.e. $\sqrt{\langle k_z^2 \hat{z}_T^2 \rangle} \ll 1$. This is called the Lamb-Dicke limit, which is a more stringent condition than saying the Lamb-Dicke parameter η is much less than 1, since η accounts only for the ground state, but the vibrational level distribution of the ion is included in the Lamb-Dicke

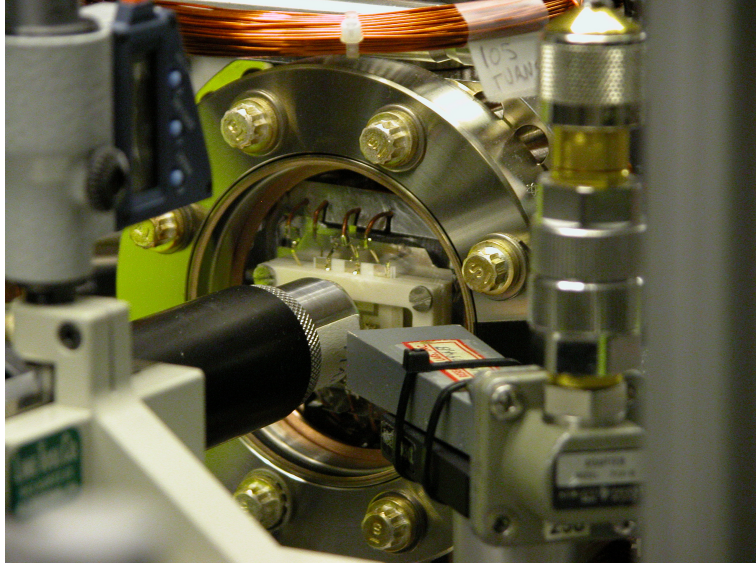
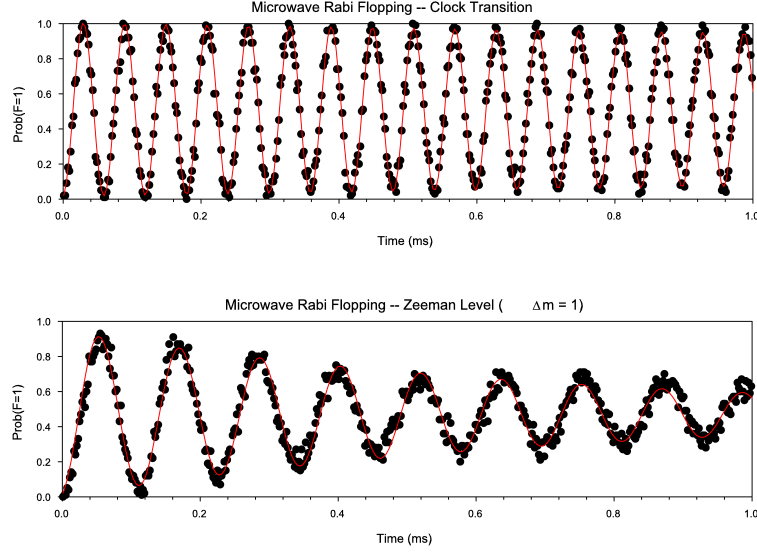


FIGURE 3.4.1. Orientation of the microwave horn. The microwave horn is the grey rectangular waveguide on the right oriented 45° with respect to the trap axis and the imaging optics supported by the black cylinder extending to the left. The quantization axis is 90° with respect to the microwave horn, angled in between the imaging tube and the trap axis (magnetic coils not visible in this picture). The copper coil on the top of the trap and another coil in an orthogonal direction are used to adjust the magnetic field so that the quantization axis is parallel to the detection beam. The microwave horn is approximately 4cm from the ion(s).

limit. In this limit, $\eta^2 n \ll 1$ is small and only terms up to the lowest order in η are evaluated.

We want to consider three types of transitions here: the carrier ($n' = n$), the first red sideband ($n' = n - 1$), and the first blue sideband ($n' = n + 1$). In the Lamb-Dicke Limit, the Debye-Waller factor is $D_{n,n} = 1$ for the carrier, $D_{n,n+1} = \eta\sqrt{n+1}$ for the first red sideband, and $D_{n,n-1} = \eta\sqrt{n}$ for the first blue sideband. The Debye-Waller factor for the j -th order sideband scales as η^j . As η approaches zero, the sideband strengths also diminishes to zero. This confirms the results from the case in section 3.2 where $\eta = 0$ and therefore has no sideband coupling. In general, $\eta\sqrt{n}$ needs to be sufficiently large to retain a reasonable sideband transition strength in order to couple to motion. Therefore, perturbation from higher order terms can sometimes be observed. For example, we can experimentally detect the changes in the carrier transition strength with respect to temperature, which closely follows the calculation that includes the next order in the Debye-Waller factor: $D_{n,n} = 1 - 2\eta^2$.



*Rabi frequency is slower for the Zeeman level transition due to the polarization of the microwave.

FIGURE 3.4.2. Rabi oscillations driven by microwaves. The frequency of the microwave is resonant with the $S_{1/2}$ ground state $|F = 0, m_F = 0\rangle \leftrightarrow |F = 1, m_F = 0\rangle$ clock transition (top) and the $|F = 0, m_F = 0\rangle \leftrightarrow |F = 1, m_F = 1\rangle$ transition (bottom). The horizontal axis indicates the length of the microwave pulse, and the vertical axis shows the probability of detecting the ion in the $|\downarrow\rangle$ state, with the ion starting in the $|\uparrow\rangle$ state initially. The bottom graph shows decoherence due to fluctuations in the magnetic field on the time scale of 1ms. The applied magnetic field is 3.75 gauss, producing a Zeeman shift of 5.25MHz.

3.4. Microwave Transitions

Single qubit transitions in cadmium ions can be driven by microwaves via magnetic dipole coupling. The ground state hyperfine qubit levels $|S_{1/2}, F = 0, m_F = 0\rangle$ and $|S_{1/2}, F = 1, m_F = 0\rangle$ have a net zero change in the total angular momentum $\Delta m_F = 0$, thereby requiring a π -polarized magnetic field for the transition according to the dipole selection rule. In the actual experiments, an amplified microwave signal is broadcasted by a horn aimed perpendicular to the quantization axis with the polarization lying parallel to the quantization axis. The trap axis (\mathbf{z}_T) and the quantization axis (\mathbf{z}) form a 45° angle, and the Lamb-Dicke parameter $\eta = kz_0/\sqrt{2} = 5 \times 10^{-6}$ for a frequency of $\omega = 2\pi \times 14.530\text{GHz}$ and a trap strength of $\omega_1 = 2\pi \times 1\text{MHz}$. This means the sideband strengths are weaker than the carrier transition by a factor of 10^{-6} , making it impractical to couple to the motion using microwaves.

Figure 3.4.2 is an example of Rabi flopping using microwaves. The ion is initialized in the $|\uparrow\rangle = |S_{1/2}, F=0, m_F=0\rangle$ state, and a pulse of microwave resonant with the transition is turned on for time t . The probability of finding the ion in the $|\downarrow\rangle = |S_{1/2}, F=1, m_F=0\rangle$ state oscillates at frequency $\Omega = 2\pi \times 16.7\text{kHz}$ as t increases, with about 1W of power applied to the horn. The amplitude of oscillation between clock states does not decay even at finite temperature since microwaves does not couple to motion and the Debye-Waller factor is the same for all vibrational levels. Commercial microwave synthesizers are also extremely stable, maintaining phase coherence for more than 50ms, which is much longer than the experiments require.

A drawback of this scheme, besides having nominally no coupling to the motion, is that individual addressing of the ions is not possible since microwaves can not be focus to the millimeter level or below. Even in traps with multiple storage regions, the separation between ions in different trap zones is still on the order of a millimeter or less. Therefore, microwaves do not satisfy the requirement of arbitrary individual single qubit rotation for quantum computation when there is more than one ion present. A better method that avoids both problems is to drive stimulated Raman transitions, which is discussed in the next section. However, qubit transitions via microwaves is still a useful tool in the experiments for one or two qubit operations and for diagnostic purposes. For example, a scan of the microwave frequency enables us to pinpoint the exact energy separation of the qubit levels without Raman transitions and without the effects of light shift, and also measures the Zeeman splitting of the $F=1$ triplet (with a mixed polarization).

3.5. Stimulated Raman Transitions

Stimulated Raman transition is a two photon process involving three levels: in this case, two qubit levels $|\uparrow\rangle$ and $|\downarrow\rangle$ in the ground state and an excited electronic state $|e\rangle$ having respective optical frequency spans $\tilde{\omega}_{\uparrow,e}$ and $\tilde{\omega}_{\downarrow,e} = \tilde{\omega}_{\uparrow,e} + \omega_0$. Two optical fields $\mathbf{E}_l(\mathbf{r}) = \tilde{E}_l(\mathbf{r}) \cos(\mathbf{k}_l \cdot \mathbf{r} - \omega_l t - \phi_l) \epsilon_l$ with $l = \alpha, \beta$, connect each of the qubit levels $|\uparrow\rangle$ and $|\downarrow\rangle$, respectively, to state $|e\rangle$ through electric dipole operators μ_{\uparrow} and μ_{\downarrow} (analogous to the magnetic dipole). We assume that the optical fields have a difference frequency $\omega_{\beta} - \omega_{\alpha} = \omega_0 + \delta\omega$ near the frequency splitting of the two spin states, and are both detuned from the excited-state resonance by $\Delta = \tilde{\omega}_{\uparrow,e} - \omega_{\alpha}$, as drawn in Figure 3.5.1.

The dipole interaction $H = -\boldsymbol{\mu} \cdot \mathbf{E}$ can be transformed to a rotating frame at frequency ω_{α} in order to remove all terms varying with optical frequencies, and under the usual optical rotating wave approximation (RWA), the interaction Hamiltonian

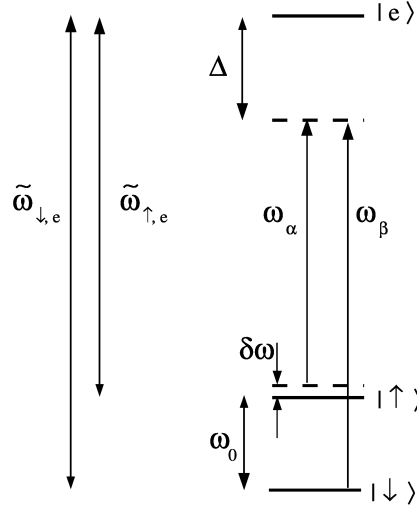


FIGURE 3.5.1. Stimulated Raman transition via an excited state. Fields at frequency ω_α and ω_β couple the qubit levels $|\uparrow\rangle$ and $|\downarrow\rangle$ via the excited state $|e\rangle$. The fields are detuned from the excited state resonances $\tilde{\omega}_{\uparrow,e}$ and $\tilde{\omega}_{\downarrow,e}$ by frequency Δ .

between the fields and the ions is

$$\begin{aligned}
 \hat{H}_I = & \frac{\hbar g_{\uparrow,\alpha}}{2} (e^{i\mathbf{k}_\alpha \cdot \hat{\mathbf{r}} + i\phi_\alpha} |e\rangle \langle \uparrow| + h.c.) \\
 (3.5.1) \quad & + \frac{\hbar g_{\downarrow,\beta}}{2} (e^{i\mathbf{k}_\beta \cdot \hat{\mathbf{r}} + i\phi_\beta} e^{-i(\omega_0 + \delta\omega)t} |e\rangle \langle \downarrow| + h.c.) + \frac{\hbar \Delta}{2} |e\rangle \langle e|.
 \end{aligned}$$

In this expression, the dipole coupling strengths between qubit state $|m\rangle = |\uparrow\rangle, |\downarrow\rangle$ and excited state $|e\rangle$ from laser field l are given by $\hbar g_{m,l} = -\mu_m \cdot \epsilon_l \tilde{E}_l(\mathbf{r})/2$.

When the detuning Δ of the optical fields from electronic resonance is much larger than the excited state linewidth γ and the coupling strengths $|g_{m,l}|^2$, spontaneous emission during the optical coupling is negligible [26] and the excited state $|e\rangle$ can be adiabatically eliminated. Applying RWA on the microwave frequencies, we find

$$\begin{aligned}
 \hat{H}_I = & \frac{\hbar \Omega}{2} (e^{i(\Delta \mathbf{k} \cdot \hat{\mathbf{r}} - (\delta\omega)t + \Delta\phi)} |\uparrow\rangle \langle \downarrow| + h.c.) \\
 (3.5.2) \quad & + \frac{\hbar \chi_\downarrow}{2} |\downarrow\rangle \langle \downarrow| + \frac{\hbar \chi_\uparrow}{2} |\uparrow\rangle \langle \uparrow|
 \end{aligned}$$

where $\Delta \mathbf{k} = \mathbf{k}_\beta - \mathbf{k}_\alpha$ and $\Delta \phi = \phi_\beta - \phi_\alpha$ are the differences in the wave-vector and the phase of the two applied fields, $\Omega = g_{\uparrow,\alpha} g_{\downarrow,\beta}^*/2\Delta$ is the “base Rabi frequency” directly coupling the qubit states, and $\chi_m = (|g_{m,\alpha}|^2 + |g_{m,\beta}|^2)/2\Delta$ corresponds to the light

shift on the qubit level $|m\rangle$ by both optical fields. In terms of spin operators,

$$(3.5.3) \quad \hat{H}_I = \frac{\hbar\Omega}{2} (\hat{\sigma}_+ e^{i(\Delta\mathbf{k}\cdot\hat{\mathbf{r}} - (\delta\omega)t + \Delta\phi)} + \hat{\sigma}_- e^{-i(\Delta\mathbf{k}\cdot\hat{\mathbf{r}} - (\delta\omega)t + \Delta\phi)}) + \frac{\hbar\chi_-}{2} \hat{\sigma}_z,$$

where $\chi_- = (\chi_\uparrow - \chi_\downarrow)/2$ is the difference in the light shift on both levels. The common light shift $(\chi_\uparrow + \chi_\downarrow)/2$ has no real effect on the spin system and is removed from the Hamiltonian. In the interaction frame of the vibrational levels, Equation 3.5.2 becomes

$$(3.5.4) \quad \hat{H}_I = \frac{\hbar\Omega}{2} (\hat{\sigma}_+ e^{i\eta(\hat{a}e^{-i\omega t} + \hat{a}^\dagger e^{i\omega t})} e^{-i(\delta\omega)t} e^{i(\Delta k r_0 + \Delta\phi)} + h.c.) + \frac{\hbar\chi_-}{2} \hat{\sigma}_z.$$

This interaction Hamiltonian appears to be similar to eq 3.3.1, with the phase ϕ replaced by the phase difference $\Delta\phi$, the Lamb-Dicke parameter $\eta = \Delta k_z z_0$, and an extra term for the light shift [35].

3.5.1. AC Stark shift. The interaction Hamiltonian from eq 3.5.4 contains a term that shifts the relative energy of the two qubit levels by an amount $\hbar\chi$ proportional to the intensity of the fields. This light shift (also called AC Stark shift) in turn changes the resonant coupling frequency for stimulated Raman transitions. Transforming into a new rotating frame with $e^{i\omega'_0 \hat{\sigma}_z t/2} H_I e^{-i\omega'_0 \hat{\sigma}_z t/2}$, the interaction Hamiltonian becomes

$$(3.5.5) \quad \hat{H}_I = \frac{\hbar\Omega}{2} (\hat{\sigma}_+ e^{i\eta(\hat{a}e^{-i\omega t} + \hat{a}^\dagger e^{i\omega t})} e^{-i(\delta\omega')t} e^{i(\Delta k r_0 + \Delta\phi)} + h.c.)$$

where $\delta\omega' = \omega_\beta - \omega_\alpha - \omega'_0$ is the detuning from the new Stark-shifted resonance $\omega'_0 = \omega_0 + \chi_-$ in the presence of the optical fields E_α and E_β . This now has the same form as eq 3.3.1, except the detuning $\delta\omega$ is replaced by $\delta\omega'$ the detuning from the Stark-shifted resonance. This interaction Hamiltonian now guides the qubit in the Stark-shifted rotating frame, satisfying Schrödinger's equation $i\hbar \left| \dot{\psi}(t) \right\rangle = \hat{H}_I |\psi(t)\rangle$ for the coefficients $\{\tilde{c}_{\uparrow,n}(t), \tilde{c}_{\downarrow,n}(t)\}$ in

$$(3.5.6) \quad |\psi(t)\rangle = \sum_{n=0}^{\infty} \left\{ \tilde{c}_{\uparrow,n}(t) e^{i\omega'_0 t/2} |\uparrow\rangle + \tilde{c}_{\downarrow,n}(t) e^{i\omega'_0 t/2} |\downarrow\rangle \right\} e^{i\omega_0 t} |n\rangle.$$

Note that this also advances the relative phase between the two qubit levels by $e^{i(\omega'_0 - \omega_0)t}$ with respect to the natural rotation frequency after the field has been turned on for time t .

3.5.2. Copropagating Raman Fields. For copropagating Raman fields, the wave-vector difference $\Delta\mathbf{k}$ is zero, as is the Lamb-Dicke parameter η . Therefore, this interaction provides no coupling to the motion. This can be considered in terms the momentum transfer as the ion absorbs a photon from one field and emits a photon into the other field in the process of making the transition. If the absorbed photon

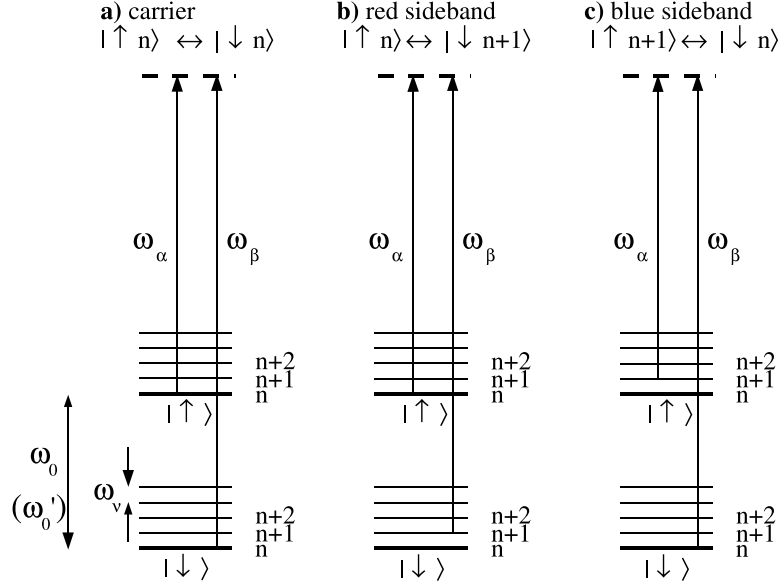


FIGURE 3.5.2. Stimulated Raman transition between vibrational levels. Coupling depends on the beat note of the two Raman fields $\omega_\beta - \omega_\alpha$: a) ω'_0 for carrier transition, b) $\omega'_0 - \omega_\nu$ for the first red sideband transition, and c) $\omega'_0 + \omega_\nu$ for the first blue sideband transition. The qubit frequency splitting shifts from ω_0 to ω'_0 due to AC Stark effect when the fields are turned on.

and the emitted photon propagate in the same direction, there is no net momentum transfer to the ion. Similarly, if the vector difference $\Delta\mathbf{k}$ is not zero but $\Delta\mathbf{k} \cdot \mathbf{z}_T = 0$ has no component in the direction of oscillation, there is no coupling to the motion. In these cases, the Raman fields can only drive carrier transitions where the vibrational state is unchanged ($\Delta n = 0$). When $\delta\omega'$ is zero, i.e. the frequency difference is equal to the Stark shifted resonance $\omega_\beta - \omega_\alpha = \omega'_0$, then the Hamiltonian in eq 3.5.5 couples the qubit states $|\uparrow, n\rangle \leftrightarrow |\downarrow, n\rangle$ resonantly with Rabi frequency $|\Omega|$ for all n .

3.5.3. Non-copropagating Raman Fields. In the experiments, the non-copropagating Raman beams form a 90° angle and are both 45° with respect to the trap axis \mathbf{z}_T (see figure 3.5.3). Due to the beam geometry, the wave vector difference becomes $\Delta k_z = \sqrt{2}k$. The final result is $\eta = 0.39/\sqrt{\nu_1/\text{MHz}}$ for a wavelength of $\lambda = 214.5\text{nm}$, ion mass $M = 111 \times (1.67 \times 10^{-27}\text{kg})$, and a trap frequency ν_1 in MHz. This is a reasonable value for driving the first few sideband transitions for typical trap frequencies on the order of MHz.

3.5.4. Polarization. For the cadmium ion qubit, stimulated Raman transition couples to the excited P states through electric dipoles. Since both qubit states must couple to the same excited state, the available channels are restricted by the selection

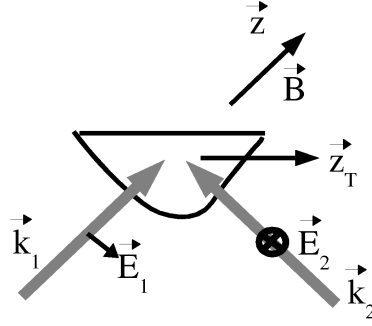


FIGURE 3.5.3. Diagram of non-copropagating Raman beam setup. The Raman fields propagate in orthogonal directions, and each beam form a 45° angle with the trap axis z_T . The wave vector difference $\Delta k = k_2 - k_1$ has a component in the direction z_T and therefore can transfer momentum to the ion's vibration in that direction. Δk also has no component in the x_T and y_T directions and therefore do not couple to transverse motion. The quantization axis provided by the applied magnetic field is also 45° with respect to the trap axis z_T , and the polarization of the two Raman fields are perpendicular to each other as shown in the diagram to maximize the transition rate.

rule, which demands the fields to be polarized in specific directions. The P state has two fine structure manifolds with total electronic angular momentum $J = 1/2$ and $J = 3/2$, separated by 74 THz. The only excited states that couple to both qubit levels $S_{1/2}(F = 0, m_F = 0)$ and $S_{1/2}(F = 1, m_F = 0)$ are $P_J(F = 1, m_F = \pm 1)$ levels for $J = 1/2$ and $J = 3/2$. Figures 3.5.4 and 3.5.5 show the Clebsch-Gordon coefficients for all electric dipole couplings between the S ground states and the excited P states. Note that if the photons in both fields have angular momentum $+1$ in the direction of the quantization axis, then the fields drive stimulated Raman transitions via $P_J(F = 1, m_F = 1)$ state. If the photons in both fields have angular momentum -1 in the direction of the quantization axis, then the fields drive stimulated Raman transitions via $P_J(F = 1, m_F = -1)$ state. Since the absorbed photon and the emitted photon have the same angular momentum, the total angular momentum of the ion remains unchanged $\Delta m_F = 0$.

In the experiment setup, one of the Raman fields travels parallel to the quantization axis while the other travels perpendicular to it (along the x -axis). The latter must be linearly polarized along the y -axis, which contains both σ_+ and σ_- polarization, since π -polarized light can not be used to drive transitions. The field parallel to the quantization axis can be circularly polarized, but the transition rate is reduced

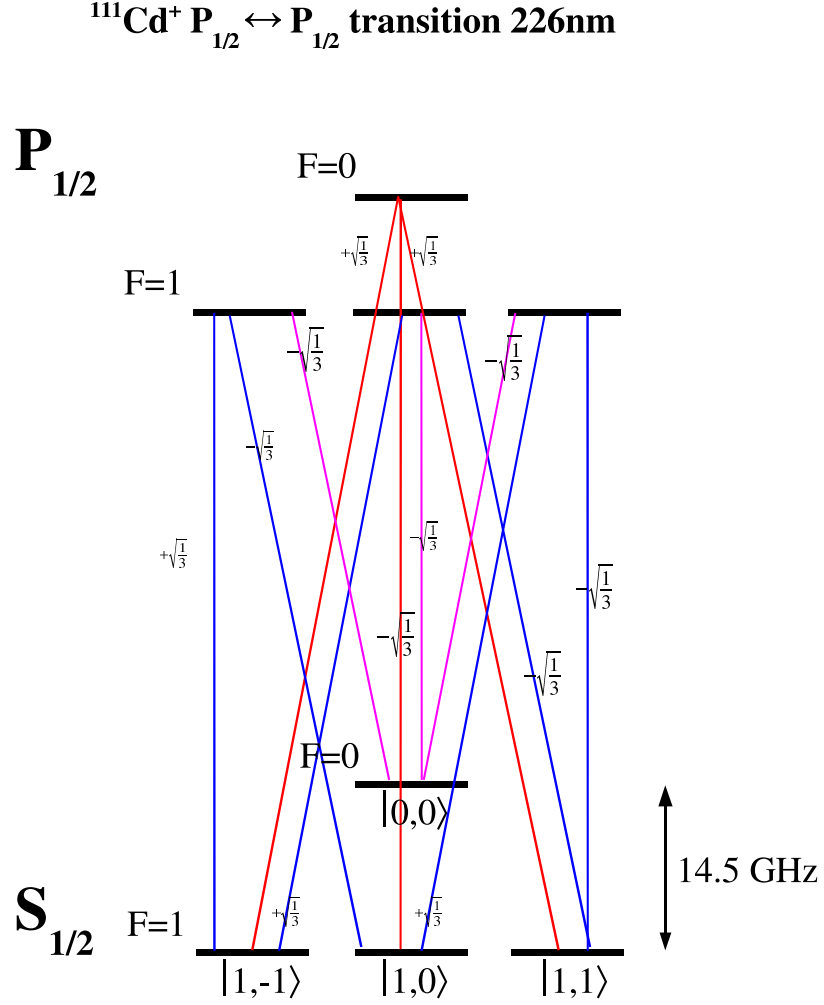


FIGURE 3.5.4. Branching ratios of the $S_{1/2} \leftrightarrow P_{1/2}$ transitions

by $1/\sqrt{2}$ because only half the intensity ($1/\sqrt{2}$ of the field) in the other beam with the same polarization is utilized in driving the transition. Alternatively, both beams can be linear polarized. The Clebsch-Gordon coefficients show that coupling through the $m_F = 1$ state ($2/3 \times 1/6$ for $P_{3/2}$, $-1/3 \times 1/3$ for $P_{1/2}$) has equal amplitude but opposite phase compared to the coupling through the $m_F = -1$ state ($2/3 \times -1/6$ for $P_{3/2}$, $-1/3 \times -1/3$ for $P_{1/2}$). Therefore, the product of the field components driving transitions via one path $E_{+, \alpha} E_{+, \beta}^*$ must have a π phase shift relative to the the product of the field components driving transitions via the other path $E_{-, \alpha} E_{-, \beta}^*$. If both

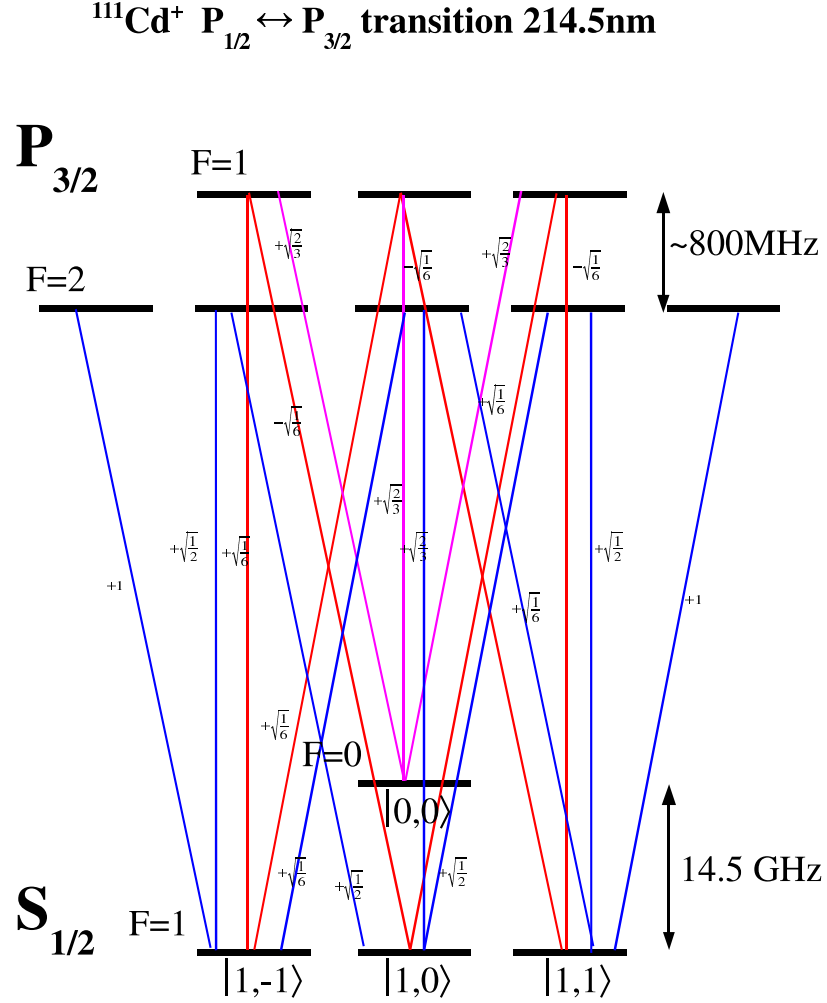


FIGURE 3.5.5. Branching ratios of the $S_{1/2} \leftrightarrow P_{3/2}$ transitions

fields are polarized along y , then the product of the field components have the same sign $E_{+,\alpha}E_{+,\beta}^* = E_{-,\alpha}E_{-,\beta}^*$ and the transition amplitudes cancel each other. However, if the field traveling parallel to the quantization axis is polarized along x , then the σ_+ component and the σ_- component have the same phase while the field polarized along y have the two circular components phase shifted by π . Therefore, the field products $E_{+,\alpha}E_{+,\beta}^* = -E_{-,\alpha}E_{-,\beta}^*$ also have a π phase shift relative to each other, resulting in the transition amplitudes to add. This polarization turns out to be as efficient as having counter-propagating beams with pure σ_+ polarization of the same intensities,

since the intensities in each σ component is exactly one half of the total intensity in each beam, which contributes one half the coupling strength from each path. This is true only because the coupling strength is proportional to the product of the electric field rather than the product of the intensities. However, the Lamb-Dicke parameter η at 90° geometry is still smaller than the counter-propagating geometry by a factor of $\sqrt{2}$.

3.5.5. Spontaneous Emission. Spontaneous emission is an unavoidable source of decoherence since the coupling between the ion and the vacuum field can never be turned off, but the spontaneous emission rate is dependent on the field intensity and detuning which can be varied to our advantage. To quantify the amount of error per Rabi cycle due to spontaneous emission, we can compare the spontaneous emission rate to the Raman transition rate. For a large detuning Δ where $(2\Delta/\gamma)^2 \gg (1+s)$, the spontaneous emission rate can be approximated as $\gamma_p = s\gamma^3/(4\Delta^2)$ where $s = I/I_{sat}$ is the saturation parameter. Compared to the Raman transition rate $\Omega = s\gamma^2/\Delta$, the ratio between the spontaneous emission rate and the Raman transition rate is $\gamma_p/\Omega = \gamma/(4\Delta)$. This means in the time to make a spin flip, the qubit has a $\gamma/(2\Delta)$ chance of decaying. Therefore, the further the detuning Δ , the lower the decoherence per Rabi cycle from spontaneous emission. However, this approximation is only valid when the detuning Δ is much smaller than the P excited state fine structure splitting of 74THz and coupling to the other P_J state is negligible. If the detuning is on the order of the fine structure splitting, then cancellation between couplings via the two P_J states become significant and the Rabi frequency is greatly reduced. In general, the detuning should be balanced between keeping the spontaneous emission rate per cycle low and maintaining a reasonable actual Rabi frequency so that other sources of decoherence (such as laser fluctuations) can also be kept low. In the experiments, the detuning varies from 150GHz to 12THz, with spontaneous emission rates of 10^{-3} or less per Rabi cycle. However, the actual observed spontaneous emission rate is higher by almost an order of magnitude than the expected values, and the reason for this difference remains unknown.

In a recent experiment, Ozeri et al showed that coherence between hyperfine levels can be preserved in the presence of spontaneous photon scattering [36]. Spontaneous scattering is the sum of elastic Rayleigh scattering, which leaves the particle in the same internal state, and inelastic Raman scattering, which transfers the particle to a different internal state. Therefore the coherence of a hyperfine superposition is preserved in the event of Rayleigh scattering, but not spontaneous Raman scattering. In the limit where detuning is much larger than the hyperfine splitting $\Delta \ll \omega_{HF}$, the total scattering rate decreases as $1/\Delta^2$, while Raman scattering alone scales as $1/\Delta^4$.

The AC Stark shift of the two levels also decreases according to $1/\Delta^2$. Therefore the number of spontaneous Raman scattered photons during a Rabi cycle is proportional to $1/\Delta^2$ for $\Delta \ll \omega_{HF}$. This means at detunings larger than the fine structure splitting, decoherence from spontaneous emission per Rabi cycle continues to decrease with detuning, even as the Rabi frequency decreases as $1/\Delta^2$ (compared to $1/\Delta$ in the limit of $\Delta < \omega_{HF}$).

3.6. Generating Coherent Optical Fields with a Microwave Frequency Splitting

The large ground state hyperfine splitting, while excellent for the detection fidelity, poses a technical challenge in the laboratory. Phase-locking two UV lasers is extremely difficult, and conventional AOMs can not operate at such a large frequency ($\omega_0 = 14.5\text{GHz}$). While electro-optic modulators (EOM) can typically operate at up to 10 GHz, the modulated field requires additional modification in order to drive stimulated Raman transitions [37].

Since a 14.5GHz EOM is not available commercially, nor is a high frequency EOM for a 229nm (or 214.5nm) ultraviolet (UV) carrier, consider the following setup in the laboratory: a 458nm (or 429nm) laser is phase-modulated with a resonant EOM at $\omega'_0/2$. The optical field following the EOM can be written as [38]

$$(3.6.1) \quad E_1 = \frac{E_0}{2} e^{i(kx - \omega t)} \sum_{n=-\infty}^{\infty} J_n(\phi) e^{in((\delta k)x - \omega'_0 t/2)} + c.c.,$$

where E_0 is the unmodulated field amplitude, $J_n(\phi)$ is the n -th order Bessel function with modulation index ϕ , and $\delta k = \omega'_0/2c$. The field is subsequently frequency-summed in a build-up cavity containing a BBO crystal, where the free spectral range (fsr) of the cavity is carefully tuned to be a subharmonic of the modulation frequency ($\omega_{fsr} = \omega'_0/8$ in the actual experiments) so that the carrier and all the sidebands resonate simultaneously (see appendix B for details of the cavity modifications). The resulting UV radiation consists of a comb of frequencies centered at 229nm and separated by $\omega'_0/2$ and has an electric field

$$(3.6.2) \quad E_2 = \zeta E_1 E_1 = \zeta \frac{E_0^2}{4} e^{2i(kx - \omega t)} \sum_{n=-\infty}^{\infty} J_n(2\phi) e^{in((\delta k)x - \omega'_0 t/2)} + c.c.,$$

where ζ is the harmonic conversion efficiency (assumed constant over all frequencies considered). This is effectively the same as modulating the UV at frequency $\omega'_0/2$ with twice the modulation index. All pairs of spectral components of electric field separated by frequency ω'_0 can individually drive a stimulated Raman transition in

the ion, and the total Rabi frequency is the sum of all transition amplitudes

$$\Omega = \frac{\mu_1 \mu_2 \langle E_2 E_2^* e^{i\omega'_0 t} \rangle}{\hbar^2 \Delta} = 2\Omega_0 \sum_{n=-\infty}^{\infty} J_n(2\phi) J_{n+2}(2\phi) e^{i2(\delta k)x} = 0.$$

where μ_1 and μ_2 are the matrix elements of the electric dipole moment for a transition between the respective hyperfine states and the excited state, and the fields are time-averaged under the rotating wave approximation ($\Omega \ll \omega'_0 \ll \Delta$). The base Rabi frequency $\Omega_0 = \frac{\mu_1 \mu_2}{\hbar^2 \Delta} |\eta E_0^2/4|^2$ pertains to the usual case of stimulated Raman transition with a pair of monochromatic Raman beams separated in frequency by ω_0 and each with field amplitude $\eta E_0^2/4$. Unfortunately, the properties for infinite sums of Bessel functions are such that the net Rabi frequency always reduces to zero. In fact, this is true for any pairing of n -th nearest neighbors (see appendix C for properties of infinite sums of Bessel functions). The following subsections contain three schemes that modify the relative phases and/or amplitudes of the spectral components in Eq 3.6.2 in order to avoid complete cancellation in the total transition rate.

3.6.1. Mach-Zehnder Setup. One approach to phase shift sidebands is to employ a Mach-Zehnder interferometer, where the modulated beam is split and recombined at another location with path length difference Δx (this is already true for non-copropagating Raman beam geometry where the field is split and recombined at the ion). The field in path A and B are given as follows

$$(3.6.3) \quad E_A = \zeta \frac{E_0^2}{4} e^{2i(kx - \omega t)} \sum_{n=-\infty}^{\infty} J_n(2\phi) e^{in((\delta k)x - \omega'_0 t/2)} + c.c.,$$

$$E_B = \zeta \frac{E_0^2}{4} e^{2i(kx - \omega t)} e^{2ik\Delta x} \sum_{n=-\infty}^{\infty} J_n(2\phi) e^{in((\delta k)x - \omega'_0 t/2)} e^{in(\delta k)\Delta x} + c.c..$$

Note that the n -th sideband is phase shifted by a different amount $e^{in(\delta k)\Delta x}$ proportional to n . The expression for the Rabi frequency is

$$(3.6.4) \quad \Omega = \Omega_0 e^{i(\delta k)(2x + \Delta x)} \sum_{n=-\infty}^{\infty} J_n(2\phi) J_{n-2}(2\phi) \cos[(2k + (n-1)\delta k)\Delta x],$$

For $(\delta k) \cdot \Delta x = (2j+1)\pi$, where j is an integer, the Rabi frequency can be as high as $\Omega = 0.487\Omega_0$ for $\phi = 0.764$. The problem in setting this up in the laboratory is that the $k\Delta x$ factor in the cosine term in Eq 3.6.4 requires optical stability of the Mach-Zehnder interferometer. This problem can be circumvented by introducing a relative frequency shift $\Delta\omega \gg \Omega$ between the two paths of the Mach-Zehnder. This shift can be compensated by changing the modulation frequency of the EOM by $\pm\Delta\omega/2$,

resulting in a Rabi frequency of

$$\begin{aligned}
(3.6.5) \quad \Omega &= \Omega_0 e^{-ik\Delta x} e^{-2i(\delta k)\Delta x} \sum_{n=-\infty}^{\infty} J_n(2\phi) J_{n-2}(2\phi) e^{in(\delta k)\Delta x} \\
&= \Omega_0 e^{-ik\Delta x} e^{-2i(\delta k)\Delta x} J_2 \left(4\phi \sin \left(\frac{\delta k \Delta x}{2} \right) \right),
\end{aligned}$$

where $\Delta\omega \ll \omega'_0$. Note that the $k\Delta x$ factor in the cosine term has been replaced by a phase factor $e^{-ik\Delta x}$, thus eliminating the effects of small changes in Δx on the magnitude of the Rabi frequency. However, the phase of the Raman drive fields relative to a microwave field generated by a phase-locked synthesizer is still dependent on $k\Delta x$ and therefore is not stable, but in later chapters we will show that this phase instability can be removed from quantum logic operations. In this case, the stimulated Raman transition Rabi frequency can be as high as $\Omega = 0.244\Omega_0$ for $\phi = 0.764$ and $\delta k \Delta x = (2j+1)\pi$, where j is an integer.

3.6.2. Cavity Detuning. We can also shaped the sideband spectrum without using a Mach-Zehnder interferometer by detuning the free spectral range of the frequency doubling cavity slightly from a subharmonic of the EOM frequency. This detuning modifies the amplitude and phase of each sideband with respect to the carrier, resulting in a Rabi frequency of

$$\begin{aligned}
(3.6.6) \quad \Omega &= 2\Omega_0 e^{2i(\delta k)x} \sum_{n=-\infty}^{\infty} \sum_{m=-\infty}^{\infty} \sum_{l=-\infty}^{\infty} \left(\frac{J_{n-m}(\phi)}{1 - i2(n-m)\delta} \right) \left(\frac{J_m(\phi)}{1 - i2m\delta} \right) \\
&\quad \times \left(\frac{J_{n+2-l}(\phi)}{1 + i2(n+2-l)\delta} \right) \left(\frac{J_l(\phi)}{1 + i2l\delta} \right),
\end{aligned}$$

where $\delta < 1$ is the number of cavity linewidths by which the first sideband is detuned from a cavity resonance.

3.6.3. Sideband Suppression. Another possible scheme involves the suppression of certain spectral components. By setting the free spectral range of the cavity to be $\omega'_0/(2n+1)$ where n is an integer, only alternating sidebands will resonate. When the even or odd sidebands are selected, we find

$$(3.6.7) \quad \Omega_{even} = \Omega_0 e^{-2i(\delta k)x} \sum_{n=-\infty}^{\infty} \sum_{m=-\infty}^{\infty} \sum_{l=-\infty}^{\infty} J_{2(n-m)}(\phi) J_{2m}(\phi) J_{2(n+1-l)}(\phi) J_{2l}(\phi).$$

$$(3.6.8) \quad \Omega_{odd} = \Omega_0 e^{-2i(\delta k)x} \sum_{n=-\infty}^{\infty} \sum_{m=-\infty}^{\infty} \sum_{l=-\infty}^{\infty} J_{2(n-m)+1}(\phi) J_{2m+1}(\phi) J_{2(n+1-l)+1}(\phi) J_{2l+1}(\phi).$$

The maximum Ω_{even} is $0.230\Omega_0$ at modulation frequency $\phi = 1.173$, while the maximum Ω_{odd} is $0.279\Omega_0$ at $\phi = 1.603$.

3.7. Experiment Details

The previous sections in this chapter contain the theory on how to implement single qubit rotations and couple to the ion's motion in the trap through stimulated Raman transitions. The discussion included the analysis of beam setup and how to generate the necessary fields. In this section, we describe the hardware used in the experiments, and in the next section, compare the results from the experiments to the theory.

3.7.1. Lasers and Optics. Two different lasers have been successfully used to drive Raman transitions. The first is a Melles Griot Nd:NVO₄ laser operating at 457nm with a 400mW optical power. The output is phase modulated by an EOM before harmonic frequency generation in a BBO cavity similar to the detection beam. The second harmonic at 229nm is 12GHz detuned from the $S_{1/2}$ to $P_{1/2}$ transition in $^{111}\text{Cd}^+$ and contains about 7mW of optical power, though only 2.5mW in each Raman beam actually enters the trap. The other is a Ti:Sapphire laser similar to the detection laser described in section 2.3. The UV at 214.5nm is about 150GHz detuned (858.15nm in the IR) from the $S_{1/2}$ to $P_{3/2}$ transition. Out of the 4.5mW UV generated by the BBO, about 500 μ W in each Raman beam enters the trap.

3.7.2. rf sources. The rf sources for various modulators are a series of phase-locked frequency synthesizers. Figure 3.7.1 lists the models used in the experiments and the frequency range they operate at. A stable 10MHz clock signal from an DS345 arbitrary waveform generator with a 10ppb high stability timebase from Stanford Research Systems is connected to each synthesizer, and each synthesizer must have spectral purity of at least -100 dBc at 100Hz offset from carrier frequency at 1Hz bandwidth. The EOM is driven by a modified HP8672A that uses an external local oscillator (DS345) to obtain 1 Hz resolution. The AOM source is an octupled frequency of DS345 generators, typically operating around $8 \times 26\text{MHz} = 208\text{MHz}$. With extremely stable phase-locked signals from the DS345 and the spectral purity of the octupler, their combined performance surpasses most frequency synthesizers at the 200MHz range (and more cost effective too). Multiple DS345 synthesizers are multiplexed through the rf switches so that different frequencies can be accessed by the Raman AOM during the experiment. An HP 8660C is used for the other Raman AO and typically stay fixed in frequency.

A side note on the HP8672A: in fact, the phase lock at 7.266GHz and 14.5 GHz are not stable on the order of a second, as verified by mixing signals from two HP8672A

model	range	function
HP8672A	3GHz-18GHz	drives EOM and/or microwave horn; modified to use an external local oscillator for better resolution
HP8660C	10kHz-400MHz	drives AOM
DS345	DC-30MHz	octupled frequency drives AOM

FIGURE 3.7.1. Synthesizers with phase lock capability for generating coherent Raman beams

and comparing the frequency difference with the 10MHz clock. Therefore, for the experiments to maintain phase coherence, a single HP8672A source provides the signal to the EOM, and microwaves are generated by frequency doubling the 7.266GHz signal and mixing with a lower frequency rf to reach the qubit frequency ω_0 .

3.7.3. Computer Software and Data Collection. As described in section 2.4, the LabView software controls the experiment through the National Instrument pulser card and receives data from the counter card. Typical experiments follow the pulse sequence outlined in section 2.4, starting with the basic Doppler cooling pulse, the initialization pulse, and the detection pulse. This section describes how the routine functions are implemented in the experiments.

Alignment. Pulse sequences are used daily for the alignment of the lasers on the ions. The detection beam can be aligned by maximizing the photon counts received during the detection pulse for a bright state, and the optical pumping beam can be aligned by observing the efficiency of pumping into the dark state, indicated by the low photon counts. The Raman beams are aligned by adding a long Raman pulse (typically 10ms, or several orders of magnitude more than the π pulse time) in the pulse sequence before detection. This results in a high probability of spontaneous emission when the ion interacts with the Raman field, providing an unmistakable signature when the beam overlaps with the ion. The two Raman beams can be aligned independently using this method.

Frequency Scan. Once the Raman beams are aligned, a spectrum is obtained to allow fine tuning of the frequencies. This is important since the Stark shift changes depending on the exact optical power of the laser during the experiment, and the most precise frequency for the experiment condition is the one measured during the actual experiment. For the Raman spectrum, a scan range and step size is specified by the user. For each frequency step, the computer sets the user-defined frequency synthesizer to that particular frequency via GPIB before running the pulse sequence, and then the computer repeats the pulse sequence a number of times (typically set to 50). The data is downloaded from the hardware buffer, analyzed and plotted on

a graph, before moving on to the next frequency setting. The real time feedback is very helpful in observing anomalies such as the ion disappearing during the scan and various other errors that may cause unexpected results in the data. The full data set for the spectrum can be saved at the end of the scan. Each scan takes on the order of a minute, depending on the number of experiments per step and the frequency range and step size of the scan.

The spectrum taken using frequency scan often yields important information about the appropriate frequency settings for that particular experiment setting. The software is set up so that the user can set the frequency of a synthesizer by dragging a cursor over the plotted graph for a quick tuning to resonance.

Time Scan. Instead of changing the frequency, the software can also scan the timing of any pulse or pulses. The program stores the preset pulse sequence in a list of chapters, and each line in a chapter indicates the timing for a specified set of 32-bit signal to be sent. The user can scan a line containing the stop signal for a pulse over a range of delay times, effectively changing the length of time when the pulse is on. When the scan starts, the computer programs the pulser to send out pulses for the initial time delay, and before every time step the pulser card is reprogrammed to send out pulses with the new time setting for that step. A user-specified number of experiments are repeated in each time step before the data is downloaded to the hardware buffer, and the averages and histograms are plotted real time on the monitor. The user can also scan the chapter delay or a line containing the start signal of a pulse to vary the time between pulses.

The software also allows flexibility in terms of managing the timing of the rest of the pulses with respect to the event whose timing is being varied. Typically, the pulse events following the scanned event track the scanned event, i.e. scanning the stop signal of the first pulse will change the timing of the second pulse so that the time between the end of the first pulse and the start of the next pulse remains constant. However, there are situations similar to a Ramsey experiment where the timing of later pulses should be fixed as a particular pulse is being scanned. In those cases, the user can choose a setting where the pulses do not track the pulse event that is being scanned.

Phase Scan. Phase scan is similar to frequency scan except rather than changing the frequency at each time step, the phase of the selected frequency synthesizer is varied. The computer sets the phase via GPIB before taking data during each time step. The user also have the option to change the phase or reset the relative zero phase using the graphical interface.

3.8. Experiment Data

3.8.1. Mach-Zehnder Interferometer. For the Mach-Zehnder setup described in section 3.6.1, the cavity enclosing the BBO crystal is tuned such that the free spectral range is exactly $1/4$ of 7266MHz (to within 1MHz). The UV output of the BBO cavity passes through two AOMs. The first order Bragg deflection from the first AOM is directed into the trap, while the zeroth order deflection is modulated by a second AOM with its first order Bragg deflection also directed into the trap at a 90° angle with respect to the other beam. Two mirrors at 90° retroreflects one of the beams for an easy change of the beam path length without requiring major beam alignment. Typically, the frequency of one AOM is kept fixed (at 212MHz) while the frequency of the other remains flexible depending on the requirements for the experiment. The optical power of the two Raman beams are also balanced to be approximately the same, typically around 300mW, and the beams are focused at the ion with a beam waist of approximately $20\mu\text{m}$ diameter.

The Raman spectra become rather complicated since there are multiple frequency settings that can drive the same transitions. For example, to drive a Raman transition between two levels with an energy splitting of $\hbar\omega_{\text{transition}}$, the modulation frequency of the EOM can be set to $2\omega_{EO} < \omega_{\text{transition}}$. The modulated beam is split into two paths, with the beam in path A frequency shifted by ω_A and the beam in path B frequency shifted by $\omega_A + \omega_{\text{transition}} - 2\omega_{EO}$. The two beams are recombined at the ion, with wave-vector \mathbf{k}_A and \mathbf{k}_B respective to beam path A and B. In this case the wave-vector difference $\Delta\mathbf{k}$ for the Raman transition is equal to $\mathbf{k}_B - \mathbf{k}_A$, since the beam in path B has higher frequency. The beam in path B can also be frequency shifted by $\omega_A + 2\omega_{EO} - \omega_{\text{transition}}$ instead, in which case the wave-vector difference $\Delta\mathbf{k}$ would be $\mathbf{k}_A - \mathbf{k}_B$ since the beam in path A would have the higher frequency.

Figure 3.8.1 shows a typical scan of the EOM frequency. In this experiment, the Raman beams are applied for a $20\mu\text{s}$ pulse between the initialization and the detection of the qubit, and the frequency of the EOM is scanned and the averages are plotted vs frequency. For this spectrum, the AOM frequencies are set to 209MHz and 210MHz. As shown in the figure, two different EOM frequencies 1MHz apart can drive the same transition. The trap frequency is 2.1MHz, and the coupling to different sidebands are visible with non-copropagating Raman beams.

Figure 3.8.2 shows a typical scan of the AOM frequency. For this spectrum, the EOM frequency is fixed at 7266GHz and the AOM frequency $\omega_A/2\pi$ is fixed at 212MHz while the frequency of the other AOM $\omega_B/2\pi$ is scanned. Again, two different frequencies can drive the same transition, but the two sets of transitions are mirrored this time, as in $\omega_B = \omega_A \pm (2\omega_{EO} - \omega_{\text{transition}})$. Changing the AOM frequency is

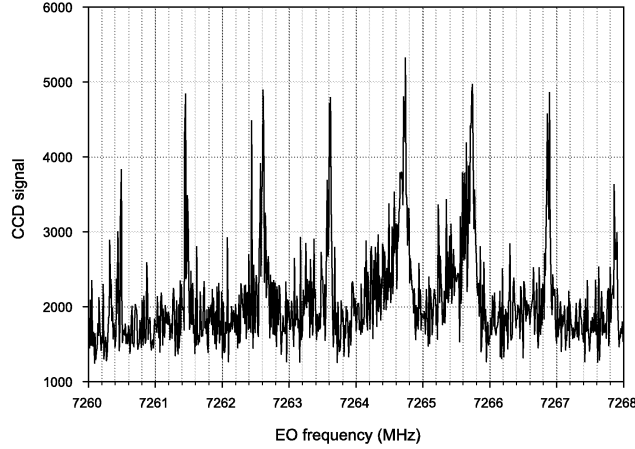


FIGURE 3.8.1. Single ion Raman spectrum from scanning the EOM frequency. The non-copropagating Raman beams couple to the vibrational sidebands spaced by 2.1MHz. The AOMs are set to 1MHz frequency difference, and the Raman beams are applied for $20\mu s$ in each experiment before the qubit state is detected. The fluorescence from the ion indicating the qubit is in $|\uparrow\rangle$ is collected by the CCD camera and the signal is plotted versus the EOM frequency. Frequencies satisfying $\omega_{EO}/2\pi = (\omega_{transition}/2\pi - 1MHz)/2$ produce a carrier transition at 7264.7MHz, a first red sideband transition at 7262.6MHz, a first blue sideband transition at 7666.8, and a second red sideband transition at 7260.5MHz. Frequencies satisfying $\omega_{EO}/2\pi = (\omega_{transition}/2\pi - 1MHz)/2$ produce a carrier transition at 7265.7MHz, a first red sideband transition at 7263.6MHz, a first blue sideband transition at 7667.8, and a second red sideband transition at 7261.5MHz. A weak copropagating Raman transition is also visible at 7265.25MHz.

the preferred method of changing the Raman beat note frequency, since the different AOM frequencies can be preset before the experiment and multiplexed through the rf switches, and the free spectral range of the BBO can remain matched to the static EOM frequency.

The resonant frequency of a Raman transition including the AC Stark shift is determined from the spectrum, and a scan of the Raman pulse length shows Rabi oscillation in the probability of the qubit being in the $|0\rangle$ (or $|1\rangle$) state. Figure 3.8.3 shows a Rabi flopping curve using stimulated Raman transition coupling via the $P_{3/2}$ excited state. From the Rabi flopping curve, the Rabi frequency can be extracted by fitting the curve to $\sin^2(\Omega t/2)$.

To verify the theory in section 3.6.1, we set the difference in AOM frequencies to be $\Delta\omega=2\pi \times 4MHz$ and measure the Rabi frequency Ω as the relative path length

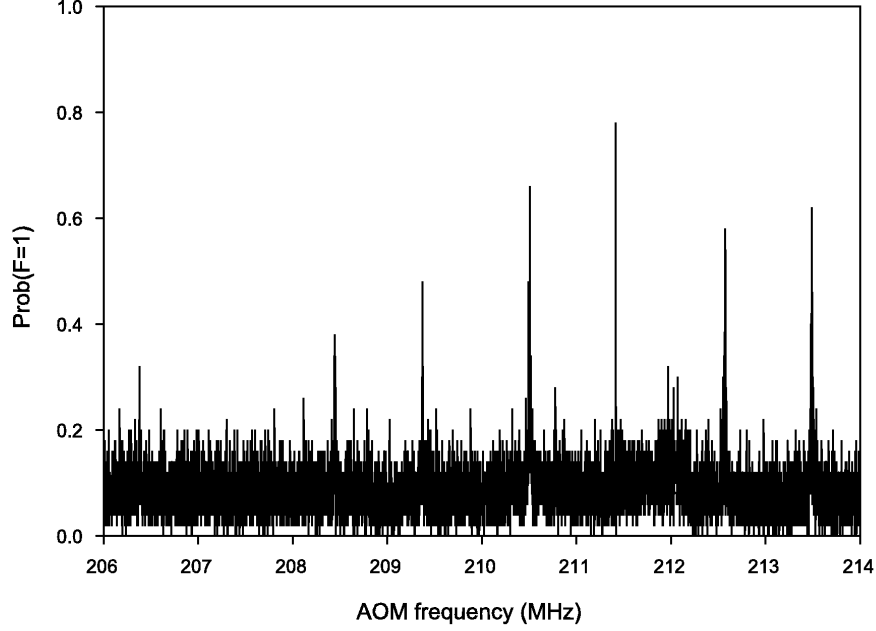


FIGURE 3.8.2. Single ion Raman spectrum from scanning the AOM frequency. In this case, the EOM modulation frequency is set to $\omega_{EO}/2\pi = (\omega_0/2\pi + 1.5\text{MHz})/2 = 7266\text{MHz}$. The frequency of one AOM is set to 212MHz, and the frequency of the other AOM is shown on the x-axis. The trap frequency is 2.1MHz. The carrier transition appears at $212 \pm 1.5\text{MHz}$ (210.5MHz and 213.5MHz), with corresponding first blue sideband transition at 212.6MHz and 211.4MHz, first red sideband transition at 215.6MHz (not shown) and 208.4MHz, second blue sideband transition at 209.3MHz, and second red sideband transition at 206.3MHz.

Δx of the Mach-Zehnder interferometer is varied. We fit Ω to Eq 3.6.5 to extract the modulation index ϕ , which is also independently measured with a Fabry-Perot spectrum analyzer. The results are plotted in Figure 3.8.4. The dependence on gross path length difference with spatial period $\Delta x = 2\pi/\delta k = 4.13\text{cm}$ is clearly visible [39].

3.8.2. Cavity Detuning. For the cavity detuning setup described in section 3.6.2, the free spectral range of the BBO cavity is set to 1/4 of 7262MHz (the linewidth of the cavity is 1.5MHz, and the cavity detuning $\delta \sim 3.25\text{MHz}/15\text{MHz} \sim 0.2$). Using this scheme, only one Raman beam is required, with the EOM modulation frequency satisfying $\omega_{EO} = \omega'_0/2 = 2\pi \times 7265.2\text{MHz}$. The single Raman beam carries multiple frequency components from the phase modulation from the EOM, and constitutes as two copropagating Raman fields. Therefore this setup can only drive carrier Raman

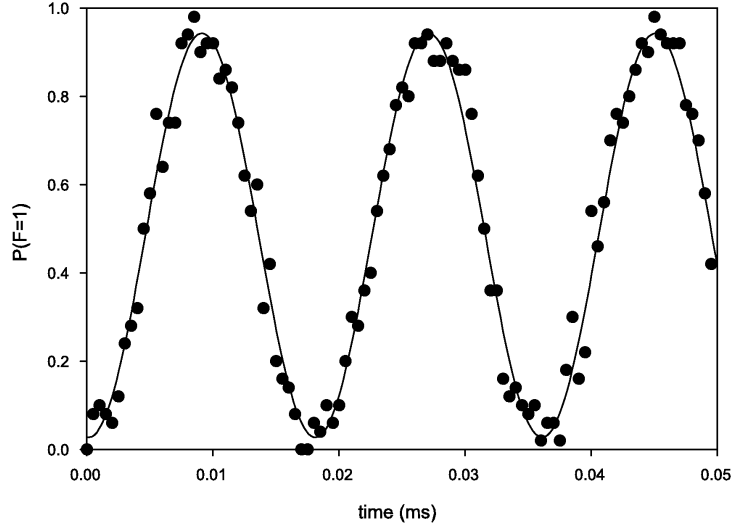


FIGURE 3.8.3. Rabi flopping on a single ion using stimulated Raman transition with motion sensitive, non-copropagating beam geometry. The ion is initialized in the $|\uparrow\rangle$ state and the Raman beams couple to the other hyperfine level $|\downarrow\rangle$ via the $P_{3/2}$ excited states (detuning $\Delta = 2\pi \times 150\text{GHz}$) without changing the vibrational level. The probability of the ion in the $|\downarrow\rangle$ state vs. Raman pulse time t is plotted here, with the Rabi frequency of $\Omega = 2\pi \times 55\text{kHz}$. The data is taken using the CCD camera with the discriminator set to distinguish the bright and dark states, and each point represents an average of 50 experiments.

FIGURE 3.8.4. Rabi frequency vs. Mach-Zehnder path length difference for two values of EOM modulation index ϕ . The lines are theory, and the data are fitted to Eq 3.6.5 using the y-axis scale and modulation index as parameters. The fits agree with independent measurements of the modulation index using a Fabry-Perot cavity.

FIGURE 3.8.5. Rabi flopping on a single ion driven by copropagating Raman beams. The cavity is detuned from resonance in order to produce the non-zero Rabi frequency. The Rabi frequency here is $\Omega = 2\pi \times 3.8\text{kHz}$. The difference in the Rabi frequency compared to the Mach-Zehnder setup is mainly due to the large detuning of the Raman field ($\Delta = 2\pi \times 12\text{THz}$) for this data, using the Melles-Griot 458nm laser coupling via the $P_{3/2}$ excited states.

transition (no change in vibrational level). Figure 3.8.5 shows the Rabi flopping of a single ion using this cavity detuning setup.

FIGURE 3.8.6. Rabi frequency vs EOM modulation index at different cavity detuning δ . The free spectral range of the BBO build-up cavity is detuned by δ with respect to the EOM modulation frequency, scaled to the cavity linewidth. The lines are theory, and the data are fitted to Eq 3.6.6 using the y-axis scale and detuning as parameters. The fits agree with independent measurements of the cavity free spectral range and EOM modulation frequency.

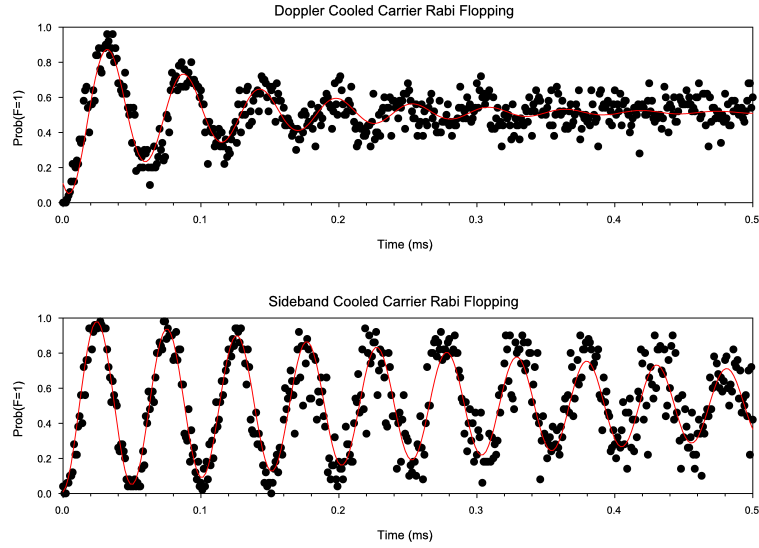


FIGURE 3.9.1. Rabi flopping at high temperature vs low temperature. After Doppler cooling, the ion is in a thermal distribution of vibrational states with average vibrational number $\bar{n} = 13$. Each vibrational has a different Rabi frequency due to the Debye-Waller factor, therefore the Rabi oscillation dephases after several cycles (top). When the ion is sideband cooled to near the ground state, the Rabi oscillation dephases less (bottom). The decoherence in sideband cooled ion is most due to spontaneous emission and beam instability rather than temperature effect.

To verify the results from section 3.6.2, the Rabi frequency is extracted from the Rabi flopping curves for different modulation strength at different cavity detunings. Figure 3.8.6 displays the Rabi frequency Ω versus the modulation index ϕ for various cavity detunings, and the data agree with Eq 3.6.6.

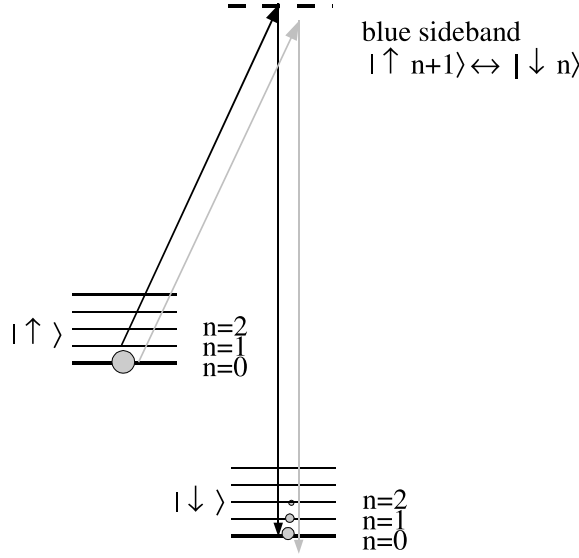


FIGURE 3.9.2. Raman sideband cooling process: the ion is initialized in the $|\uparrow\rangle$ state and a blue sideband transition reduces the vibrational energy by $\hbar\omega_1$ as the spin is flipped. The optical pumping beam is then turned on to reinitialize the ion to the $|\uparrow\rangle$ state. This process is repeated many times (typically 40 cycles) until the ion is cooled to the ground state. When the ion is in the $|n=0\rangle$ vibrational state, it can no longer make a blue sideband transition since $|n=-1\rangle$ state does not exist, and remains in the $|\uparrow, n=0\rangle$ state.

3.9. Cooling to the Ground state of motion

At finite temperature T , the system has average energy $\langle E \rangle = k_B T = \bar{n}\hbar\omega_1$ and follows Maxwell-Boltzmann distribution with probability of being in vibrational state n being [40]

$$(3.9.1) \quad P_n = \frac{1}{1 + \bar{n}} \left(\frac{\bar{n}}{1 + \bar{n}} \right)^n e^{-n\hbar\omega_1/k_B T}.$$

The ion is in an incoherent mixture of vibrational states, leading to dephasing when driving Raman transitions since each vibrational level has a different Debye-Waller factor and therefore a different Rabi frequency. The effect is especially significant for sideband transitions which have strong dependences on n . For quantum logic operations, the ion ideally should be in a single energy eigenstate of motion. In fact, the original entangling scheme for ions proposed by Cirac and Zoller [10] requires that the ion be initialized to the ground state of motion. However, more recent entangling gate proposals only requires the ion to be in the Lamb-Dicke limit, thereby lessening the error due to finite temperature and heating. In either case, the gate errors can be reduced by cooling to the ground state.

As explained in chapter 2, ions are Doppler cooled in the trap to the Doppler cooling limit of $\bar{n} = 0.43\gamma/\omega_1$. For a typical trap strength of 2MHz, the mean vibrational number is $\bar{n} = 13$, which is not within the Lamb-Dicke Limit since $\langle k_z z \rangle = \bar{n}\eta^2 \approx 1$. To reach below Doppler limit, additional Raman sideband cooling is necessary. Raman cooling has previously been shown to be effective for cooling trapped beryllium ions [41], and the method used here is similar. The idea is to start with a Doppler-cooled thermal state initialized to $|\uparrow\rangle$. The blue Raman sideband transition flips the spin to $|\downarrow\rangle$ while changing the vibrational state by $\Delta n = -1$. The ion is then optically pumped back to the $|\uparrow\rangle$ state, on average broadening the energy distribution by a photon recoil of $\hbar^2 k^2 / 2M = 38\text{kHz}$. This process is repeated many times. When the ion reaches the lowest vibrational state $n = 0$, the Raman transition stops automatically since there is no $n = -1$ state to couple to. [42]

In the experiments, a LabView subroutine accepts the trap frequency and π -pulse time for $n = 0$ vibrational ground state blue sideband transition as parameters and calculates the π -pulse time for each of the N iterations of Raman cooling. For a typical $N = 40$ Raman cooling pulses, the program first optically pumps the ion to the $|\uparrow\rangle$ state and then turns on the Raman beams for the exact time to make a complete transition from $|\uparrow, n = 40\rangle$ to $|\downarrow, n = 39\rangle$. In the second iteration, the Raman beam pulse time is calibrated to make a complete transition from $|\uparrow, n = 39\rangle$ to $|\downarrow, n = 38\rangle$. In each subsequent iteration, the Raman pulse time matches the next $\Delta n = -1$ step until the last pulse makes a π -pulse for $|\uparrow, n = 1\rangle$ to $|\downarrow, n = 0\rangle$. The π -pulse times are computed using eq 3.3.4 to determine the Rabi frequency for the $|\uparrow, n = 1\rangle$ to $|\downarrow, n = 0\rangle$ transition and take the inverse $t_{n,n-1} = \pi/\Omega_{n,n-1}$. The exact expression with the Laguerre polynomials is used since the larger vibrational levels are usually well outside of the Lamb-Dicke Limit and the approximation $\Omega \sim \eta\sqrt{n}\Omega_0$ fails. Typically, a separate frequency synthesizer needs to be calibrated to the blue sideband resonance by taking a Raman spectrum. The frequency synthesizer is used for Raman cooling only and is independent from the rest of the experiment. For the experiment, a Raman pulse driving the first blue sideband transition is inserted before the detection pulse, and a time scan of the length of the pulse yields the transition time for an ion with an average vibrational number $\langle n \rangle$ at the Doppler limit. From that piece of information, an estimate of the π -pulse time for $n = 0$ is given (approximately twice as long as the observed time of maximum transition).

The Raman cooling routine is then inserted between the Doppler cooling pulse and the initialization of the experiment, and to observe the effect of Raman cooling, a time scan is performed on an additional Raman probe pulse in the experiment. Raman cooling is actually quite robust even when the π -pulse time is off by as much as a

factor of 2. If Raman cooling works, the ion would most likely be in the ground state before the time-varying pulse and no blue sideband transition would be observed. To measure the π -pulse time for $n = 0$, a microwave π -pulse is inserted right before the probe pulse. The time scan then starts out measuring the ion in the $|\downarrow\rangle$ bright state, and after a π -pulse time for the first blue sideband at $n = 0$, the ion is completely transferred to the $|\uparrow\rangle$ dark state. The contrast should be nearly perfect when the ion is close to entirely in the ground state, and the Raman cooling pulse lengths can be calibrated in this manner. It is also interesting to note that as sideband transition strengths decreases as n decreases, and the sideband resonance have been observed to shift on the order of several kHz, possibly due to a change in AC Stark shift from beam steering by the changing duty cycle of the AOM. Therefore, the frequency of the Raman probe pulse in the experiment (which is independent of the frequency used in the Raman cooling) can be scanned to find the resonance with Raman cooling on. The frequency used for Raman cooling is usually adjusted to match this new resonance as well. The process of frequency scan, time scan to find the π -pulse time for $n = 0$, and calibrating the actual Raman cooling routine pulse time may need to be repeated several times until all parameters are consistent with one another for optimal cooling.

The average vibrational number \bar{n} is extracted through the measured asymmetry in the first upper and first lower sideband strengths; for a thermal distribution of vibrational levels, the probability of making a red (or blue) sideband transition from an initial $|\uparrow\rangle$ state is

$$\begin{aligned}
P_{rsb}(\downarrow) &= \sum_{n=0}^{\infty} P_n \sin^2(\Omega_{n,n-1}t/2) \\
P_{bsb}(\downarrow) &= \sum_{n=1}^{\infty} P_n \sin^2(\Omega_{n,n+1}t/2) \\
&= \sum_{n=0}^{\infty} P_{n+1} \sin^2(\Omega_{n,n-1}t/2)
\end{aligned}$$

where the initial probability distribution of vibrational levels P_n is defined in equation 4.2.6. From the ratio $P_{n+1}/P_n = \bar{n}/(1 + \bar{n})$, the ratio of the blue sideband strength to the red sideband strength is calculated to be $P_{bsb}(\downarrow)/P_{rsb}(\downarrow) = \bar{n}/(1 + \bar{n})$ for any time t . Raman spectra for the first red sideband and the blue sideband are shown in Fig. 3.9.3 for both Doppler cooling and with subsequent Raman cooling in the quadrupole trap with $\omega_x/2\pi = 5.8\text{MHz}$ ($\eta_x \simeq 0.12$). The change in the sideband asymmetries indicates cooling from approximately $\bar{n} \simeq 5(3)$ to $\bar{n} \simeq 0.03(2)$, corresponding to a probability of $P_0 \simeq 97\%$ of ground-state occupation. No further cooling is observed when more than about 40 Raman cooling cycles are used, and the results are largely independent

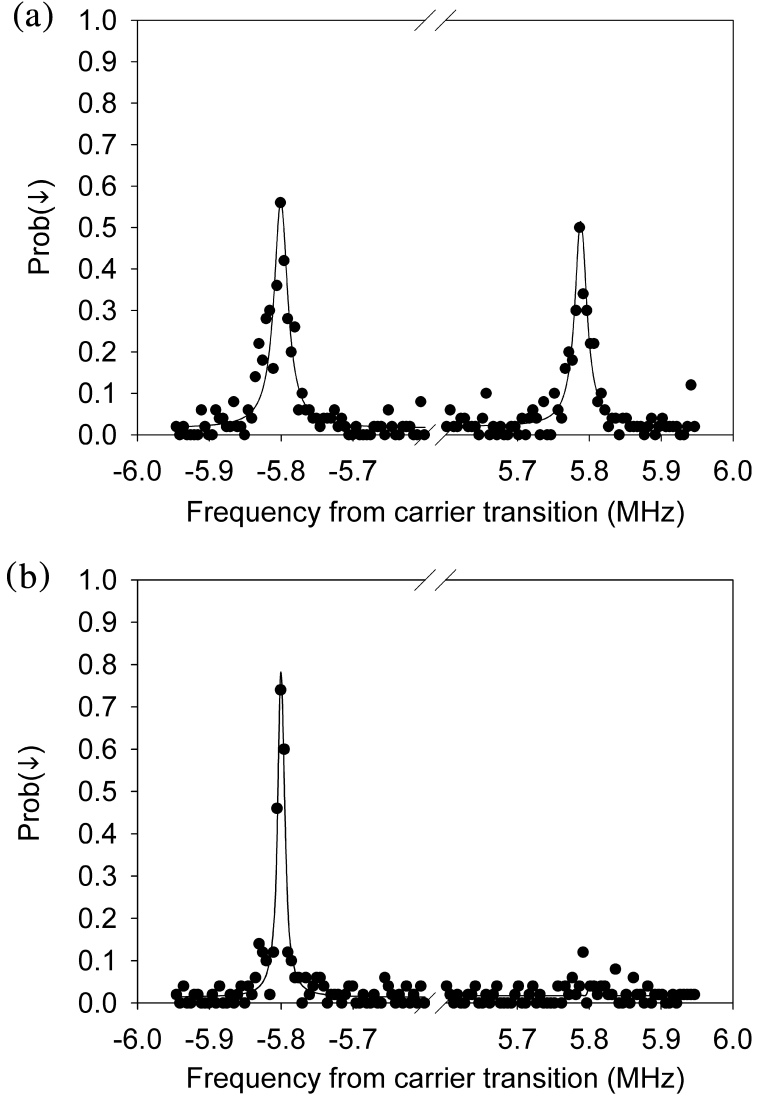


FIGURE 3.9.3. Raman spectra for Doppler cooling and sideband cooling. The ion is in the quadrupole trap with a secular frequency of $\omega_1 = 2\pi \times 5.8\text{MHz}$. Both plots show the probability for population transfer to the bright state $P(\downarrow)$ vs. frequency from the carrier transition. Both red sideband (left) and the blue sideband (right) are displayed following (a) Doppler cooling to $\bar{n} \approx 5(3)$ and (b) subsequent Raman cooling to $\bar{n} \approx 0.03(2)$ where the blue sideband vanishes. The strength of the transitions are $\Omega_0 \approx 2\pi \times 100\text{kHz}$ and $\Omega_{0,1} \approx 10\text{kHz}$. The Raman probe pulse is exposed for $80\mu\text{s}$. The lines are a fit to the data. [42]

of the details of the Raman cooling schedule. For instance, a uniform setting for the Raman cooling sideband pulses works nearly as well as lengthening the Raman pulses appropriately as the ion is cooled. Similar results are observed in both the

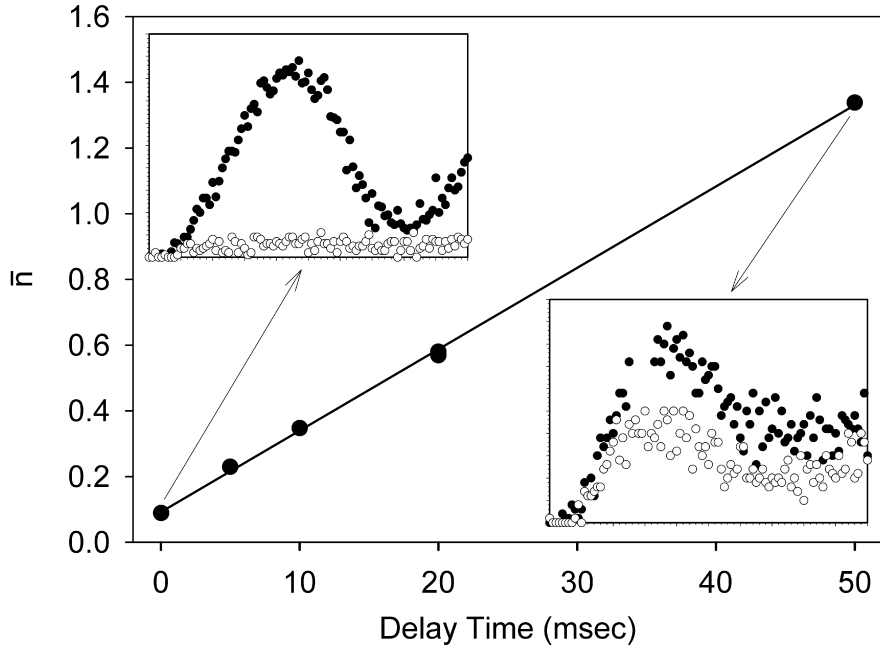


FIGURE 3.9.4. An example of heating data taken in the quadrupole trap, with trap frequency $\omega_1 = 2\pi \times 5.8\text{MHz}$. Mean motional quanta \bar{n} is plotted vs. time delay. The insets show sideband Rabi oscillations, from which is inferred; the black points represent the red sideband and the open points represent the blue sideband. The solid line is a linear fit to the data from which a heating rate of $\dot{\bar{n}} \approx 0.0248(3)\text{quanta/msec}$ is obtained. [42]

quadrupole and the linear traps for various frequencies between 1.3 and 5.8MHz. In the linear trap with $\omega_x/2\pi = 2.69\text{MHz}$ ($\eta_x \simeq 0.17$), we reach a probability $P_0 \simeq 83\%$ of ground-state occupation, requiring no more than 60 Raman cooling cycles.

Uncontrolled interactions with the environment can thermally drive the ion to higher motional energies. In order to measure the heating rates, a time delay with no laser interaction is introduced between the ground-state cooling and the measurement of \bar{n} . These measurements of \bar{n} are repeated with increasing time delay until a heating rate can be extracted. An example of data from the quadrupole trap ($\omega_x/2\pi = 5.8\text{MHz}$) is shown in figure 3.9.4, where a linear fit of the data (\bar{n} vs time delay) yields a heating rate of $\dot{\bar{n}} = 0.0248(3)$ quanta/msec. In the three-layer linear trap, the heating rate is measured to be $\dot{\bar{n}} \approx 0.2$ quanta/msec at 3.8MHz and $\dot{\bar{n}} \approx 0.4$ quanta/msec at 2.1MHz.

CHAPTER 4

Spin-Dependent Forces

In the previous chapter, we have shown that stimulated Raman transitions can couple the spin to the ion’s vibrational levels. However, there is another way to entangle spin and motion – through the application of spin-dependent forces that displace the atomic wavepacket associated with orthogonal spin orientations by different magnitude and/or direction. Our interest in spin-dependent forces stems from several quantum logic gate schemes [13, 14, 16, 20] that utilize this mechanism to entangle qubits stored in the internal states of the ions. These gates are less sensitive to finite temperature effects and vibrational heating compared to the Cirac-Zoller scheme [10], where stimulated Raman transition mapping the qubit state to the vibrational levels require the vibration to be initialized to the ground state. The focus here is on the resolved-sideband limit, where a spin-dependent force is applied steadily over multiple trap periods and couples to only a single mode of vibration.

A differential force can be applied to the eigenstates of any spin operator $\hat{\sigma} \cdot \hat{\mathbf{n}}$, where the unit vector $\hat{\mathbf{n}}$ points in an arbitrary direction on the Bloch sphere. The interactions are classified by the vector $\hat{\mathbf{n}}$: a “ σ_z force” apply a differential force on the energy eigenstates $|\uparrow\rangle$ and $|\downarrow\rangle$, while a “ $\hat{\sigma}_\phi$ force” apply a differential force on the eigenstates $|\uparrow_\phi\rangle$ and $|\downarrow_\phi\rangle$ of $\hat{\sigma} \cdot \hat{\phi}$, where $\hat{\phi} = \cos\phi\hat{\mathbf{x}} + \sin\phi\hat{\mathbf{y}}$ is a vector lying on the equatorial plane of the Bloch sphere. In this chapter, we create Schrödinger’s cat states through the application of differential forces on a single trapped ion, and the measurements from the experiments are compared to theoretical predictions. This data reveal important systematic parameters for the entangling gates, which we will further investigate in the next chapter.

4.1. Spin-Dependent Forces

In an analysis of a force applied to a quantum harmonic oscillator, the wavefunction can be best described in terms of coherent states. A force is represented by a Hamiltonian of the form $\hat{H}_1 \sim \mathbf{F} \cdot \hat{\mathbf{z}}_T = F(t)z_0 (\hat{a} + \hat{a}^\dagger)$, which is a generator of the displacement operator $\hat{D}(\alpha) = e^{\alpha\hat{a}^\dagger + \alpha^*\hat{a}}$. Coherent states, defined as

$$(4.1.1) \quad |\alpha\rangle = e^{-\frac{1}{2}|\alpha|^2} \sum_{n=0}^{\infty} \frac{\alpha^n}{\sqrt{n!}} |n\rangle,$$

are eigenstates of the creation and annihilation operators, and can be translated in the momentum/position phase space by displacement operators using the property

$$(4.1.2) \quad \hat{D}(\beta) |\alpha\rangle = e^{i\text{Im}(\alpha^*\beta)} |\alpha + \beta\rangle,$$

where the imaginary component $\text{Im}(\alpha^*\beta)$ is called the *geometric phase*. In other words, an applied force translates a coherent state $|\alpha\rangle$ in phase space by a vector $\beta = \Delta z/2z_0 + i\Delta p/2p_0$, where the vector β is controlled by the magnitude and the duration of the applied force.

In the entangling gate schemes we are interested in, a periodic force $F(t) = |F| \sin[(\omega_1 - \delta)t + \phi]$ near resonant to the ion's vibrational frequency is applied (for more than one ion, ω_1 can be replaced with the frequency of any vibrational mode). In the rotating frame of the harmonic oscillator, the interaction Hamiltonian is

$$(4.1.3) \quad \hat{H}_I = \frac{F^* z_0}{2} \hat{a} e^{-i\delta t} + \frac{F z_0}{2} \hat{a}^\dagger e^{i\delta t},$$

where $F = |F| e^{i\phi}$ defines the magnitude and phase of the oscillating force. For an ion in an initial ground state $|0\rangle$, the coherent state evolves as (see appendix C)

$$(4.1.4) \quad \alpha(t) = \frac{F z_0}{2\hbar\delta} (1 - e^{i\delta t}).$$

The coherent state has a circular trajectory in phase space with a diameter of $F z_0/\hbar\delta$ and a period of $\tau = 2\pi/\delta$. In each complete round-trip, the state also gathers a geometric phase equal to the area enclosed by the trajectory:

$$(4.1.5) \quad \Phi = \text{Im}\left(\int_0^\tau \alpha(t')^* d\alpha(t')\right) = \frac{\pi |F z_0|^2}{2(\hbar\delta)^2}$$

When the force is spin-dependent, say an eigenstate $|\uparrow_{\mathbf{n}}\rangle$ of $\hat{\sigma} \cdot \mathbf{n}$ experiences a force $F_{\uparrow_{\mathbf{n}}}$ while the orthogonal eigenstate $|\downarrow_{\mathbf{n}}\rangle$ experiences a different force $F_{\downarrow_{\mathbf{n}}}$, the interaction Hamiltonian is the sum over the interaction applied to each individual spin state:

$$(4.1.6) \quad \hat{H}_I = \sum_{m=\uparrow_{\mathbf{n}}, \downarrow_{\mathbf{n}}} \left(\frac{F_m^* z_0}{2} \hat{a} e^{-i\delta t} + \frac{F_m z_0}{2} \hat{a}^\dagger e^{i\delta t} \right) |m\rangle \langle m|,$$

In terms of the $\hat{\sigma} \cdot \mathbf{n}$ operator, the Hamiltonian can be written as

$$(4.1.7) \quad \hat{H}_I = \left(\frac{F_+^* z_0}{2} \hat{a} e^{-i\delta t} + \frac{F_+ z_0}{2} \hat{a}^\dagger e^{i\delta t} \right) \hat{I} + \left(\frac{F_-^* z_0}{2} \hat{a} e^{-i\delta t} + \frac{F_- z_0}{2} \hat{a}^\dagger e^{i\delta t} \right) \hat{\sigma} \cdot \mathbf{n},$$

where \hat{I} is the identity operator, $F_+ = (F_{\uparrow_{\mathbf{n}}} + F_{\downarrow_{\mathbf{n}}})/2$ and $F_- = (F_{\uparrow_{\mathbf{n}}} - F_{\downarrow_{\mathbf{n}}})/2$. The first term involving the identity operator \hat{I} has no effect on the dynamics of the system and therefore can be ignored, and the rest of the interaction Hamiltonian is

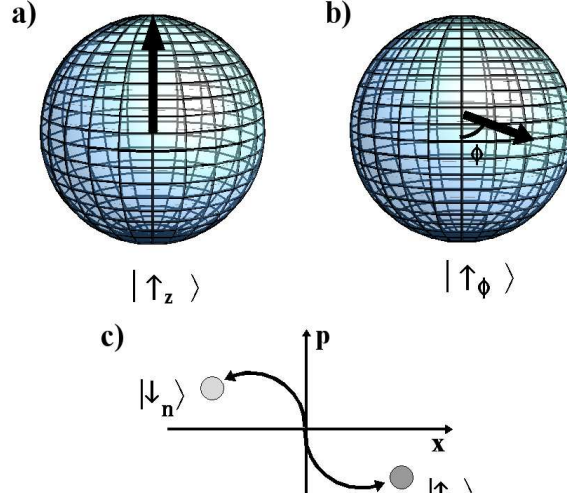


FIGURE 4.1.1. A spin-dependent force applied to the eigenstates of $\hat{\sigma} \cdot \mathbf{n}$. The eigenstate of a) $\hat{\sigma} \cdot \mathbf{z}$ and b) $\hat{\sigma} \cdot \phi$ corresponding to the eigenvalue +1 are represented on the Bloch sphere. A spin-dependent force creates two separate coherent states in phase space corresponding to the eigenstates of $\sigma \cdot \mathbf{n}$, as represented in c), thus entangling the internal spin with the external motion of the ion.

proportional to the operator $\hat{\sigma} \cdot \mathbf{n}$. The wavefunction as the result of this interaction evolves in time as

$$(4.1.8) \quad |\psi(t)\rangle = \sum_{m=\uparrow_{\mathbf{n}}, \downarrow_{\mathbf{n}}} a_m e^{i\Phi(t)} |m\rangle |\alpha_m(t)\rangle,$$

where a_m is the initial amplitude in the state $|m\rangle$, $\alpha_m(t) = (F_m z_0 / 2\hbar\delta) (1 - e^{i\delta t})$ defines the coherent state associated with spin $|m\rangle$, and $\Phi_m(t) = \text{Im}(\int_0^t \alpha_m(t')^* d\alpha_m(t'))$ is the geometric phase acquired by the coherent state $|\alpha_m(t)\rangle$.

The state defined in eq 4.1.8 is reminiscent of Schrödinger's thought experiment where his cat is placed in a superposition of “dead” and “alive” states entangled with the decay of a particle [43]. In this case, the position of the ion is placed in a superposition of “here” and “there” entangled with the spin of the ion. When the two entangled coherent states have very little overlap, i.e. $|\alpha_{\uparrow_{\mathbf{n}}} - \alpha_{\downarrow_{\mathbf{n}}}| \gg 1$, the separation between the expectation values of position $\langle \hat{z}_T \rangle$ of the two spin states is

large compared to the uncertainty in the position associated with each spin state $\sqrt{\langle \hat{z}_T^2 \rangle_m}$. Experiments with Schrödinger-cat-like states in mesoscopic systems have been demonstrated in superconductors [44], nanoscale magnets [45], cavity-QED [46], C₆₀ molecules [47], and trapped ions [48]. The study here is more in-depth than the experiments in ref [48] in that the dynamic evolution of the wavefunction as each of the spin-dependent forces is applied is observed using interference between the two spin states, which offer us precise control of the interaction parameters. In addition, we use the Schrödinger's cat state to demonstrate phase control of the σ_ϕ force, which is essential in its application towards a two-qubit logic gate, as we will see in the next chapter.

4.2. The $\hat{\sigma}_\phi$ -force

The $\hat{\sigma}_\phi$ force is based on the entangling gate scheme proposed by Mølmer and Sørensen [13, 20], which uses simultaneous addressing of a detuned red sideband field and a detuned blue sideband field with equal coupling strengths and opposite detunings. The interaction Hamiltonian of the $\hat{\sigma}_\phi$ force is simply the sum of a Jaynes-Cummings Hamiltonian (produced by the red sideband) and an “anti-Jaynes-Cummings Hamiltonian” (produced by the blue sideband):

$$(4.2.1) \quad \hat{H}_I = \frac{\hbar\eta\Omega}{2} (\hat{\sigma}_+ \hat{a} e^{-i(\delta t - \phi_r)} + \hat{\sigma}_- \hat{a}^\dagger e^{i(\delta t - \phi_r)}) \\ + \frac{\hbar\eta\Omega}{2} (\hat{\sigma}_+ \hat{a}^\dagger e^{i(\delta t + \phi_b)} + \hat{\sigma}_- \hat{a} e^{-i(\delta t + \phi_b)}),$$

where δ is the detuning from the first sideband resonances, and ϕ_r and ϕ_b are the phase from the driving field for the red and blue sidebands respectively. This assumes the system is in the Lamb-Dicke Limit ($\eta^2 n \ll 1$), where η^2 and higher order terms can be neglected. With some rearrangement, this expression can be simplified to

$$(4.2.2) \quad \hat{H}_I = \frac{\hbar\eta\Omega}{2} (\hat{a} e^{-i(\delta t + \phi_M)} + \hat{a}^\dagger e^{i(\delta t + \phi_M)}) \hat{\sigma} \cdot \phi_S.$$

where $\phi_S = -(\phi_b + \phi_r)/2$ is the phase associated with the spin and $\phi_M = (\phi_b - \phi_r)/2$ is the phase associated with the motion. The operator $\hat{\sigma} \cdot \phi_S \equiv \hat{\sigma}_+ e^{-i\phi_S} + \hat{\sigma}_- e^{i\phi_S}$ has eigenstates

$$(4.2.3) \quad |\uparrow_{\phi_S}\rangle = \frac{1}{\sqrt{2}} (|\uparrow\rangle + e^{i\phi_S} |\downarrow\rangle) \\ |\downarrow_{\phi_S}\rangle = \frac{1}{\sqrt{2}} (-e^{-i\phi_S} |\uparrow\rangle + |\downarrow\rangle),$$

corresponding to eigenvalues $+1$ and -1 respectively. We call this a $\hat{\sigma}_\phi$ force because the Hamiltonian is proportional to $\hat{\sigma} \cdot \phi_S$, where $\phi_S = \cos(\phi_S)\mathbf{x} + \sin(\phi_S)\mathbf{y}$ is a vector lying on the xy plane forming an angle ϕ_S with respect to the x axis. Eq 4.2.2 is

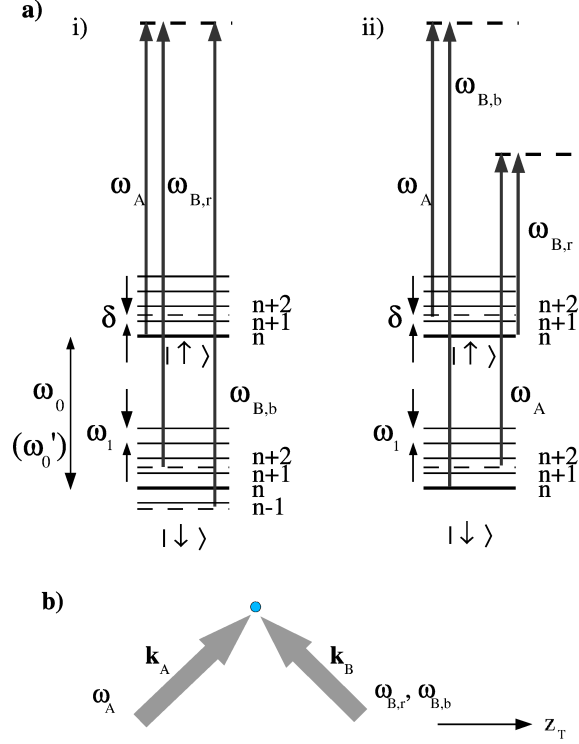


FIGURE 4.2.1. Optical fields generating a $\hat{\sigma}_\phi$ -dependent force. A $\hat{\sigma}_\phi$ -dependent force is driven by simultaneous coupling to two vibrational sideband transitions. a) Two optical fields separated in frequency by $\omega'_0 - \omega_1 - \delta$ drive a detuned red sideband and a third optical field whose frequency differs by $\omega'_0 + \omega_1 + \delta$ from one of the other fields to drive a detuned blue sideband. i) and ii) are two examples of possible frequency configurations. The optical fields can have overlapping wave-vectors, but any pair of frequencies that drives a sideband must have a non-zero wave-vector difference with a component in the x direction, as shown in b).

analogous to eq 4.1.7 defining the Hamiltonian of a spin-dependent force, and here the eigenstates of $\hat{\sigma} \cdot \phi_S$ experience a force of equal magnitude in opposite directions.

When the ion is initialized in $|\uparrow\rangle$ and the vibration is in the ground state $|0\rangle$, the wavefunction evolves under the application of the $\hat{\sigma}_\phi$ force as

$$(4.2.4) \quad |\psi(t)\rangle = \frac{1}{\sqrt{2}} e^{i\Phi(t)} |\uparrow_{\phi_S}\rangle |\alpha(t)\rangle - \frac{e^{i\phi_S}}{\sqrt{2}} e^{i\Phi(t)} |\downarrow_{\phi_S}\rangle |-\alpha(t)\rangle,$$

where $\alpha(t) = \alpha_0 (1 - e^{i\delta t})$ with $\alpha_0 = \eta\Omega/(2\delta)$, and $\Phi(t)$ is the geometric phase acquired from the displacement, which is the same for both $|\alpha(t)\rangle$ and $|-\alpha(t)\rangle$. The

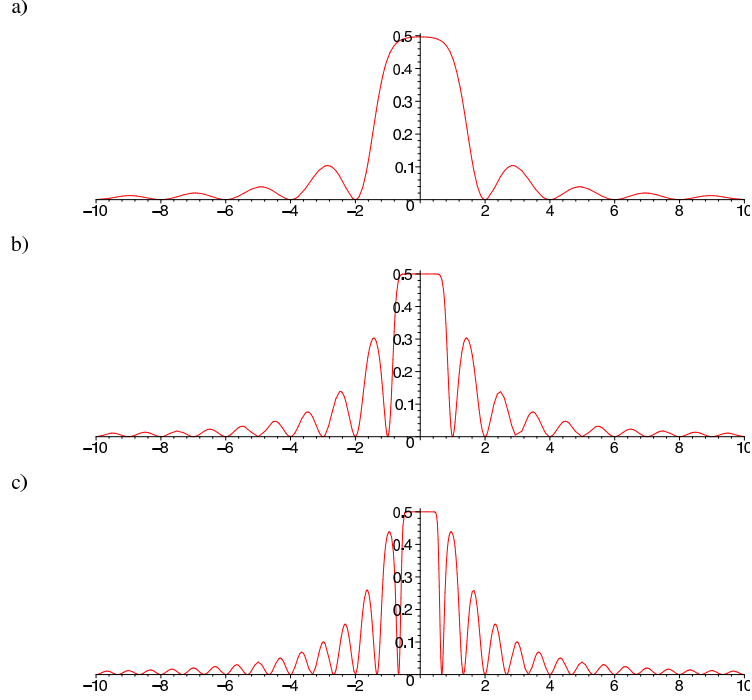


FIGURE 4.2.2. Fluorescence signal vs detuning of the $\hat{\sigma}_\phi$ force. Probability $P(\downarrow)$ is plotted versus detuning δ according to eq 4.2.5 for a) $t = \pi/\eta\Omega$, b) $t = 2\pi/\eta\Omega$, c) $t = 3\pi/\eta\Omega$. The horizontal axis (detuning δ) is normalized to $\eta\Omega$, i.e. $\alpha_0 = 1$ at $\delta = \eta\Omega/2$. At $\delta t = 2n\pi$ where n is an integer, the coherent state associated with each spin both return to the initial position, resulting in $P(\downarrow) = 0$. When the separation between the two coherent states is large compared to the uncertainty in position for each coherent state, then the two coherent states do not interfere with one another and the probability $P(\downarrow)$ approaches $1/2$. As δ approaches zero, the separation $2\alpha(t) = \eta\Omega(1 - e^{i\delta t})/\delta$ also increases.

probability of finding the ion in the $|\downarrow\rangle$ state becomes [49]

$$(4.2.5) \quad P(\downarrow) = |\langle\downarrow|\psi(t)\rangle|^2 = \frac{1}{2} \left\{ 1 - e^{-\frac{1}{2}|2\alpha(t)|^2} \right\},$$

This transition probability has dependence on both the detuning δ and the duration t of the applied force, which are two parameters that can be controlled in the laboratory. This result can be used to confirm the production of Schrödinger's cat states if the data indeed agree with eq 4.2.5, and the size of $\alpha(t)$ can quantify the physical separation of the two coherent states.

4.2.1. Effects of temperature and heating. Thus far we have not considered the decoherence caused by temperature and heating, which could result in deviations in the experiment results from equation 4.2.5. Recall from section 3.9, the system at

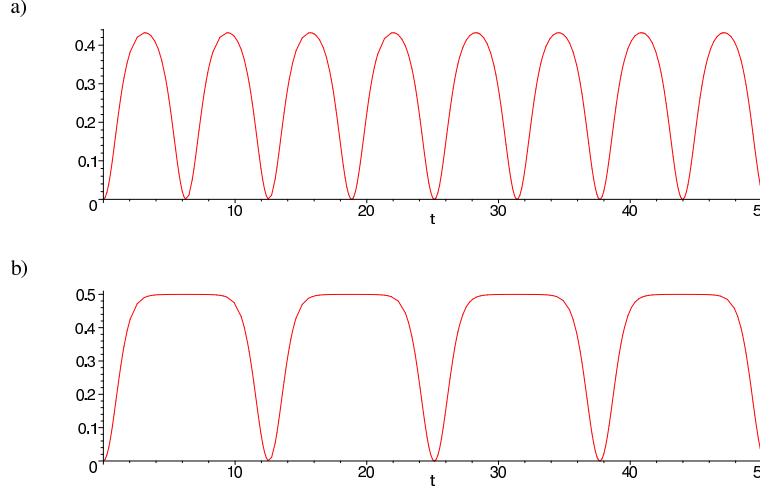


FIGURE 4.2.3. Fluorescence signal vs duration of the $\hat{\sigma}_\phi$ force. Probability $P(\downarrow)$ is plotted versus duration t of the $\hat{\sigma}_\phi$ force according to eq 4.2.5 for a) $\delta = \eta\Omega$, b) $\delta = \eta\Omega/2$. $P(\downarrow)$ returns to 0 at $t = 2\pi/\delta$ when the two coherent states overlap each other.

finite temperature T has average energy $\langle E \rangle = k_B T = \bar{n}\hbar\omega_1$ and follows Maxwell-Boltzmann distribution with probability of being in vibrational state n being

$$(4.2.6) \quad P(n) = \left(\frac{\bar{n}}{1 + \bar{n}} \right)^n e^{-\bar{n}\hbar\omega_1/k_B T}.$$

We note that each initial vibration level $|n\rangle$ is transformed by the displacement operator and evolves as

$$|\psi_n(t)\rangle = \frac{1}{\sqrt{2}} e^{i\Phi(t)} |\uparrow_{\phi_S}\rangle \hat{D}(\alpha(t)) |n\rangle - \frac{e^{i\phi_S}}{\sqrt{2}} e^{i\Phi(t)} |\downarrow_{\phi_S}\rangle \hat{D}(-\alpha(t)) |n\rangle.$$

The probability of finding the ion in the $|\downarrow\rangle$ state from an initial thermal state can then be determined by summing over the Maxwell-Boltzmann distribution of all initial vibrational levels of a single mode:

$$(4.2.7) \quad \begin{aligned} P_{thermal}(\downarrow) &= \sum_{n=0}^{\infty} \frac{1}{1 + \bar{n}} \left(\frac{\bar{n}}{1 + \bar{n}} \right)^n |\langle \downarrow | \psi_n(t) \rangle|^2 \\ &= \frac{1}{2} - \frac{1}{2} e^{-(\bar{n} + \frac{1}{2})|2\alpha|^2}. \end{aligned}$$

Background heating can be modeled as random displacements in phase space, and the interference pattern for a given displacement can be calculated and averaged over the distribution of the displacement. This is valid since the heating reservoir is classical. If we assume the state $|\alpha\rangle$ and $|\alpha\rangle$ were both displaced by a random variable β at a random time t_1 during the trajectory, then the state of the system

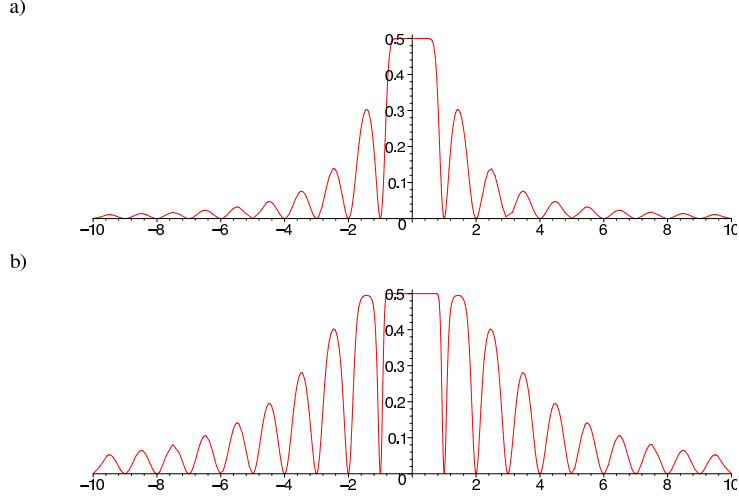


FIGURE 4.2.4. Fluorescence signal from a thermal ion vs detuning of the $\hat{\sigma}_\phi$ force. Probability $P_{thermal}(\downarrow)$ is plotted versus detuning δ according to eq 4.2.7 for a) $\bar{n} = 0$, b) $\bar{n} = 2$. The horizontal axis (detuning δ) is normalized to $\eta\Omega$, and $t = 2\pi/\eta\Omega$. At higher average vibrational number \bar{n} (higher temperature), a small displacement can destroy the coherence between the motion associated with each spin, resulting in a higher probability of measuring the ion in \downarrow state at higher values of δ . In comparison, higher temperature produces a larger envelope over the probability $P_{thermal}(\downarrow)$ and narrower fringes. Decoherence due to vibrational heating $\dot{n}t$ results in similar changes in $P(\downarrow)$.

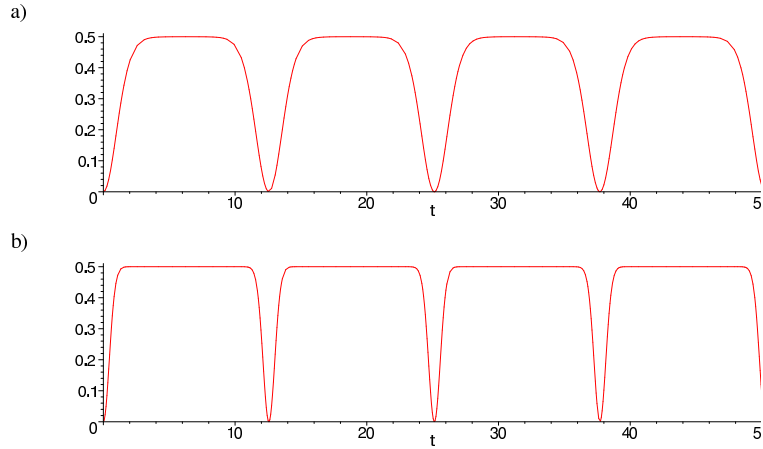


FIGURE 4.2.5. Fluorescence signal from a thermal ion vs detuning of the $\hat{\sigma}_\phi$ force. Probability $P_{thermal}(\downarrow)$ is plotted versus duration t of the $\hat{\sigma}_\phi$ force according to eq 4.2.7 for a) $\bar{n} = 0$, and b) $\bar{n} = 2$. The fringe contrast is narrower at higher temperature. Decoherence due to vibrational heating $\dot{n}t$ results in similar changes in $P(\downarrow)$.

after the displacement becomes

$$(4.2.8) \quad |\psi_\beta(t_1)\rangle = \frac{e^{i\theta}}{\sqrt{2}} |\uparrow_{\phi_S}\rangle |\alpha_{\uparrow_{\phi_S}}(t_1)\rangle - \frac{e^{i(\phi_S-\theta)}}{\sqrt{2}} |\downarrow_{\phi_S}\rangle |\alpha_{\downarrow_{\phi_S}}(t_1)\rangle,$$

where

$$\begin{aligned} \alpha_{\uparrow_{\phi_S}}(t_1) &= \alpha_0 e^{i\phi_M} (1 - e^{i\delta t_1}) + \beta, \\ \alpha_{\downarrow_{\phi_S}}(t_1) &= -\alpha_0 e^{i\phi_M} (1 - e^{i\delta t_1}) + \beta, \\ \theta &= \text{Im} \left\{ \alpha_0^* e^{-i\phi_M} (1 - e^{-i\delta t_1}) \beta \right\}. \end{aligned}$$

Here θ is the geometric phase due to the displacement by β . For time $t > t_1$,

$$(4.2.9) \quad |\psi_\beta(t)\rangle = \frac{e^{i(\theta+\mu_1)}}{\sqrt{2}} |\uparrow_{\phi_S}\rangle |\alpha_{\uparrow_{\phi_S}}(t)\rangle - \frac{e^{i(\phi_S-\theta+\mu_2)}}{\sqrt{2}} |\downarrow_{\phi_S}\rangle |\alpha_{\downarrow_{\phi_S}}(t)\rangle,$$

where the coherent states evolve as

$$\begin{aligned} \alpha_{\uparrow_{\phi_S}}(t) &= \alpha_0 e^{i\phi_m} (1 - e^{i\delta t}) + \beta \\ \alpha_{\downarrow_{\phi_S}}(t) &= -\alpha_0 e^{i\phi_m} (1 - e^{i\delta t}) + \beta, \end{aligned}$$

and the geometric phase from the displacement for each α_m are

$$\begin{aligned} \mu_1 &= \text{Im} \left\{ \int_{t_1}^t \alpha_{\uparrow_{\phi_S}}^*(t') d\alpha_{\uparrow_{\phi_S}}(t') \right\}, \\ \mu_2 &= \text{Im} \left\{ \int_{t_1}^T \alpha_{\downarrow_{\phi_S}}^*(t') d\alpha_{\downarrow_{\phi_S}}(t') \right\}. \end{aligned}$$

The random variable β has a Gaussian distribution with a variance of $\sigma^2 = \hbar t/2$ for both the real and the imaginary component, for a heating rate \dot{n} and duration time t of the applied differential force. To find the probability of the ion in $|\downarrow\rangle$ state, each of the variables are integrated over all possible values of β with a Gaussian distribution:

$$(4.2.10) \quad P_{\text{heating}}(\downarrow) = \int_{-\infty}^{\infty} d\beta P(\beta) |\langle \downarrow | \psi_\beta(t) \rangle|^2 = \frac{1}{2} \left\{ 1 - e^{-\frac{1}{2}\dot{n}t|4\alpha_0|^2} e^{-\frac{1}{2}|2\alpha(t)|^2} \right\}.$$

Combining the results from eq 4.2.5, eq4.2.7, and eq 4.2.10 to account for both temperature and heating effects, the probability of the ion making a transition from $|\uparrow\rangle$ to $|\downarrow\rangle$ is

$$(4.2.11) \quad P_c(\downarrow) = \frac{1}{2} \left\{ 1 - e^{-\frac{1}{2}\dot{n}t|4\alpha_0|^2 - (\bar{n} + \frac{1}{2})|2\alpha(t)|^2} \right\},$$

where $\alpha(t) = \alpha_0 e^{i\phi_M} (1 - e^{i\delta t})$ and $\alpha_0 = \eta\Omega/(2\delta)$.

4.2.2. Experiment Setup. The simultaneous detuned first red and first blue sidebands are generated using the existing non-copropagating Raman beam setup described in chapter 3. As shown in figure 4.2.6, the EOM frequency is fixed at 7266GHz and one arm of the Mach-Zehnder interferometer (designated by wave vector

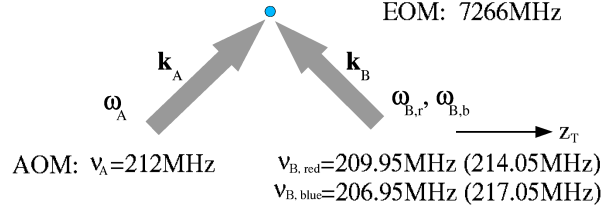


FIGURE 4.2.6. Vector and frequency configurations for applying the $\hat{\sigma}_\phi$ force. In the experiment, the trap frequency is set to $\nu_1 = 3.55\text{MHz}$, with the qubit frequency at $\nu_0 = 14530.5\text{MHz}$. The EOM modulates the optical fields at 7266MHz , and two AOMs, one along each wave vector k_A and k_B , act as beam switches and shifts the optical fields to the frequencies necessary to drive simultaneous Raman sideband transitions. The modulation frequency of the AOM along wave vector k_A is kept fixed at 212MHz , while the AOM along wave vector k_B is modulating at both 209.95MHz and 206.95MHz to drive the red sideband and the blue sideband transitions respectively. Alternative modulation frequencies are 214.05MHz for the red sideband and 217.05MHz for the blue sideband. The frequencies must satisfy $\nu_0 - \nu_1 - \delta = 2 \times \nu_{EOM} \pm (\nu_A - \nu_{B,\text{red}})$ for the detuned red sideband and $\nu_0 + \nu_1 + \delta = 2 \times \nu_{EOM} \pm (\nu_A - \nu_{B,\text{blue}})$ for the detuned blue sideband.

\mathbf{k}_A) is frequency shifted by an AOM modulating at 212MHz . For a $\omega_1 = 3.55\text{MHz}$ trap frequency in the linear trap, the other arm of the Mach-Zehnder interferometer (designated by wave vector \mathbf{k}_B) is frequency shifted by 214.05MHz or 209.95MHz to drive the first blue sideband, and at 217.05MHz or 206.95MHz to drive the first red sideband. The choice of frequencies affects the phase of the spin-dependent force, which is important for a later discussion. For the moment, a 209.95MHz signal and a 206.95MHz signal are multiplied using a mixer, and the output is used to drive the AOM along vector \mathbf{k}_B . The two rf frequencies produce the bichromatic Raman field for the interaction described by eq 4.2.1.

Before the experiment, Raman sideband cooling is setup according to the procedures described in section 3.9. For the $\hat{\sigma}_\phi$ force, two frequency synthesizers separate from the one controlling Raman cooling are frequency octupled independently to produce 209.95MHz and 206.95MHz frequencies before mixing. The mixed frequency has an envelope at the difference frequency, and the power is attenuated such that the maximum amplitude does not exceed the saturation power of the amplifier, as to avoid frequency distortion (the problem is similar for the octupler for both over-saturation and under-saturation if the signal is mixed first). This change in the rf power also changes the resonance of the transitions due to AC Stark effect, and each sideband frequency is recalibrated for the spin-dependent force by scanning one rf frequency

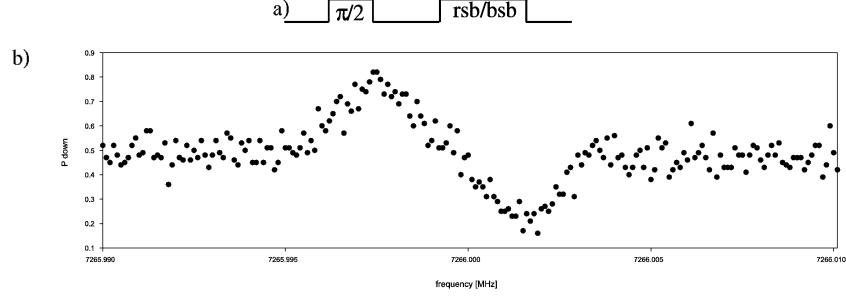


FIGURE 4.2.7. Calibration of sideband detunings δ_r and δ_b . The pulse sequence is shown in a), where a $\pi/2$ carrier pulse is followed by the application of the $\hat{\sigma}_\phi$ force with the red and blue sidebands having opposite detunings $\delta_r = -\delta_b = 2\pi \times 5\text{kHz}$. The frequency of the EOM is scanned and the plot of $P(\downarrow)$ vs EOM frequency is shown in b). The initial vibrational level is mostly in the ground state, and the $\pi/2$ carrier pulse places the ion in an equal superposition of \uparrow and \downarrow , as indicated by $P(\downarrow) = 1/2$ in the background. When the EOM reaches the resonant frequency of the red sideband transition, only a transition from $|\downarrow, n=0\rangle$ to $|\uparrow, n=1\rangle$ is allowed but not $|\uparrow, n=0\rangle$ to $|\downarrow, n=1\rangle$, resulting in a dip in the scan. The reverse is true when the EOM reaches the resonant frequency of the blue sideband transition, resulting in a peak in the scan. Using those two reference points, the EOM frequency is set to exactly half way in between, thus calibrating the detunings δ_r and δ_b to within $2\pi \times 100\text{Hz}$ difference.

while driving the AOM with both rf frequencies. The other rf frequency is detuned from its associated sideband transition so that it is not driving any transition during the frequency scan. The transition rates of the red sideband and the blue sideband are also calibrated to be equal by a variable attenuator attached to one rf source. The difference in the transition rates is caused by the optical separation in the two frequencies ($\leq 5\%$ of the beam waist), and the difference in rf power caused by the bandwidth of the octupler, the difference in cable lengths, and different attenuation from the rf switches. The transition rates are balanced to better than 10%.

Once the nominal rf frequencies are set, the detunings δ_r from the red sideband and δ_b from the blue sideband are balanced even more precisely using the following procedure. The frequencies are set to $\delta_r = -\delta_b = 5\text{kHz}$, or in this case, $+5\text{kHz}$ from resonance for both rf frequencies. A microwave $\pi/2$ -pulse is turned on first before the bichromatic Raman pulse, and the EOM frequency is scanned within a 20kHz range centered around 7266MHz. Figure 4.2.7 shows a typical set of data collected from the scan, with the dispersion shape indicating the precise red sideband resonance at the peak and the precise blue sideband resonance at the valley. When the ion is in the ground state, the red sideband transition is allowed from $|\uparrow 0\rangle \rightarrow |\downarrow 1\rangle$ but not

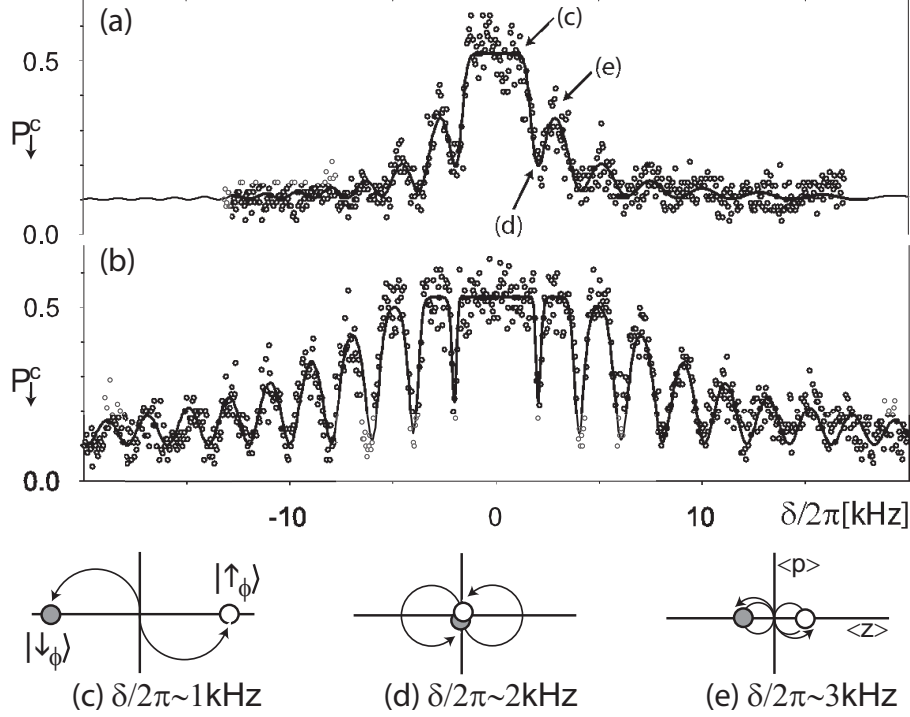


FIGURE 4.2.8. Probability $P(\downarrow)$ plotted vs. detuning δ of the $\hat{\sigma}_{\phi}$ force for (a) a ground state cooled and (b) a Doppler cooled ion, initially prepared in $|\uparrow\rangle$. The force is applied for $500\mu\text{s}$. Data is run-time averaged with 100 shots/point. Solid lines show fits to Eq E.0.5 modified to include overall peak and contrast factors (for spontaneous emission) and a detuning drift across the data. An initial fit for data in (a) with $\bar{n} = 0.05$ fixed gives $\Omega_{sb}/2\pi = 1.62(3)\text{kHz}$ and $\dot{\bar{n}} = 0.44(2)\text{ms}^{-1}$. A subsequent fit for data in (b) with $\Omega_{sb}/2\pi = 1.62\text{kHz}$ fixed $\bar{n} = 5.6(1)$ and $\dot{\bar{n}} = 0.62(6)\text{ms}^{-1}$. The values of $\dot{\bar{n}}$ are 2-3 times larger than the directly measured heating rate of 0.2ms^{-1} in the three-layer linear trap. Phase space sketches (c)-(e) indicate ion evolution at detunings referenced in (a). [49]

$|\downarrow 0\rangle \rightarrow |\uparrow -1\rangle$, resulting in the population gathering in the $|\downarrow\rangle$ state. The inverse is true for the blue sideband, resulting in the population gathering in the $|\uparrow\rangle$ state. To balance the detunings δ_r and δ_b , the EOM frequency is set to be exactly in between the peak and the valley. This gives a precision between the two detunings δ_r and δ_b to better than 100Hz.

4.2.3. Experiments. An experiment in which the duration T of the force is fixed but the detuning is varied is shown in figure 4.2.8. When the detuning is far from resonance, the spin-dependent force is weak and the coherent states move in small but fast circular trajectories. As the detuning gets closer to resonance, the diameter of the orbit becomes larger, and the two coherent states become separated in space, as shown

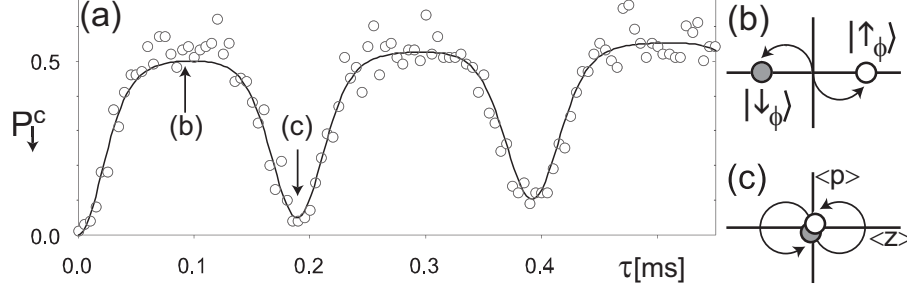


FIGURE 4.2.9. Single-ion evolution due to a spin-dependent bichromatic force. (a) Probability P_{\downarrow}^c of measuring state $|\downarrow\rangle$ plotted vs. force duration τ . Ion is initially Doppler cooled. Data is run-time averaged (100 shots/point) and smoothed. Solid line is a fit to eq E.0.5, modified to include a linear change in peak and contrast (from spontaneous emission) and a detuning drift across the data. Fit parameters include $\Omega_{sb}/2\pi = 2.2\text{kHz}$ (fixed), $\delta/2\pi = -5.46(3)\text{kHz}$ and $\bar{n} = 8.1(3)$. (b) & (c) Phase space sketches of the ion motion at points indicated in (a). [49]

in figure 4.2.8(c). In the measurement, the $|\uparrow_{\phi_S}\rangle$ and $|\downarrow_{\phi_S}\rangle$ no longer interfere with each other since the overlap in position is small, and each state contributes a equal mixture of $|\uparrow\rangle$ and $|\downarrow\rangle$ states, resulting in the probability $P(\downarrow) = 1/2$. At detunings $\delta = 2j\pi/T$ where j is an integer, the coherent states complete their orbits and return to their initial position, as shown in figure 4.2.8(d). The two parts of the cat interfere with each other to suppress the $|\downarrow\rangle$ state, represented by a dip in the $P(\downarrow)$ signal. This experiment is performed for two different initial temperatures of the ion, a “hot” case of a Doppler cooled ion and a “cold” case of a ion cooled to near the ground. The data is fit to eq E.0.5 and temperature and heating rate are extracted from the fit. On resonance where the force is strongest, the inferred cat state separation in 4.2.8 is $\Delta z \approx 10z_0$, a factor of 2.8 larger than the rms size of the “hot” ion’s thermal state. The hot case has a broader envelope and narrower fringes because of the average over the initial thermal distribution quickly draws the experiment outcome towards $P(\downarrow) = 1/2$, even for small displacements. Nevertheless, all initial states should return on themselves at the same moment (within the Lamb-Dicke approximation) giving a full revival. The overall decrease of contrast, particularly visible in the non-zero baseline, is due to spin decoherence and optical pumping induced by spontaneous emission. The detuning dependent fringe contrast is consistent with motional decoherence with has a characteristic exponential sensitivity to the size of the cat state, largest near resonance ($\delta \sim 0$).

Another experiment in which the duration of the force is varied before qubit detection demonstrates the periodic entanglement in single ion evolution (see Fig

4.2.9). In this case, the coherent states follow the same orbit, and the spin state is measured at different points along the orbit. A transition to $P(\downarrow) = 1/2$ indicates when a Schrödinger cat is formed. At this point, the motional wavepackets of the cat state are sufficiently far separated that the spin interference is inhibited, yielding equal probability of $|\uparrow\rangle$ and $|\downarrow\rangle$ in the measurement basis. At fringe minima corresponding to $\delta\tau = 2j\pi$ with j an integer, the motional states return to their original position and overlap. The spin interference is restored, giving the initial state $|\downarrow\rangle$ such that $P(\downarrow) \approx 0$. This coherent process of periodic entanglement and disentanglement of the spin and motional degrees of freedom continues with reasonable signal quality for at least two oscillations.

4.2.4. Phase Coherence. Eq 4.2.2 contains two phases: $\phi_M = (\phi_b - \phi_r)/2$ which determines the orientation of the trajectory in phase space, and $\phi_S = -(\phi_b + \phi_r)/2$ which determines the spin orientation to which the differential force is applied. Here we want to investigate the stability of these phases and the effect on the coherence of the entangling gate.

What is the stability of ϕ_S and ϕ_M ? The component phases ϕ_r and ϕ_b have dependence on the phase of the AOM modulation, the EOM modulation, and the phase difference between the two Raman fields. The first two can be controlled reliably given a stable phase-lock loop between the different frequency synthesizers. The phase difference between two Raman fields depend on $k_A x_A - k_B x_B \simeq k\Delta x$ the path length difference between the two arms of the Mach-Zehnder interferometer. To keep $k\Delta x$ stable to much less than a 2π cycle, the beam path length difference Δx must be stable at the sub-wavelength scale, a condition which is satisfied on the time scale of a single gate $\sim 100\mu s$ but difficult to maintain on a longer time scale due to mechanical vibrations of the optics and the trap. Therefore, the corresponding phases ϕ_S and ϕ_M may not be stable beyond a gate pulse.

In the experiments described previously, the phases ϕ_S and ϕ_M need not be correlated beyond the duration of an applied spin-dependent force pulse. However, for the quantum entangling gate, these phases play a critical role. In a standard phase gate construction, the spin-dependent force is applied with a detuning and duration where every coherent state can complete an integer number of loops. At the finish of the gate pulse, the spin and motion are no longer entangled, but the internal states of the two ions are now entangled. This prevents the loss of quantum information due to motional decoherence outside the gate duration. In these scenarios, the subsequent gates have no memory of the motion phase ϕ_M from previous gates, but the spin phase ϕ_S from previous gates is retained in the internal states of the operated qubits. Therefore, the spin phase ϕ_S need to be consistent throughout multiple experiments,

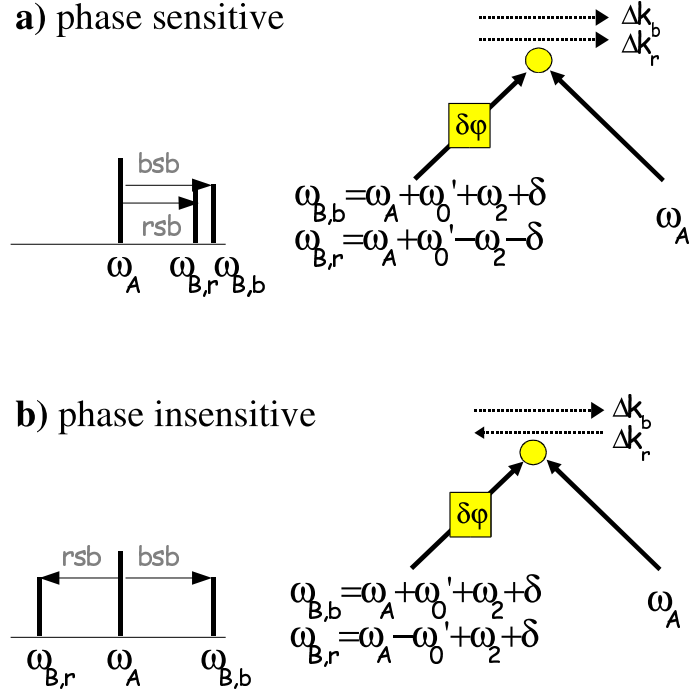


FIGURE 4.2.10. Possible beam configurations for the σ_ϕ gate (in a simplified case where the Raman fields have no sidebands). a) Phase sensitive configuration. The wave-vector difference for pairs of frequencies driving the red sideband and the blue sideband travel in the same direction $\Delta\mathbf{k}_r = \Delta\mathbf{k}_b$, using the frequency configuration shown in Figure 4.2.1 a) i)). A phase shift $\delta\phi$ in one beam path results in a phase shift in the spin of the entangled state. b) Phase insensitive configuration. The wave-vector difference for pairs of frequencies driving the red sideband and the blue sideband travel in the opposite direction $\Delta\mathbf{k}_r = \Delta\mathbf{k}_b$, using the frequency configuration shown in Figure 4.2.1 a) ii). A phase shift $\delta\phi$ in one beam path results in no net phase shift in the spin of the entangled state.

while the requirements for the motion phase ϕ_M is less stringent. However, both ϕ_S and ϕ_M still need to be stable during a gate pulse.

Phase sensitive geometry. Consider the following scenario in the experiment: the modulation frequency of the EOM is fixed at $\omega_{EO} = 2\pi \times 7266\text{MHz}$ and the modulation frequency of the AOM in path A of the Mach-Zehnder interferometer is fixed at $\omega_A = 212\text{MHz}$, and the AOM in path B of the interferometer is modulating at $\omega_{B,r} = \omega_A - (2\omega_{EO} - \omega_0 - \omega_1 - \delta) = 2\pi \times 206.9\text{MHz} + \delta$ for the red sideband transition and $\omega_{B,b} = \omega_A - (2\omega_{EO} - \omega_0 + \omega_1 + \delta) = 2\pi \times 214.1\text{MHz} - \delta$ for the blue sideband

transition. Each frequency component in path A combined with its second lower sideband in path B drives a red sideband (or blue sideband) transition. Therefore the phases ϕ_r and ϕ_b are both directly correlated with $k_A x_A - k_B x_B = -k\Delta x$. The phase ϕ_S therefore also suffers the same sensitivity to the path length difference $-k\Delta x$ of the Mach-Zehnder interferometer.

If the AOM in path B is instead modulating at $\omega_{B,r} = \omega_A + 2\omega_{EO} - \omega_0 - \omega_1 - \delta = 2\pi \times 217.1\text{MHz} - \delta$ for the red sideband and $\omega_{B,b} = \omega_A + 2\omega_{EO} - \omega_0 + \omega_1 + \delta = 2\pi \times 209.9\text{MHz} + \delta$ for the blue sideband, then each frequency component in path A combined with its second higher sideband in path B drives a red sideband (or blue sideband). This time the phases ϕ_r and ϕ_b are correlated to $+k\Delta x$, and the spin phase ϕ_S still suffers a sensitivity to changes in the path length difference, except in the opposite direction as before.

Phase insensitive geometry. But what if the AOM modulates at opposite frequency components for the two sideband transitions? For example, if the AOM modulates at $\omega_{B,r} = \omega_A - (2\omega_{EO} - \omega_0 - \omega_1 - \delta) = 2\pi \times 206.9\text{MHz} + \delta$ for the red sideband transition and $\omega_{B,b} = \omega_A + 2\omega_{EO} - \omega_0 + \omega_1 + \delta = 2\pi \times 209.9\text{MHz} + \delta$ for the blue sideband transition, then ϕ_r is correlated with $-k\Delta x$ while ϕ_b is correlated with $+k\Delta x$. Any change in Δx will cancel itself in ϕ_S , allowing ϕ_S to remain independent of fluctuations in the Mach-Zehnder interferometer beam path lengths, but the user still maintains control of ϕ_S through phase of the rf frequencies driving the EOM and the AOMs. Interestingly, the phase drift due to changes in the path length difference Δx is now shifted to the motion phase $\phi_M = (\phi_b - \phi_r)/2$. This means the trajectories of the coherent states in phase space will rotate by a random angle depending on $k\Delta x$, but as long as $k\Delta x$ remains stable during the gate, the outcome of the gate operation will remain the independent of $k\Delta x$.

Phase stability experiment. In order to observe the phase sensitivity of the Mølmer-Sørensen force, an interference technique is required. Ramsey interferometry combined with Schrödinger cat formation provides a fluorescence signal that is sensitive to the orientation of the force's spin basis, characterized by the phase ϕ_s . The essence of the procedure is to rotate the spin of the initial state $|\uparrow\rangle$ with a $\pi/2$ -pulse into the xy -plane at some azimuthal angle ϕ_0 . This results in the state

$$\begin{aligned}
 (4.2.12) \quad & \frac{1}{\sqrt{2}} (|\uparrow\rangle + e^{i\phi_0} |\downarrow\rangle) \\
 & = e^{i\frac{(\phi_0 - \phi_S)}{2}} \cos\left(\frac{\phi_0 - \phi_S}{2}\right) |\uparrow_{\phi_S}\rangle + ie^{i\frac{(\phi_0 + \phi_S)}{2}} \sin\left(\frac{\phi_0 - \phi_S}{2}\right) |\downarrow_{\phi_S}\rangle
 \end{aligned}$$

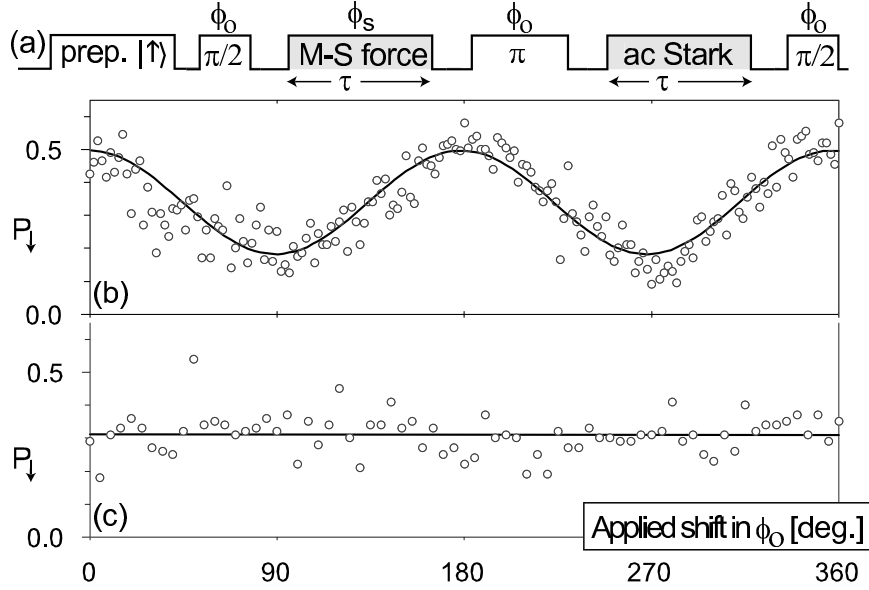


FIGURE 4.2.11. Phase sensitivity of the σ_ϕ force for different beam configurations. (a) Pulse sequence of a photon-echo experiment for testing optical phase sensitivity of the σ_ϕ force. The echo pulses are carrier transitions driven by non-copropagating Raman beams propagating along the same wave-vectors as the σ_ϕ force, and an applied phase shift ϕ_0 is added using an acousto-optic modulator that controls the timing of the pulse. The σ_ϕ force is applied for sufficient time such that the two motional states corresponding to spin states $|\uparrow_\phi\rangle$ and $|\downarrow_\phi\rangle$ have very little overlap at time τ . A separate pulse in the other arm of the echo experiment cancels the residual AC Stark shift induced by the field driving the σ_ϕ force (the ratio ω_0/Δ is significant enough to produce a non-negligible differential Stark shift between the two qubit states in this experiment). (b) Probability of detecting $|\downarrow\rangle$ vs. applied shift in the phase of the echo pulses ϕ_0 using the phase sensitive configuration described in section 2.3.1 and Figure 4.2.10a. The fringe contrast shows coherence between the phase ϕ in the σ_ϕ force and the phase ϕ_0 in the Raman carrier pulses (Probability should vary sinusoidally from 0 to 0.5 when there is no decoherence). (c) Same plot using the phase insensitive configuration described in section 2.3.2 and Figure 4.2.10b. This time there is no coherence between the phase-insensitive σ_ϕ force and the phase-sensitive non-copropagating Raman carrier pulses.

where ϕ_0 is the reference phase associated with the $\pi/2$ -pulse. The Mølmer-Sørensen force is then applied, and the state after the pulse (factoring out an overall geometric phase) is

$$(4.2.13) \quad e^{i\frac{(\phi_0 - \phi_S)}{2}} \cos\left(\frac{\phi_0 - \phi_S}{2}\right) |\uparrow_{\phi_S}\rangle |\alpha(\tau)\rangle + ie^{i\frac{(\phi_0 + \phi_S)}{2}} \sin\left(\frac{\phi_0 - \phi_S}{2}\right) |\downarrow_{\phi_S}\rangle |-\alpha(\tau)\rangle.$$

Finally a $3\pi/2$ analysis pulse, represented by the operator in the $\{|\uparrow\rangle, |\downarrow\rangle\}$ basis

$$(4.2.14) \quad R' = \begin{pmatrix} -1 & -e^{-i\phi_0} \\ e^{i\phi_0} & -1 \end{pmatrix},$$

returns the spin to the z-axis before measurement, resulting in the state

$$(4.2.15) \quad \left\{ -\frac{1}{2} [1 + \cos(\phi_0 - \phi_s)] |\uparrow\rangle + \frac{ie^{i\phi_0}}{2} \sin(\phi_0 - \phi_s) |\downarrow\rangle \right\} |\alpha(\tau)\rangle \\ + \left\{ \frac{i}{2} [1 - \cos(\phi_0 - \phi_s)] |\uparrow\rangle - \frac{ie^{i\phi_0}}{2} \sin(\phi_0 - \phi_s) |\downarrow\rangle \right\} |-\alpha(\tau)\rangle.$$

A signal sensitive to $\phi_s - \phi_0$ is obtained as follows:

$$(4.2.16) \quad P(\downarrow) = P_c(\downarrow) \sin^2(\phi_0 - \phi_s)$$

where $P_c(\downarrow)$ is given by Eq E.0.5. As long as the detuning and duration of τ are chosen to generate a significant displacement ($\alpha(\tau) \gg 1$), the signal is approximately $\frac{1}{2} \sin^2(\phi_0 - \phi_s)$. If the initial $\pi/2$ pulse rotates the ion's spin into a state in which the force is diagonal ($\phi_0 = \phi_s + m\pi$ with m being an integer), a displacement occurs but no entangled cat state is formed. Therefore following the analysis pulse, the ion's spin returns to its initial state $|\uparrow\rangle$ such that $P(\downarrow) = 0$. On the other hand, if the rotated initial state deviates from this special condition ($\phi_0 \neq \phi_s + m\pi$), then the state is a superposition of the force's spin basis and a Schrödinger cat is formed. This is revealed by a net fluorescence signal on analysis.

For the experiment, we use the optical Raman carrier transition to drive the $\pi/2$ pulses. The actual pulse sequence for the interferometry employs a photon echo scheme where the $3\pi/2$ analysis pulse is divided into a π and a $\pi/2$ pulse (see fig 4.2.11(a)). This provides a convenient way to cancel the effect of Stark shifts (~ 20 kHz) from the optical carrier pulses as well as from the MS force itself. The Stark-induced phase from the MS pulse is canceled by introducing a bichromatic pulse, far detuned from the motional resonance, into the second echo zone. For the data shown in the top graph in figure 4.2.11(b), the rf modulating frequencies are set to $\omega_{B,r} = 2\pi \times 206.9$ MHz for the red sideband transition, $\omega_{B,b} = 2\pi \times 214.1$ MHz for the blue sideband transition, and $\omega_{B,c} = (\omega_{B,b} + \omega_{B,r})/2 = 2\pi \times 210.5$ MHz for the carrier transition. The carrier must be exactly half way in between the red sideband and the blue sideband frequency to maintain a consistent relative phase between the different rf signals for each trial in the experiment. The carrier pulses which act as a phase reference are subject to the same optical phase drifts as the sidebands creating the bichromatic force. Therefore the interferometric signal $P(\downarrow)$ is expected to be stable for the phase sensitive Raman setup in Fig 4.2.10(a) where fluctuation in the force's spin phase ϕ_s are common to the reference phase ϕ_0 . A scan of the reference phase

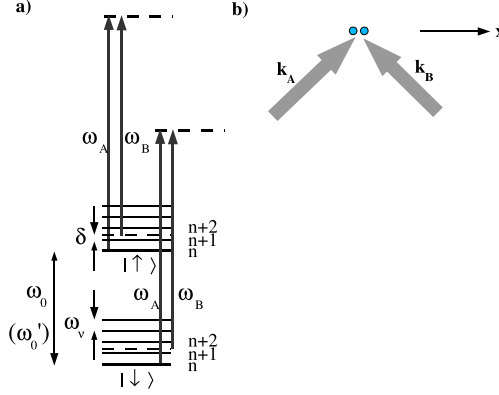


FIGURE 4.3.1. Optical fields generating a $\hat{\sigma}_z$ -dependent force. A $\hat{\sigma}_z$ -dependent force is driven by electromagnetic fields with two frequencies separated by $\omega_\nu + \delta$ as shown in a). These fields couple the two qubit states to the excited states with different coupling strengths (depending on polarization), producing a differential AC Stark shift that oscillates at $\omega_\nu + \delta$. The two fields must have a non-zero wave-vector difference $\Delta \mathbf{k} = \mathbf{k}_\beta - \mathbf{k}_\alpha$ with a component in the z_T direction.

in Fig 4.2.11(b) shows interference fringes with nearly full contrast (maximum being $1/2$). This remains the case even with a piezoelectric transducer slowly modulating at 1Hz one Raman arm by an optical wavelength.

When the MS force is generated with the phase insensitive setup in Fig 4.2.10(b), the phase correlation in the interferometric signal is washed out. In this case, the force's spin dependence, now decoupled from instabilities, is no longer correlated with the optical phase fluctuations on the carrier pulses. The data shown in the bottom graph of Fig 4.2.11(b) uses the rf modulating frequencies at $\omega_{B,r} = 2\pi \times 206.9\text{MHz}$ for the red sideband transition, $\omega_{B,b} = 2\pi \times 209.9\text{MHz}$ for the blue sideband transition, and $\omega_{B,c} = 2\pi \times 212\text{MHz} - (\omega_{B,b} - \omega_{B,r})/2 = 2\pi \times 210.5\text{MHz}$ for the carrier transition. This configuration did not require the addition of any Raman path-length modulation to spoil the fringe contrast as inherent phase drifts on the optical table were a sufficient source of noise over the 200ms experiment averaging time.

4.3. The $\hat{\sigma}_z$ -force

When the interaction Hamiltonian has a term proportional to $\hat{\sigma} \cdot \mathbf{z}$, the interaction of equation 4.1.7 creates a differential force on the eigenstates of the unperturbed Hamiltonian. This interaction is special because it does not directly couple the two eigenstates of σ_z , and thus the Raman beam frequencies only need to differ by the vibrational frequency rather than the much larger qubit frequency. In this case, the

Raman beams form a beating wave, and the ions sample the beats at a rate of the frequency difference as they travel along the weakest trap dimension. Due to the AC Stark effect, this wave becomes essentially a moving periodic potential, exerting a near-resonant force on the ion in the direction of travel. If the AC Stark effect has different amplitudes on the qubit states, then the forces experienced by the two states will also be different.

The $\hat{\sigma}_z$ force is driven by two non-copropagating beams with frequency difference $\omega_1 - \delta$, where ω_1 is the frequency of vibration and δ is the detuning from the vibration frequency. We apply two fields $E_A e^{i(\mathbf{k}_A \cdot \mathbf{x} - \omega_A t - \phi_A)} \epsilon_A + E_B e^{i(\mathbf{k}_B \cdot \mathbf{x} - \omega_B t - \phi_B)} \epsilon_B$ where the frequency difference $\omega_B - \omega_A = \omega_1 - \delta$ is slightly detuned from the stretch mode frequency. The field couples each of the spin states to the excited P state, and is detuned by a large frequency Δ (see Figure 4.3.1). Using the same RWA and adiabatic elimination of the excited state used to obtain Equation ??, the interaction Hamiltonian for a single ion becomes

$$(4.3.1) \quad \hat{H}_I = \frac{\hbar}{2} \left\{ \left[\chi_{\uparrow} + \left(\Theta_{\uparrow} e^{i(\Delta \mathbf{k} \cdot \hat{\mathbf{R}} - (\omega_1 - \delta)t - \Delta\phi)} + h.c. \right) \right] |\uparrow\rangle \langle\uparrow| \right. \\ \left. + \left[\chi_{\downarrow} + \left(\Theta_{\downarrow} e^{i(\Delta \mathbf{k} \cdot \hat{\mathbf{R}} - (\omega_1 - \delta)t - \Delta\phi)} + h.c. \right) \right] |\downarrow\rangle \langle\downarrow| \right\}$$

where $\chi_m = (|g_{m,A}|^2 + |g_{m,B}|^2)/2\Delta$ is the time-averaged Stark shift on the state $m = \uparrow, \downarrow$ and $\Theta_m = g_{m,A}^* g_{m,B} / \Delta$ is the time-varying component in the Stark shift due to the variation in the intensity formed by the interference pattern that pushes the ion. Here $g_{m,l} = \mu_m \cdot \epsilon_l E_l / 2\hbar$ is the single photon Rabi frequencies associated with each field l coupling qubit state $|m\rangle$ to excited level $|e\rangle$, $\Delta \mathbf{k} = \mathbf{k}_B - \mathbf{k}_A$ is the wave vector difference, and $\Delta\phi = \phi_B - \phi_A$ is the phase difference between the driving fields. The time-averaged Stark shifts can be equalized ($\chi_{\uparrow} = \chi_{\downarrow}$) by carefully choosing the Raman detuning Δ (with coupling to auxiliary excited levels) and the polarizations ϵ_A and ϵ_B [50]. The Θ_m terms result in a time-dependent force applied to each state. For $\Theta_{\uparrow} \neq \Theta_{\downarrow}$, a differential Stark shift creates a differential force between the qubit states. In the Lamb-Dicke limit, assuming that the detunings Δ are approximately the same for the two spin states ($\Delta \gg \omega_0$), the interaction Hamiltonian for two ions can be written as

$$(4.3.2) \quad \hat{H}_I = \frac{\hbar}{2} \sum_{m=\uparrow, \downarrow} \eta \Theta_m D_{n,n'} (\hat{a} e^{-i(\delta t - \phi)} + \hat{a}^\dagger e^{i(\delta t - \phi)}) |m\rangle \langle m| \\ = \sum_{m=\uparrow, \downarrow} \left(\frac{F_m^* z_0}{2} \hat{a} e^{-i\delta t} + \frac{F_m z_0}{2} \hat{a}^\dagger e^{i\delta t} \right) |m\rangle \langle m|,$$

where $F_m z_0 = (\hbar \eta D_{n,n'} / \Delta) \Theta_m e^{i\phi}$, and $\phi = \Delta\phi$.

This $\hat{\sigma}_z$ force can be applied only when the instantaneous differential Stark shifts are different for the two qubit levels ($\Theta_\uparrow \neq \Theta_\downarrow$), which is not true for all pairs of qubit states. For example, magnetic field insensitive states have no differential Stark shift in the limit of large Raman detuning $\Delta \gg \omega_0$ (see Appendix F). Therefore, in order to apply this $\hat{\sigma}_z$ force, we must either select magnetic field sensitive states as qubit levels, or have a smaller Raman detuning approximately of the order of the qubit frequency ($\Delta \sim \omega_0$). Here we choose to use magnetic field sensitive states as qubit levels, with $|\uparrow\rangle \equiv S_{1/2} |F=0, m_F=0\rangle$ and $|\downarrow\rangle \equiv S_{1/2} |F=1, m_F=1\rangle$ as the qubit states. The two driving fields have a lin \perp lin polarization and wave-vectors as shown in figure 3.5.3, resulting in a balanced average Stark shift between the spin states $\chi_\uparrow = \chi_\downarrow$ in the limit of large detuning $\Delta \gg \omega_0$. However, the contributions to the differential Stark shift from the σ_+ component of the fields and the σ_- component of the fields have opposite signs, resulting in a complete cancellation of differential Stark shift $\Theta_\uparrow = 0$ for the $|\uparrow\rangle$ state and a non-zero net force $\Theta_\downarrow = (2/3) \times g_A^* g_B / \Delta$ for the $|\downarrow\rangle$ state, with the factor of 2/3 as the difference in the branching ratios of the two polarization components.

4.3.1. Experiment. The σ_z force can be demonstrated similarly to the experiment for the σ_ϕ force. The ion is first prepared in a superposition of the two spin states $(|\uparrow\rangle + |\downarrow\rangle) / \sqrt{2}$ and a pulse of $\hat{\sigma}_z$ force is applied. The resulting state is

$$(4.3.3) \quad \frac{1}{\sqrt{2}} |\uparrow\rangle |0\rangle + \frac{1}{\sqrt{2}} e^{i\Phi(t)} |\downarrow\rangle |\alpha(t)\rangle.$$

The coherent state associated with the $|\uparrow\rangle$ component of the wavefunction is stationary because the force on $|\uparrow\rangle$ is zero, while the coherent state associated with the $|\downarrow\rangle$ translates in time as $\alpha(t) = \alpha_0 e^{-i\phi} (1 - e^{-i\delta t})$ with $\alpha_0 = \eta D_{n,n'} \Theta_\downarrow e^{i\phi} / 2\delta\Delta$, and accumulates a geometric phase $\Phi(t)$. To obtain an interference fringe between $|0\rangle$ and $|\alpha(t)\rangle$, a final $3\pi/2$ carrier pulse is applied. The probability of the ion in $|\downarrow\rangle$ state is

$$(4.3.4) \quad \begin{aligned} P(\downarrow) &= \left| \frac{1}{2} |0\rangle + e^{i\Phi(t)} |\alpha(t)\rangle \right|^2 \\ &= \frac{1}{2} \left(1 - e^{-2|\alpha(t)|^2} \cos[\Phi(t)] \right). \end{aligned}$$

Accounting for decoherence due to temperature and motional heating, the expected signal from the experiment is

$$(4.3.5) \quad P(\downarrow) = \frac{1}{2} \left(1 - e^{-\frac{1}{2}\dot{n}t|4\alpha_0|^2 - (\bar{n} + \frac{1}{2})|2\alpha(t)|^2} \cos[\Phi(t)] \right).$$

In the experiment, two beams from a monochromatic UV laser source $\Delta = 150\text{GHz}$ detuned from the $P_{3/2}$ resonance are combined at the ion. The duration of the force is fixed while the detuning δ is varied by scanning the rf modulation frequency of

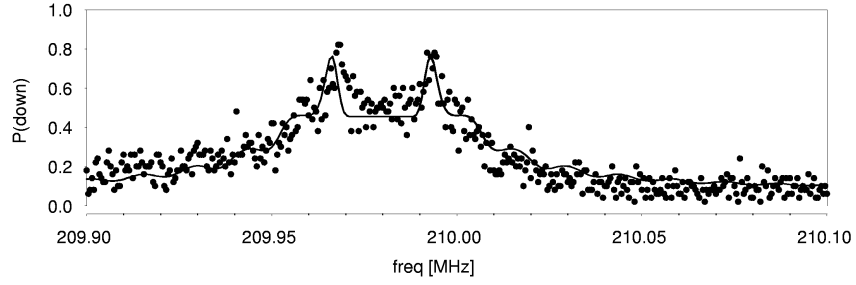


FIGURE 4.3.2. Probability $P(\downarrow)$ vs. detuning of the $\hat{\sigma}_z$ -force. The probability is plotted versus the AOM modulation frequency, with 209.98MHz corresponding to detuning $\delta = 0$ of the $\hat{\sigma}_z$ force. The ion is initially prepared in $|\uparrow\rangle$ and $\hat{\sigma}_z$ force is applied for $56\mu\text{s}$. Data is run-time averaged with 50 shots/point. The solid line shows fits to equation 4.3.5 modified to account for spontaneous emission.

an AOM in one beam path while holding the rf modulation frequency of the AOM in the other beam path constant at 212MHz. The ion is Doppler cooled before each trial of the experiment with no additional Raman sideband cooling. Microwaves fields are used to drive the carrier transitions, and the $3\pi/2$ pulse is divided into a π and $\pi/2$ pulse, and an additional optical pulse in the second echo zone cancels the Stark-induced phase shift. The result is shown in figure 4.3.2.

Because the $\hat{\sigma}_z$ force can only operate on magnetic field sensitive states, fluctuating magnetic field becomes the main source of decoherence. As the result of Ramsey experiment in figure 4.3.3 shows, the magnetic field sensitive qubit maintains its coherence for less than $100\mu\text{s}$. This indicates that a $\hat{\sigma}_z$ force induced quantum logic gate must operate in much less than $100\mu\text{s}$, and the signal in figure 4.3.2 demonstrates that this time constraint can not be satisfied unless a significant increase in optical power is available.

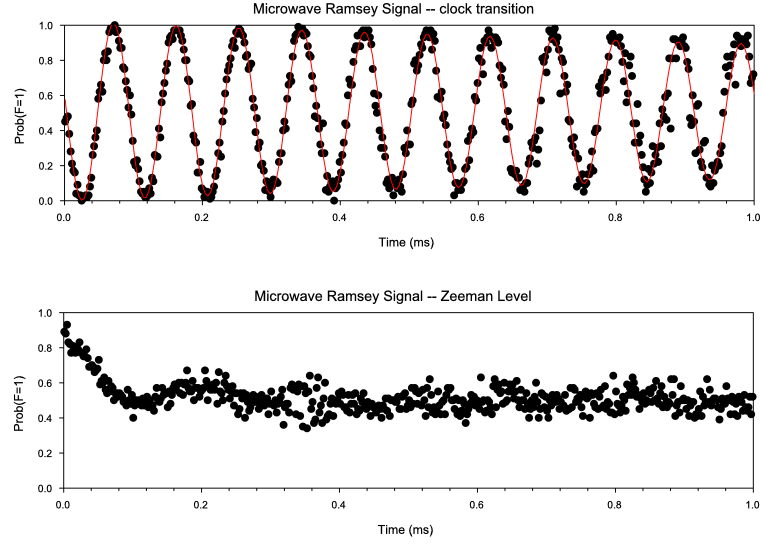


FIGURE 4.3.3. Ramsey experiment to test the coherence of qubits. The results for magnetic field insensitive clock qubit (top) and magnetic field sensitive qubit (bottom) are shown in the graphs. The ion is initially in the $|\uparrow\rangle = |S_{1/2}, F = 0, m_F = 0\rangle$ state, and two carrier microwave $\pi/2$ pulses are applied at times separated by delay time t . The probability of transfer to the $|\downarrow\rangle$ (defined as $|S_{1/2}, F = 1, m_F = 0\rangle$ for the top graph and $|S_{1/2}, F = 1, m_F = 1\rangle$ for the bottom graph) is plotted versus the delay time. The magnetic field insensitive qubit suffers almost no phase decoherence after 1ms delay, while the magnetic field sensitive qubit has no phase coherence after $100\mu\text{s}$.

CHAPTER 5

Two-Ion Entangling Gates

To understand the entanglement of two ions through their collective motion, we examine the original entanglement scheme proposed by Cirac and Zoller, which implements a controlled-NOT (CNOT) gate through coupling of each qubit to a common mode of motion in the trap. The CNOT gate flips the state of a target qubit (e.g. $|\downarrow_2\rangle \leftrightarrow |\uparrow_2\rangle$) only when the control qubit is in state $|\downarrow_1\rangle$. This universal two qubit logic gate yields the following truth table:

$$\begin{aligned}
 (5.0.1) \quad & |\uparrow\uparrow\rangle \rightarrow |\uparrow\uparrow\rangle \\
 & |\uparrow\downarrow\rangle \rightarrow |\uparrow\downarrow\rangle \\
 & |\downarrow\uparrow\rangle \rightarrow |\downarrow\downarrow\rangle \\
 & |\downarrow\downarrow\rangle \rightarrow |\downarrow\uparrow\rangle
 \end{aligned}$$

How can the spin of one state be rotated coherently conditional on the state of the other qubit? Upon closer examination of the scheme, the CNOT gate can be decomposed into three steps:

- (1) a carrier $\pi/2$ pulse on the target qubit with associated phase ϕ
- (2) a π phase gate on two ions
- (3) a carrier $-\pi/2$ pulse on the target qubit with phase ϕ (step (1) reversed).

Steps (1) and (3) are simply carrier couplings on the target qubit ion, and step (2) contains the essential entangling process. In the original proposal, the internal qubit state of the control ion is mapped onto the collective motion, and a 2π pulse coupling a specific spin and motion state of the target ion to an auxiliary state outside of the spin/motion system is applied, resulting in a π phase shift only for that particular state. The motion is then mapped back to the control qubit. The key mechanism here is to obtain a phase that is dependent on the qubits' state, which is satisfied by the resonance condition for accessing the auxiliary level. This π phase gate produces a truth table:

$$\begin{aligned}
 (5.0.2) \quad & |\uparrow\uparrow\rangle \rightarrow |\uparrow\uparrow\rangle \\
 & |\uparrow\downarrow\rangle \rightarrow |\uparrow\downarrow\rangle
 \end{aligned}$$

$$\begin{aligned} |\downarrow\uparrow\rangle &\rightarrow |\downarrow\uparrow\rangle \\ |\downarrow\downarrow\rangle &\rightarrow -|\downarrow\downarrow\rangle \end{aligned}$$

An alternative method for generating a π phase gate is to apply a spin-dependent force on two (or more) ions simultaneously. The forces on the two ions add, creating a state-dependent displacement in the momentum/position phase space. The spin-dependent forces are designed such that upon completion of the displacement, each of the phase space trajectories returns to the initial state, removing any entanglement between the spin and motion while leaving a state-dependent geometric phase. The geometric phase acquired by each trajectory contains a nonlinearity that can result in an entangled final spin state that can not be separated into the two independent qubit subspaces. This is the central concept in the σ_ϕ force gate proposed by Mølmer and Sørensen [13, 20], the σ_z force gate proposed by Milburn [14], and also in ultrafast gates that operate on a time scale of less than a trap period [16]. The slower spin-dependent force gates operating in the resolved sideband limit have previously been demonstrated experimentally [15, 17]. However, the σ_ϕ force gate was implemented in a regime where the force is far detuned from the vibrational frequency, as described in the original proposal by Mølmer and Sørensen. In our experiments, a near resonant spin-dependent σ_ϕ force is applied to create Schrödinger’s cat states similar to the ones described in the previous chapter, and the spin states acquire the appropriate geometric phases in one complete orbit that results in an operation equivalent to a π phase gate. This method creates maximum entanglement in the shortest possible gate time for a given optical power. In section 5.1, we will generalize the construction of a phase gate using the spin-dependent forces described in the previous chapter, followed by the experimental implementation of σ_ϕ gate in section 5.2.

5.1. Entanglement through geometric phases

For two ions in the same harmonic potential coupled through Coulomb interaction, the normal modes of vibration are defined by the center-of-mass coordinate $\hat{q}_1 = (\hat{z}_1 + \hat{z}_2)/\sqrt{2}$ and a “stretch” coordinate $\hat{q}_2 = (\hat{z}_1 - \hat{z}_2)/\sqrt{2}$ [31]. The Hamiltonian for the collective system is summed over both ions and both vibrational modes:

$$(5.1.1) \quad \hat{H}_0 = \sum_{i=1,2} \frac{\hbar\omega}{2} \hat{\sigma}_z^{(i)} + \sum_{\nu=1,2} \hbar\omega_\nu \hat{a}_\nu^\dagger \hat{a}_\nu,$$

where ω_1 (equal to the harmonic oscillator frequency) and $\omega_2 = \sqrt{3}\omega_1$ are the frequencies associated with the center-of-mass and stretch modes, respectively, and \hat{a}_ν^\dagger and \hat{a}_ν are their respective harmonic oscillator creation and annihilation operators.

The z component of the position operator $\hat{\mathbf{r}}_i$ for ion i can be rewritten in the normal mode coordinates

$$(5.1.2) \quad \hat{\mathbf{z}}_i = \frac{q_1}{\sqrt{2}} (\hat{a}_1 + \hat{a}_1^\dagger) \pm \frac{q_2}{\sqrt{2}} (\hat{a}_2 + \hat{a}_2^\dagger),$$

where $q_\nu = \sqrt{\hbar/2M\omega_\nu}$ is the root mean square spatial spread of the ground state wavepacket for the normal mode ν of oscillation in the trap, M is the single ion mass and the plus (minus) sign refers to ion $i = 1$ ($i = 2$). The Lamb-Dicke parameters are given by $\eta_1 = \Delta k_z q_1 / \sqrt{2}$ and $\eta_2 = \Delta k_z q_2 / \sqrt{2} = \eta_1 / \sqrt[4]{3}$, representing the strength of coupling between the fields and each normal mode.

A spin-dependent force applied simultaneously to two ions in the same trapping potential must couple to one of the normal modes of vibration. In this case we choose the stretch mode because of its lower heating rate (requires a field gradient to excite the stretch mode) [51]. The total force on the system is now dependent on the spin of both ions. The interaction Hamiltonian becomes

$$\hat{H}_I = \sum_{m_1, m_2 = \uparrow_n, \downarrow_n} \left(\frac{F_{m_1, m_2}(t) q_2}{2} \hat{a}_2^\dagger + \frac{F_{m_1, m_2}^*(t) q_2}{2} \hat{a}_2 \right) |m_1, m_2\rangle \langle m_1, m_2|,$$

where m_1 and m_2 denote the internal qubit states of ion 1 and ion 2, respectively, and $F_{m_1, m_2} = F_{m_1} + F_{m_2}$ is the total force applied to the state $|m_1, m_2\rangle$. In an enclosed loop, the geometric phase is $\Phi_{m_1, m_2} = 2\pi |F_{m_1, m_2} q_2|^2 / (\hbar\delta)^2$. For simplicity, we consider the special case where the force applied to both ions has equal magnitude but opposite phase, i.e. $F_{m_1} = -F_{m_2}$ for $m_1 = m_2$. Each spin state is transformed after one enclosed orbit as:

$$(5.1.3) \quad \begin{aligned} |\uparrow_n \uparrow_n\rangle &\rightarrow |\uparrow_n \uparrow_n\rangle \\ |\uparrow_n \downarrow_n\rangle &\rightarrow e^{i\Phi_{odd}} |\uparrow_n \downarrow_n\rangle \\ |\downarrow_n \uparrow_n\rangle &\rightarrow e^{i\Phi_{odd}} |\downarrow_n \downarrow_n\rangle \\ |\downarrow_n \downarrow_n\rangle &\rightarrow |\downarrow_n \uparrow_n\rangle \end{aligned}$$

where $\Phi_{odd} = 2\pi |F_{\uparrow_n, \downarrow_n} q_2|^2 / (\hbar\delta)^2$. When $\Phi_{odd} = \pi/2$, the gate is equivalent to the π phase gate in the σ_n basis states with a phase shift of $\pi/2$ on both qubits. This entanglement operation from σ_n basis where $n = \sin\theta\cos\phi\hat{x} + \sin\theta\sin\phi\hat{y} + \cos\theta\hat{z}$ can be converted to the standard π phase gate in the σ_z basis using the following steps:

- (1) A rotation $R(\theta, \phi + \pi)$ that brings \uparrow to \uparrow_n
- (2) perform the geometric phase gate in σ_n basis with $\Phi_{odd} = \pi/2$
- (3) A rotation $R(\theta, \phi - \pi)$ that brings \uparrow_n back to \uparrow
- (4) Perform a phase shift $R_z(-\pi/2)$

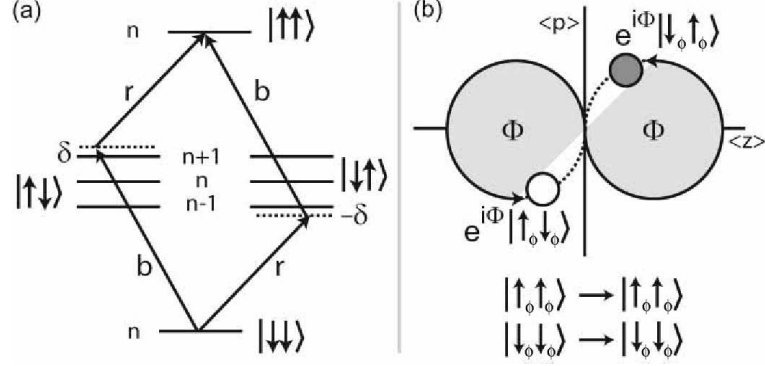


FIGURE 5.2.1. Two views of the Mølmer-Sørensen $\hat{\sigma}_\phi \otimes \hat{\sigma}_\phi$ entangling gate, for two ions in (a) energy space [13], and (b) motional phase space for the gate in diagonal spin basis [35]. The quantum number n and phase space co-ordinates describe a given collective motional mode. Red and blue Raman sideband couplings are labeled by r and b and have detuning $\delta_b = -\delta_r = \delta$. For a closed phase space trajectory, the geometric phase Φ depends only on the area enclosed. The original proposal by Mølmer and Sørensen operates in a regime where the detuning δ sufficiently large such that coherent states are not far separated in phase space but rather requires many orbits to acquire a $\pi/2$ geometric phase, and therefore the off-resonant coupling picture in (a) is more appropriate. In our case where the coherent state separation is large, the phase space picture in (b) is more appropriate.

5.2. σ_ϕ force gate

In the original gate proposal by Mølmer and Sørensen, the σ_ϕ force interaction is described in the limit where the frequency of the force is detuned from the resonant vibration frequency farther than the Rabi frequency, i.e. $\delta \gg \Omega$, where the orbits of the coherent states are small and geometric phase is accumulated over many cycles [13, 20]. In such a regime, the operation can be viewed as a transition between $|\uparrow\uparrow n\rangle$ and $|\downarrow\downarrow n\rangle$ via off-resonant couplings to $|\uparrow\downarrow n \pm 1\rangle$ and $|\downarrow\uparrow n \pm 1\rangle$ in a four-level ladder system. Here we focus on the near resonant case where the orbits are so large that the odd parity states acquire a $\pi/2$ geometric phase in one complete cycle $t = 2\pi/\delta$. Therefore, the interaction here is described in terms of spins and displaced motional states as is done in chapter 4.

Recall the σ_ϕ force employs simultaneous addressing of both ions with bichromatic fields, one detuned from the red sideband of a vibrational mode (stretch mode in this case) by frequency δ and the other from the blue sideband by $-\delta$. The scheme assumes uniform intensity across both ions, with no individual addressing necessary. The two sidebands have equal strength $\eta_2\Omega/2$, and the detuning δ is small compared to the vibration frequency spacing $\omega_2 - \omega_1$ such that we can assume the force couples only

to the stretch mode. Similar to eq 4.2.1, the interaction Hamiltonian is the sum of the red sideband and the blue sideband with detuning δ acting on both ions:

$$(5.2.1) \quad \hat{H}_I = -\frac{\hbar\eta_2\Omega}{2} \sum_{i=1,2} (\hat{\sigma}_+^{(i)} \hat{a}_2 e^{-i(\delta t - \phi_{r,i})} + \hat{\sigma}_+^{(i)} \hat{a}_2^\dagger e^{i(\delta t + \phi_{b,i})} + h.c.)$$

where $\Omega_{sb} = \eta_2\Omega_0 D'_{n_2, n'_2}$ is the sideband Rabi frequency, and $\phi_{r,i}$ and $\phi_{b,i}$ are the phases of the red and blue sidebands respectively at the position of ion i . We can simplify this expression to:

$$(5.2.2) \quad \begin{aligned} \hat{H}_I &= \sum_{i=1,2} \frac{F_i q_2}{2} \hat{\sigma}_{\phi_{S,i}} (e^{i\phi_{M,i}} \hat{a}_2 e^{i\delta t} + e^{-i\phi_{M,i}} \hat{a}_2^\dagger e^{-i\delta t}), \\ &= \sum_{m_1, m_2 = \uparrow_{\phi_{S,1}}, \downarrow_{\phi_{S,1}}} \left(\frac{F_{m_1, m_2}^* q_2}{2} \hat{a}_2 e^{i\delta t} + \frac{F_{m_1, m_2} q_2}{2} \hat{a}_2^\dagger e^{-i\delta t} \right) |m_1 m_2\rangle \langle m_1 m_2| \end{aligned}$$

where

$$(5.2.3) \quad \hat{\sigma}_{\phi_{S,i}}^{(i)} = \hat{\sigma}_i \cdot [\cos(\phi_{S,i})\mathbf{x} + \sin(\phi_{S,i})\mathbf{y}] = \hat{\sigma}_+^{(i)} e^{-i\phi_{S,i}} + \hat{\sigma}_-^{(i)} e^{i\phi_{S,i}}.$$

Here $F_i = \hbar\eta_2\Omega e^{i\phi_{M,i}}/q_2$ is the differential force on the i -th ion, $\phi_{S,i} = -(\phi_{b,i} + \phi_{r,i})/2$ is the spin phase of the i -th ion, $\phi_{M,i} = (\phi_{b,i} - \phi_{r,i})/2$ is the phase of the force on the i -th ion, and $F_{m_1, m_2} = \pm F_1 e^{-i\phi_{M,1}} \pm F_2 e^{-i\phi_{M,2}}$ where $+F_i$ ($-F_i$) corresponds to the force on the spin state $m_i = \uparrow_{\phi_{S,i}}$ ($m_i = \downarrow_{\phi_{S,i}}$) on the i -th ion. Following the formula for a geometric phase gate prescribed in the previous section, we set the phase of the force acting on the two ions to be opposite, i.e. $F_1 e^{i\phi_{M,1}} = -F_2 e^{i\phi_{M,2}}$, and choose δ and F such that the round-trip geometric phase satisfies the condition $\Phi_0 = 2\pi |F_1 q_2|^2 / (\hbar\delta)^2 = \pi/2$. The resulting state from the interaction is the transformation in eq 5.1.3 with $\mathbf{n} = (\phi_{S,1} + \phi_{S,2})/2$. Written in the $\hat{\sigma}_z$ basis produces the following truth table:

$$(5.2.4) \quad \begin{aligned} |\uparrow\uparrow\rangle &\rightarrow \frac{1}{\sqrt{2}} \{ |\uparrow\uparrow\rangle - ie^{i(\phi_{s1} + \phi_{s2})} |\downarrow\downarrow\rangle \} \\ |\uparrow\downarrow\rangle &\rightarrow \frac{1}{\sqrt{2}} \{ |\uparrow\downarrow\rangle - i |\downarrow\uparrow\rangle \} \\ |\downarrow\uparrow\rangle &\rightarrow \frac{1}{\sqrt{2}} \{ |\downarrow\uparrow\rangle - i |\uparrow\downarrow\rangle \} \\ |\downarrow\downarrow\rangle &\rightarrow \frac{1}{\sqrt{2}} \{ |\downarrow\downarrow\rangle - ie^{-i(\phi_{s1} + \phi_{s2})} |\uparrow\uparrow\rangle \} \end{aligned}$$

Note that after the gate, only the spin phase remains, while the motion phase has no effect on the final state.

As we have shown in chapter 4, the frequency selection of Raman fields can determine whether there is a correlation between the spin phase $\phi_{S,1} + \phi_{S,2}$ and the random phase due to the interferometric instability of the Raman beams. Similar to the Schrödinger cat experiments, phase stability between the σ_ϕ gate operation and single qubit operations can be maintained by requiring the same phase dependence

for both entangling gate and single qubit rotations. For the phase sensitive geometry, the single qubit rotation should be performed using non-copropagating Raman fields with the same phase sensitivity as the red and blue sidebands, and for the phase insensitive geometry, the single qubit rotations should be performed using microwaves or copropagating Raman fields. However, the phase insensitive geometry contains a motion phase that is dependent on the interferometric fluctuations, and the relative motion phase between the two ions needs to be calibrated using the ion spacing. To ensure the force on the two ions are opposite in the stretch mode, the phase of the Raman fields must be the same at both ions' locations, which can be accomplished by setting the ion spacing equal to an integer multiple of wavelengths ($x_1 - x_2 = n\lambda$). If the center-of-mass mode is used instead, then the ion spacing should be a half-integer multiple of wavelengths ($x_1 - x_2 = (n + 1/2)\lambda$) so the ions experience opposite phases of the Raman fields and therefore an opposite force on the two ions in the center-of-mass mode. Incidentally, the gate can operate with both integer and half-integer multiple of wavelengths for ion spacing, though in some cases it is the even parity states ($\uparrow\uparrow$ and $\downarrow\downarrow$) that acquires the geometric phase rather than the odd parity states. The phase sensitive geometry always has the same relative red/blue sideband phases, and therefore the ions always experience a force in the opposite direction for the stretch mode and in the same direction for the center-of-mass mode.

To establish long term phase stability of an extended sequence of quantum logic operations, the spin phase dependence between multiple gates can be removed completely by recasting the σ_ϕ gate into a π phase gate in the σ_z basis using the procedure outlined at the end of section 5.1. The π phase gate explicitly written in eq 5.0.2 is independent of the reference qubit phase, and therefore the spin phase in the σ_ϕ gate becomes irrelevant outside of the conversion to the π phase gate in σ_z basis. This allows the computing algorithm to continue for longer than the coherence time of the Mach-Zehnder interferometer even when the entangling gate is accomplished using the phase sensitive geometry, as long as the single qubit operations outside the π phase gates maintain coherence (as can be achieved with microwaves or copropagating Raman beams generated by a signal phase-locked to an atomic clock).

Similar to the Schrödinger cat experiment in the previous chapter, the generation and the evolution of the entangled spin/motion state can be observed by varying the time and detuning of the applied force. With an initial state of $|\uparrow\uparrow\rangle$, the state evolves in time as

$$(5.2.5) \quad |\psi(t)\rangle = \frac{1}{2} \left\{ |\uparrow_{\phi_{s,1}} \uparrow_{\phi_{s,2}}; 0\rangle - e^{i\phi_{S,1}} e^{i\Phi(t)} |\downarrow_{\phi_{s,1}} \uparrow_{\phi_{s,2}}; \alpha(t)\rangle \right. \\ \left. - e^{i\phi_{S,2}} e^{i\Phi(t)} |\uparrow_{\phi_{s,1}} \downarrow_{\phi_{s,2}}; -\alpha(t)\rangle + e^{i(\phi_{s,1} + \phi_{s,2})} |\downarrow_{\phi_{s,1}} \downarrow_{\phi_{s,2}}; 0\rangle \right\}.$$

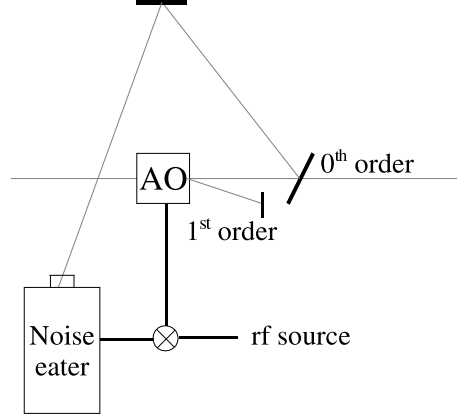


FIGURE 5.2.2. Schematic of the noise eater feedback loop. The intensity of the zeroth order diffraction of the AOM is monitored by a photo-diode and stabilized around a set point. The noise eater circuit outputs an error signal between 0 and 1 volt, which is mixed with the rf modulation signal to control the modulation strength (diffraction efficiency) of the AOM depending on how much correction in the power is required. Excess optical power is removed by the first order diffraction of the AOM.

where the coherent states are defined by $\alpha(t) = \eta_2 \Omega (e^{i\delta t} - 1)/\delta$ and the geometric phase is $\Phi(t) = (\eta_2 \Omega)^2 (\delta t - \sin(\delta t))/\delta^2$. The measurement in the experiment is the average number of atoms in the $|\downarrow\rangle$ (bright) state, which is defined to be $\bar{S} = P(\uparrow\downarrow) + P(\downarrow\uparrow) + 2 \times P(\downarrow\downarrow)$. From eq 5.2.5 we can calculate the probabilities in the measurement to be

$$\begin{aligned}
 (5.2.6) \quad P(\uparrow\uparrow) &= \frac{1}{4} \left\{ 1 + 2e^{-\frac{1}{2}|\alpha(t)|^2} \cos\Phi(t) + \frac{1}{2} \left(1 + e^{-2|\alpha(t)|^2} \right) \right\} \\
 P(\uparrow\downarrow) &= \frac{1}{8} \left\{ 1 - e^{-2|\alpha(t)|^2} \right\} \\
 P(\downarrow\uparrow) &= \frac{1}{8} \left\{ 1 - e^{-2|\alpha(t)|^2} \right\} \\
 P(\downarrow\downarrow) &= \frac{1}{4} \left\{ 1 - 2e^{-\frac{1}{2}|\alpha(t)|^2} \cos\Phi(t) + \frac{1}{2} \left(1 + e^{-2|\alpha(t)|^2} \right) \right\}.
 \end{aligned}$$

Therefore the expected average number of ions in the $|\downarrow\rangle$ state is

$$(5.2.7) \quad \bar{S} = \frac{1}{2} \left\{ 1 - e^{-\frac{1}{2}|\alpha(t)|^2} \cos\Phi(t) \right\}.$$

5.2.1. Laser intensity stabilization. The spin-dependent force induced entangling gates are extremely sensitive to laser intensity fluctuations, mainly because of the long duration (on the order of $100\mu s$) of the ion-field interaction compared to the

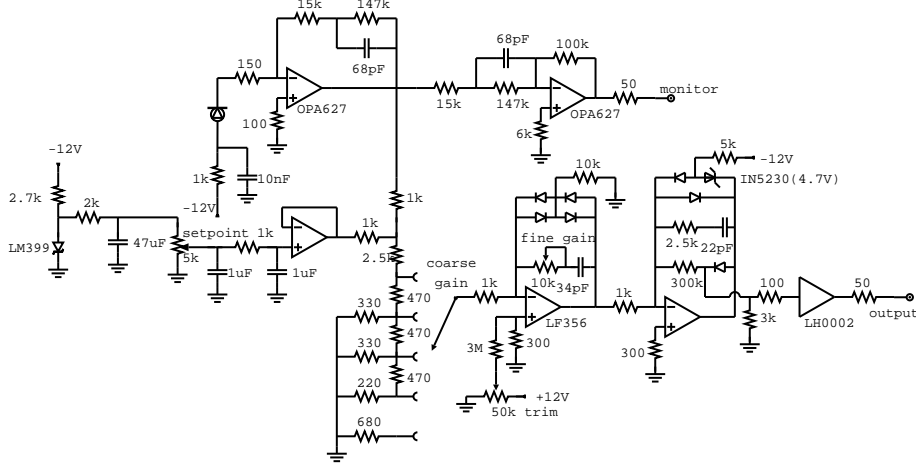


FIGURE 5.2.3. Circuit diagram for the noise eater. The photodiode biased at -12V produces about 0.01Amp per watt of optical power. Typically, the photodiode receives about $300\mu\text{W}$ of optical power, producing a 300mV signal at the monitor output. The input is locked to the setpoint control, and the gain of the circuit (controlled by a discrete coarse gain knob and a continuous tuning fine gain knob as shown in the diagram) is tuned to right below the point where the signal starts to oscillate due to the feedback. The bandwidth of the entire feedback loop is $\sim 100\text{MHz}$, limited by the rise time of the acousto-optic modulator. The gain profile of the circuit rolls off approximately as 9dB/octave, crossing unity gain at around 250kHz.

Raman transitions (on the order of $10\mu\text{s}$ for a π -pulse carrier transition). The fluctuation in the intensity translates to a variation in the magnitude of the spin-dependent force, resulting in a variation in the geometric phase that becomes a source of decoherence for the entangling gate. In the laboratory, we use several passive and active methods to stabilize the laser intensity at the ions in order to improve the performance of the entangling gate.

An important observation regarding the stability of the laser intensity is the significant beam steering of the 214.5nm UV light due to air currents. A simple experiment is performed with a 214.5nm UV beam partially masked by an ion trap electrode. The scattering pattern can be seen by the naked eye on a piece of paper covered in fluorescent dye. When the air around the laser beam path is fanned, the scattering pattern flicker drastically compared to a slower movement in the scattering pattern when the air is not being actively fanned. To reduce the amount of air current, plastic tubes ($\sim 1.5''$ in diameter) are constructed around the beam paths to shield the beams from its surrounding environment. In addition, the section of the optics table containing the UV beams is also enclosed in plexiglass and heavy plastic sheets, and curtains are placed around the optics table to block the airflow around the experiment.

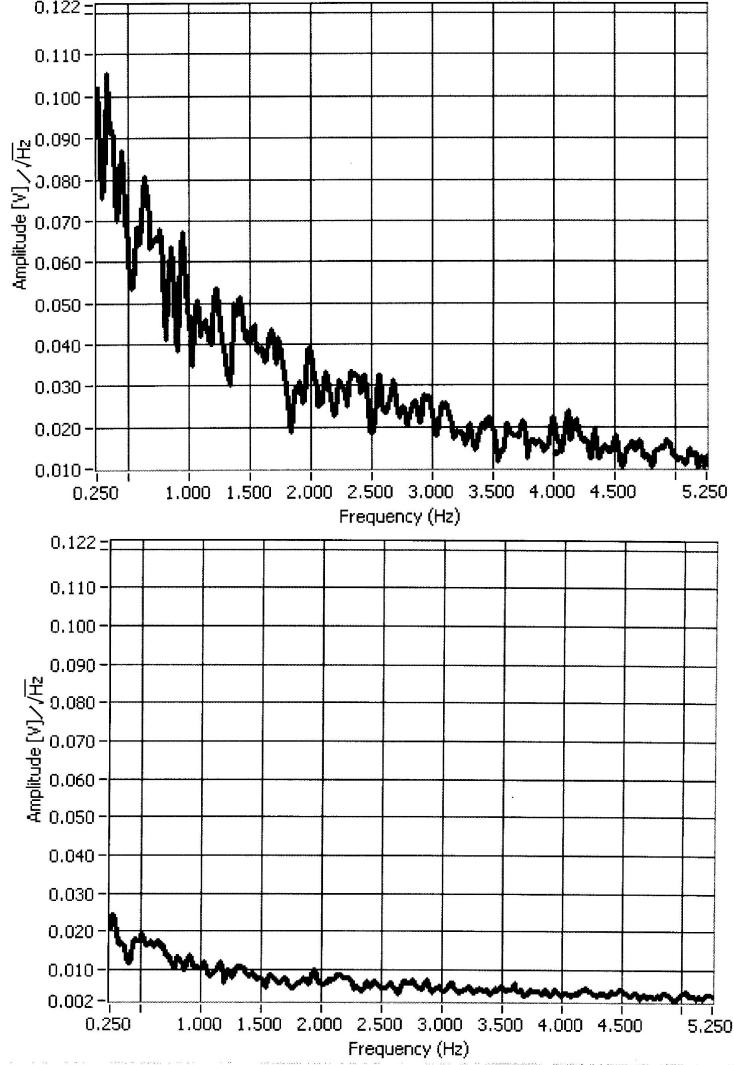


FIGURE 5.2.4. Noise spectrum comparison with and without the noise eater. The optical power is measured by an independent photo-diode, and a spectrum analyzer samples the output voltage signal and performs an FFT. The results are plotted as a function of frequency. The top graph shows the spectrum when the noise eater is on, and the bottom graph shows the spectrum when the noise eater is off. The average signal is $\sim 3\text{V}$, and the bandwidth of the spectra is 0.0167Hz . The noise between DC to 5Hz has been suppressed by $\sim -7\text{dB}$. The bandwidth of the feedback loop is $\sim 100\text{kHz}$.

An active noise eater is placed at the output of the BBO frequency doubling cavity to reduce the intensity fluctuation at the laser source (see figure 5.2.2). The optical power of the UV beam is monitored on a photo-diode, and the excess optical power is removed by increasing the first order diffraction of the AOM. Thus the optical power of the zeroth order beam at the output of the AOM is maintained at a constant setpoint. The noise eater allows the user to control the gain and the setpoint

to optimize its performance. The performance of the noise eater setup is shown in figure 5.2.4. The low frequency noise is strongly suppressed, and also observed but not shown in the figure is the suppression of an 80Hz modulation due to the etalon lock signal in the MBR-110 Ti:Sapphire laser. The noise eater reduces noise up to $\sim 1\text{MHz}$, though the gain drops off with frequency to avoid oscillation.

The entangling gate experiment involves two ions in the same potential, and their equilibrium position due to the mutual Coulomb repulsion are located along the weakest trap axis z_T with spacing

$$(5.2.8) \quad |z_1 - z_2| = \Delta z = \left(\frac{e^2}{2\pi\epsilon_0 m \omega_1^2} \right)^{1/3}.$$

For a 2MHz trap, the ion spacing $\Delta z = 2.5\mu\text{m}$ is a significant fraction of the beam waist size of $\sim 10\mu\text{m}$. Therefore it is important to keep the intensity equal at both ions' locations. A Ramsey experiment measuring the AC Stark shift of each ion due to the fields is used to analyze the field intensity difference. The beam to be measured is turned on for a duration between two microwave $\pi/2$ -pulses before the ions are measured. The AC Stark effect shifts the qubit phase between the $\pi/2$ pulses, creating an oscillation in the final state as the duration of the pulse is varied. A differential AC Stark shift between the two ions creates a beat note at the difference frequency. Figure 5.2.5 shows a plot of a beam alignment with unequal intensity at the two ions' locations (top), and a plot where the intensity at the ions' locations are equal (bottom). Each Raman beam is aligned to have equal intensity at both ions' locations.

The Raman spectrum for two ions also appears more complicated due to the additional stretch mode sideband transitions. For a $\omega_1 = 2.1\text{MHz}$ trap, the stretch mode frequency is $\omega_2 = \sqrt{3}\omega_1 = 3.6\text{MHz}$. Figure 5.2.6 shows the two-ion Raman spectrum as the AOM frequency is varied. For the experiment, the phase insensitive geometry is used, with the modulation frequency of the AOM in one Raman beam path set to 212MHz and the modulation frequency of the AOM in the other Raman beam path to be $212\text{MHz} + 1.5\text{MHz} - 3.6\text{MHz} = 209.9\text{MHz}$ for the first blue sideband of the stretch mode and $212\text{MHz} - 1.5\text{MHz} - 3.6\text{MHz} = 206.9\text{MHz}$ for the first red sideband of the stretch mode. Both vibrational modes are Raman cooled to near the ground state before each experiment.

5.2.2. Results. In the first experiment, we apply the bichromatic field for time τ to the initial state $|\uparrow\uparrow\rangle$ while scanning the detuning δ , and the average number of bright ions is compared to the predicted values from eq 5.2.7. The results are shown in fig 5.2.7. When the time τ is set to $2\pi/\eta_2\Omega$, this plot allows us to pinpoint the required gate detuning to $\eta_2\Omega$, which is exactly when $S = 1$. The initial τ is

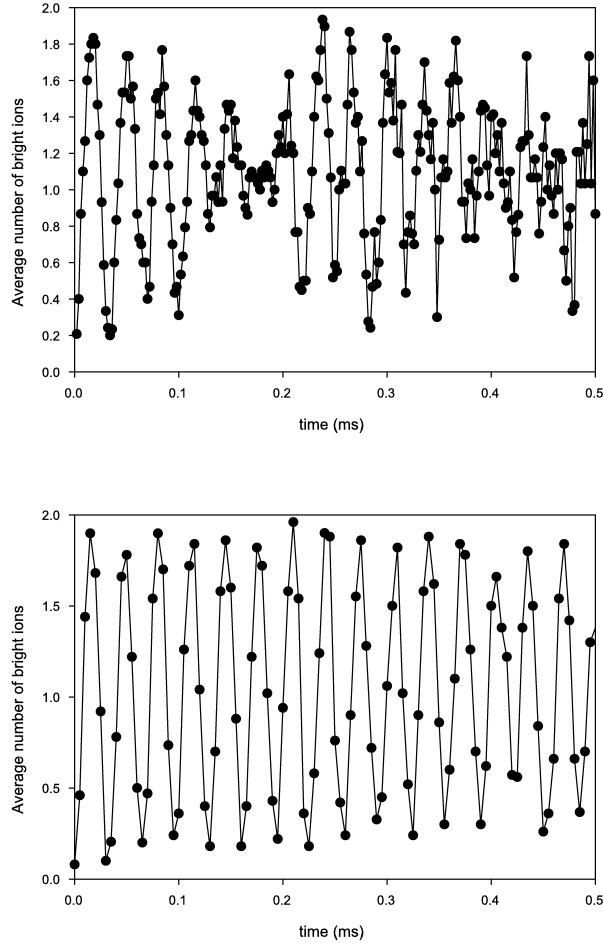


FIGURE 5.2.5. Measurement of the differential AC Stark shifts on two ions, induced by a non-uniform optical power across the ions' positions. A Ramsey experiment, where two $\pi/2$ carrier microwave pulses surrounds a pulse of off-resonant UV radiation, measures the induced AC Stark shifts. The duration of the applied UV field is varied, and the results are plotted versus the pulse duration. The top graph shows a $\sim 5\text{kHz}$ differential AC Stark shift between the two ions, as indicated by the beat note of the sinusoid. The bottom graph shows no measurable differential Stark shift, which is the aim when aligning the Raman beams.

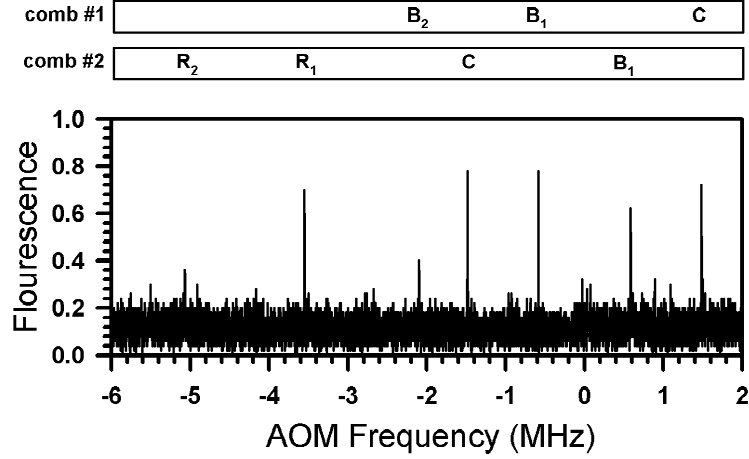


FIGURE 5.2.6. Raman spectrum of two ions in the trap, using a frequency comb generated by an electro-optic modulator (modulation frequency $\omega_{EO} - \omega_0 = 1.5\text{MHz}$ in this case). The x-axis shows the frequency difference between the fields along the two beam paths. The carrier transition appears at $\pm 1.5\text{MHz}$ (C), with corresponding first center-of-mass blue sideband transition at $\mp 0.6\text{MHz}$ (B_1) ($\omega_1/2\pi = 2.1\text{MHz}$), first center-of-mass red sideband transition at $\pm 3.6\text{MHz}$ (R_1), first stretch mode blue sideband at $\mp 2.1\text{MHz}$ (B_2) ($\omega_2/2\pi = 3.6\text{MHz}$), and first stretch mode red sideband at $\pm 5.1\text{MHz}$ (R_2).

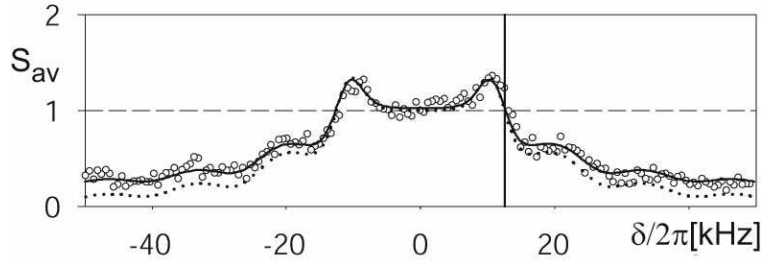


FIGURE 5.2.7. Average brightness S versus σ_ϕ force gate detuning δ (fit to eq 5.2.7). Applied gate time ($75\mu\text{s}$) is within 10% of the ideal. Dotted line indicates expected signal modified to include an initial temperature $\bar{n}_s = 0.3$ as measured in the experiment. Solid line is a fit including offset and contrast factors to account for imperfections such as spontaneous emission. The fit gives a sideband Rabi frequency $\eta_2\Omega/2\pi = 6.3\text{kHz}$ and initial stretch mode temperature $\bar{n}_s = 0.3$. Vertical line shows ideal gate operation point $\delta = 2\eta_2\Omega$, roughly at $S = 1$. Each point is the average of 150 PMT measurements.

determined by driving the sideband transition under an identical set of experiment conditions. Note that a complete two ion sideband transfer occurs at $t = \pi/\sqrt{6}\eta_2\Omega$ (see Appendix G).

The average brightness S exceeds 1 at certain detunings in the two ion case while the average brightness never exceeds 1/2 in the single ion case (see figure 4.2.8) because the geometric phase acquired by each of the four eigenstates of $\hat{\sigma}_\phi \otimes \hat{\sigma}_\phi$ are not the same. In the single ion case, the two eigenstates of $\hat{\sigma}_\phi$ have the same geometric phase even though they experience opposite forces, and therefore the interference can not result in $P(\downarrow) > 1/2$. For two ions, the two eigenstates of $\hat{\sigma}_\phi \otimes \hat{\sigma}_\phi$ that are displaced in phase space acquire the same geometric phase while the other two stationary eigenstates acquire no geometric phase. The interference is similar to the peaks seen in figure 4.3.2 where the applied $\hat{\sigma}_z$ force results in the two eigenstates having unequal geometric phase.

In the second experiment, the detuning δ is set to $\eta_2\Omega$ as determined from the detuning scan in the first experiment, and the duration of the gate pulse is scanned. The result is shown in figure 5.2.8. The peaks of the parity signal

$$(5.2.9) \quad \Pi = (P_{\uparrow\uparrow} + P_{\downarrow\downarrow}) - (P_{\uparrow\downarrow} + P_{\downarrow\uparrow}) = 1/2(1 + e^{-2|\alpha(\tau,\delta)|^2})$$

in fig. 5.2.8(b) indicates when the phase-space trajectories return to the initial position. The gate operation time (80 μ s in the figure), corresponds to the first return when the initial state $|\uparrow\uparrow\rangle$ has evolved ideally to $\Psi_1 = 1/\sqrt{2}(|\uparrow\uparrow\rangle - ie^{i(\phi_{s,1}+\phi_{s,2})}|\downarrow\downarrow\rangle)$. After two consecutive gate pulses, the ion evolves to state $|\downarrow\downarrow\rangle$.

The performance of the gate can be measured by the fidelity $F = \langle\Psi|\rho|\Psi\rangle$ of the actual density matrix ρ compared to the ideal entangled state $|\Psi\rangle$. The fidelity for creating the Bell-like state $\Psi_1 = 1/\sqrt{2}(|\uparrow\uparrow\rangle - ie^{i(\phi_{s,1}+\phi_{s,2})}|\downarrow\downarrow\rangle)$ is simply the sum of the two relevant diagonal population terms of ρ and the corresponding pair of off-diagonal coherences. Explicitly, the fidelity is

$$(5.2.10) \quad F = (|\rho_{\uparrow\uparrow,\uparrow\uparrow}|^2 + |\rho_{\downarrow\downarrow,\downarrow\downarrow}|^2 + |\rho_{\uparrow\uparrow,\downarrow\downarrow}|^2 + |\rho_{\downarrow\downarrow,\uparrow\uparrow}|^2)$$

where $\rho_{m_1m_2,m'_1m'_2} = \langle m_1m_2|\rho|m'_1m'_2\rangle$. The density matrix elements for a perfect Bell state Ψ_1 are $\rho_{\uparrow\uparrow,\uparrow\uparrow} = \rho_{\downarrow\downarrow,\downarrow\downarrow} = 1/2$ and $\rho_{\uparrow\uparrow,\downarrow\downarrow} = \rho_{\downarrow\downarrow,\uparrow\uparrow}^* = ie^{-i(\phi_{s,1}+\phi_{s,2})}/2$, with all other matrix elements being zero. Each of the four diagonal elements contributes 1/4 to the total fidelity $F = 1$.

The sum of the diagonal elements of the density matrix for the actual Bell state produced by the $\hat{\sigma}_\phi$ force can be extracted from the fluorescence signal on the PMT after the entangling gate pulse produces the target state. Fig 5.2.9 shows a histogram of the photon counts collected by the PMT after the entangling gate. The $|\uparrow\uparrow\rangle$ and

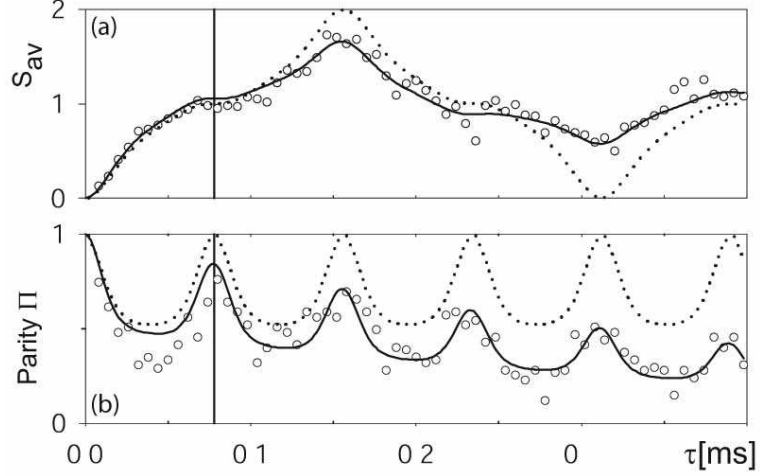


FIGURE 5.2.8. Time scan of σ_ϕ force gate showing (a) average brightness S (eq 5.2.7) and (b) parity Π . Ideal gate evolution shown as dotted lines with best fit including exponential damping shown with solid line. The fit gives a sideband Rabi frequency $\eta_2\Omega/2\pi=6.6\text{kHz}$ and detuning $\delta/2\pi=12.8\text{kHz} \approx 2\eta_2\Omega/2\pi$ with other parameters the same as in figure 5.2.7. Vertical line shows gate operation time $\tau=2\pi/\delta \approx 80\mu\text{s}$.

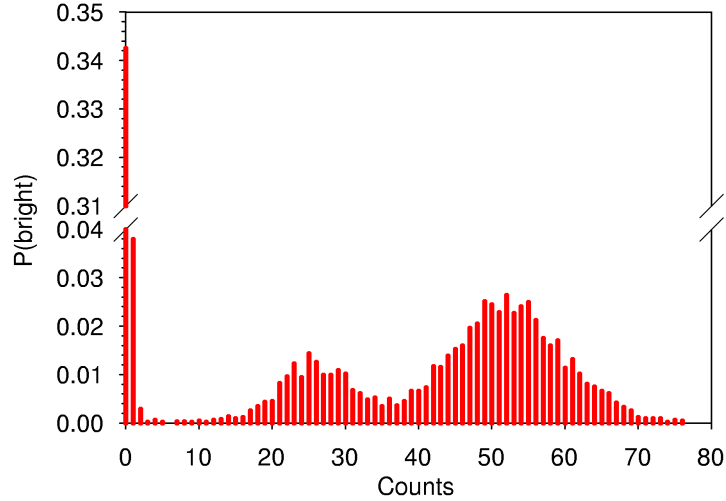


FIGURE 5.2.9. Histogram of photon counts collected from the entangled state $|\uparrow\uparrow\rangle + e^{i(\phi_{S,1}+\phi_{S,2})}|\downarrow\downarrow\rangle$ generated by the σ_ϕ force. When the discriminator is set to 3 and 38 for distinguishing between 0, 1, and 2 bright ($|\downarrow\rangle$) ions, the probabilities are $P(\uparrow\uparrow) = 0.383$ and $P(\downarrow\downarrow) = 0.449$ for the even parity states, and $P(\uparrow\downarrow) + P(\downarrow\uparrow) = 0.168$ for the odd parity states. These numbers also represent the diagonal elements of the density matrix $\rho_{m_1m_2,m_1m_2} = P(m_1m_2)$.

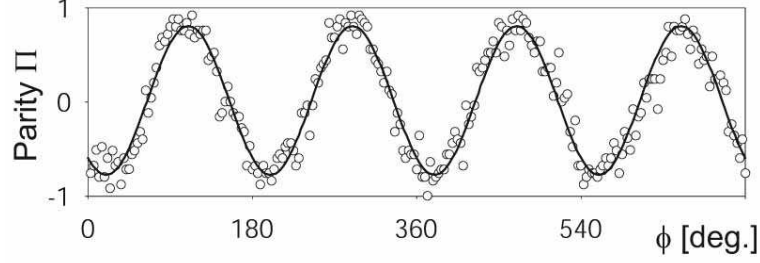


FIGURE 5.2.10. Parity vs phase of analysis $\pi/2$ pulse applied to the Bell state Ψ_1 . The solid line is a sinusoidal fit yielding an amplitude 0.79(2). The fidelity of the state shown is 0.81(2). Each point is an average over 50 PMT measurements and other parameters are as in text.

$|\downarrow\downarrow\rangle$ states can be distinguished from the odd parity states. The data show the ion has a 0.83 probability of being in $|\uparrow\uparrow\rangle$ or $|\downarrow\downarrow\rangle$ after the entangling gate has been applied.

The off-diagonal elements of the density matrix require an additional $\pi/2$ analysis pulse applied to both ions after the gate. For a rotation $R(\pi/2, \phi)$ (as defined by eq 3.2.8) operating on both qubits in the Bell state Ψ_1 , the final state becomes

$$(5.2.11) \quad \Psi_f = \frac{1}{2\sqrt{2}} [1 + ie^{i(\phi_{s,1} + \phi_{s,2} - 2\phi)}] (|\uparrow\uparrow\rangle - ie^{i2\phi} |\downarrow\downarrow\rangle) \\ - \frac{ie^{i\phi}}{2\sqrt{2}} [1 + ie^{i(\phi_{s,1} + \phi_{s,2} - 2\phi)}] (|\uparrow\downarrow\rangle + |\downarrow\uparrow\rangle).$$

The parity depends on ϕ as

$$\Pi = \cos(\phi_{s,1} + \phi_{s,2} - 2\phi),$$

which oscillates as $\cos(2\phi)$. In general, the density matrix after a rotation is applied to ρ is

$$\rho_f = R^{\otimes 2} \left(\frac{\pi}{2}, \phi \right) \rho R^{\otimes 2} \left(-\frac{\pi}{2}, \phi \right),$$

which produces a parity signal oscillating at frequency π with respect to phase ϕ and with amplitude equal to the sum of the off-diagonal elements $\rho_{\uparrow\uparrow,\downarrow\downarrow} + \rho_{\downarrow\downarrow,\uparrow\uparrow}$ [15, 52]. In the experiment, the $\pi/2$ pulse must be phase correlated to the spin phase of the gate pulse. Fig. 5.2.10 shows the corresponding parity oscillation versus phase of the analysis pulse, for an amplitude of 0.79 (which must exceed 0.5 to achieve entanglement [15, 53]). Combining the diagonal and off-diagonal elements of the density matrix, we conclude that the fidelity of the Bell state is 0.81(2).

CHAPTER 6

Quantum State Tomography

In previous chapters, we have demonstrated the necessary components for universal quantum computation. The σ_ϕ force entangling gate combined with arbitrary single qubit rotations are sufficient to perform any set of logic instructions [54]. However, several issues arise when a sequence of multiple logic gates are applied to two qubits. While the necessity of calibrating and maintaining phase coherence between the qubits and the logic operations may seem self-evident, the technical aspects of enforcing an absolute phase across all parts of the experiment can be rather complicated. For instance, the AC Stark effect contributes an energy shift to the qubits during interaction with optical fields, and the resulting phase shift must be factored in for the subsequent operations. Since the rf/microwave frequencies generating the Raman beat note are locked to the Stark shifted frequency ω'_0 instead of the qubit's unperturbed frequency ω_0 , great care must be taken to ensure a consistent relative phase between the Raman beat note and the qubit's phase in every optical pulse. Although the AC Stark effect can be reduced with increasing Raman detuning Δ , an increase in the power of the Raman beams is required to maintain the speed of the entangling gate (as well as Raman cooling). At the maximum optical power of the existing laser system in our laboratory, the AC Stark shift induced on the ions is approximately 50kHz, which is still significant compared to the gate speeds. Therefore, these phase issues must be addressed in order for successful operation of multiple logic gates.

On top of managing phase shifts due to the AC Stark effect, performing a single qubit operation on an individual ion in the presence of a second ion also poses a challenge, since the ion traps available for this thesis work lack the ability to shuttle ions to separate trapping zones as the scalable architecture demands. Individual ion addressing is also impractical since as the σ_ϕ force entangling gate requires uniform illumination across both ions. Our solution is to introduce an intensity gradient between two ions and take advantage of the differential phase shift in composite pulse sequences to rotate the two ions separately.

In this chapter, we explore some of these technical challenges and present specific solutions to address these problems. The solutions allow us to combine logic gate operations to perform tomographic analysis of qubit states, including Bell states formed by the σ_ϕ force as a gauge on the performance of the entangling gate.

6.1. Tracking the phase

In the discussion of phase stability in chapter 4, we showed that the phase of logic gate operations can be controlled by either the rf/microwave modulation from the EOM and the AOMs only, or with additional sensitivity to the phase of the optical fields as determined by the relative beam path lengths of the two Raman fields. When the execution time of a sequence of logic gate operations is within the coherence time of the effective Mach-Zehnder interferometer formed by the Raman fields, one can choose to perform gate operations completely independent of the phase of the optical fields, or perform gate operations completely dependent on the phase of the optical fields. Although the reference phase in the latter scenario is arbitrary relative to the phase of the rf/microwave modulation, it is constant throughout the computation sequence, and therefore the probability of measuring the qubits in a particular state at the end of the computation will be constant despite the phase instability of the optical fields between each trial of the experiment. However, when it exceeds the coherence time of the Mach-Zehnder interferometer, the computation will no longer yield the desired result if the gate operations are dependent on the fluctuating phase. Therefore, it is best to use only logic gates that retain no memory of the phase of the optical fields when the gate operation is finished, as to avoid the limitation imposed by the difficulty in stabilizing the Mach-Zehnder interferometer. In an ideal situation, the rf and microwave frequency synthesizers are phase-locked to an atomic clock, and the coherence of the qubits are limited only by fluctuating magnetic fields, which is a second order effect for clock qubits. But for the experiments in this thesis and any experiment in general, the minimum requirement is a reference clock signal that is stable over the execution time of each experiment in the phase-lock loop of the frequency synthesizers.

In the implementation of the two qubit quantum algorithms, we use a microwave signal at the qubit frequency ω_0 as our reference phase. At the beginning of each computation sequence, every qubit is initialized to \uparrow state. The microwave frequency is calibrated to the qubit frequency ω_0 using a Ramsey experiment with a 5ms delay, to within 10Hz of the actual ω_0 . When the ions interact with optical fields and their phases are shifted due to the AC Stark effect, the phase shifts are immediately negated and the qubits are returned to the reference phase. This can be accomplished by a

photon echo method using auxiliary beams calibrated to induce the same Stark shift but provided no other interactions [55]. A spin flip is applied to the qubits after the intended operation, and the auxiliary beam is applied for the same amount of time as the intended operation, resulting in both spin states acquiring an overall phase that can be ignored. The qubits are then returned to their original state with a second spin flip. This method is robust against fluctuation in the field intensity provided that the auxiliary fields and the interacting fields originate from the same laser source. However, prolonged exposure to optical fields increases the likelihood of spontaneous emission. Therefore, we use an alternative phase shifting sequence to compensate for the Stark shift, with the assumption that the laser intensity is stable and the induced phase shift for each gate operation is repeatable over the overall experiment. The induced phase shift for each type of operation used is measured before the execution of a given quantum algorithm, and the classical computer controlling the experiment adds a qubit rotation R_z around the z-axis that cancels the induced phase shift after each operation. The phase shift R_z can be constructed using a composite pulse sequence

$$(6.1.1) \quad R_z(\phi) = R\left(\frac{\pi}{2}, -\frac{\pi}{2}\right) R(\phi, 0) R\left(\frac{\pi}{2}, \frac{\pi}{2}\right) = \begin{pmatrix} e^{-i\phi/2} & 0 \\ 0 & e^{i\phi/2} \end{pmatrix}.$$

Another alternative in accounting for the AC Stark shift is to add the phase shift to all subsequent logic gate operation instead of removing the phase shift from the qubit. The capability of phase shifting rf frequencies without the large overhead in time, if available, would allow the reference phase of any signal generator to be shifted to the qubit's phase at any point in the algorithm rather than constantly shifting the qubit's phase to align with the reference phase. For a large number of qubits, this method also has an additional cost of keeping a careful record of the relative phase of each qubit. Based on these considerations, we elect to use compensating qubit phase rotations R_z to maintain a consistent reference phase for all qubits.

A separate issue that arises from the AC Stark effect is generating rf/microwave signals with specific phases when the signals are oscillating at different frequencies. As mentioned earlier, the modulation frequency generating the coherent Raman fields is not equivalent to the qubit frequency ω_0 but instead is at frequency ω'_0 , which includes the AC Stark shift. This means the phase of a qubit rotation using Raman transition is revolving in time with respect to the reference/qubit phase, at a frequency equal to the AC Stark shift frequency $\omega'_0 - \omega_0$. To solve this problem, first we ensure that the reference microwave signal and the Stark shifted modulation signals have the same relative phase at the start of each computation sequence by triggering the experiment

on a periodic signal oscillating at the AC Stark shift frequency $\omega'_0 - \omega_0$. The σ_ϕ entangling gate is calibrated to have a definite spin-phase $\phi_{s,1} + \phi_{s,2} = 0$ relative to the reference phase of the microwave at time t_0 after the start of the experiment. All entangling gate pulses must start at time $t_0 + 2\pi/(\omega'_0 - \omega_0)$ where n is an integer to guarantee that the phase of the entangling gate remain the same. The single qubit rotations in the experiments are driven by microwave radiation through direct magnetic dipole coupling, and therefore the frequency of the drive is resonant with the qubit frequency splitting ω_0 . If instead the single qubit rotations are driven via copropagating Raman transitions, then a phase calibration similar to the entangling gate would be required for the copropagating Raman transitions as well since the optical fields also induce an AC Stark shift on the qubits they operate on.

In certain cases, such stringent requirements on the phase of all operations may be unnecessary and some of the phase compensation or calibration procedures can be dispensed with when *a priori* knowledge about the algorithm or the possible input states suggest that the procedures do not affect the outcome, examples of which are included in the following sections. In general, the AC Stark shifts must be treated carefully to ensure that the interactions provide the intended quantum logic operation for the system.

6.2. Individual qubit rotation

Given only a single trap region that confines two ions in the same harmonic potential, how can the qubit stored in the internal state of one ion be rotated coherently without altering the state of the other qubit? Although the fields are not focused to a beam waist size smaller than the ion spacing to address each ion individually without disturbing the other, the solution to this dilemma lies in the non-uniformity of the optical illumination between two ions, which was evident from figure 5.2.5. This intensity gradient across the ions' locations can be exacerbated by an intentional misalignment of an incident field, and the differential phase shift caused by the AC Stark effect combined with common mode rotations can be utilized in a composite pulse sequence to yield the desired individual rotations.

Figure 6.2.2 is an example of a Ramsey experiment that measures the differential AC Stark shift on the ions. A global $\pi/2$ pulse is applied to both ions, and then an optical field induces a differential AC Stark shift on the ions. A second $\pi/2$ pulse again applied to both ions rotates the two qubits into different states since the two qubits have different phases. The final state of each ion at the end of the experiment is measured using a CCD camera, and the results are plotted as the phase of the second $\pi/2$ pulse is scanned. The differential phase shift between the two ions is

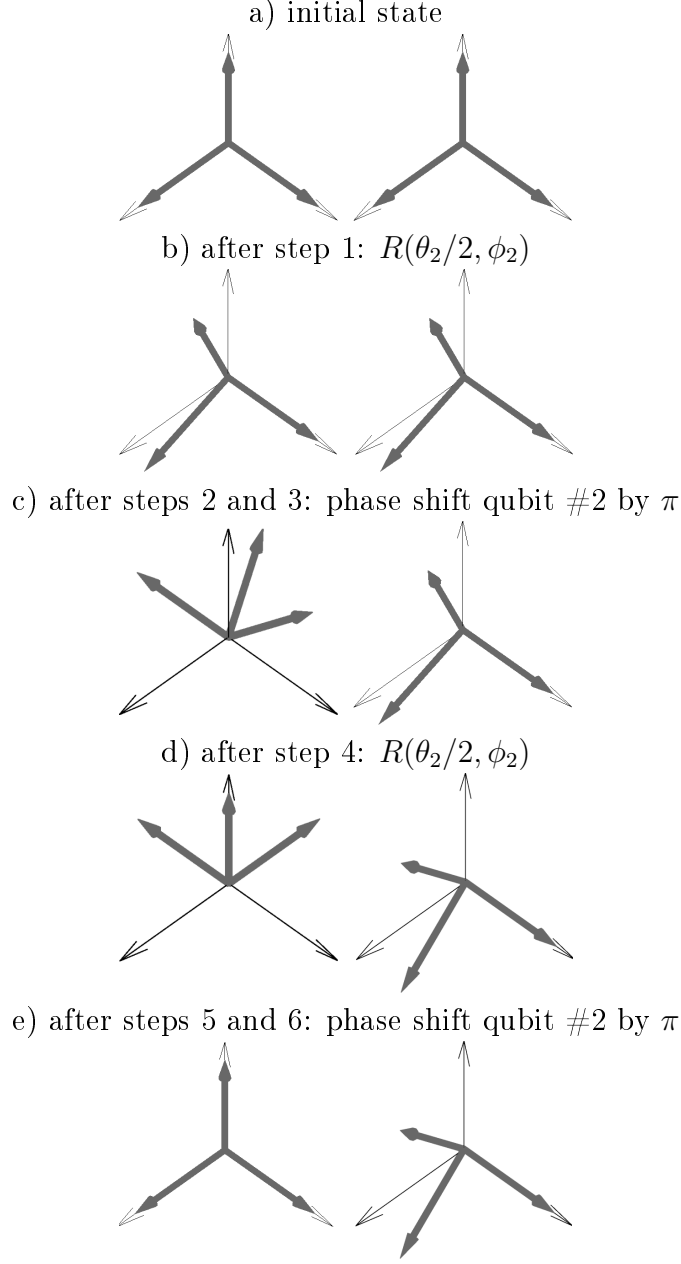


FIGURE 6.2.1. Composite pulse sequence for individual qubit rotations. Qubit #2 is rotated by $R(\theta_2, \phi_2)$ (with $\phi_2 = 0$ here for simplicity) while leaving qubit #1 in its original state. The rotations $R(\theta_2/2, \phi_2)$ in steps 1 and 4 are applied to both ions. Steps 2 and 3 (or 5 and 6) combined effectively phase shift qubit #2 by a phase π while leaving the phase of ion #1 unchanged. The diagram shows the rotation of all three initial axes after each step.

extracted from the data and can be controlled by varying the duration of the optical pulse.

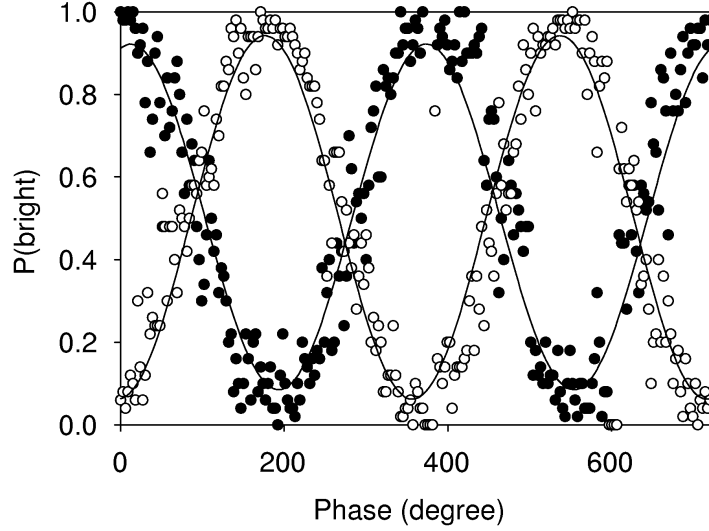


FIGURE 6.2.2. Measurement of the differential AC Stark shift between two ions. A Ramsey experiment is conducted where the optical field is turned on for $54\mu\text{s}$ between two $\pi/2$ pulses, and the probability of each ion being in the $|\downarrow\rangle$ state is plotted against the phase of the second $\pi/2$ pulse. The filled circles indicate the state of ion #1 and the open circles indicate the state of ion #2. The fit shows that the optical field induced a 1.09π differential phase shift between ion #1 and ion #2.

As an exercise, we can examine an arbitrary qubit rotation $R(\theta_1, \phi_1)$ as defined by eq 3.2.8 on the first qubit while leaving the second qubit in its original state. This can be accomplished by the following composite pulse sequence:

- (1) Rotate both qubits by $R(\theta_1/2, \phi_1)$
- (2) Apply differential AC Stark shift such that ion 1 is phase shifted by φ_{SS} and ion 2 is phase shifted by $\varphi_{SS} + \pi$
- (3) Apply a rotation around the z axis $R_z(-\varphi_{SS})$
- (4) Rotate both qubits by $R(\theta_1/2, \phi_1)$
- (5) Apply differential AC Stark shift such that ion 1 is phase shifted by φ_{SS} and ion 2 is phase shifted by $\varphi_{SS} + \pi$
- (6) Apply a rotation around the z axis $R_z(-\varphi_{SS})$

To rotate the second qubit by $R(\theta_2, \phi_2)$ without disturbing the first qubit, a similar pulse sequence can be applied, replacing θ_1 with θ_2 and ϕ_1 with ϕ_2 , and replacing step 3 and 6 with $R_z(-\varphi_{SS} + \pi)$. A graphical example is shown in figure 6.2.1.

In the laboratory, individual rotations in quantum algorithms can often be simplified further when restrictions can be placed on the input states or when the phase after the rotation is inconsequential. For example, in tomographic analysis, measurements of the qubits' projection along an axis can be obtained by rotating the

measurement axis to the z axis and collapse the wavefunction into the eigenstates of σ_z regardless of the exact orientation of the orthogonal axes. In those cases, steps 5 and 6 can be ignored since the phase shifts induced do not affect the outcome of the measurement. Therefore, individual rotations are tailored to suit the requirements of each experiment using the principles for rotation of a single ion by an arbitrary angle and phase described above.

6.3. Tomography

Quantum state tomography can be used to characterize the gate performance for the creation of all four entangled Bell-like states. Previous applications of quantum state tomography with ions include the reconstruction of non-classical states of motion [56–58] as well as entangled states of optical ion-qubits composed of electronic levels [59]. A tomographic analysis maps the full density matrix of a state without making any assumptions about the density matrix. Following the tomographic approach previously demonstrated in photonic systems as outlined in refs [60, 61], the density matrix can be decomposed in terms of a tensor product basis $\rho = \sum_{i,j=0}^3 r_{ij} \sigma_i \otimes \sigma_j$ where $\sigma_0 \equiv \mathbb{I}$, $\sigma_1 \equiv \sigma_x$, $\sigma_2 \equiv \sigma_y$ and $\sigma_3 \equiv \sigma_z$ are the usual single-qubit Pauli matrices. In the experiment we choose to perform projective measurements in the nine basis combinations $\{\sigma_i \otimes \sigma_j, i, j = x, y, z\}$ each yielding four possible outcomes for a total of twenty-seven independent measurements accounting for normalization. Independent single-qubit rotations are used to transform the measurement basis into the σ_z basis before making a measurement in the σ_z basis.

The experiment is setup with resonant microwaves set to three different phases: 0, $\pi/2$, and $-\pi/2$. An off-resonant laser beam detuned by 200GHz from resonance and with a moderate waist ($\lesssim 10\mu\text{m}$ compared with the $2.5\mu\text{m}$ ion spacing) is aligned to be off-center with respect to the two ions, giving rise to a phase shift difference between the two qubits of $\pi/2$ in a $10\mu\text{s}$ exposure. The differential Stark shifts are calibrated using the following Ramsey experiment: a differential Stark shift pulse sandwiched between two $\pi/2$ pulses of the same phase is varied in duration, and the probability of each ion resulting in the \downarrow state is plotted versus the pulse duration. From the difference in the Stark shift frequency of the two ions due to the pulse, the time $t_{\pi/2}$ for ion 1 to advance in phase by $\pi/2$ relative to ion 2 can be extracted. The pulse duration is set to time $t_{\pi/2}$, and an additional phase shift $R_z(\phi)$ is added between the Stark shift pulse and the final $\pi/2$ pulse, and the phase shift ϕ is scanned. The phase correction for the common mode Stark shift is set to the phase where ion 2 returns to its initial state \uparrow and ion 1 has an equal probability of being in \uparrow and \downarrow . The differential Stark shift pulse with a $\pi/2$ relative phase advance and the phase shift

projection basis	rotation	DD	DB	BD	BB
$\sigma_z \otimes \sigma_z$	none	$\uparrow_z \uparrow_z$	$\uparrow_z \downarrow_z$	$\downarrow_z \uparrow_z$	$\downarrow_z \downarrow_z$
$\sigma_z \otimes \sigma_y$	$R(\frac{\pi}{2}, \frac{\pi}{2}); DS; R(\frac{\pi}{2}, 0)$	$\uparrow_z \downarrow_y$	$\uparrow_z \uparrow_y$	$\downarrow_z \downarrow_y$	$\downarrow_z \uparrow_y$
$\sigma_z \otimes \sigma_x$	$R(\frac{\pi}{2}, 0); DS; R(\frac{\pi}{2}, \frac{\pi}{2})$	$\downarrow_z \uparrow_x$	$\downarrow_z \downarrow_x$	$\uparrow_z \uparrow_x$	$\uparrow_z \downarrow_x$
$\sigma_y \otimes \sigma_x$	$DS; R(\frac{\pi}{2}, \frac{\pi}{2})$	$\uparrow_y \uparrow_x$	$\uparrow_y \downarrow_x$	$\downarrow_y \uparrow_x$	$\downarrow_y \downarrow_x$
$\sigma_x \otimes \sigma_x$	$R(\frac{\pi}{2}, \frac{\pi}{2})$	$\downarrow_x \downarrow_x$	$\downarrow_x \uparrow_x$	$\uparrow_x \downarrow_x$	$\uparrow_x \uparrow_x$
$\sigma_x \otimes \sigma_y$	$DS; R(\frac{\pi}{2}, 0)$	$\uparrow_x \downarrow_y$	$\uparrow_x \uparrow_y$	$\downarrow_x \downarrow_y$	$\downarrow_x \uparrow_y$
$\sigma_x \otimes \sigma_z$	$R(\frac{\pi}{2}, 0); DS; R(\frac{\pi}{2}, 0)$	$\uparrow_x \uparrow_z$	$\uparrow_x \downarrow_z$	$\downarrow_x \uparrow_z$	$\downarrow_x \downarrow_z$
$\sigma_y \otimes \sigma_z$	$R(\frac{\pi}{2}, \frac{\pi}{2}); DS; R(\frac{\pi}{2}, \frac{\pi}{2})$	$\uparrow_y \uparrow_z$	$\uparrow_y \downarrow_z$	$\downarrow_y \uparrow_z$	$\downarrow_y \downarrow_z$
$\sigma_y \otimes \sigma_y$	$R(\frac{\pi}{2}, 0)$	$\uparrow_y \uparrow_y$	$\uparrow_y \downarrow_y$	$\downarrow_y \uparrow_y$	$\downarrow_y \downarrow_y$

FIGURE 6.3.1. Projective measurements for tomography. The second column contains the composite pulse sequence to transforms the projection basis to the σ_z basis before measurement. A $\pi/2$ differential AC Stark shift pulse is denoted by DS , which includes the phase correction for common mode phase shift of the two ions using an R_z rotation. The last four columns list the projection of the states corresponding to a measurement of both ions dark, first ion dark and second ion bright, first ion bright and second ion dark, and both ions bright.

$R_z(\phi)$ correction combined to be the differential Stark shift (DS) pulse referred to in table 6.3.1. After differential Stark shift is calibrated, the projective measurements on a prepared state are acquired by performing the nine rotations listed in table 6.3.1. Repeated preparation of a target state followed by tomographic measurement is performed for 200 shots per measurement basis. The total reconstruction time takes about 60s, dominated by the cooling cycle and camera readout time.

A fast, direct inversion for the density matrix can be made with a minimum complete measurement set of fifteen values r_{ij} . However, this process in general leads to an unphysical density matrix due to experimental error. Instead, maximum likelihood estimation is used to fit the data to a density matrix form constrained to be Hermitian, normalized and positive semidefinite. The inclusive and mutually exclusive nature of the four measurement outcomes for each basis is taken into account by least-squares weighting according to a multinomial distribution [62]. The probability of measuring a success x_n times in N trials in one of four possible outcomes $n = \{1..4\}$ given a probability of success p_n is

$$(6.3.1) \quad P(x_1, x_2, x_3, x_4) = \frac{N!}{x_1!x_2!x_3!x_4!} p_1^{x_1} p_2^{x_2} p_3^{x_3} p_4^{x_4}.$$

The density matrix defines the probabilities $\{p_1, p_2, p_3, p_4\}$ of measuring $\{DD, DB, BD, BB\}$ for each projective measurement $\sigma_i \otimes \sigma_j$, where D indicates the ion is in the dark state $|\uparrow\rangle$ and B indicates the ion is in the bright state $|\downarrow\rangle$. Using the multinomial distribution in eq 6.3.1, a numerical algorithm finds the density matrix with the

	DD	DB	BD	BB
$\sigma_z \otimes \sigma_z$	0.965(1.00)	0.010(0.00)	0.025(0.00)	0.000(0.00)
$\sigma_z \otimes \sigma_y$	0.610(0.50)	0.295(0.50)	0.060(0.00)	0.035(0.00)
$\sigma_z \otimes \sigma_x$	0.010(0.00)	0.025(0.00)	0.420(0.50)	0.545(0.5)
$\sigma_y \otimes \sigma_x$	0.200(0.25)	0.215(0.25)	0.225(0.25)	0.360(0.25)
$\sigma_x \otimes \sigma_x$	0.210(0.25)	0.215(0.25)	0.225(0.25)	0.360(0.25)
$\sigma_x \otimes \sigma_y$	0.405(0.25)	0.170(0.25)	0.230(0.25)	0.195(0.25)
$\sigma_x \otimes \sigma_z$	0.400(0.50)	0.020(0.00)	0.520(0.50)	0.060(0.00)
$\sigma_y \otimes \sigma_z$	0.430(0.50)	0.010(0.00)	0.510(0.50)	0.050(0.00)
$\sigma_y \otimes \sigma_y$	0.265(0.25)	0.295(0.25)	0.220(0.25)	0.220(0.25)

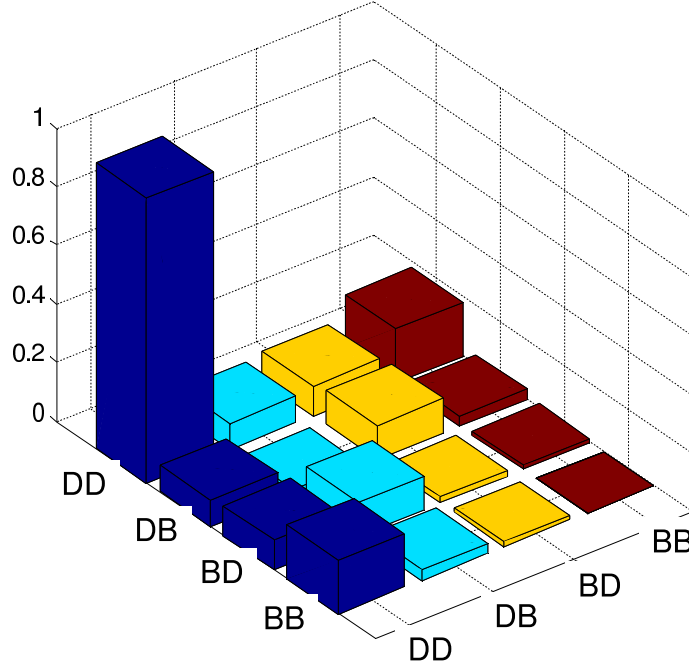


FIGURE 6.3.2. Tomography of $|\uparrow\uparrow\rangle$ state. The projective measurements are performed using the rotations listed in 6.3.1, and the results are shown in the table, with the expected values listed in the parenthesis. The reconstructed density matrix is shown in the plot, with $D=|\uparrow\rangle$ and $B=|\downarrow\rangle$.

highest probability of producing the set of results $\{x_1, x_2, x_3, x_4\}$ that corresponds to the nine projective measurements.

6.3.1. Tomography of the basis states. In an experiment, qubit states $|\uparrow\uparrow\rangle$ and $|\downarrow\uparrow\rangle$ are generated using individual spin rotations and tomography is performed on each of these states. The ions are initialized in the $|\uparrow\uparrow\rangle$ state, and no additional rotation is required before each projective measurement. To generate the $|\downarrow\uparrow\rangle$ state, the following sequence of pulses is performed: 1) $R(\pi/2, \pi/2)$; 2) a π differential AC

	DD	DB	BD	BB
$\sigma_z \otimes \sigma_z$	0.065(0.00)	0.010(0.00)	0.850(1.00)	0.075(0.00)
$\sigma_z \otimes \sigma_y$	0.030(0.00)	0.005(0.00)	0.525(0.50)	0.440(0.50)
$\sigma_z \otimes \sigma_x$	0.490(0.5)	0.405(0.5)	0.045(0.00)	0.060(0.00)
$\sigma_y \otimes \sigma_x$	0.280(0.25)	0.275(0.25)	0.205(0.25)	0.240(0.25)
$\sigma_x \otimes \sigma_x$	0.225(0.25)	0.195(0.25)	0.290(0.25)	0.290(0.25)
$\sigma_x \otimes \sigma_y$	0.340(0.25)	0.100(0.25)	0.410(0.25)	0.150(0.25)
$\sigma_x \otimes \sigma_z$	0.450(0.50)	0.045(0.00)	0.445(0.50)	0.060(0.00)
$\sigma_y \otimes \sigma_z$	0.475(0.50)	0.040(0.00)	0.430(0.50)	0.055(0.00)
$\sigma_y \otimes \sigma_y$	0.115(0.25)	0.480(0.25)	0.060(0.25)	0.345(0.25)

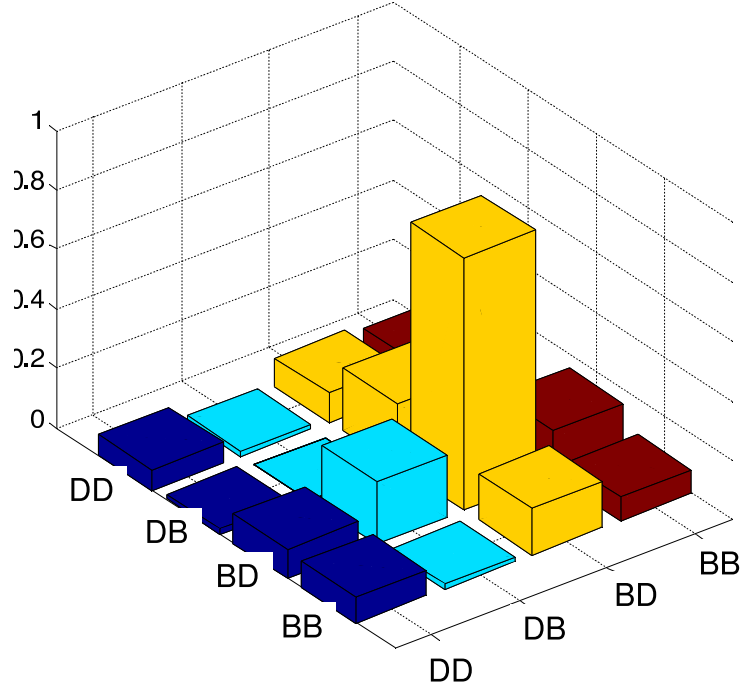


FIGURE 6.3.3. Tomography of $|\downarrow\uparrow\rangle$ state. The projective measurements are performed using the rotations listed in 6.3.1, and the results are shown in the table, with the expected values listed in the parenthesis. The reconstructed density matrix is shown in the plot, with $D=|\uparrow\rangle$ and $B=|\downarrow\rangle$.

Stark shift pulse; 3) $R_z(\phi)$ where ϕ is the AC Stark shift induced on ion #1 in step 3; 4) $R(\pi/2, \pi/2)$. The projection measurements and the reconstructed density matrix for these two states are shown in figures 6.3.2 and 6.3.3. For this set of data, the fidelity of the $|\uparrow\uparrow\rangle$ is $F = 0.97$, limited by the detection error of the CCD camera, and the fidelity of the $|\downarrow\uparrow\rangle$ is $F = 0.85$, with the calibration and the stability of the differential AC Stark shift being the main source of error.

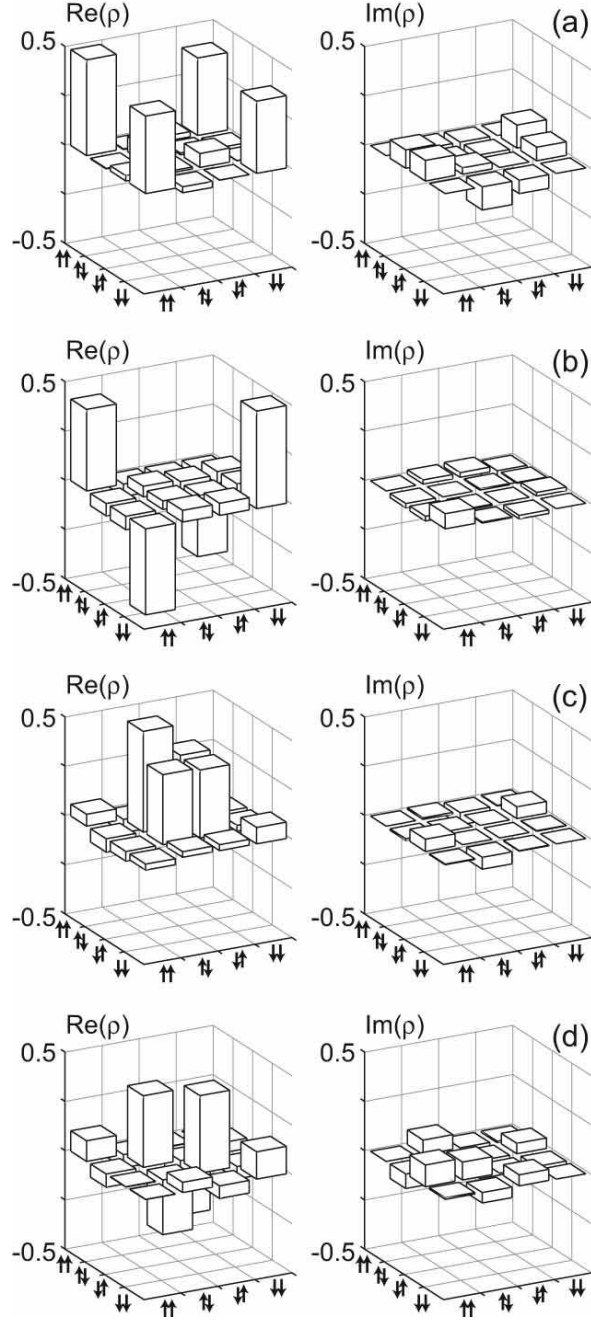


FIGURE 6.3.4. Tomographically reconstructed density matrices for the four Bell-like entangled states (a)–(d) corresponding to Ψ_1 through Ψ_4 as per Eq. 6.3.2. Each state reconstruction uses 27 independent projective camera measurements averaged over 200 runs [49].

6.3.2. Tomography of Bell states. The σ_ϕ force is applied to four initial computational states followed by a Stark shift phase correction to generate four Bell

states:

$$\begin{aligned}
 (6.3.2) \quad |\uparrow\uparrow\rangle &\rightarrow \Psi_1 = \frac{1}{\sqrt{2}} \{|\uparrow\uparrow\rangle + |\downarrow\downarrow\rangle\} \\
 |\downarrow\downarrow\rangle &\rightarrow \Psi_2 = \frac{1}{\sqrt{2}} \{|\uparrow\uparrow\rangle - |\downarrow\downarrow\rangle\} \\
 |\uparrow\downarrow\rangle &\rightarrow \Psi_3 = \frac{1}{\sqrt{2}} \{|\uparrow\downarrow\rangle + |\downarrow\uparrow\rangle\} \\
 |\downarrow\uparrow\rangle &\rightarrow \Psi_4 = \frac{1}{\sqrt{2}} \{|\uparrow\downarrow\rangle - |\downarrow\uparrow\rangle\}
 \end{aligned}$$

Figure 6.3.4 shows their reconstructed density matrices. The reconstructed density matrices are rotated into the real coordinate to allow direct comparison of diagonal and off-diagonal elements. Systematics of the tomographic process are assessed after the fact based on tomographic control runs of input states $|\uparrow\uparrow\rangle$ and $|\downarrow\downarrow\rangle$ assumed to be ideal. The results from the controls are used to extract detection biases (on the order of a few percent), microwave Rabi frequency and applied AC Stark shifts used for qubit rotations.

The inferred fidelities for the target states Ψ_1 through Ψ_4 are $F = \{0.82(3), 0.89(3), 0.78(3), 0.66(3)\}$. The tomographically obtained fidelity for Ψ_1 agrees well with a simple parity-based assessment like that discussed above. The fidelity for creating the odd-parity states $\Psi_{3,4}$ is worse because of inaccurate preparation of the input states $|\uparrow\downarrow\rangle$ and $|\downarrow\uparrow\rangle$ ($F \approx 0.85$). Accounting for this factor, the fidelities of all states are on par. Inseparability (entanglement) of the reconstructed two-qubit states can be tested by performing a partial transpose of the density matrix and searching for a negative value in the resultant eigenvalue spectrum [63, 64]. For example, the eigenvalue spectrum obtained for the Ψ_2 case is $\{-0.42(3), 0.40(3), 0.49(2), 0.53(2)\}$ compared with the ideal case $\{-0.5, 0.5, 0.5, 0.5\}$. The negativity N [65, 66], twice the absolute value of the negative eigenvalue, is obtained for all four target states Ψ_i with values $N = \{0.74(6), 0.84(7), 0.60(5), 0.42(6)\}$. Ranging from zero for a separable state to one for a maximally entangled one, the value gives an indication of the degree of the entanglement. Several quantitative measures of entanglement exist in the literature [67], although lacking a closed form they are in general difficult to calculate. One standard measure that is directly calculable for two qubits is the entanglement of formation E_F [68] again ranging from zero for a separable state to one for a maximally entangled one. In the context of pure states, the value of E_F can be interpreted as the number nE_F of maximally entangled states required to reconstruct n copies of a given state [53]. The experimental values for the four states shown in Fig. 6.3.4 are $E_F = \{0.65(8), 0.77(9), 0.49(6), 0.32(6)\}$. The entanglement of formation is a manifestly more strict indicator for the quality of an entangled state than the fidelity and drops quickly with decreasing fidelity. Statistical errors for parameters calculated from the reconstructed density matrix are difficult to extract directly and so are obtained using a simple numerical bootstrap method [69]. The raw

shot-by-shot data are randomly resampled with replacement to generate successive data sets from which a distribution of a parameter's value can be obtained [70].

CHAPTER 7

Conclusion

In this thesis, a two-qubit quantum computer has been implemented in a new ion species, cadmium 111. Qubits stored in particular ground state hyperfine levels of cadmium ions have long coherence times due to their insensitivity to magnetic field fluctuations. The experiments have shown that these qubits can be initialized and detected at a fidelity of greater than 99%. Universal quantum logic gates have been demonstrated by driving single qubit rotation with stimulated Raman transitions and entangling two ions through the application of a spin-dependent force. The outcomes of the quantum logic gates have been analyzed with tomography of the density matrix, establishing phase control of the quantum logic gates developed here.

While the interactions used to manipulate cadmium ion qubits have been proposed and implemented previously in other species of trapped ions, significant improvements have been made in the phase control of entanglement through the $\hat{\sigma}_\phi$ force. We have shown that the dependence of the $\hat{\sigma}_\phi$ force on the optical phase of the control fields can be removed, thereby enabling the phase of the gate to be governed solely by the modulation applied to the fields. Entanglement based on spin-dependent forces are inherently robust against temperature and heating compared to the original Cirac and Zoller proposal, but the $\hat{\sigma}_\phi$ force can also provide protection against phase decoherence due to fluctuating magnetic fields by operating on magnetic field insensitive clock states in the limit of large field detuning. These considerations suggest that the $\hat{\sigma}_\phi$ force may be the most robust entangling gate against decoherence in the resolved-sideband limit.

The atomic properties of cadmium ions also motivated the development of a cw laser at a wavelength of 214.5nm with several milliwatts of optical power, and new methods to drive stimulated Raman transitions at a large frequency spacing (14.5GHz) using electro-optic phase modulator. These techniques can be applied towards coherent manipulations of other quantum systems. However, the limited optical power currently restricts the size of the Raman detuning, resulting in significant decoherence per gate operation due to spontaneous emission. With additional optical power in the future, the potential for high fidelity quantum logic gates operating on cadmium ion qubits can be fully realized. It may also be worthwhile to investigate

the practicality of using a high power, far detuned laser to drive Raman transitions in cadmium ions for further suppression of spontaneous emission.

Since the start of this thesis work, quantum information processing in trapped ions in our laboratory as well as other research groups around the world has gone from a stage of developing the required tools for computation to a stage where simple quantum algorithms on two or three qubits can be realized. Efforts in constructing scalable ion traps are underway for the next stage where more qubits can be added to the processor. The possibility of engineering a fully-controllable macroscopic entangled system from smaller accessible subsystems is an exciting challenge, and many applications of quantum computation are likely still undiscovered at this point. The work in this thesis is part of the effort in making quantum computing a reality, offering another stepping stone for future progress in this area.

APPENDIX A

Interaction Picture

Given a Hamiltonian $H = H_0 + H_1$ where the steady-state Hamiltonian is given by

$$H_0 = \frac{\hbar\omega_0}{2}\hat{\sigma}_z + \hbar\omega_1\hat{a}^\dagger\hat{a}$$

and the interaction term given by

$$H_1 = \hbar\Omega (\hat{\sigma}_+ + \hat{\sigma}_-) \cos(\mathbf{k} \cdot \hat{\mathbf{r}} - \omega t + \phi),$$

the transformation to the interaction picture results in a simple-looking formula

$$i\hbar \frac{d}{dt} |\tilde{\psi}(t)\rangle = H_I |\tilde{\psi}(t)\rangle$$

where $H_I = U_0(t)H_1U_0^\dagger(t)$ is the “interaction Hamiltonian”, $|\tilde{\psi}(t)\rangle = U_0(t)|\psi(t)\rangle$ is the transformed state vector, and $U_0(t) = e^{iH_0t/\hbar}$ is the time evolution operator in steady-state. To obtain the interaction Hamiltonian using this transformation, we apply a useful relation in quantum mechanics

$$(A.0.1) \quad e^{\alpha\hat{A}}\hat{B}e^{-\alpha\hat{A}} = \hat{B} + \alpha [\hat{A}, \hat{B}] + \frac{\alpha^2}{2!} [\hat{A}, [\hat{A}, \hat{B}]] + \frac{\alpha^3}{3!} [\hat{A}, [\hat{A}, [\hat{A}, \hat{B}]]] \dots$$

Since the spin operators and the creation and annihilation operators commute, the two components can be treated separately:

$$(A.0.2) \quad H_I = \hbar\Omega \left\{ e^{i\frac{\omega_0 t}{2}\hat{\sigma}_z} (\hat{\sigma}_+ + \hat{\sigma}_-) e^{-i\frac{\omega_0 t}{2}\hat{\sigma}_z} \right\} \left\{ e^{i\omega_1\hat{a}^\dagger\hat{a}} \cos(\mathbf{k} \cdot \hat{\mathbf{r}} - \omega t + \phi) e^{-i\omega_1\hat{a}^\dagger\hat{a}} \right\}.$$

For the spin part, it is left as an exercise for the reader to prove that $[\hat{\sigma}_z, \hat{\sigma}_+] = 2\hat{\sigma}_+$ and $[\hat{\sigma}_z, \hat{\sigma}_-] = 2\hat{\sigma}_-$. Applying eq A.0.1,

$$\begin{aligned} e^{i\alpha\hat{\sigma}_z}\hat{\sigma}_+e^{-i\alpha\hat{\sigma}_z} &= \hat{\sigma}_+ + 2\alpha\hat{\sigma}_+ + \frac{(2\alpha)^2}{2!}\hat{\sigma}_+ + \frac{(2\alpha)^3}{3!}\hat{\sigma}_+ + \dots \\ &= e^{i2\alpha}\hat{\sigma}_+ \end{aligned}$$

Similarly,

$$\begin{aligned} e^{i\alpha\hat{\sigma}_z}\hat{\sigma}_-e^{-i\alpha\hat{\sigma}_z} &= \hat{\sigma}_- - 2\alpha\hat{\sigma}_- + \frac{(-2\alpha)^2}{2!}\hat{\sigma}_- + \frac{(-2\alpha)^3}{3!}\hat{\sigma}_- + \dots \\ &= e^{-i2\alpha}\hat{\sigma}_-. \end{aligned}$$

So terms in the first parenthesis in eq A.0.2 becomes

$$e^{i\frac{\omega_0 t}{2}\hat{\sigma}_z} (\hat{\sigma}_+ + \hat{\sigma}_-) e^{-i\frac{\omega_0 t}{2}\hat{\sigma}_z} = e^{i\omega_0 t}\hat{\sigma}_+ + e^{-i\omega_0 t}\hat{\sigma}_-.$$

The part concerning motion can be separated into two terms

$$e^{i\omega_1 \hat{a}^\dagger \hat{a}} \cos(\mathbf{k} \cdot \hat{\mathbf{r}} - \omega t + \phi) e^{-i\omega_1 \hat{a}^\dagger \hat{a}} = \frac{1}{2} e^{i(kr_0 - \omega t + \phi)} e^{i\omega_1 \hat{a}^\dagger \hat{a}} e^{i\eta(\hat{a} + \hat{a}^\dagger)} e^{-i\omega_1 \hat{a}^\dagger \hat{a}} \\ + \frac{1}{2} e^{-i(kr_0 - \omega t + \phi)} e^{i\omega_1 \hat{a}^\dagger \hat{a}} e^{-i\eta(\hat{a} + \hat{a}^\dagger)} e^{-i\omega_1 \hat{a}^\dagger \hat{a}}$$

where $e^{i\mathbf{k} \cdot \hat{\mathbf{r}}} = e^{ikr_0} e^{i\mathbf{k} \cdot \hat{\mathbf{z}}_T}$ can be separated into a phase factor due to the position of the ion and an operator $\mathbf{k} \cdot \hat{\mathbf{z}}_T = (\mathbf{k} \cdot \mathbf{z}_T) z_0 (\hat{a} + \hat{a}^\dagger) = \eta (\hat{a} + \hat{a}^\dagger)$. The phase factor e^{ikr_0} is sometimes absorbed in the phase factor $e^{i\phi}$ by defining the phase as relative to the ion's position $\phi' = kr_0 + \phi$. We can Taylor expand the exponents in $e^{i\eta(\hat{a} + \hat{a}^\dagger)}$ and consider each term independently. With some algebra one can show that

$$e^{i\omega_1 \hat{a}^\dagger \hat{a}} \{i\eta (\hat{a} + \hat{a}^\dagger)\}^n e^{-i\omega_1 \hat{a}^\dagger \hat{a}} = \{i\eta (\hat{a} e^{-i\omega_1 t} + \hat{a}^\dagger e^{i\omega_1 t})\}^n.$$

Summing over all terms in the Taylor expansion again and we get

$$e^{i\omega_1 \hat{a}^\dagger \hat{a}} e^{i\eta(\hat{a} + \hat{a}^\dagger)} e^{-i\omega_1 \hat{a}^\dagger \hat{a}} = e^{i\eta(\hat{a} e^{-i\omega_1 t} + \hat{a}^\dagger e^{i\omega_1 t})}.$$

The second parenthesis in eq A.0.2 becomes

$$e^{i\omega_1 \hat{a}^\dagger \hat{a}} \cos(\mathbf{k} \cdot \hat{\mathbf{r}} - \omega t + \phi) e^{-i\omega_1 \hat{a}^\dagger \hat{a}} = \frac{1}{2} e^{i(kr_0 - \omega t + \phi)} e^{i\eta(\hat{a} e^{-i\omega_1 t} + \hat{a}^\dagger e^{i\omega_1 t})} + c.c.$$

When the spin and motion components are combined, the terms involving $e^{\pm i(\omega_0 + \omega)t}$ are discarded in the rotating wave approximation. Keeping only $e^{\pm i(\delta\omega)t}$ terms for $\delta = \omega - \omega_0$,

$$H_I = \frac{\hbar\Omega}{2} \left\{ \hat{\sigma}_+ e^{i[\eta(\hat{a} e^{-i\omega_1 t} + \hat{a}^\dagger e^{i\omega_1 t}) + kr_0 + (\delta\omega)t + \phi]} + \hat{\sigma}_- e^{-i[\eta(\hat{a} e^{-i\omega_1 t} + \hat{a}^\dagger e^{i\omega_1 t}) + kr_0 + (\delta\omega)t + \phi]} \right\}.$$

This is the full interaction Hamiltonian for the system.

When the frequency difference in the fields is tuned to $\delta\omega = (n - n')\omega_1 + \delta$, the matrix element in the interaction Hamiltonian coupling the states $|\uparrow, n'\rangle$ and $|\downarrow, n\rangle$ is

$$\langle \uparrow, n' | H_I | \downarrow, n \rangle = \frac{\hbar\Omega}{2} e^{i(kr_0 + (\delta\omega)t + \phi)} \sum_{j=0}^{\infty} \frac{\langle n' | [i\eta (\hat{a} e^{-i\omega_1 t} + \hat{a}^\dagger e^{i\omega_1 t})]^j | n \rangle}{j!}.$$

Only terms with the right number of creation and annihilation operators in the sum has non-zero values, and those terms are left with a phase factor $e^{-i(n-n')\omega_1 t}$, conveniently reducing the phase in $e^{i(\delta\omega)t}$ to become $e^{i\delta t}$. So the sum is equivalent to

$$\sum_{j=0}^{\infty} \frac{\langle n' | [i\eta (\hat{a} e^{-i\omega_1 t} + \hat{a}^\dagger e^{i\omega_1 t})]^j | n \rangle}{j!} = \sum_{j=0}^{\infty} \frac{\langle n' | [i\eta (\hat{a} + \hat{a}^\dagger)]^j | n \rangle}{j!} = \langle n' | e^{i\eta(\hat{a} + \hat{a}^\dagger)} | n \rangle = D_{n', n}.$$

The Debye-Waller factor in explicit terms is

$$D_{n',n} = e^{-\eta^2/2} \left(\frac{n_{<}!}{n_{>}!} \right)^{1/2} \eta^{|n'-n|} L_{n_{<}}^{|n'-n|}(\eta^2),$$

where $n_{<}(n_{>})$ is the lesser (greater) of n' and n , and L_n^α is the generalized Laguerre polynomial defined as

$$L_n^\alpha(X) = \sum_{m=0}^{\infty} (-1)^m \binom{n+\alpha}{n-m} \frac{X^m}{m!}.$$

APPENDIX B

Cavity Modifications

In the laboratory, the BBO frequency-doubling cavity from Spectra-Physics requires slight modification from its factory setting. For the Raman laser, the free spectral range must be exact (7266MHz/4 for the Mach-Zehnder interferometer setup and 7263MHz/4 for the cavity detuning setup). The free spectral range of the cavity is simply

$$\nu_{fsr} = \frac{c}{L}$$

where L is the round-trip length of the cavity. Figure B.0.1 shows the schematic of the WaveTrain cavity, utilizing a “delta” configuration instead of the traditional bow-tie configuration. The positions of the input (M1) and the output (M2) mirrors, which are mounted on the casing of the doubler, can be adjusted to change the cavity size. For efficient harmonic conversion, the mode of the cavity should be such that the focus is inside the crystal, and preferably, a small waist size.

To understand the effect of cavity modifications, we must consider the stability of the cavity and the size and position of the focus. Following the derivation in chapter 20 and 21 of ref [**71**], the propagation of geometric optical rays through a round trip in the cavity can be described using ABCD matrices:

$$(B.0.1) \quad \begin{pmatrix} r2 \\ r2' \end{pmatrix} = \begin{pmatrix} A & B \\ C & D \end{pmatrix} \begin{pmatrix} r1 \\ r1' \end{pmatrix}.$$

The stability of the cavity is determined by the *stability parameter* m defined as

$$(B.0.2) \quad m \equiv \frac{A + D}{2}.$$

The cavity is stable if and only if $-1 \leq m \leq 1$. For Gaussian beams, we can write the wavefront in terms of the \tilde{q} -parameter

$$(B.0.3) \quad u(x) = \exp\left(-i\frac{\pi x^2}{q\lambda}\right),$$

where

$$(B.0.4) \quad \frac{1}{\tilde{q}} \equiv \frac{1}{R} - i\frac{\lambda}{\pi x_0^2}.$$

R is the radius of curvature, λ is the wavelength in the medium, and x_0 is the beam spot size. The complex \tilde{q} parameter propagates according to the relationship

$$(B.0.5) \quad \frac{\tilde{q}_2}{n_2} = \frac{A(\tilde{q}_1/n_1) + B}{C(\tilde{q}_1/n_1) + D}.$$

We can define a *reduced q parameter* as

$$(B.0.6) \quad \frac{1}{q} \equiv \frac{n}{\tilde{q}} = \frac{1}{\hat{R}} - i \frac{\lambda_0}{\pi x_0^2},$$

where $\hat{R} = R/n$ is the reduced radius of curvature and $\lambda_0 = n\lambda$ is the optical wavelength in vacuum. The paraxial wave transformation using the ABCD matrix elements and the q Gaussian beam parameters becomes

$$(B.0.7) \quad q_2 = \frac{Aq_1 + B}{Cq_1 + D}.$$

We can find self-consistent Gaussian q values by equating the parameter after a cavity-round-trip to its initial value:

$$(B.0.8) \quad q_2 = \frac{Aq_1 + B}{Cq_1 + D} = q_1.$$

The solutions are (only one solution is real; the other corresponds to a nonphysical Gaussian beam with a transversely increasing intensity)

$$(B.0.9) \quad \frac{1}{q} = \frac{D - A}{2B} \mp i \frac{\sqrt{1 - m^2}}{B} = \frac{1}{\hat{R}} - i \frac{\lambda_0}{\pi x_0^2}.$$

Therefore the radius of curvature of the beam at the reference plane is

$$(B.0.10) \quad R = \frac{2B}{D - A}.$$

and the waist size at the reference plane is

$$(B.0.11) \quad x_0^2 = \frac{|B| \lambda}{\pi \sqrt{1 - m^2}}.$$

Figure B.0.1 shows the schematic of the BBO cavity. The dimensions are listed in table B.0.2 for both the factory setting and the modified cavity. Based on the calculations, the modified cavity can satisfy the constraint on the free spectral range while maintaining a stable cavity with the focus inside the crystal. The increase in the size of the beam waist reduces the efficiency of harmonic generation, but still produces sufficient optical power for Raman transitions.

The free spectral range of the cavity can be measured by noting the correlation between the optical power of the output and the modulation frequency of the EOM. When the free spectral range and the modulation frequency are the same, all sidebands generated by the EOM are resonant with the cavity and the harmonic output has

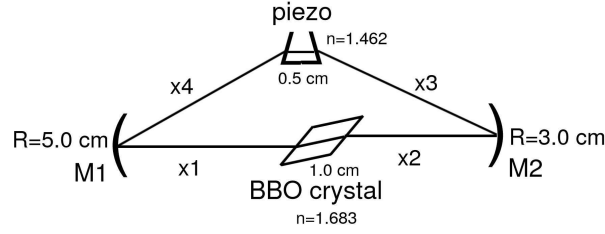


FIGURE B.0.1. Schematic of the WaveTrain BBO cavity. The WaveTrain uses a delta cavity with a factory setting free spectral range (fsr) of approximately 1.7GHz. The cavities can be modified to support 6.8GHz sidebands from the electro-optic modulator, and 7.266GHz sidebands (fsr=1.8GHz) for Raman fields. However, the conversion efficiency drops when the cavity size changes by a significant proportion. The cavity has a 15MHz linewidth. A prism mounted on a piezo allows the electronics to lock the cavity.

	factory setting	modified cavity
x_1	4.64 cm	4.05 cm
x_2	1.64 cm	1.57 cm
x_3	4.56 cm	4.49 cm
x_4	4.56 cm	3.97 cm
m	0.97	0.2
ν_{fsr}	1.68 GHz	1.818GHz
position of focus from M_1	5.18 cm / 15.56 cm	4.57 cm / 14.55 cm
beam waist at focus	23.10 μm / 16.76 μm	48.65 μm / 33.04 μm

FIGURE B.0.2. Cavity parameters for the WaveTrain doubler, before and after modification. The round-trip length of the cavity is shortened to match the fourth subharmonic of the qubit frequency, and the resulting beam waist is about twice as large as the factory setting. The efficiency of frequency doubling by the cavity decreases by a factor of ~ 3 after the adjustment. The cavity remains stable with $-1 \leq m \leq 1$.

maximum power. When the sidebands are slightly off resonant in the cavity, the output decreases. In the limit where the modulation frequency is tuned beyond the bandwidth of the EOM ($\approx \pm 25\text{MHz}$), the sideband strength decreases and the optical power returns to the carrier, resulting in efficient harmonic generation again. This produces a “W” curve on a plot of UV power versus modulation frequency, with the

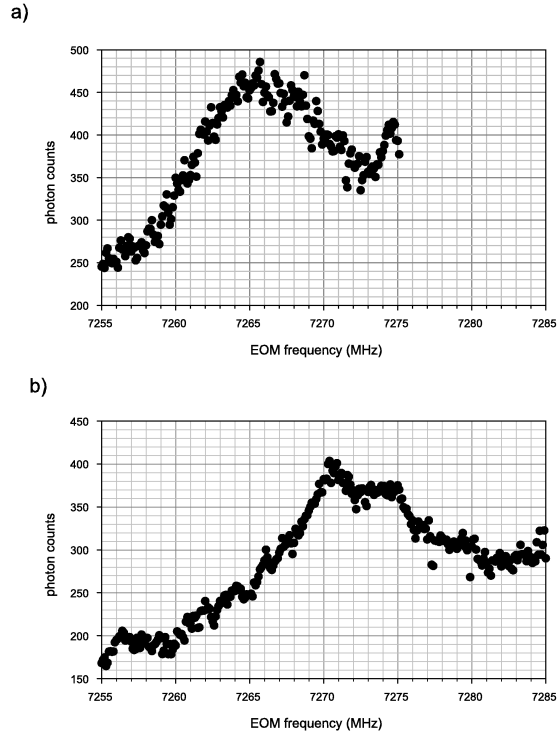


FIGURE B.0.3. Optical power of the BBO output vs modulation frequency of the EOM. The free spectral range of the BBO cavity is a) $7266\text{MHz}/4$ (ideal for the Mach-Zehnder setup), and b) $7272\text{MHz}/4$ (when the cavity is too far detuned). The plots only show the middle peak of the “W” curve that indicates the free spectral range of the cavity.

middle peak in the W aligned on an integer multiple of the free spectral range of the BBO cavity.

APPENDIX C

Mixing of EOM Frequency Sidebands

The field modified by an electro-optic phase modulator (EOM) can be written in terms of individual frequency components with Bessel functions as their coefficients. For the purpose of understanding the mixing of these fields and their interactions with the ion, this chapter will derive in detail the equations describing the fields using some properties of Bessel functions.

An rf signal $V\sin(\omega_m t)$ applied to an electro-optic phase modulator changes an incident optical field $E_0\cos(kx - \omega_L t)$ to

$$(C.0.1) \quad E_1 = E_0\cos(kx - \omega_L t + \phi\sin(\omega_m t)),$$

where ϕ is the modulation index, which depends on the amplitude of modulation V . The modulated field contains frequency sidebands equally spaced by ω_m , and can also be expressed as

$$(C.0.2) \quad E_1 = \frac{E_0}{2} e^{i(kx - \omega_L t)} \sum_{n=-\infty}^{\infty} J_n(\phi) e^{in((\delta k)x - \omega_m t)} + c.c.$$

where $J_n(\phi)$ is the n -th order Bessel function with modulation index ϕ , and $\delta k = \omega_m/c$. The field amplitudes of the n -th sideband is thus $J_n(\phi)$.

When the modulated field passes through a nonlinear medium, the $\chi^{(2)}$ mixing results in frequency sum generation,

$$\begin{aligned} E_2 &= \chi^{(2)} E_1 E_1 = \chi^{(2)} E_0^2 \cos^2(kx - \omega_L t + \phi\sin(\omega_m t)) \\ &= \chi^{(2)} \frac{E_0^2}{2} [1 + \cos(2kx - 2\omega_L t + 2\phi\sin(\omega_m t))]. \end{aligned}$$

This optical field is equivalent to modulating a harmonic field $E_0^2\cos(2kx - 2\omega_L t)/2$ with frequency ω_m and modulation index 2ϕ , or alternatively can be written as

$$E_2 = \chi^{(2)} \frac{E_0^2}{4} e^{i(2kx - 2\omega_L t)} \sum_{n=-\infty}^{\infty} J_n(2\phi) e^{in((\delta k)x - \omega_m t)} + c.c.$$

When the fields along one arm of a Mach-Zehnder interferometer is delayed by a distance Δx with respect to the field in the other arm, the recombined field has

intensity

$$I = E_A E_B^* = \left| \frac{\chi^{(2)} E_0^2}{4} \right|^2 \left\{ e^{i2\phi \sin(\delta k x - \omega_m t)} e^{-i2\phi \sin(\delta k(x+\Delta x) - \omega_m t)} e^{i2k\Delta x} + c.c. \right\}.$$

Using sine addition formula $\sin(x) - \sin(y) = 2\sin[(x-y)/2] \cos[(x+y)/2]$, the above equation can be simplified to

$$\begin{aligned} I &= E_A E_B^* = \left| \frac{\chi^{(2)} E_0^2}{4} \right|^2 \left\{ e^{i4\phi \sin(\delta k \Delta x / 2) \cos(\delta k x - \omega_m t)} e^{i2k\Delta x} + c.c. \right\} \\ &= \left| \frac{\chi^{(2)} E_0^2}{4} \right|^2 \cos \left[4\phi \sin \left(\frac{\delta k \Delta x}{2} \right) \cos(\delta k x - \omega_m t) + 2k\Delta x \right] \end{aligned}$$

Again, this expression can be represented as a sum of frequency components with Bessel functions as the amplitudes:

$$I = E_A E_B^* = \frac{1}{2} \left| \frac{\chi^{(2)} E_0^2}{4} \right|^2 e^{ik\Delta x} \sum_{n=-\infty}^{\infty} J_n \left(4\phi \sin \left(\frac{\delta k \Delta x}{2} \right) \right) e^{in(\delta k x - \omega_m t)} + c.c.$$

When the modulation frequency $\omega_m = \omega'_0/2$ is half of the AC Stark shifted qubit frequency, only components of $E_A E_B^*$ oscillating at frequency $2\omega_m = \omega'_0$ contribute to the stimulated Raman transition. Therefore, the stimulated Raman transition rate is proportional to $J_2(4\phi \sin(\delta k \Delta x / 2))$. Note that the transition rate vanishes at the zero crossings of $J_2(b)$, including when the parameter $b = 0$ is zero. To maximize the transition rate, the operand $4\phi \sin(\delta k \Delta x / 2)$ should be set to the maximum of $J_2(b)$. For example, the first local maxima of $J_2(b)$ is at $b = 3.054$, by setting $\delta k \Delta x = \pi$ and $\phi = 0.764$.

APPENDIX D

Forced Harmonic Oscillators

In order to understand the spin-dependent force, we start by considering the effects when a force is applied to a harmonic oscillator. In general, a forced harmonic oscillator has a Hamiltonian of the form [72]

$$(D.0.1) \quad \hat{H} = \hbar\omega(\hat{a}^\dagger\hat{a} + \frac{1}{2}) + f^*(t)x_0\hat{a} + f(t)x_0\hat{a}^\dagger,$$

where \hat{a} and \hat{a}^\dagger are the annihilation and creation operators respectively, and $x_0 = \sqrt{\hbar/(2M\omega)}$ is the root mean square spatial spread of the ground state wavepacket. The first term is the unperturbed Hamiltonian for the harmonic oscillator, and the last two terms correspond to an external time-dependent force $f(t)$ applied to the system. In the interaction picture

$$(D.0.2) \quad \hat{H}_I(t) = f^*(t)x_0\hat{a}e^{-i\omega t} + f(t)x_0\hat{a}^\dagger e^{i\omega t}.$$

Assuming $f(t) = Fe^{-i(\omega-\delta)t}/2$ (corresponding to a classical force $f(t) = F \sin[(\omega-\delta)t]$) is detuned from the resonant frequency ω by a frequency $\delta \ll \omega$ much smaller than the trap frequency, then the interaction Hamiltonian can be rewritten as

$$(D.0.3) \quad \hat{H}_I(t) = \frac{F^*x_0}{2}\hat{a}e^{-i\delta t} + \frac{Fx_0}{2}\hat{a}^\dagger e^{i\delta t}.$$

The state after an interaction time t is prescribed by the time-evolution operator

$$(D.0.4) \quad \hat{U}(t) = \exp \left\{ -\frac{i}{\hbar} \left(\int_0^t \hat{H}_I(t')dt' + \frac{1}{2} \int_0^t dt' \int_0^{t'} dt'' [\hat{H}_I(t'), \hat{H}_I(t'')] + \dots \right) \right\}.$$

If we consider only the first term in the exponent of the evolution operator and substituting in the interaction Hamiltonian from Equation D.0.3, the resulting operator is exactly the displacement operator

$$(D.0.5) \quad \hat{D}(\alpha) = e^{\alpha\hat{a}^\dagger + \alpha^*\hat{a}},$$

with α defined as

$$(D.0.6) \quad \alpha(t) = -\frac{i}{\hbar} \int_0^t \frac{Fx_0}{2} e^{i\delta t'} dt'.$$

The displacement operator translates motional states in position/momentum phase space without distortion. For example, a displacement on an initial ground state of

motion results in a coherent state $|\alpha\rangle = \hat{D}(\alpha)|0\rangle$, where the final state is defined in terms of number states as

$$(D.0.7) \quad |\alpha\rangle = e^{-\frac{1}{2}|\alpha|^2} \sum_{n=0}^{\infty} \frac{\alpha^n}{\sqrt{n!}} |n\rangle.$$

In terms of x-p coordinates, $\alpha = (1/2x_0)(x + ip/M\omega)$.

The remaining higher order terms in the time-evolution operator originate from the non-commutative property of the interaction Hamiltonian at a given time with itself at different times. This can be understood by considering the displacement operators, which do not commute with one another but rather follow the commutation rule $\hat{D}(\alpha)\hat{D}(\beta) = \hat{D}(\alpha + \beta)e^{iIm(\alpha\beta^*)}$. Therefore the complete time-evolution operator can be constructed by integrating over infinitesimal displacements in time:

$$(D.0.8) \quad \hat{U}(t) = e^{i\Phi(t)} \hat{D}(\alpha(t)),$$

with the geometric phase accumulated over the entire path from time 0 to t expressed as

$$(D.0.9) \quad \Phi(t) = Im\left(\int_0^t \alpha(t')^* d\alpha(t')\right).$$

For a near-resonant driving force with detuning δ (Equation D.0.3), the initial motional state moves in a circular trajectory of radius $F/(2\hbar\delta)$ with periodicity $T = 2\pi/\delta$ in the rotating frame of harmonic motion, following the path (from Equation D.0.6)

$$(D.0.10) \quad \alpha(t) = \frac{Fx_0}{2\hbar\delta} (1 - e^{i\delta t}).$$

In one period of evolution under this force, the motional state returns to its original phase space coordinates, but acquires a geometric phase of

$$(D.0.11) \quad \Phi_0 = \frac{\pi |Fx_0|^2}{2(\hbar\delta)^2}$$

equivalent to the area enclosed by the trajectory.

APPENDIX E

Quantum Interference between Coherent States

The interference fringes of the Schrödinger's cat state in our experiments usually depend on the overlap of two separate coherent states. Here we include detailed calculations for the setup in section 4.2 using some properties of coherent states.

Start with the wavefunction in eq 4.2.4

$$|\psi(t)\rangle = \frac{1}{\sqrt{2}} e^{i\Phi(t)} |\uparrow_{\phi_S}\rangle |\alpha(t)\rangle - \frac{e^{i\phi_S}}{\sqrt{2}} e^{i\Phi(t)} |\downarrow_{\phi_S}\rangle |-\alpha(t)\rangle,$$

where $\alpha(t) = \alpha_0 (1 - e^{i\delta t})$ with $\alpha_0 = \eta\Omega/(2\delta)$, the probability of finding the ion in the $|\downarrow\rangle$ state becomes

$$\begin{aligned} P(\downarrow) &= |\langle\downarrow|\psi(t)\rangle|^2 \\ &= \left| \frac{1}{\sqrt{2}} \langle\downarrow|\uparrow_{\phi_S}\rangle |\alpha(t)\rangle - \frac{e^{i\phi_S}}{\sqrt{2}} \langle\downarrow|\downarrow_{\phi_S}\rangle |-\alpha(t)\rangle \right|^2 \\ &= \left| \frac{1}{2} |\alpha(t)\rangle - \frac{1}{2} |-\alpha(t)\rangle \right|^2 \\ &= \frac{1}{4} \{ \langle\alpha(t)|\alpha(t)\rangle - \langle-\alpha(t)|\alpha(t)\rangle - \langle\alpha(t)|-\alpha(t)\rangle + \langle-\alpha(t)|-\alpha(t)\rangle \}. \end{aligned}$$

Using the property

$$(E.0.1) \quad \langle\alpha|\beta\rangle = e^{\alpha^*\beta - \frac{1}{2}|\alpha|^2 - \frac{1}{2}|\beta|^2},$$

the result is eq 4.2.5:

$$(E.0.2) \quad P(\downarrow) = \frac{1}{2} \left\{ 1 - e^{-2|\alpha(t)|^2} \right\}.$$

For the thermal state, we first consider the displacement of each initial vibration level $|n\rangle$ individually:

$$|\psi_n(t)\rangle = a_{\uparrow_{\phi_S}}(0) |\uparrow_{\phi_S}\rangle \hat{D}(\alpha_{\uparrow_{\phi_S}}(t)) |n\rangle + a_{\downarrow_{\phi_S}}(0) |\downarrow_{\phi_S}\rangle \hat{D}(-\alpha_{\uparrow_{\phi_S}}(t)) |n\rangle.$$

where $\hat{D}(\alpha)$ is the displacement operator that translates a coherent state in phase space by α . The probability of finding the ion in the $|\downarrow\rangle$ state is

$$(E.0.3) \quad P_{thermal}(\downarrow) = \sum_{n=0}^{\infty} \frac{1}{1 + \bar{n}} \left(\frac{\bar{n}}{1 + \bar{n}} \right)^n |\langle\downarrow|\psi_n(t)\rangle|^2$$

$$= \sum_{n=0}^{\infty} \frac{1}{1+\bar{n}} \left(\frac{\bar{n}}{1+\bar{n}} \right)^n \left| \frac{1}{2} \hat{D}(\alpha(t)) |n\rangle - \frac{1}{2} \hat{D}(-\alpha(t)) |n\rangle \right|^2.$$

Here we note that $\hat{D}^\dagger(-\alpha) = \hat{D}(\alpha)$ and use the commutation rule for displacement operators:

$$(E.0.4) \quad \hat{D}(\beta) \hat{D}(\alpha) = e^{i\text{Im}(\alpha^* \beta)} \hat{D}(\alpha + \beta).$$

Equation E.0.3 becomes

$$P_{thermal}(\downarrow) = \sum_{n=0}^{\infty} \frac{1}{1+\bar{n}} \left(\frac{\bar{n}}{1+\bar{n}} \right)^n \left[\frac{1}{2} - \frac{1}{4} \langle n | \hat{D}(2\alpha(t)) | n \rangle - \frac{1}{4} \langle n | \hat{D}(-2\alpha(t)) | n \rangle \right].$$

The part of a wavefunction initially in $|n\rangle$ still remaining in the vibrational state $|n\rangle$ after a displacement $\hat{D}(2\alpha(t))$ is (see ref [73])

$$\langle n | \hat{D}(2\alpha(t)) | n \rangle = e^{-\frac{1}{2}|2\alpha(t)|^2} L_n(|2\alpha(t)|^2)$$

where

$$L_n(X) = \sum_{m=0}^n (-1)^m \binom{n}{n-m} \frac{X^m}{m!}.$$

are the Laguerre polynomials. Summing over the Laguerre polynomials, we arrive at eq 4.2.7:

$$\begin{aligned} P_{thermal}(\downarrow) &= \frac{1}{2} - \frac{1}{2} e^{-\frac{1}{2}|2\alpha(t)|^2} \sum_{n=0}^{\infty} \frac{1}{1+\bar{n}} \left(\frac{\bar{n}}{1+\bar{n}} \right)^n L_n(|2\alpha(t)|^2). \\ &= \frac{1}{2} \left(1 - e^{-(\bar{n}+\frac{1}{2})|2\alpha|^2} \right). \end{aligned}$$

For calculating the decoherence of the interference signal due to background heating, we start with eq 4.2.9:

$$|\psi_\beta(T)\rangle = \frac{e^{i(\theta+\mu_1)}}{\sqrt{2}} |\uparrow_{\phi_s}\rangle |\alpha_{\uparrow_{\phi_s}}(T)\rangle - \frac{e^{i(\phi_s-\theta+\mu_2)}}{\sqrt{2}} |\downarrow_{\phi_s}\rangle |\alpha_{\downarrow_{\phi_s}}(T)\rangle.$$

where θ , μ_1 , μ_2 , $\alpha_{\uparrow_{\phi_s}}(T)$ and $\alpha_{\downarrow_{\phi_s}}(T)$ are all dependent on the displacement β . The probability of measuring the state $|\downarrow\rangle$ at time T for a given displacement β is:

$$\begin{aligned} P_\beta(\downarrow) &= |\langle \downarrow | \psi_\beta(t) \rangle|^2 \\ &= \left| \frac{e^{i(\theta+\mu_1)}}{2} |\alpha_{\uparrow_{\phi_s}}(T)\rangle - \frac{e^{i(-\theta+\mu_2)}}{2} |\alpha_{\downarrow_{\phi_s}}(T)\rangle \right|^2 \\ &= \frac{1}{2} - \frac{1}{4} \left\{ e^{i(2\theta+\mu_1-\mu_2)} \langle \alpha_{\downarrow_{\phi_s}}(T) | \alpha_{\uparrow_{\phi_s}}(T) \rangle + c.c. \right\}, \end{aligned}$$

where

$$\alpha_{\uparrow_{\phi_s}}(T) = \alpha_0 e^{i\phi_M} (1 - e^{i\delta T}) + \beta,$$

$$\alpha_{\downarrow\phi_s}(T) = -\alpha_0 e^{i\phi_M}(1 - e^{i\delta T}) + \beta,$$

and the overlap is

$$\langle \alpha_{\downarrow\phi_s}(T) | \alpha_{\uparrow\phi_s}(T) \rangle = e^{-2|\alpha(T)|^2} e^{i\varphi},$$

where $\alpha(T) = \alpha_0 e^{i\phi_M}(1 - e^{i\delta T})$ and $\varphi = 2Im \{ \alpha_0 \beta^* e^{i\phi_M}(1 - e^{i\delta T}) \}$. The result is

$$P_\beta(\downarrow) = \frac{1}{2} \left\{ 1 - e^{-\frac{1}{2}|2\alpha(T)|^2} \cos(2\theta + \mu_1 - \mu_2 + \varphi) \right\}.$$

The dependences on β for the variables are

$$\theta = Im \{ \alpha_0^* \beta e^{-i\phi_M} (1 - e^{-i\delta t_1}) \} = -Im \{ \alpha_0 \beta^* e^{i\phi_M} (1 - e^{i\delta t_1}) \}.$$

$$\mu_1 = Im \left\{ \int_{t_1}^T [\alpha_0^* e^{-i\phi_M} (1 - e^{-i\delta t}) + \beta^*] [-i\delta \alpha_0 e^{i\phi_M} e^{i\delta t}] dt \right\},$$

$$\mu_2 = Im \left\{ \int_{t_1}^T [-\alpha_0^* e^{-i\phi_M} (1 - e^{-i\delta t}) + \beta^*] [i\delta \alpha_0 e^{i\phi_M} e^{i\delta t}] dt \right\},$$

$$\mu_1 - \mu_2 = -2Im \left\{ \int_{t_1}^T i\delta \alpha_0 \beta^* e^{i\phi_M} e^{i\delta t} dt \right\},$$

$$= -2Im \{ \alpha_0 \beta^* e^{i\phi_M} (e^{i\delta T} - e^{i\delta t_1}) \}.$$

$$\cos(2\theta + \mu_1 - \mu_2 + \varphi) = \cos(-4Im \{ \alpha_0 \beta^* e^{i\phi_M} (e^{i\delta T} - e^{i\delta t_1}) \})$$

$$= \cos(-4Im \{ \alpha_0 \beta^* e^{i\phi_M} e^{i\delta T} (1 - e^{-i\delta(T-t_1)}) \})$$

The random variable β has a Gaussian distribution uniform in phase with variance $\sigma^2 = \dot{n}T$, and the variable t_1 is also random. Therefore by symmetry we can remove the phase from the expression

$$P_{heating}(\downarrow) = \int_{-\infty}^{\infty} d\beta e^{\beta^2/2\sigma^2} \frac{1}{2} \left\{ 1 - e^{-\frac{1}{2}|2\alpha(T)|^2} \cos(4|\alpha_0|\beta) \right\}.$$

For an independent Gaussian random variable x with variance σ^2 , the expectation value of a function $\cos(ax)$ is

$$\langle \cos(ax) \rangle = e^{-\frac{1}{2}(a^2\sigma^2)}.$$

So the contribution from decoherence due to heating is

$$\langle \cos(2\theta + \mu_1 - \mu_2 + \varphi) \rangle = e^{-8|\alpha_0|^2 \dot{n}T}$$

and the probability due to heating is

$$P_{heating}(\downarrow) = \frac{1}{2} \left\{ 1 - e^{-\frac{1}{2}|2\alpha(T)|^2 - \frac{1}{2}|4\alpha_0|^2 \dot{n}T} \right\}$$

Accounting for both temperature and heating effects,

$$(E.0.5) \quad P(\downarrow) = \frac{1}{2} \left\{ 1 - e^{-\frac{1}{2}\dot{\bar{n}}t|4\alpha_0|^2 - (\bar{n} + \frac{1}{2})|2\alpha(t)|^2} \right\}.$$

APPENDIX F

Differential Stark Shift on Magnetic Field Insensitive States

In this appendix we will show that magnetic field insensitive states have no differential Stark shift in the limit where the detuning from the excited state is much larger than the hyperfine splitting, i.e. $\Delta_{HF}/\Delta \rightarrow 0$. To find the field insensitive states for a system in the $S_{1/2}$ ground state with some nuclear spin I , we write down the Hamiltonian for the hyperfine interaction in the presence of a magnetic field \mathbf{B} :

$$(F.0.1) \quad \hat{H} = \mu \cdot \mathbf{B} + A\hat{\mathbf{I}} \cdot \hat{\mathbf{J}} = g_J \mathbf{B} \cdot \hat{\mathbf{J}} + g_I \mathbf{B} \cdot \hat{\mathbf{I}} + A\hat{\mathbf{I}} \cdot \hat{\mathbf{J}},$$

where $\hat{\mathbf{J}}$ is the total angular momentum of the electron, $\hat{\mathbf{I}}$ is the nuclear spin, and $A\hat{\mathbf{I}} \cdot \hat{\mathbf{J}}$ is the contact term. g_I and g_J are the Lande g-factors for the nucleus and the electron. The eigenstates of the Hamiltonian are linear combinations of the m_F states, and can be represented as $|\Psi_i\rangle = a_i |g; m_J = \frac{1}{2}, m_I = m_{F,i} - \frac{1}{2}\rangle + b_i |g; m_J = -\frac{1}{2}, m_I = m_{F,i} + \frac{1}{2}\rangle$. The coefficients a and b are functions of the magnetic field. If two states $|\Psi_1\rangle$ and $|\Psi_2\rangle$ are magnetic field insensitive, then

$$(F.0.2) \quad \frac{\partial}{\partial B} (E_1 - E_2) = 0.$$

Applying Ehrenfest theorem,

$$(F.0.3) \quad \frac{\partial E_i}{\partial B} = \langle g_J J_z + g_I I_z \rangle = |a_i|^2 \left[\frac{g_J}{2} + g_I(m_{F,i} - \frac{1}{2}) \right] + |b_i|^2 \left[\frac{g_J}{2} + g_I(m_{F,i} + \frac{1}{2}) \right].$$

Normalization of the eigenstates and solving F.0.2 gives the result $|a_1|^2 = |a_2|^2 + g_I \Delta m_F / (g_J - g_I)$. Since the dipole moment of the electron dominates the dipole moment of the nucleus, i.e. $g_I/g_J \approx 10^{-3}$, we can approximate it as

$$(F.0.4) \quad |a_1|^2 = |a_2|^2, \quad |b_1|^2 = |b_2|^2.$$

Now consider the Stark shift for each of these magnetic field insensitive states. The AC Stark shift is given by

$$(F.0.5) \quad \chi_i = \sum_{m_J, m_I} \frac{\langle \Psi_i | E \cdot d | e, m_J m_I \rangle \langle e, m_J m_I | E \cdot d | \Psi_i \rangle}{\Delta - E_1 + E_i},$$

where $|e; m_J, m_I\rangle$ is the excited state with the corresponding z-component of the electron and nuclear spins. Since the electric dipole only couples the orbital angular momentum of the electron, Ψ_i only couples to the states with the same m_I . So the expression can be simplified to

(F.0.6)

$$\chi_i = |a_i|^2 \sum_{m_J} \frac{|\langle g; m_J = \frac{1}{2} | E \cdot d | e, m_J \rangle|^2}{\Delta - E_1 + E_i} + |b_i|^2 \sum_{m_J} \frac{|\langle g; m_J = -\frac{1}{2} | E \cdot d | e, m_J \rangle|^2}{\Delta - E_1 + E_i}.$$

If the energy difference between the two states Ψ_1 and Ψ_2 is small compared to Δ , and applying the results from equation F.0.4, then we find that $\chi_1 = \chi_2$. So we conclude that the energy shift due to Stark effect is the same for any two magnetic field insensitive states.

APPENDIX G

Two-ion Interactions

For small oscillations, there are two normal modes defined by the center-of-mass coordinate $\hat{q}_1 = (\hat{z}_1 + \hat{z}_2)/\sqrt{2}$ and a “stretch” coordinate $\hat{q}_2 = (\hat{z}_1 - \hat{z}_2)/\sqrt{2}$. The Hamiltonian for the collective system now sums over both ions and both vibrational modes:

Starting with the general Hamiltonian for two ions:

$$(G.0.1) \quad \hat{H}_0 = \sum_{i=1,2} \frac{\hbar\omega}{2} \hat{\sigma}_z^{(i)} + \sum_{\nu=1,2} \hbar\omega_\nu \hat{a}_\nu^\dagger \hat{a}_\nu,$$

where the normal modes of oscillation are defined by the center-of-mass coordinate $\hat{q}_1 = (\hat{z}_1 + \hat{z}_2)/\sqrt{2}$ and a “stretch” coordinate $\hat{q}_2 = (\hat{z}_1 - \hat{z}_2)/\sqrt{2}$, with oscillation frequency of each mode being ω_1 and $\omega_2 = \sqrt{3}\omega_1$ respectively, and \hat{a}_ν^\dagger and \hat{a}_ν the harmonic oscillator creation and annihilation operators for the normal modes $\nu = 1, 2$.

The interaction Hamiltonian for two ions becomes

$$(G.0.2) \quad \hat{H}_I = \sum_{i=1,2} \frac{\hbar\Omega_i}{2} \left(\sigma_+^{(i)} e^{i(\Delta\mathbf{k}\hat{\mathbf{r}}_i - (\delta\omega')t + \Delta\phi_i)} + \sigma_-^{(i)} e^{-i(\Delta\mathbf{k}\hat{\mathbf{r}}_i - (\delta\omega')t + \Delta\phi_i)} \right).$$

In the interaction frame of the vibrational levels, eq G.0.2 becomes

$$(G.0.3) \quad \hat{H}_I = \sum_{i=1,2} \frac{\hbar\Omega_i}{2} \left(\sigma_+^{(i)} e^{i[\eta_1(\hat{a}_1 e^{-i\omega_1 t} + \hat{a}_1^\dagger e^{i\omega_1 t}) \pm \eta_2(\hat{a}_2 e^{-i\omega_2 t} + \hat{a}_2^\dagger e^{i\omega_2 t})]} e^{-i((\delta\omega')t - \Delta\phi_i)} \right) + h.c.$$

The Lamb-Dicke parameters are given by $\eta_1 = \Delta k_z q_1/\sqrt{2}$ and $\eta_2 = \Delta q_2/\sqrt{2} = \eta_1/\sqrt[4]{3}$, representing the strength of coupling between the fields and each normal mode.

G.1. carrier transition

When the difference frequency of the optical sources is tuned to the free ion qubit resonance $\delta\omega' = 0$ (compensating for possible differential Stark shifts, assumed to be equal for the two ions), then

$$(G.1.1) \quad \hat{H}_I = \sum_{i=1,2} \sum_{n_1, n_2} \left(\frac{\hbar\Omega_i D_{n_1; n_2}}{2} \hat{\sigma}_+^{(i)} e^{i(\Delta k z_0^{(i)} - \Delta\phi_i)} + h.c. \right) |n_1, n_2\rangle \langle n_1, n_2|,$$

where the Debye-Waller factor $D_{n_1; n_2} = D_{n_1, n_1} \times D_{n_2, n_2} = e^{-(\eta_1^2 + \eta_2^2)/2} L_{n_1}(\eta_1^2) L_{n_2}(\eta_2^2)$ accounts for both modes. Assuming the Rabi frequencies are the same for both ions,

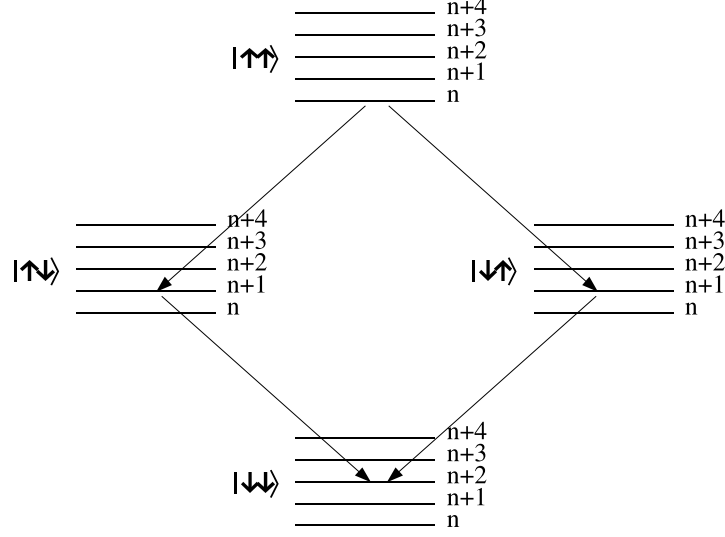


FIGURE G.2.1. Vibrational sideband transition with two ions. The red sideband field shown above couples $|\uparrow\uparrow n\rangle$ to $|\uparrow\downarrow n+1\rangle$ and $|\downarrow\uparrow n+1\rangle$, which in turn are coupled to $|\downarrow\downarrow n+2\rangle$ by the same driving fields. Therefore, the transition from $|\uparrow\uparrow n\rangle$ to $|\downarrow\downarrow n+2\rangle$ is $\sqrt{2(2n+3)}$ times faster than for a single ion to transfer from $|\uparrow n\rangle$ to $|\downarrow n+1\rangle$.

an initial state $|\uparrow\uparrow\rangle$ evolve as

$$\begin{aligned}
 |\psi(t)\rangle &= \left(\cos\left(\frac{\Omega t}{2}\right) |\uparrow_1\rangle - ie^{-i\phi_1} \sin\left(\frac{\Omega t}{2}\right) |\downarrow_1\rangle \right) \\
 &\times \left(\cos\left(\frac{\Omega t}{2}\right) |\uparrow_2\rangle - ie^{-i\phi_2} \sin\left(\frac{\Omega t}{2}\right) |\downarrow_2\rangle \right) |n_1, n_2\rangle.
 \end{aligned}$$

Each ion oscillates between the qubit states independently at the same Rabi frequency $D_{n_1; n_2} \Omega_0$, each with its own phase that depends on the phase of the fields at each ion's location $\Delta k z_0^{(i)}$.

G.2. First sideband transitions

The dynamics of sideband transition for two ions is very different from that of one ion because both ions are trying to change the same collective vibrational mode

simultaneously. The transition now couples $|\uparrow\uparrow n\rangle$ to $|\uparrow\downarrow n+1\rangle$ and $|\downarrow\uparrow n+1\rangle$, which in turn are coupled to $|\downarrow\downarrow n+2\rangle$ by the same driving fields. The Hamiltonian is

$$\hat{H}_I = \sum_{i=1,2} \sum_{n_1, n_2} \left(\frac{\eta_\nu \hbar \Omega_i D'_{n_1; n_2}}{2} \hat{\sigma}_+^{(i)} \hat{a}_\nu e^{i(\Delta k z_0^{(i)} - \Delta \phi_i)} + h.c. \right),$$

where $D'_{n_\nu; n_{\nu'}} = e^{-(\eta_1^2 + \eta_2^2)/2} (n_{\nu-1}!)^{-1} L_{n_\nu-1}^1(\eta_\nu^2) L_{n_{\nu'}-1}^1(\eta_{\nu'}^2)$ is the Debye-Waller factor for the first sideband, with $\nu' \neq \nu$ the 'spectator' mode of motion. The evolution follows the set of equations:

$$\begin{aligned} i\hbar \dot{a}_{\uparrow\uparrow n} &= \sqrt{n+1} \Omega' a_{\uparrow\downarrow n+1} + \sqrt{n+1} \Omega' a_{\downarrow\uparrow n+1}, \\ i\hbar \dot{a}_{\uparrow\downarrow n+1} &= \sqrt{n+1} \Omega'^* a_{\uparrow\uparrow n+1} + \sqrt{n+2} \Omega' a_{\downarrow\downarrow n+2}, \\ i\hbar \dot{a}_{\downarrow\uparrow n+1} &= \sqrt{n+1} \Omega'^* a_{\uparrow\uparrow n+1} + \sqrt{n+2} \Omega' a_{\downarrow\downarrow n+2}, \\ i\hbar \dot{a}_{\downarrow\downarrow n+2} &= \sqrt{n+2} \Omega'^* a_{\uparrow\downarrow n+1} + \sqrt{n+2} \Omega'^* a_{\downarrow\uparrow n+1}, \end{aligned}$$

where $\Omega' = \eta D'_{n_\nu; n_{\nu'}} \Omega_0$. For an initial condition of $a_{\uparrow\uparrow n}(0) = 1$ and $a_{\uparrow\downarrow n+1}(0) = a_{\downarrow\uparrow n+1}(0) = a_{\downarrow\downarrow n+2}(0) = 0$, the solution is [51]

$$\begin{aligned} a_{\uparrow\uparrow n}(t) &= 1 - \frac{n+1}{2n+3} \left[1 - \cos \left(\sqrt{2(2n+3)} t \right) \right], \\ a_{\uparrow\downarrow n+1}(t) &= a_{\downarrow\uparrow n+1}(t) = \sqrt{\frac{n+1}{2(2n+3)}} \sin \left(\sqrt{2(2n+3)} t \right), \\ a_{\downarrow\downarrow n+2}(t) &= \frac{\sqrt{(n+1)(n+2)}}{2n+3} \left[\cos \left(\sqrt{2(2n+3)} t \right) - 1 \right]. \end{aligned}$$

For $n=0$ ground state of vibration, the ions transfer from $|\uparrow\uparrow 0\rangle$ to $|\downarrow\downarrow 2\rangle$ in time $t = \pi/\Omega_{sb}$, where $\Omega_{sb} = \sqrt{6}\eta\Omega$.

Bibliography

- [1] R P Feynman. Simulating physics with computers. *Int. J. Th. Phys.*, 21(6/7):467–488, 1981.
- [2] P W Shor. Algorithms for quantum computation: Discrete logarithms and factoring. In *Proceedings of the 35th Annual Symposium on the Foundations of Computer Science*, page 124, New York, 1994. IEEE Computer Society, IEEE Computer Society Press.
- [3] C H Bennett, G Brassard, and N David Mermin. Quantum cryptography without Bell’s theorem. *Phys. Rev. Lett.*, 68:557–559, 1992.
- [4] A K Ekert. Quantum cryptography based on bell’s theorem. *Phys. Rev. Lett.*, 67:661–664, 1991.
- [5] Lov K Grover. Quantum mechanics helps in searching for a needle in a haystack. *Phys. Rev. Lett.*, 79(2):325–328, July 1997.
- [6] H G Dehmelt. *Phys. Rev.*, 103:1125, 1962.
- [7] W Paul, O Osberghaus, and E Fischer. *Forschungsber. Wirtsch. Verkehrsminist. Nordrhein-Westfalen*, 415, 1958.
- [8] D J Wineland and W M Itano. Laser cooling of atoms. *Phys. Rev. A*, 20(4):1521–1540, October 1979.
- [9] D J Wineland, W M Itano, and R S VanDyck. High resolution spectroscopy of stored ions. *Adv. Atom. Mol. Phys.*, 19:135–186, 1983.
- [10] J I Cirac and P Zoller. Quantum computation with cold, trapped ions. *Phys. Rev. Lett.*, 74(20):4091–4094, May 1995.
- [11] C Monroe, D M Meekhof, B E King, W M Itano, and D J Wineland. Demonstration of a fundamental quantum logic gate. *Phys. Rev. Lett.*, 75(25):4714–4717, December 1995.
- [12] F Schmidt-Kaler, H Häffner, M Riebe, S Gulde, G P T Lancaster, T Deuschle, C Becher, C F Roos, J Eschner, and R Blatt. Realization of the cirac-zoller controlled-not quantum gate. *Nature*, 422:408–411, 2003.
- [13] K Mølmer and A Sørensen. Multiparticle entanglement of hot trapped ions. *Phys. Rev. Lett.*, 82:1835–1838, 1999.
- [14] G J Milburn, S Schneider, and D F V James. Ion trap quantum computing with warm ions. *Fortschr. Phys.*, 48:9–11, 801–810, 2000.
- [15] C A Sackett, D Kielpinski, B E King, C Langer, V Meyer, C J Myatt, M Rowe, Q A Turchette, W M Itano, D J Wineland, and C Monroe. Experimental entanglement of four particles. *Nature*, 404:256–258, March 2000.
- [16] J J Garcia-Ripoll, P Zoller, and J I Cirac. Speed optimized two-qubit gates with laser coherent control techniques for ion trap quantum computing. *Phys. Rev. Lett.*, 91:157901, 2003.
- [17] D Leibfried, B DeMarco, V Meyer, D Lucas, M Barrett, J Britton, W M Itano, B Jelenkovic, C Langer, T Rosenband, and D J Wineland. Experimental demonstration of a robust, high-fidelity geometric two ion-qubit phase gate. *Nature*, 422:412–415, 2003.

- [18] D. Kielpinski, C Monroe, and D J Wineland. Architecture for a large-scale ion-trap quantum computer. *Nature*, 417:709–711, 2002.
- [19] D P Divincenzo. The physical implementation of quantum computation. *Fortschritte der Physik*, 48:771–783, 2000.
- [20] A Sørensen and K Mølmer. Quantum computation with ions in thermal motion. *Phys. Rev. Lett.*, 82:1971–, 1999.
- [21] W Paul. Electromagnetic traps for charged and neutral particles. *Rev. Mod. Phys.*, 62:531–540, 1990.
- [22] M Abramowitz and I A Stegun. *Handbook of Mathematical Functions*. U.S. Gov’t. Printing Office, Washington, D.C., 1964.
- [23] J H Moore, C C Davis, and M A Coplan. *Building Scientific Apparatus: A Practical Guide to Design and Construction*. Addison-Wesley Publishing Company, Reading, Massachusetts, 1983.
- [24] W W Macalpine. Coaxial resonators with helical inner conductor. *Proceedings of the IRE*, 47:2099, 1959.
- [25] Nist atomic spectra database, version 3.0, 2005.
- [26] D J Wineland, C Monroe, W M Itano, D Leibfried, B E King, and D M Meekhof. Experimental issues in coherent quantum-state manipulation of trapped atomic ions. *J. Res. Nat. Inst. Stand. Tech.*, 103:259–328, May 1998.
- [27] B Blinov, L Deslauriers, P Lee, M Madsen, R Miller, and C Monroe. Sympathetic cooling of trapped cd^+ isotopes. *Phys. Rev. A*, 65:040304, 2002.
- [28] U Tanaka, H Imajo, K Hayasaka, R Ohmukai, M Watanabe, and S Urabe. Determination of the ground-state hyperfine splitting of trapped $^{113}\text{cd}^+$ ions. *Phys. Rev. A*, 53:3982–3985, 1996.
- [29] J Cariou and P Luc. *Atlas du spectre d’absorption de molecule d’iode*. Laboratoire Aime-Cotton, CNRS, Orsay, France, 1977.
- [30] J Cariou and P Luc. *Atlas du spectre d’absorption de la molecule de tellure*. Laboratoire Aime-Cotton, CNRS, Orsay, France, 1980.
- [31] D James. Quantum dynamics of cold trapped ions with applications to quantum computing. *Appl. Phys. B*, 66:181–190, 1998.
- [32] R Miller, T E Northup, K M Birnbaum, A Boca, A D Boozer, and H J Kimble. Trapped atoms in cavity qed: coupling quantized light and matter. *J. Phys. B: Atom. Mol. Phys.*, 38:S551–S565, 2005.
- [33] A Blais, R Huang, A Wallraff, S M Girvin, and R J Schoelkopf. Cavity quantum electrodynamics for superconducting electrical circuits: An architecture for quantum computation. *Phys. Rev. A*, 69:062320, 2004.
- [34] H J Metcalf and P van der Straten. *Laser Cooling and Trapping*. Springer, New York, 1999.
- [35] P J Lee, K A Brickman, L Deslauriers, P C Haljan, L M Duan, and C Monroe. Phase control of trapped ion quantum gates. *J. Opt. B: Quantum Semiclass. Opt.*, 7:S371–S383, 2005.
- [36] R Ozeri, C Langer, J D Jost, B DeMarco, A Ben-Kish, B R Blakestad, J Britton, J Chiaverini, W M Itano, D B Hume, D Leibfried, T Rosenband, P O Schmidt, and D J Wineland. Hyperfine coherence in the presence of spontaneous photon scattering. *Phys. Rev. Lett.*, 95:030403, 2005.
- [37] P J Lee, B B Blinov, K Brickman, L Deslauriers, M J Madsen, R Miller, D L Moehring, D Stick, and C Monroe. Atomic qubit manipulations with an electro-optic modulator. *Optics Lett.*, 28:1852, 2003.

- [38] A Yariv and P Yeh. *Optical Waves in Crystals*. John Wiley & Sons, New York, 1984.
- [39] M Kasevich and S. Chu. Measurement of the gravitational acceleration of an atom with a light-pulse atom interferometer. *Appl. Phys. B*, 54:321–328, 1992.
- [40] Q A Turchette, D Kilepinski, B E King, D Leibfried, D M Meekhof, C J Myatt, M A Rowe, C A Sackett, C S Wood, W M Itano, C Monroe, and D J Wineland. Heating of trapped ions from the quantum ground state. *Phys. Rev. A*, 61:063418, June 2000.
- [41] C Monroe, D M Meekhof, B E King, S R Jefferts, W M Itano, D J Wineland, and P Gould. Resolved-sideband raman cooling of a bound atom to the 3d zero-point energy. *Phys. Rev. Lett.*, 75(22):4011–4014, November 1995.
- [42] L Deslauriers, P C Haljan, P J Lee, K-A Brickman, B B Blinov, M J Madsen, and C Monroe. Zero-point cooling and low heating of trapped cd ions. *Phys. Rev. A*, 70:043408, 2004.
- [43] E Schrödinger. The present situation in quantum mechanics. *Naturwissenschaften*, 23:807–812,823,844–849, 1935.
- [44] J R Friedman, V Patel, W Chen, S K Tolpygo, and J E Lukens. Quantum superposition of distinct macroscopic states. *Nature*, 406:43–46, 2000.
- [45] W Wernsdorfer, E Bonet Orozco, K Hasselbach, A Benoit, D Mailly, O Kubo, H Nakano, and B Barbara. Macroscopic quantum tunneling of magnetization of single ferrimagnetic nanoparticles of barium ferrite. *Phys. Rev. Lett.*, 79:4014–4017, 1997.
- [46] M Brune, E Hagley, J Dreyer, X Maître, A Maali, C Wunderlich, J Raimond, and S Haroche. *Phys. Rev. Lett.*, 77:4887, 1996.
- [47] M Arndt, O Nairz, J Vos-Andreae, C Keller, G Van Der Zouw, and A Zeilinger. Wave-particle duality of C₆₀ molecules. *Nature*, 401:680–682, 1999.
- [48] C Monroe, D M Meekhof, B E King, and D J Wineland. A “Schrödinger Cat” superposition state of an atom. *Science*, 272:1131–1136, May 1996.
- [49] P C Haljan, K-A Brickman, L Deslauriers, P J Lee, and C Monroe. Spin-dependent forces on trapped ions for phase-stable quantum gates and motional schrödinger cat states. *Phys. Rev. Lett.*, 94:153602, 2005.
- [50] D J Wineland, M Barrett, J Britton, J Chiaverini, B DeMarco, W M Itano, B Jelenković, C Langer, D Leibfried, V Meyer, T Rosenband, and T Schätz. Quantum information processing with trapped ions. page 0212079, 2002.
- [51] B E King, C S Wood, C J Myatt, Q A Turchette, D Leibfried, W M Itano, C Monroe, and D J Wineland. Cooling the collective motion of trapped ions to initialize a quantum register. *Phys. Rev. Lett.*, 81:1525–1528, August 1998.
- [52] J J Bollinger, W M Itano, D J Wineland, and D J Heinzen. Optimal frequency measurements with maximally correlated states. *Phys. Rev. A*, 54(6):R4649–R4652, December 1996.
- [53] C H Bennett, G Brassard, S Popescu, B Schumacher, J A Smolin, and W K Wootters. Purification of noisy entanglement and faithful teleportation via noisy channels. *Phys. Rev. Lett.*, 76:722, 2002.
- [54] D P DiVincenzo. Two-bit gates are universal for quantum computation. *Phys. Rev. A*, 51(2):1015–1022, February 1995.
- [55] H Häffner, S Gulde, M Riebe, G Lancaster, C Becher, , J Eschner, F Schmidt-Kaler, and R Blatt. Precision measurement and compensation of optical stark shifts for an ion-trap quantum processor. *Phys. Rev. Lett.*, 90:143602, 2003.

- [56] D Leibfried, R Blatt, C Monroe, and D Wineland. Quantum dynamics of single trapped ions. *Rev. Mod. Phys.*, 75:281, 2003.
- [57] D M Meekhof, C Monroe, W M Itano, B E King, and D J Wineland. Generation of nonclassical motional states of a trapped atom. *Phys. Rev. Lett.*, 76(11):1796–1799, March 1996.
- [58] D Leibfried, D M Meekhof, B E King, C Monroe, W M Itano, and D J Wineland. Experimental determination of the motional quantum state of a trapped atom. *Phys. Rev. Lett.*, 77(21):4281–4285, November 1996.
- [59] C F Roos, G P T Lancaster, M Riebe, H Häffner, W Hänsel, S Gulde, C Becher, J Eschner, F Schmidt-Kaler, and R Blatt. Bell states of atoms with ultralong lifetimes and their tomographic state analysis. *Phys. Rev. Lett.*, 92:220402, 2004.
- [60] D F V James, P G Kwiat, W J Munro, and A G White. Measurement of qubits. *Phys. Rev. A*, 64:052312, 2001.
- [61] J B Altepeter, D F V James, and P G Kwiat. *Lecture Notes in Physics*, 649:113, 2004.
- [62] A Stuart and J K Ord. *Kendall’s Advanced Theory of Statistics vol. 1*. Oxford University Press, Oxford, 1987.
- [63] A Peres. *Phys. Rev. Lett.*, 77:1413, 1996.
- [64] M Horodecki, P Horodecki, and R Horodecki. *Phys. Rev. A*, 223:1, 1996.
- [65] G Vidal and R F Werner. *Phys. Rev. A*, 65:032314, 2002.
- [66] J Eisert and M B Plenio. *J. Mod. Opt.*, 46:145, 1999.
- [67] M B Plenio and S Virmani. *quant-ph/0504163*, 2002.
- [68] W K Wootters. Entanglement of formation of an arbitrary state of two qubits. *Phys. Rev. Lett.*, 80:2245–2248, 1998.
- [69] B Efron and R J Tibshirani. *An introduction to the Bootstrap*. Chapman and Hall, 1993.
- [70] P C Haljan, P J Lee, K A Brickman, M Acton, L Deslauriers, and C Monroe. Entanglement of trapped-ion clock states. *quant-ph/0504163*, 2005.
- [71] A E Siegman. *Lasers*. Stanford University Press, Stanford, 1986.
- [72] E Merzbacher. *Quantum Mechanics*. John Wiley and Sons, Inc, New York, third edition, 1998.
- [73] P Carruthers and M M Nieto. Coherent states and the forced quantum oscillator. *Am. J. Phys.*, 33:537–544, 1965.

Index

- scan
 - frequency, 53
- AC Stark shift, 43
 - clock states, 133
 - two ions, 97
- AC Stark shift
 - two ions, 106
- acousto-optic modulator, *see* modulator
- average vibrational number, 59
- BBO, 20, 52
- Bell state, 100
- Bessel function, 49, 125
- branching ratio, 46, 47
- cadmium
 - neutral, 11
- camera, 27
- cavity, 121
 - BBO, 123
 - detuning, 51, 56
 - stability parameter, 121
- Cirac-Zoller scheme, 65
- clock states, 18
 - AC Stark shift, 133
- coherent state, 128
 - interference (thermal), 70
 - interference, 69, 93
- coherent state
 - interference, 129
- collision
 - background gas, 12
- computer interface, 28
- controlled-NOT gate, 2, 88
- cooling
 - Doppler, 12
 - effects of micromotion, 15
 - Raman sideband, 58
 - sympathetic, 14
- Debye-Waller factor, 38
- density matrix, 100
- detection
 - CCD, 112
 - error, 29
 - fidelity, 30
 - histogram, 31
 - qubit state, 18
 - two ions, 31
 - CCD, 27
 - error, 32
 - fidelity, 33
 - two ions, 32
- displacement operator, 66, 127
 - commutation rule, 128
- Doppler cooling, 12
 - effects of micromotion, 15
- electro-optic modulator, *see* modulator
- entanglement of formation, 114
- evolution operator, 127
- fidelity, 100, 112, 114
- forced harmonic oscillator, 127
- free spectral range, 49
- frequency doubler, 20, 121, 125
 - LBO, 20
 - BBO, 20
- frequency scan, 53

- geometric phase
 - definition, 128
- geometric phase gate, 90
- GPIB, 53, 54
- Grover's algorithm, 1
- Hamiltonian
 - magnetic dipole, 36
 - steady state, 35, 36
- harmonic oscillator, 118
 - forced, 127
 - two ions, 135
- heating, 64, 70, 130
- hyperfine interaction, 18, 133
- imaging, 14, 27, 32
- initialization, 18
- interaction picture, 118
- ion trap, 6
 - lifetime, 12
 - micromotion, 5
 - pseudo-potential, 5
 - secular motion, 5
- ion trap
 - linear, 6
 - loading, 9
 - asymmetric quadrupole, 4
- isotope, 13, 17
- isotope
 - energy shift, 13
- LabView, 27, 52
- Laguerre polynomial, 38, 120, 130
- Lamb-Dicke Limit, 38
- Lamb-Dicke parameter, 38, 40, 43, 44
- Lande g-factors, 133
- Langevin rate, 12
- laser, 19
 - lock, 20
 - noise, 94
- lasers, 52
 - Melles-Griot, 52
 - Nd:YAG, 19
 - Ti:Sapphire, 20, 24, 52
- LBO, 20
- linewidth
 - $\text{Cd}^+ P_{3/2}$, 13
- Mach-Zehnder, 50, 54, 56
- Mathieu equation, 5
- matrices, 121
- maximum likelihood estimation, 110
- Maxwell-Boltzmann distribution, 58, 71
- micromotion, 5
- micromotion
 - cancellation, 7
 - measurement, 14
- microwave, 40
- modulator
 - acousto-optic (AOM), 25
 - electro-optic (EOM), 26, 49, 125
- Molmer-Sorensen gate, 68, 91, 92
 - fidelity, 100
- motion, 37
- negativity, 114
- noise
 - laser, 94
- noise-eater, 96
- nuclear spin, 18
- parity, 100
- PCI card
 - counter, 28
 - pulse generator, 27
- phase coherence, 87, 93
 - σ_ϕ force, 78
- phase gate, 89
- phase scan, 54
- photoionization, 11
- photomultiplier tube (PMT), 19
- Polarization
 - Raman fields, 44
- polarization
 - detection, 18
 - initialization, 18
- pseudo-potential, 5
- pulse sequence, 27

- quantization axis, 45
- qubit, 17, 34
 - detection, 18
 - initialization, 18
 - rotation, 37
- Rabi oscillation, 36
 - Raman transition, 56
 - temperature effects, 59
 - microwave, 40
- Rabi oscillation
 - motion sensitive, 38
- Raman cooling, 58
- Raman spectrum
 - AO scan, 57
 - EO scan, 55
- Raman transition, 41
 - copropagating, 43
 - detuning, 42
 - sideband, 60
 - two ions, 135
- Raman transition
 - non-copropagating, 44
 - sideband, 68
- rf, 8
 - modulator signals, 52
 - resonator, 8
- Rotating Wave Approximation (RWA), 36
- rotation, 37, 105, 106, 108, 110
- rotation
 - arbitrary, 37
- saturation intensity, 13, 19, 29
- saturation parameter, 13
- scan
 - phase, 54
 - time, 54
 - frequency, 75, 76
 - time, 77
- Schrödinger's cat, 67
- second harmonic generation, 20, 49, 123
- secular motion, 5
- Shor's algorithm, 1
- sideband cooling, 58
- spectrum, 54
 - AO scan, 99
- spin-dependent force, 65
 - σ_ϕ , 91
 - σ_z , 133
 - σ_ϕ , 68
- spin-dependent force
 - σ_z , 84
- spontaneous emission, 48
 - large detuning, 48
- spontaneous emission
 - rate, 13
- sum frequency generation, 20, 49, 123
- switch
 - rf, 27
- sympathetic cooling, 14
- tellurium, 20
- thermal distribution, 58, 71
- thermal state
 - coherent state, 130
- time scan, 54
- time-evolution operator, 127
- tomography, 109
- trap axis, 6, 35, 45
- TTL, 27
- universal logic, 3
- vacuum, 7
 - cadmium oven, 9
 - electron gun, 9
 - ion lifetime, 12
- vibration
 - normal modes, 135
 - coupling, 37
 - normal modes, 90